

DISS ETH No. 30216

# Dielectric phenomena at magnetic quantum critical points

A thesis submitted to attain the degree of

DOCTOR OF SCIENCES  
(Dr. sc. ETH Zurich)

presented by

DANIEL FLAVIÁN BLASCO



2024



DISS. ETH NO. 30216

# Dielectric phenomena at magnetic quantum critical points

A thesis submitted to attain the degree of

DOCTOR OF SCIENCES  
(Dr. sc. ETH Zurich)

presented by

DANIEL FLAVIÁN BLASCO

MSc ETH in Physics  
ETH Zurich

born on 22.03.1996

accepted on the recommendation of  
Prof. Dr. Andrey Zheludev  
Prof. Dr. Premala Chandra

2024



## Abstract

The interplay between magnetic and dielectric degrees of freedom gives rise to novel emergent phases in condensed matter systems. In the proximity to quantum critical points, exotic phenomena are stabilized by quantum fluctuations. In this work, we investigate experimentally dielectric phenomena at magnetic quantum critical points. Our focus are the highly frustrated quasi-one-dimensional quantum magnets  $\text{Rb}_2\text{Cu}_2\text{Mo}_3\text{O}_{12}$  and  $\text{Cs}_2\text{Cu}_2\text{Mo}_3\text{O}_{12}$ . These systems offer several experimentally accessible field-induced quantum critical points, all of which can be described in terms of Bose-Einstein Condensation (BEC) of magnons.

Electrometry is shown as an extremely sensitive technique to detect phase transitions and map out the magnetic phase diagrams on both materials. Our data uncovers yet unnoticed presaturation phases in  $\text{Rb}_2\text{Cu}_2\text{Mo}_3\text{O}_{12}$ .

More importantly, we demonstrate how magneto-electric coupling provides completely new perspectives on quantum criticality. A comprehensive set of dielectric permittivity data shows that the domes of long-range order are in fact multiferroic. The bilinear coupling that arises at the spin saturation transition between ferroelectric polarization and staggered magnetization implies that both quantities are primary order parameters at the quantum phase transition. As a result, the critical susceptibility,  $\chi$ , of this BEC quantum critical point can be unprecedentedly accessed via the dielectric channel, and measured directly in a probe-response experiment. Our results in both  $\text{Rb}_2\text{Cu}_2\text{Mo}_3\text{O}_{12}$  and  $\text{Cs}_2\text{Cu}_2\text{Mo}_3\text{O}_{12}$  are in agreement with long-standing predictions of BEC criticality.

The main observation of this work is the emergence of a new magneto-electric phenomenon in the dielectric response of  $\text{Cs}_2\text{Cu}_2\text{Mo}_3\text{O}_{12}$ : the relaxation of electric dipoles mediated by quantum critical magnons. Complex capacitance measurements in the millikelvin regime reveal a distinct dissipative feature, with its temperature-dependent amplitude due to low-energy lattice excitations and an activation behavior of the relaxation time. The activation energy softens the a field-tuned magnetic quantum critical point ( $H = H_c$ ) and follows the single-magnon Zeeman energy for  $H > H_c$ , showing its magnetic origin. These measurements firmly prove the electrical activity of coupled low-energy spin and lattice excitations, an example of quantum multiferroic behavior.

Dipolar relaxation is also found in  $\text{Rb}_2\text{Cu}_2\text{Mo}_3\text{O}_{12}$ , albeit mediated by optical phonons. This hints at the origin of the electric dipoles being specific vacancies in both materials, however a microscopic model for the coupling to magnetic fluctuations is lacking.

On a different note, this work also explores the magnetism of the highly frustrated, 2D kagome rare-earth magnet  $\text{Nd}_3\text{BWO}_9$ . The lack of intrinsic disorder in single crystals and the strong antiferromagnetic interactions without long-range order qualify it as a prime candidate for realize the long-sought quantum spin liquid. Yet our experimental investigation reveals a completely different scenario. A study of the crystal electric field shows that the low-energy physics can be described in terms of  $j_{eff} = 1/2$  spins, with significant Ising anisotropy. Thermodynamic and magnetic measurements are combined to map out the magnetic phase diagram, finding several domes of long-range order is found below 300 mK. Strikingly, fractional magnetization plateaux are found for all field geometries, with different structures for each. Neutron diffraction elucidates the magnetic structures, revealing complex spin-density wave behavior. All the results highlight the strong frustration in  $\text{Nd}_3\text{BWO}_9$  while showing that it is a network of weakly coupled 1D-spin tubes, perpendicular to the kagome planes.



## Zusammenfassung

Das Zusammenspiel zwischen magnetischen und dielektrischen Freiheitsgraden führt zu neuartigen emergenten Phasen in Systemen aus kondensierter Materie. In der Nähe von quantenkritischen Punkten werden exotische Phänomene durch Quantenfluktuationen stabilisiert. In dieser Arbeit untersuchen wir experimentell dielektrische Phänomene an magnetischen Quantenkritischen Punkten. Unser Fokus sind die hoch frustrierten quasi-eindimensionalen Quantenmagnete  $\text{Rb}_2\text{Cu}_2\text{Mo}_3\text{O}_{12}$  und  $\text{Cs}_2\text{Cu}_2\text{Mo}_3\text{O}_{12}$ . Diese Systeme bieten mehrere experimentell zugängliche, feldinduzierte quantenkritische Punkte, die alle mit Hilfe der Bose-Einstein-Kondensation (BEC) von Magnonen beschrieben werden können.

Elektrometrie erweist sich als äußerst empfindliche Technik zum Nachweis von Phasenübergängen und zur Kartierung der magnetischen Phasendiagramme beider Materialien. Unsere Daten decken bisher unentdeckte Vorsättigungsphasen in  $\text{Rb}_2\text{Cu}_2\text{Mo}_3\text{O}_{12}$  auf.

Was noch wichtiger ist: die magneto-elektrische Kopplung eröffnet völlig neue Perspektiven auf die Quantenkritikalität. Ein umfangreicher Datensatz zur Dielektrizitätskonstante zeigt, dass die Kuppeln mit weitreichender Ordnung in der Tat multiferroisch sind. Die bilineare Kopplung, die am Spin-Sättigungsübergang zwischen ferroelektrischer Polarisation und versetzter Magnetisierung auftritt, impliziert, dass beide Größen primäre Ordnungsparameter am Quantenphasenübergang darstellen. Infolgedessen kann die kritische Suszeptibilität  $\chi$  dieses kritischen BEC-Quantenpunkts über den dielektrischen Kanal erreicht und direkt in einem Probe-Response-Experiment gemessen werden. Unsere Ergebnisse sowohl für  $\text{Rb}_2\text{Cu}_2\text{Mo}_3\text{O}_{12}$  als auch für  $\text{Cs}_2\text{Cu}_2\text{Mo}_3\text{O}_{12}$  stimmen mit langjährigen Vorhersagen zur BEC-Kritikalität überein.

Die Hauptbeobachtung dieser Arbeit ist das Auftreten eines neuen magneto-elektrischen Phänomens in der dielektrischen Reaktion von  $\text{Cs}_2\text{Cu}_2\text{Mo}_3\text{O}_{12}$ : die Relaxation von elektrischen Dipolen, die durch quantenkritische Magnonen vermittelt wird. Komplexe Kapazitätsmessungen im Millikelvin-Bereich zeigen ein ausgeprägtes dissipatives Merkmal mit einer temperaturabhängigen Amplitude, die auf niederenergetische Gitteranregungen und ein Aktivierungsverhalten der Relaxationszeit zurückzuführen ist. Die Aktivierungsenergie wird an einem auf das Feld abgestimmten magnetischen Quantenkritischen Punkt ( $H = H_c$ ) abgeschwächt und folgt der Einzelmagnon Zeeman-Energie für  $H > H_c$ , was ihren magnetischen Ursprung beweist. Diese Messungen belegen eindeutig die elektrische Aktivität von gekoppelten niederenergetischen Spin- und Gitteranregungen, ein Beispiel für quantenmultiferroisches Verhalten.

Dipolare Relaxation findet sich auch in  $\text{Rb}_2\text{Cu}_2\text{Mo}_3\text{O}_{12}$ , allerdings vermittelt durch optische Phononen. Dies deutet darauf hin, dass der Ursprung der elektrischen Dipole spezifische kristallographische Leerstellen in beiden Materialien sind, allerdings fehlt ein mikroskopisches Modell für die Kopplung mit magnetischen Fluktuationen.

Weiters wurde in dieser Arbeit der Magnetismus des stark frustrierten 2D-Kagome Seltene-Erden-Magneten  $\text{Nd}_3\text{BWO}_9$  untersucht. Das Fehlen intrinsischer Unordnung in Einkristallen und die starken antiferromagnetischen Wechselwirkungen ohne langreichweitige Ordnung qualifizieren ihn als Hauptkandidaten für die Realisierung der lange gesuchten Quanten-Spinflüssigkeit. Unsere experimentellen Untersuchungen zeigen jedoch ein völlig anderes Szenario. Eine Analyse des elektrischen Feldes des Kristalls zeigt, dass die Niederenergiephysik mit  $j_{eff} = 1/2$  Spins beschrieben werden kann, wobei eine deutliche Ising-Anisotropie vorliegt. Durch die Kombination von thermodynamischen und magnetischen Messungen wird das

magnetische Phasendiagramm abgebildet, wobei mehrere Phasen langreichweitiger Ordnung unter 300 mK gefunden werden. Bemerkenswert ist, dass fraktionierte Magnetisierungsplateaus für alle Feldgeometrien gefunden werden, mit jeweils unterschiedlichen Strukturen. Neutronenbeugung klärt die magnetischen Strukturen auf und offenbart ein komplexes Spin-Dichte-Wellenverhalten. Alle Ergebnisse heben die starke Frustration in  $\text{Nd}_3\text{BWO}_9$  hervor und zeigen gleichzeitig, dass es sich um ein Netzwerk von schwach gekoppelten 1D-Spinröhren handelt, die senkrecht zu den Kagome-Ebenen verlaufen.

# Aknowledgements

First and foremost, I would like to express my gratitude to my supervisor, Andrey Zheludev, for his support throughout the whole length of this project. Not only on the scientific side his guidance was always on point, but on an extended professional perspective his advice and mentoring has been extremely welcome.

I want to extend my appreciation to all the team of the Neutron Scattering and Magnetism during my time at ETH Zurich. A big thanks goes to Jakob Nagl for backing me in the development of our shared project(s) and the enriching physics exchanges. Thanks to Shohei Hayashida for always taking me under his wing during the beginning of my learning curve and beyond. Thanks to Kirill Povarov for sharing his unending knowledge in magnetism. Thanks to Seva Gvasaliya for his constant striving for perfectly functioning machines, even if it was not always easy. Thanks to Lena Stoppel for all her support and kindness (and schoggi!). Thanks to Zewu Yan for his patience in the lab, showing me his art. Thanks to Mengze for all the random theoretical discussions. Thanks to Florian, Dominc, Vivek, Leonardo, Simon, Dalmau, Viola for always being there and your support. Thanks also to all my students: Mirek, Anna, Adrian, Fabian, Midori, and Luca. Your contribution to this big work is very valuable. Last but not least, I want to really thank Danish and Alexandra for always been there, and being a rock when I needed one.

The presented work would not have been possible without the invaluable contributions from many collaborators around the world. I am indebted to Pavel Volkov for his extended input and help in figuring out how to understand our data. The constant loop between experiment and interpretation made possible to give some sense to a big chunk of this thesis. The same goes for Premala Chandra, who I also thank for being part of my examination committee. I want to thank Sebastian Huber and his team: Agnes Valenti, Kukka Huhtinen and Luca Giobbi for all the support with numerical simulations on my complex magnetic systems.

Lots of thanks are also extended to the many instrument scientists that I had the pleasure to work with over these years and from whom I could learn so much. Thanks to Tom Fennell, Oksana Zaharko, Denis Cheptiakov, Vladimir Pomjakushin, Gediminas Simutis, and Hubertus Luetkens from PSI (Switzerland). Thanks to Eric Ressouche, Ketty Beauvois, and Jacques Ollivier from ILL; and also to Dmitry Chernyshov from ESRF (France). Thanks to Naoki Murai, Seiko Ohira-Kawamura and Maiko Kofu from J-PARC (Japan). Finally thank you to Ross Stewart, Pascal Manuel, and Dmitry Khalyavin from ISIS; and Dave Allan and Mark Warren from Diamond (United Kingdom).

I would like to thank all my friends in Zurich and outside that were always on my side during these years. The warmest appreciation goes for my parents and my sister for their unending support.

Lastly, I want to thank to Luis, my partner in this long trip that is life. I could not have managed without you.

In short, thanks to each and everyone. Thanks for making this possible.

# Contents

<b>1</b>	<b>Introduction</b>	<b>1</b>
<b>2</b>	<b>Preliminaries</b>	<b>3</b>
2.1	Quantum magnetism . . . . .	3
2.2	Quantum criticality . . . . .	9
<b>3</b>	<b>Methods</b>	<b>17</b>
3.1	Calorimetry . . . . .	17
3.2	Dielectric measurements . . . . .	20
3.3	Neutron scattering . . . . .	22
3.4	X-Ray scattering . . . . .	29
3.5	Magnetometry . . . . .	30
3.6	Crystal growth and sample synthesis . . . . .	32
<b>4</b>	<b>Quantum multiferroicity and BEC criticality in <math>\text{Rb}_2\text{Cu}_2\text{Mo}_3\text{O}_{12}</math></b>	<b>37</b>
4.1	Introduction . . . . .	37
4.2	Refining the spin Hamiltonian . . . . .	39
4.3	Dielectric measurements in $\text{Rb}_2\text{Cu}_2\text{Mo}_3\text{O}_{12}$ . . . . .	42
4.4	Criticality at a Bose-Einstein Condensation of magnons . . . . .	50
4.5	Conclusions . . . . .	57
<b>5</b>	<b>Dielectric relaxation by quantum critical magnons in <math>\text{Cs}_2\text{Cu}_2\text{Mo}_3\text{O}_{12}</math></b>	<b>59</b>
5.1	Introduction . . . . .	59
5.2	The crystal structure of $\text{Cs}_2\text{Cu}_2\text{Mo}_3\text{O}_{12}$ . . . . .	60
5.3	The dielectric response of $\text{Cs}_2\text{Cu}_2\text{Mo}_3\text{O}_{12}$ . . . . .	61
5.4	Dielectric relaxation by quantum critical magnons . . . . .	69
5.5	Are $\text{Rb}_2\text{Cu}_2\text{Mo}_3\text{O}_{12}$ and $\text{Cs}_2\text{Cu}_2\text{Mo}_3\text{O}_{12}$ different? . . . . .	80
5.6	Conclusion . . . . .	82
<b>6</b>	<b>Unveiling the magnetism of the quantum antiferromagnet <math>\text{Nd}_3\text{BWO}_9</math></b>	<b>85</b>
6.1	Introduction . . . . .	85
6.2	The crystal structure of $\text{Nd}_3\text{BWO}_9$ . . . . .	87
6.3	The single-ion perspective . . . . .	88
6.4	Bulk measurements . . . . .	93
6.5	Magnetic diffraction and magnetic structures . . . . .	104
6.6	Discussion . . . . .	117

6.7 Conclusion . . . . .	120
<b>7 Conclusions and outlook</b>	<b>121</b>
<b>List of publications</b>	<b>125</b>
<b>A Experimental details</b>	<b>127</b>
A.1 Chapter 4: Quantum multiferroicity and BEC criticality in $\text{Rb}_2\text{Cu}_2\text{Mo}_3\text{O}_{12}$ .	127
A.2 Chapter 5: Dielectric relaxation by quantum critical magnons in $\text{Cs}_2\text{Cu}_2\text{Mo}_3\text{O}_{12}$ . . . . .	128
A.3 Chapter 6: Unveiling the magnetism of the quantum antiferromagnet $\text{Nd}_3\text{BWO}_9$ . . . . .	129
<b>B The crystal structures of <math>\text{Cs}_2\text{Cu}_2\text{Mo}_3\text{O}_{12}</math> and <math>\text{Rb}_2\text{Cu}_2\text{Mo}_3\text{O}_{12}</math></b>	<b>133</b>
B.1 Crystal structure of $\text{Cs}_2\text{Cu}_2\text{Mo}_3\text{O}_{12}$ . . . . .	133
B.2 Low temperature crystal structures . . . . .	134
<b>C The crystal structure of <math>\text{Nd}_3\text{BWO}_9</math></b>	<b>139</b>
<b>D Details on the symmetry analysis of the magnetic structures in <math>\text{Nd}_3\text{BWO}_9</math></b>	<b>141</b>
D.1 Basis vectors for $\mathbf{k} = (0,0,1/3)$ . . . . .	141
D.2 Basis vectors for $\mathbf{k} = (1/3,1/3,1/3)$ . . . . .	141
D.3 Basis vectors for $\mathbf{k} = (0,0,0)$ . . . . .	142
<b>Bibliography</b>	<b>153</b>

# Chapter 1

## Introduction

In our everyday experience, the matter around us appears simple, consisting primarily of atomic nuclei and surrounding electrons. One might expect that describing this familiar world mathematically would be straightforward - simply construct a Hamiltonian incorporating the positions of all electrons and nuclei, and include Coulomb interactions to account for their mutual influence. This approach has been considered as part of the quest for a 'Theory of Everything,' capable of explaining all ordinary phenomena [1]. Quantum mechanics offers methods for solving such problems by diagonalizing the Hamiltonian. However, attempting to extend this approach to systems with more than a handful of particles fails dramatically. This is especially true in the context of condensed matter physics, where one must grapple with systems containing approximately  $10^{24}$  particles.

Fortunately, it is precisely the sheer size of particle ensembles gives rise to self-organization mechanisms as a result of interactions. This concept was famously articulated by Anderson with his statement 'more is different' [2]. Emergent phenomena in condensed matter physics encompass a wide range, from the formation of periodic crystals to more exotic phenomena like superconductivity, superfluidity, magnetism, and topologically protected states. The low-energy properties of these systems, universally defined by their symmetries rather than their specific constituents, capture their physics effectively in simple models controlled by few parameters.

This work focuses on the realm of magnetic condensed matter systems and the phase transitions they undergo. Magnetic insulators, with their localized magnetic moments, offer endless versatility in hosting different physical models and phenomena. The particularity of magnetic interactions allows us to effectively create one- and two-dimensional systems within regular three-dimensional materials. Reduced dimensionality boosts quantum effects, breaking down classical behavior and stabilizing exotic magnetic phases and unconventional phenomenology. Specifically, we explore the coupling of magnetic and electric degrees of freedom as a source of novel emergent phenomena close to absolute zero temperature. Our work shows that this coupling provides new tools for studying magnetism that have been largely overlooked. Case in point, we demonstrate a new channel to otherwise experimentally inaccessible physical quantities. Notably, we uncover a qualitatively new form of interaction between electric dipoles and magnetic excitations at cryogenic temperatures.

The contents of this work are organized as follows:

*Chapter 2* introduces and motivates the research topic. A presentation of the basic concepts in quantum magnetism and quantum critical phenomena is provided, with an emphasis on the physics that is explored in the following chapters.

*Chapter 3* covers the experimental techniques and methods that have been used during the course of the thesis. In particular, calorimetry, magnetometry, and dielectric techniques are outlined, alongside an introduction to neutron and X-ray scattering techniques. A description of the synthesis and crystal growth of the different materials studied is also provided.

*Chapter 4* is devoted to the quantum spin-ladder system  $\text{Rb}_2\text{Cu}_2\text{Mo}_3\text{O}_{12}$ . The origin of previously reported ferroelectric behaviour in this system is clarified and found to be spurious. However, low temperature measurements of dielectric properties reveal an intriguing multiferroic ground state. The coupling of electric and magnetic degrees of freedom is exploited to provide a new perspective on BEC criticality. In particular, the critical susceptibility at a 3D BEC QCP is directly measured in a novel probe-response experiment.

*Chapter 5* deals with the physics of  $\text{Cs}_2\text{Cu}_2\text{Mo}_3\text{O}_{12}$ , another spin-ladder system isostructural to  $\text{Rb}_2\text{Cu}_2\text{Mo}_3\text{O}_{12}$ , where an equivalent interplay of ferroelectricity and antiferromagnetism is observed. In addition, a novel mechanism of dielectric relaxation is unveiled, where electric dipoles relax mediated by quantum critical magnons. Though a microscopic model is lacking, it suggests that magnons in  $\text{Cs}_2\text{Cu}_2\text{Mo}_3\text{O}_{12}$  are endowed with a dipolar electric moment.

*Chapter 6* is dedicated to the rare-earth antiferromagnet  $\text{Nd}_3\text{BWO}_9$ . With its purported 2D kagome lattice, it has been proposed promising platform for the study of spin-liquid physics. A thorough investigation of the single-ion physics and bulk thermodynamic response reveals a complex ground-state with several fractional magnetization plateaux. Neutron diffraction provides insight on the magnetic structures, suggesting the dominant role of one-dimensional couplings.

*Chapter 7* concludes this work with a summary of the main conclusions and an outlook on implications and further directions.

## Chapter 2

# Preliminaries

Magnetism arises from the presence of unpaired electrons within a system. Despite extensive research, magnetic systems continue to unveil new exotic phases of matter and intricate phenomena. Leveraging their versatility and simplicity, magnets serve as testbeds for exploring a multitude of physical models. In the following sections, we introduce several key concepts fundamental to the findings presented in this work.

We start with an overview of quantum magnetism, elucidating the existence of low-dimensional magnetic systems within three-dimensional materials, the influence of the choice of magnetic ion, and how electric and magnetic degrees of freedom become entangled.

Subsequently, we delve into the concept of quantum criticality, which underscores the existence of phase transitions precisely at zero temperature. The behavior of materials near such transitions becomes remarkably intricate as a result of quantum fluctuations, giving rise to the stabilization of exotic phenomena. Specifically, we introduce the notion of Bose-Einstein condensation of magnetic excitations and Quantum Spin-Liquid phases.

### 2.1 Quantum magnetism

Magnetism is an intrinsic manifestation of quantum mechanics, as the Bohr-van Leeuwen theorem proves. Yet, many phenomena can be explained in a semiclassical framework by considering the spins as classical vectors (disregarding the non-commutativity of angular momentum operators) and treating interactions in a mean field approach. Loosely speaking, one can define quantum magnetism as all the vast phenomenology in magnetism that cannot be captured in such a semiclassical approach. This is usually the situation for small spin systems, like  $S = 1/2$  or  $S = 1$ . In addition, low-dimensionality and competing interactions break mean-field theories down, bring about magnetic ground states with no classical analogs. The full machinery of quantum mechanics is thus needed to understand the resulting physics.

#### Low-dimensional magnetism in real materials

Real materials are always three dimensional. In fact, it can be explicitly shown that 1D and 2D crystals are unstable [3–6]. 2D materials such as graphene may only exist thanks

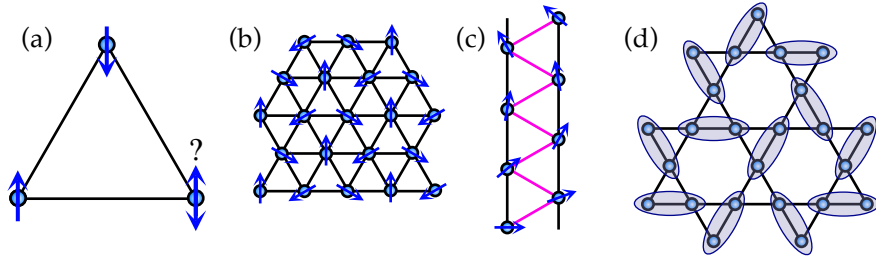


**Figure 2.1:** Examples of magnetic frustration in different models of magnetism. (a) A triangle of antiferromagnetically coupled spins in inherently frustrated. (b) Frustration in the 2D antiferromagnetic triangular lattice results in the stabilization of a  $120^\circ$  structure. (c) Competition between ferromagnetic (pink) and antiferromagnetic (black) bonds in a linear chain gives rise to a spiral structure. (d) Frustration in the kagome lattice of corner-sharing triangles is a complex problem. A pinwheel valence-bond-solid structure of non-magnetic singlets (ellipses) has been proposed under certain conditions [13].

to 3D warping, that stabilizes them [7]. However, one of the beauties of magnetic systems is that the interactions between magnetic ions can be effectively low-dimensional, even within a perfectly ordered three dimensional crystal. The reason lies in the strongly local and directional nature of magnetic exchange.

Mathematically, the magnetic degrees of freedom can be described as spin operators  $\mathbf{S}$ , that in an insulator correspond to electrons sitting in a fixed point in the lattice. Spins interact due, precisely, to the overlap of their electronic wave functions. A combination of Coulomb repulsion and Pauli's exclusion principle results in an interaction that is effectively spin dependent. This interaction may even happen in the absence of direct overlap, through virtual electron hopping between nearby atoms as was first described by Anderson in his seminal work on the theory of superexchange [8]. Regardless of the origin, the interaction can be described in terms of the Heisenberg Hamiltonian  $\mathcal{H}_{1,2} = J\mathbf{S}_1 \cdot \mathbf{S}_2$ , where  $J$  is the so called exchange coupling. The sign of  $J$  determines whether a parallel (ferromagnetic, FM) or antiparallel (antiferromagnetic, AFM) spin arrangement is favorable. Depending on the microscopic details, the interactions may be as large as 250 meV [9].

Magnetic interaction, stemming on the overlap between atomic orbitals, does show a strong directional dependence in space. It is possible to imagine a situation where one engineers this idea into a material where magnetic couplings are very strong along one direction, and negligible along another. Many magnetic systems realize such structures, which opened a way to study the complex world of one-dimensional and two-dimensional magnetism [10]. Celebrated examples include the 1D spin-chain compound  $\text{Sr}_2\text{CuO}_3$  [9] or the 2D magnet  $\text{La}_2\text{CuO}_4$  [11, 12], parent of cuprate superconductors. The intricacies of one and two dimensions give rise to extremely complex magnetic phenomenology, resulting in quasiparticle fractionalization (spinons/QSL), hidden order (Haldane) or topological charges (vortices) to name a few examples.

The the pattern of interactions within a magnetic lattice can be designed to boost certain effects. By inducing competition between interactions, classical order is destroyed and exotic phases come into play. This is the essence of the concept of *geometrical frustration* [14], that is beautifully exemplified by a triangular arrangement of spins coupled

antiferromagnetically (Fig. 2.1.(a)). Geometry imposes an irresolvable competition where no spin arrangement that can minimize the energy of all bonds. As a result the famous 120-degree structure appears as a global compromise in the Heisenberg triangular-lattice antiferromagnet (Fig. 2.1.(b)). This effect can be extended into many geometries, of which possibly the most intriguing is the kagome lattice of corner-sharing triangles (Fig. 2.1.(d)) with its macroscopically degenerate ground state. In this work, we will approach to two kinds of strongly frustrated systems: 1D spin ladders with competing FM and AFM couplings (Fig. 2.1.(c)), and a distorted AFM kagome system.

Finally, a magnetic model depends strongly on the nature of the magnetic ions that give the magnetic degrees of freedom, as those determine the spin value and the allowed interactions. The effect of spin-orbit coupling and crystal electric fields differs significantly between different elements and conditions the magnetic Hamiltonian strongly. In the following we shortly introduce the phenomenology for transition-metal and rare-earth magnetism.

### Transition-metal magnetism

In a free ion, the ground-state angular momenta of the multi-electron shell is characterized by the valence electrons. Different levels are described by the eigenvalues of angular momentum operators  $\hat{L}$ ,  $\hat{S}$ , and  $\hat{J}$ . In the LS-coupling approach,  $L$  and  $S$  are the sum of the individual  $l_i$  and  $s_i$  for each unpaired electron in the valence shell. The two first Hund's rules indicate how atomic orbitals must be filled in order to minimize Coulomb repulsion between electrons. In essence, out of all possible combinations of spin and orbital angular momenta, the configuration with largest  $S$ , and within that the one with largest  $L$ , will be the lowest energy one. Orbital and Spin momenta further couple via relativistic spin-orbit coupling, which can be simplistically expressed as

$$\mathcal{H}_{SO} = \lambda \hat{L} \cdot \hat{S} \quad (2.1)$$

This interaction imposes additional conditions on the total angular momentum  $\hat{J} = \hat{L} + \hat{S}$  [15, 16]. A third Hund rule dictates the value of  $J$  for a free ion, and its ground state can be defined by the quantum numbers  $L$ ,  $S$ ,  $J$ , and  $m_J$ .

However, this approach is not good for  $3d$  transition-metal ions when they are placed in a solid-state environment. The effect of the surrounding atoms is to create a local crystal electric field (CEF) on the magnetic ion, that strongly changes the hierarchy of orbital eigenstates as a result of electrostatic interaction. In general, the CEF strength ( $\Delta_{CEF} \sim 1$  eV) is much larger than spin-orbit coupling ( $\lambda \sim 10$  meV), lifting the degeneracy in  $L$ , which is no longer a good quantum number. The resulting structure of energy levels can be worked out from a group-theoretical approach, in accord to the point symmetry around the ion. In a low symmetry environment, the degeneracy may be completely lifted and the orbital momentum is thus quenched ( $L = 0$ ). In that case, there are no orbital degrees of freedom and the system is spin-only. The effect of spin-orbit coupling is translated into anisotropic terms on a single-ion level, or on the exchange interactions.

The case of magnetic divalent copper is a particularly straightforward one. With its  $3d^9$  configuration,  $\text{Cu}^{2+}$  gives rise to  $S = 1/2$  spin degrees of freedom. Its  $L = 2$  orbital

**Table 2.1:** Ground state multiplet  $|L, S, J\rangle$  of some trivalent rare earth ions,  $R^{3+}$ .

Ion	$L$	$S$	$J$	$g_J$	$\mu_f$
$\text{La}^{3+} (4f^0)$	0	0	0	-	0
$\text{Pr}^{3+} (4f^2)$	5	1	4	4/5	$3.58 \mu_B$
$\text{Nd}^{3+} (4f^3)$	6	3/2	9/2	8/11	$3.62 \mu_B$

momentum is fully quenched in our target materials, resulting in very simple single-ion magnetic properties. In addition, as a  $S = 1/2$  system, single-ion anisotropy is not allowed, and anisotropy will be apparent only in the magnetic couplings. The Heisenberg Hamiltonian is replaced by  $\mathcal{H}_{1,2} = \hat{\mathbf{S}}_1 \Gamma \hat{\mathbf{S}}_2$ , where  $\Gamma$  is the effective anisotropy tensor. The structure of this tensor is discussed in Chapter 4 in deeper detail.

### Rare-earth magnetism

Rare-earth elements are found in their trivalent form in magnetic compounds. In contrast to  $3d$  ions, their magnetism can be traced back to a well defined total angular momentum  $J$ . In these elements, the valence  $4f$  electrons lie deep within the electronic cloud resulting in a strong spin-orbit coupling. The spin-orbit coupling parameter grows significantly with the atomic number and it is strong for such heavy ions ( $\lambda \sim 100$  to  $250$  meV [17]). In addition to that, the  $4f$  electrons lie below the filled  $5s$  and  $5p$  electron shells, which results in a strong localization and screening from external electric fields [18], making CEF the weakest energy scale in this case.

For ions where the valence shell is less than half filled, the spin orbit coupling parameter  $\lambda$  in (2.1) is negative, and the minimal energy state is that with  $J = |L - S|$ . This is the content of the third Hund's rule. The resulting ground state  $|L, S, J\rangle$  configurations for La, Pr, and Nd are summarized in Table 2.1. The low energy physics is determined by the  $2J + 1$ -fold degenerate ground state. Invoking Wigner-Eckart theorem the expectation value of any vector operator is proportional to the matrix elements of  $\hat{\mathbf{J}}$  within a  $J$  multiplet, which allows to write the magnetic moment as

$$\hat{\mu} = g_J \mu_B \hat{\mathbf{J}} \quad (2.2)$$

where  $g_J$  is the proportionality factor and is referred to as the Landé factor. It can be written in terms of expectation values of  $\hat{\mathbf{J}}^2$ ,  $\hat{\mathbf{L}}^2$ , and  $\hat{\mathbf{S}}^2$  as

$$g_J = 1 + \frac{J(J+1) + S(S+1) - L(L+1)}{2J(J+1)} \quad (2.3)$$

The corresponding values are also given in Table 2.1, along with the so called effective moments,  $\mu_f = \sqrt{g_J J(J+1)}$ .

In a crystalline environment, the CEF on a rare-earth ion splits the  $(2J+1)$ -fold degenerate ground state multiplet. Since the  $4f$  electrons only are subject to a screened field, its effects can typically be treated as a small perturbation that does not mix different  $J$  multiplets. The result is a ground state that is a linear combination of  $|J, m_J\rangle$  free-ion

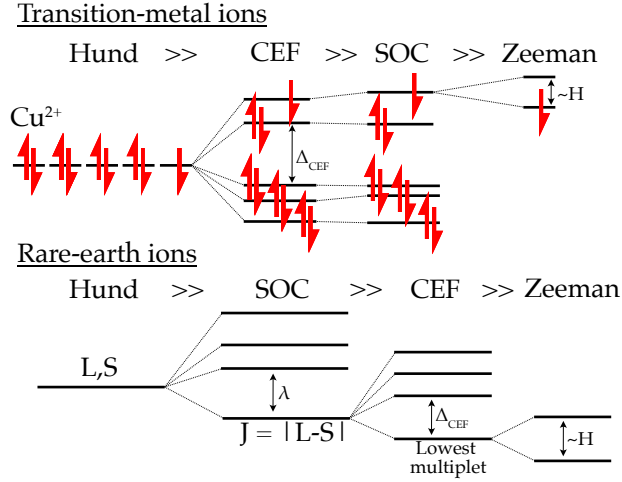


**Figure 2.2:** Hierarchy of energy scales in transition metal ions (a) and rare-earths (b). In transition metal ions CEF splits the orbital degeneracy, while the spin number remains well defined. In  $\text{Cu}^{2+}$  ions, the (single-ion) effect of the spin orbit coupling (SOC) is to shift the energy levels slightly and create an anisotropic g-factor, which is reflected in the Zeeman energy.

states. Typical CEF splitting energies are in the range of tens of meV, comparable to the thermal energy at room temperature. This has an impact on the temperature dependence of magnetic properties of rare-earth magnets, due to the depopulation of excited CEF levels.

Importantly, for those ions with an odd number of valence electrons (as in  $\text{Nd}^{3+}$ ) Kramers theorem applies, stating that each state is at least doubly degenerate in the presence of time reversal symmetry. As a result, the ground state for  $\text{Nd}^{3+}$  must be at least a magnetic doublet. At low enough temperatures  $k_B T \ll \Delta_{\text{CEF}}$ , the high energy CEF levels can be completely depleted and the resulting single-ion physics are strictly dictated by the lowest multiplet. An effective Hamiltonian can be constructed by projecting a Heisenberg-like Hamiltonian built on the full  $J$  basis onto the ground state wave functions.

Finally, as a result of the strong localization of  $4f$  electrons, trivalent rare-earth ions in magnets display generally very small exchange couplings. The overlap between  $4f$  electrons and superexchange ligands is reduced by the localization of the former. As a result, it is not rare to only find magnetically ordered phases in the millikelvin regime.

## Magneto-electric coupling

Just as magnetic degrees of freedom give rise to ordered, time-reversal-symmetry-broken phases, electric degrees of freedom in an insulator (electric dipoles) can also give rise to ordered states with broken inversion symmetry, called ferroelectrics. Magnetism and ferroelectricity may coexist independent of one another, as is the case of type-I multiferroics [19]. In these systems, usually each effect comes from independent phenomena, and therefore have negligible coupling. However, there is a vast range of systems where a complex interplay between electric and magnetic degrees of freedom gives rise to novel cooperative phenomena [20]. The coupling between electric polarization and magnetiza-

tion is the foundation of the magneto-electric effect [21], whereby magnetization can be controlled by an electric field, and conversely polarization by a magnetic field. One of the main goals of this thesis is precisely to study how this coupling can lead new qualitative observations.

The origin of electric polarization  $\mathbf{P}$  in magnetic systems has been intensively studied and many models have been proposed [20, 22]. Most studied multiferroics of spin origin are based on transition-metal perovskites [23]. However, many low dimensional magnets have been by now identified also as electrically ordered [24, 25]. Though relativistic spin-orbit coupling is not a required ingredient in a recipe for magneto-electric coupling, its presence does facilitate it by binding lattice and spin degrees of freedom together. The three microscopic mechanisms of spin-driven ferroelectricity are the following:

1. *Spin current model.* Also termed Inverse Dzyaloshinskii–Moriya interaction, it is based on antisymmetric exchange interaction due to spin-orbit coupling. The elastic energy loss by displacing an anion out of the center between magnetic cations (which creates an electric dipole moment) is outweighed by the gain in antisymmetric exchange energy. For a particular bond, the resulting polarization can be expressed in terms of the spin chirality (cross product of spins) as

$$\mathbf{P} = \eta \mathbf{e}_{ij} \times (\mathbf{S}_i \times \mathbf{S}_j) \quad (2.4)$$

where  $\mathbf{e}_{ij}$  is the vector connecting  $\mathbf{S}_i$  and  $\mathbf{S}_j$ , and  $\eta$  is a coupling constant proportional to the spin-orbit coupling. Equation (2.4) shows that a electric polarization may appear in helimagnets and spin spirals, but only if the spin precession axis is not collinear with the magnetic propagation vector. Then, the electric polarization appears always perpendicular to both vectors.

2. *Spin-dependent  $p$ - $d$  hybridization.* In covalent bonds, there is a certain tendency to hybridize the electronic orbitals participating in the bond. This is a fundamental effect in organic molecules for example, where hybrid orbitals are delocalized over the whole molecule. In the bond between a transition metal ion with a ligand, this is the case between the  $d$  orbitals of the former and the  $p$  orbitals of the latter. For particular electronic configurations of the transition metal, this hybridization becomes spin-dependent as a result of spin-orbit coupling, giving rise to an electric polarization as

$$\mathbf{P} = (\mathbf{S} \cdot \mathbf{e})^2 \mathbf{e} \quad (2.5)$$

with  $\mathbf{e}$  a vector connecting the magnetic ion with the ligand. This mechanism is the result of individual spins and leads to electric polarization with more generic ordering, including proper screws and collinear structures.

3. *Exchange-striction model.* Lastly, dimerization of magnetic ions with different valence may lead to ferroelectricity. As a result of a spin-Peierls instability a solid of spin-singlet pairs may form. This is a common phenomenon in 1D systems as a result of nesting. If the magnetic ions have different charge, each dimer becomes effectively a dipole and the system becomes ferroelectric as a result of exchange striction. The resulting polarization is proportional to the scalar product of neighboring spins

$$\mathbf{P} = \Pi_{ij} (\mathbf{S}_i \cdot \mathbf{S}_j) \quad (2.6)$$

where  $\Pi_{ij}$  is a vector that depends on the particular crystal structure. It must be noted, that spin-orbit coupling is not necessary in this mechanism as opposed to the previous two.

The presented mechanisms are based on different premises. Generally, knowledge of the crystal symmetries and the magnetic structure is enough to pinpoint the particular mechanism that is at play in a material. However, it is not always possible when several of them are allowed or coexist, and access to experimental results is key. In chapters 4 and 5 we will discuss the extensive exploration of the magneto-electric response of the family of quasi-1D systems  $A_2\text{Cu}_2\text{Mo}_3\text{O}_{12}$  ( $A = \text{Cs}, \text{Rb}$ ), that show a quantum multiferroic ground state.

Finally, the existence of magneto-electric coupling has an impact on the fundamental excitations of the system. A dynamical magneto-electric response has been observed to provide magnetic spin waves with an electrical activity [20], creating hybrid quasiparticles called electromagnons [26]. Such quasiparticles have been identified experimentally in a variety of magnetic perovskites [26–29], proposing models for their electrical activity within the long-range-ordered multiferroic phases of the materials [30–32]. However, the reasons why a magnon may acquire an electric moment in general are not trivial and are still the subject of extensive investigation. As it will be discussed in detail in Chapter 5 the low temperature dielectric response of  $\text{Cs}_2\text{Cu}_2\text{Mo}_3\text{O}_{12}$  is significantly influenced by the coupling of electric dipoles and magnons, which are seen to possess an electric dipolar moment regardless the magnetic ground state.

## 2.2 Quantum criticality

Condensed matter systems are constituted by a tremendous amount of strongly interacting particles. Even if the Coulomb force mediating the interaction has been known for a long time, understanding its effect such many body systems is cumbersome. Yet, in their collectivity, these systems reveal new manners of simplicity. The low energy behavior of a condensed matter system can be described with very few parameters, resulting in all sorts of coherent states such as superconductivity or band insulation [2].

This simplicity is only accentuated at the boundary between different states, in the vicinity of the phase transitions. As a system is brought towards a continuous phase transition, bubbles of order proliferate within it. At the transition point, also called the critical point, these bubbles become free of scale, meaning that order develops over all possible distances and the system acquires self similarity. As a consequence, all physical quantities become critical and can be described by power laws. The beauty of this behavior is that the exponents of those power laws are universal, and only defined by their universality class [33]. This class depends on some qualitative properties such as the symmetry of the underlying model, range of the interactions, number of components of the order parameter, and the space dimensionality; but is completely independent of the microscopic details. As a result, the exact same behavior can be observed at phase transitions in systems as disparate as alloys [34], magnets [35] or lattice gases [36].

Thermodynamic phase transitions, like the demagnetization of a ferromagnet, are driven by thermal fluctuations. As temperature is elevated, thermal motion increasingly

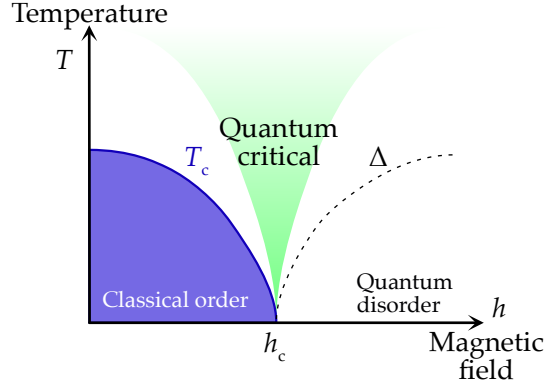


**Figure 2.3:** A magnetic field may tune a system through a quantum phase transition. The fan-shaped quantum critical regime emerges from a quantum critical point.

agitates the ordered spins until magnetic order is completely lost. At exactly zero temperature, thermal energy vanishes completely, but fluctuations may remain as a result of Heisenberg’s uncertainty principle. These *quantum* fluctuations, may play a similar role in destabilizing order even at zero temperature, giving rise to the so called *quantum phase transitions* (QPT). Just as thermal fluctuations can be tuned with temperature, quantum fluctuations can be tuned with other control parameters (other than temperature) to reach a quantum critical point (QCP). Examples of control parameters inducing QCPs include magnetic fields, electron density, chemical composition or hydrostatic pressure.

A QCP is strictly only defined at absolute zero temperature. From an experimental perspective, it is impossible to reach it. However, just as the critical regime close to a conventional phase transition spans a certain temperature range, the existence of a QCP alters the properties of a material at a *finite* temperature. This influence elevates quantum criticality from a theoretical abstraction at absolute zero to a real-world phenomenon [37–39]. It is in this way that the universal fan-shaped quantum critical region arises from the quantum critical points (Fig. 2.3), which can be used as an experimental proxy to study them [40]. The dominance of quantum fluctuations in this region of phase space results in exotic material behavior, where quantum critical exponents replace classical ones. Importantly, the dynamics of the system acquires a pivotal importance, and all critical exponents depend on the dynamic exponent,  $z$ , of the dispersion of low energy excitations  $\omega \propto k^z$ . One particular and key consequence is that the effective dimensionality of a system at a QCP is enhanced, as  $d_{eff} = d + z$ , where  $d$  is the spacial dimension. As a result, QPTs tend realize simple mean-field criticality.

One of the best and most widespread platforms for the study of QCPs is that of magnetic insulators [39]. As already discussed, all sorts of models, geometries and dimensionalities can be realized in real 3D materials. In addition, their local interactions and clean Hamiltonians allow for a simple characterization of degrees of freedom and energy scales at play. To top it up, magnetic field provides an incredibly simple and easily tunable control parameter, allowing very fine control over QPTs.

While the phenomenology that we have discussed is extremely general, the physics that one finds at a QCP is ultimately given by its universality class. Most of the QCPs

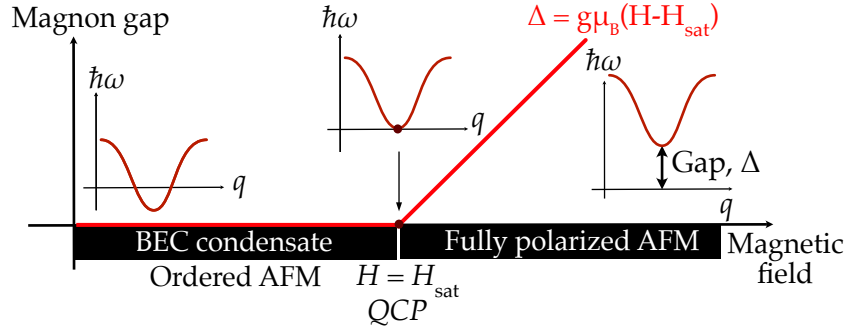


**Figure 2.4:** The BEC correspondence in an antiferromagnet. Magnon excitations that are gapped in the fully-polarized high-field phase, become gapless at the QCP. At this point they *condense* forming a macroscopically large coherent ground state giving rise to static AFM order.

that are studied in this text belong to the 3D Bose-Einstein universality class, which is discussed in the following.

To wrap up we devote some words to the quantum spin liquid, a ground state of an antiferromagnet where quantum fluctuations preserve all symmetries of the Hamiltonian unbroken. The result is an extremely correlated state, with intriguing properties. Sought-after for decades, the quest to experimentally identify such a state in two and three dimensions is focus of much current research.

## BEC correspondence in antiferromagnets

Originally proposed for photons in 1924 [41, 42], the condensation of Bose-Einstein is likely one of the most celebrated theories for a phase transition. It describes a process, whereby a macroscopic number of bosonic particles form a single collective quantum state at low temperatures. This state (which is prohibited for fermions by Pauli's exclusion principle) was promptly understood as a new fundamental state of matter. Nowadays it is known that it serves as a basis for superfluidity, superconductivity [43], and several other phenomena ranging from semiconductors [44, 45] to ferromagnetic films [46]. In addition, it is a prime example of a quantum phase transition, as it can be found in the limit of zero temperature [47], as is the case e.g. in the gapless superfluid to a gapped Mott insulator transition found in lattice gases [48, 49].

In its original formulation, a critical temperature ( $T_c$ ) is defined, below which a non-interacting system of particles with a certain density,  $n$ , develops a macroscopically occupied coherent ground state:

$$T_c = 3.3125 \frac{\hbar^2 n^{2/3}}{mk_B} \quad (2.7)$$

where for any laboratory accessible particle densities these temperature are below the microkelvin regime. Such condensates have been observed in cold gas condensates [50, 51]. However, extremely complex systems are needed to stabilize them even for fractions of seconds, restricting the experimental maneuverability.

A much more approachable realization can be found in magnetic insulating systems. Fundamental excitations in magnetic systems, called magnons, carry an integer spin and

thus are bosons. As such, they may undergo a condensation in the Bose-Einstein fashion. Field-induced saturation transitions in conventional Heisenberg antiferromagnets [52], as well as soft-mode ordering transitions in gapped quantum paramagnets [53–56] can be described in terms of a BEC of magnons.

An exact mapping between spin  $S = 1/2$  particles and hard-core bosons was devised Matsuda and Matsubara in a  $d$ -dimensional system [56, 57]. Therefore, interacting  $S = 1/2$  systems can be treated as gases of bosons, and thus may undergo BEC. However, the crucial factor defining which systems will show BEC is particle number conservation (in the form of  $U(1)$  symmetry). Naturally preserved in a Bose gas, number conservation translates into uniaxial symmetry in a magnet, i.e.  $O(2)$  rotational symmetry. An example of such Hamiltonian is the XXZ model

$$\mathcal{H}_{XXZ} = J \sum_{\langle ij \rangle} \left( S_i^x S_j^x + S_i^y S_j^y + \gamma S_i^z S_j^z \right) - g_{zz} \mu_B H \sum_i S_i^z. \quad (2.8)$$

with antiferromagnetic  $J$ . Note that a magnetic field must be applied along the symmetry axis, chosen here to be  $z$  by  $\gamma$ . The hard-core boson condition forbids multiple magnons to sit in a single site which results in strong interaction at large densities. However, in the proximity of spin saturation the density of bosons is small (as is the ordered moment) and this constraint becomes unimportant. After applying the mentioned mapping and going to momentum space, we can rewrite (2.8) as

$$\mathcal{H}_{XXZ} = \sum_{\mathbf{q}} [\hbar\omega(\mathbf{q}) - \mu] \hat{a}_{\mathbf{q}}^\dagger \hat{a}_{\mathbf{q}} \quad (2.9)$$

where  $\hat{a}_{\mathbf{q}}^\dagger$  and  $\hat{a}_{\mathbf{q}}$  are creation and annihilation operators for magnons with wavevector  $\mathbf{q}$  and dispersion  $\hbar\omega = J \sum_v (1 + \cos \mathbf{q} \cdot \mathbf{l}_v)$ , and  $\mathbf{l}_v$  are vectors linking nearest neighbors. Upon applying the Matsuda-Matsubara transformation, the total magnetization  $\sum_i S_i^z$  is mapped to the total number of bosons, which is a conserved quantity of (2.9). This correspondence is the one that guarantees that magnons will, in fact, condense. The magnetic field acts as a chemical potential controlling the magnon population, as  $\mu = g_{zz} \mu_B (H - H_{sat})$ , with  $g_{zz} \mu_B H_{sat} = dJ(1 + \gamma)$ . At  $H = H_{sat}$  the magnon Zeeman gap closes and spontaneous antiferromagnetic order appears with propagation vector  $\mathbf{q}_0 \neq 0$ . Note that  $z = 2$  as for small momenta  $\omega \approx Jq^2/2$  at the saturation field because, which can be regarded as a consequence of coupling the magnetic field to a conserved quantity. The magnon gap becomes a measure of the distance to the QCP (Fig. 2.4).

Looking at the ordered state (condensate) the nature of the order parameter is revealed. In a Bose gas, the particle system condenses into a macroscopic ground state which is described by a single complex wave function  $\psi$ . The  $U(1)$  symmetry breaking implies a spontaneous choice of a global phase  $e^{-i\theta}$ , where the order parameter is the amplitude of the wave function  $|\psi|$ . In the magnet, spontaneous breaking of the  $O(2)$  symmetry leads to transverse antiferromagnetic (staggered) order, perpendicular to the anisotropy axis [52, 55]. The order parameter becomes the amplitude of  $\langle S_i^x + iS_i^y \rangle$ , where the phase corresponds to the angle of the spin in the plane. As a result, a characteristic of the transition is the divergence of the staggered magnetic susceptibility,  $\chi_\perp$ . A summary of the analogy between the Bose gas and its antiferromagnet counterpart is shown in Table 2.2.

**Table 2.2:** Correspondence between the BEC condensation in a Bose gas and a quantum antiferromagnet. Adapted from [55].

Bose gas	Antiferromagnet
Particles	Spin excitations ( $S = 1$ quasiparticles)
Boson number $N$	Spin component $S^z$
Charge conservation $U(1)$	Rotational invariance $O(2)$
Condensate wavefunction $\langle \psi(\mathbf{r}) \rangle$	Transverse magnetic order $\langle S_i^x + iS_i^y \rangle$
Chemical potential $\mu$	Magnetic field $H$
Superfluid density $\phi_s$	Transverse spin stiffness

The same situation occurs in gapped spin quantum paramagnets, where the ground state is actually a disordered one at zero field [55]. An external field (that preserves the  $SO(2)$  symmetry), may induce magnetic long-range order by the same mechanism that was proposed above. In this case, two quantum critical points are realized, at the *lower* critical field  $H_{c1}$  where order is induced from the gapped state, and at the *upper* critical field  $H_{c2}$  where the system reaches saturation.

This framework allows us to predict the critical behavior at the verge of a magnetic BEC. For  $z = 2$  any system with  $d > 2$  will be described in mean-field theory. Renormalization group provides relations for all critical exponents close to  $H = H_c$  defined as

$$C \sim T^{-\alpha}, \quad \chi \sim T^{-\gamma}, \quad |H - H_c| \sim T^\phi, \quad (2.10)$$

with  $\alpha = 3/2$ ,  $\gamma = 3/2$ , and  $\phi = 2/3$  for a three dimensional magnet [58].

Note that, despite the effective low-dimensionality of the magnetic systems that are presented in this work, magnetic order is the result of residual three-dimensional couplings. It is the interplay of frustration and the low scale of the 3D couplings that prevent the onset of magnetic long-range-order down to very low temperatures. However, close enough to the QCP, its true dimensionality is revealed and the 3D results will be the only ones needed here.

As a remark, the case of the divergent susceptibility in a BEC QCP is a curious one. No physical conjugate field is associated to the order parameter (amplitude of a complex wave function), and thus the critical susceptibility has no physical meaning. In Chapter 4 we use a workaround based on the BEC correspondence presented here to not only make it into an observable quantity, but use magneto-electric coupling to actually measure it directly in a gapped quantum magnet.

## Quantum spin liquids

Interacting spins on a regular lattice realize ordered structures in order to minimize their interaction energy. However, thermal and quantum fluctuations act to destabilize this order. In the case of simple Neel antiferromagnets, quantum fluctuations are inherent and deviate the ordered structures slightly from the semiclassical antiparallel order even at zero temperature. One can embrace these fluctuations and look for systems where, despite the strong coupling between spins, no magnetic order develops leaving an

extremely correlated ground state with exotic properties. This was the pioneering idea on Anderson [59], where the ground state of the antiferromagnet Heisenberg triangular lattice is described as a 'quantum liquid', though later found to realize a  $120^\circ$  structure.

Quantum fluctuations may be promoted by geometric frustration, small spins and (optionally) low-dimensionality. The key about quantum fluctuations is that they may be phase-coherent over macroscopic distances, as opposed to thermal fluctuations that act randomly on individual spins. If they become large enough, a system enters develops a so-called *quantum spin liquid* (QSL) state [60]. This state is a quantum superposition of a macroscopic number of degenerate ground-state wave functions that does not break any symmetry. Such states constitute new phases of matter, where the spins are correlated in very peculiar, and often hidden, ways. As a result of long-range quantum entanglement, very exotic phenomena have been predicted in QSLs such hosting of quasiparticles with fractional quantum numbers or the generation of artificial gauge fields. Depending on the exact nature of the QSL, excitations can be fermions or bosons, or even anyons. The phenomenology of QSLs is vast and is the focus of intense research. Good reviews on the state of the art can be found in [61–64].

Due to the distinctive lack of magnetic order in 1D systems, QSL states have been repeatedly identified theoretically and experimentally. The ground state of the simple spin  $S = 1/2$  Heisenberg antiferromagnetic chain model is a quantum spin liquid as identified by Bethe ansatz [65]. Materials realizing this model have been seen to host continua of spinons in its excitation spectrum [66, 67], a signature of the spin-liquid state. The situation is much more complex going to higher dimensions, as magnetic order is generally stabilized.

A prime candidate to realize QSL physics in 2D is the Heisenberg kagome-lattice antiferromagnet [68]. With its network of corner-sharing triangles it realizes a macroscopically degenerate ground state. However, this deceptively simple system remains a key outstanding problems in quantum magnetism. In the  $S = 1/2$  case, the exact nature of its QSL ground state [59], let alone the spin excitation spectrum, is still largely debated [69] Anderson's short-range resonant valence bond state results in a system with an energy gap, but long-range singlet fluctuations result in a gapless state [70]. Over the years, numerical calculations on finite systems have favored the gapped state [71]. Nonetheless, recent application of tensor-network methods on infinite systems points towards the gapless scenario [72].

Precisely when experimental data could provide valuable input for theory, it remains unavailable due to a lack of good model materials. Despite the existence of many material realizing magnetic kagome lattices, the hunt for experimental solid evidence for a kagome QSL state (such as quasiparticle fractionalization) is hampered for three main reasons. First is the onset of long-range order due to non-kagome interactions. In real materials, anisotropic Dzyaloshinskii-Moriya terms and interactions beyond nearest neighbors are significant, which may lift frustration and precipitate magnetic ordering [73, 74]. The presence of chemical disorder embodies the second reason. Structural disorder can mimic the response of a coherent QSL through several mechanisms, as is the case in the celebrated Herbertsmithite [75]. Finally, the lack of single-crystal specimens clouds the interpretations of experiments [76]. The intrinsic spherical-average of measurements on polycrystal hinders an unambiguous interpretation of any experimental data. Avoiding these three pitfalls is key to access QSL physics.

The search for QSL candidates continues with an ever growing list of potential materials. New models are proposed, where deviations from the putative kagome Heisenberg AFM contribute to stabilize a QSL state [13, 77, 78]. In chapter 6 we tackle the study of one such system,  $\text{Nd}_3\text{BWO}_9$ . This member of the more extended rare-earth magnet family  $R_3\text{BWO}_9$  shows significant AFM couplings in on a crystal structure where antisite disorder is not allowed. Absence of magnetic order in single crystals down to cryogenic temperatures qualifies it as a prime platform to study the largely sought after quantum spin liquid.



# Chapter 3

## Methods

This chapter provides an overview and a description of the main experimental techniques that have been used in this work. A description of the actual experimental details can be found in Appendix A.

### 3.1 Calorimetry

Calorimetric techniques aim to determine the change of internal energy of a system with respect to a variety of parameters. As such, they are extremely versatile in the information they may provide in solid state systems. Sensitive to any changes in the physical state of a system these techniques are a witness of phase transitions of any kind: structural, ferroelectric, magnetic, etc. In the vast majority of cases, the quantity of interest is heat capacity. Not only extremely insightful *per se*, accurate measurements of it give access to other important physical properties, such as entropy or the Grüneisen parameter. In the following we outline two techniques that have been used in this work.

#### Relaxation calorimetry

When two bodies are kept in contact their temperatures will tend to equalize. If one of the bodies is a large energy reservoir, the second will always give or take energy from it to mimic its temperature. The time scale over which this process happens is related to the coupling between the bodies, and to their heat capacity. This is the base of the so called *relaxation calorimetry*. By applying a heat pulse to a sample one can measure the characteristic time that takes to recover the equilibrium temperature (that of the reservoir) and obtain a measurement of its specific heat. An example of such process is shown in Fig. 3.1.(b).

The implementation of the measurement system is depicted in Fig. 3.1.(a). The sample of interest (with heat capacity  $C_s$ ) is installed on top of a sample stage (with heat capacity  $C_h$ ). This stage is connected to the energy reservoir through calibrated contacts with conductivity,  $\kappa_h$ . Importantly, all is kept in ultra-high vacuum so that heat flows exclusively through those contacts. In general, sample and stage have an excellent thermal, they are always in equilibrium and one can see them as one system with total heat capacity  $C_t = C_s + C_h$ . As long as the applied heat pulse is small, one can consider the to-

tal heat capacity constant over the temperature range induced by the pulse. Under these conditions, the relaxation process can be described with a single characteristic timescale through the following relation

$$\frac{dT_s}{dt} = -\tau(T_s - T_0) + P(t) \quad (3.1)$$

where  $T_0$  is the temperature of the bath, and  $P(t)$  is the power of the applied heat pulse. The solution to this first order equation (assuming a constant pulse  $P(t) = P_0$ ) is a single exponential function over the characteristic time  $\tau$ , which precisely equals  $C_t/\kappa_h$ . Measurements with and without sample allow a precise determination of  $C_s = C_t - C_h$ .

Perfect contact between sample and platform cannot always be realized, which leads to unequal temperatures between them and internal relaxation processes. The reasons for a finite thermal coupling vary, but are more prominent at low temperatures if the sample specific heat is significantly larger than that of the platform. The strongly reduced thermal conductivity found at cryogenic temperatures results in very slow thermalization. The effect of a finite heat flow between sample and platform can be captured in the so called *two-tau model*, where a link of thermal conductance  $k_s$  is assumed between them. In this model the relaxation becomes more complex

$$C_h \frac{dT_h}{dt} = -\kappa_h(T_h(t) - T_0) + \kappa_s(T_s(t) - T_h(t)) + P(T) \quad (3.2)$$

$$C_s \frac{dT_s}{dt} = -\kappa_s(T_s(t) - T_h(t)) \quad (3.3)$$

where  $T_s(t)$  and  $T_h(t)$  are the sample and platform temperatures and the conductivities are as depicted in Fig. 3.1.(a). This process is ruled by two separate timescales, however a simple connection between them and the sample heat capacity can no longer be drawn. Solution of the coupled equations gives a relaxation profile as shown in Fig. 3.1.(b), where two regimes can be identified. Measurements with and without sample allow again a precise determination of  $C_s$  and  $\kappa_s$ . This model was essential to understand the relaxation measurements in Chapter 6.

Finally, it is important to understand how the energy flows within the system to appropriately interpret the results. A heat pulse generates lattice vibrations (or phonons) in the target sample. Thanks to their coupling to electrons, energy is transferred to electronic, magnetic, etc. degrees of freedom at timescales much shorter than the typical measurement times (tens of milliseconds to several seconds). However, when it comes to nuclear degrees of freedom this scenario changes. Nuclear degrees of freedom are only relevant at extremely low temperatures (tens to hundreds of millikelvins). Their coupling to the lattice is mediated through electronic fluctuations and phonons, which are vanishing at such low temperatures. As a result, one may have an incomplete thermalization of nuclear spins, even over times as long as minutes. It may also lead to a complete decoupling of nuclei to lattice, meaning we may not be able to probe the nuclear contribution to specific heat under certain circumstances. This issue is addressed in more detail in Chapter 6.

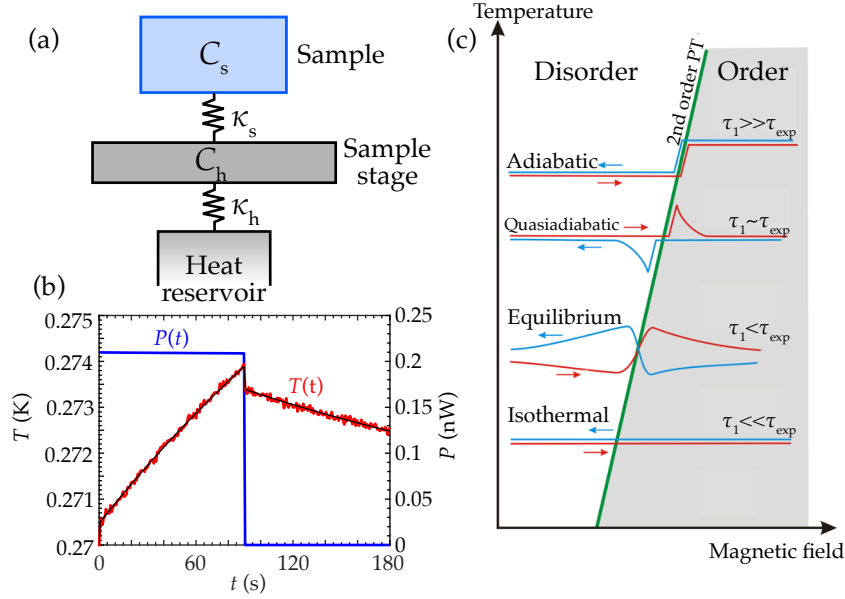


**Figure 3.1:** (a) Schematic representation of the heat capacity probe. (b) Example of a measurement where a two-tau model is a necessary to reproduce the relaxation profile. Red: measured temperature. Blue: supplied power pulse. Black: fit to a two-tau model. (c) Different regimes for magnetocaloric effect with their characteristic lineshapes. Adapted from [79].

## Magnetocaloric effect

The entropy of a magnetic system changes as a result of applying an external magnetic field. Such changes in entropy materialize in changes of temperature in a fully isolated system. This change has been used in many applications (such as magnetic cooling, [80]) and is the essence of the magnetocaloric effect (MCE). Subjecting a quantum magnet to a changing magnetic field generates a change in its temperature  $T(t)$  that can be easily recorded with a thermometer in contact with the sample [79]. Such measurements are not only extremely sensitive to phase transitions, but can also indicate whether they are first or second order.

Interpreting the temperature profiles can be complex and depends strongly on the experimental conditions. As discussed above, a sample of heat capacity  $C_s$  in a thermal bath (at temperature  $T_0$  and coupled to the sample by a thermal link of conductivity  $\kappa$ ) relaxes to the bath temperature with a time constant  $\tau_s = C_s/\kappa$ . If we call  $\tau_{exp}$  the characteristic time over which the magnetic field is changed, we find several experimental regimes depending on the ratio of  $\tau_s$  to  $\tau_{exp}$ . Adiabatic conditions are given when the field is swept extremely fast,  $\tau_{exp} \ll \tau_s$  and no heat is lost to the environment. Semiadiabatic conditions correspond to  $\tau_{exp} \sim \tau_s$ . In equilibrium conditions,  $\tau_{exp} \gg \tau_s$  and the system is left to almost equilibrate at each point, however some changes can be observed in temperature. In isothermal limit, the system is driven always in thermal equilibrium and sweeping the field produces no changes in temperature.

All the MCE measurements in this work have been taken under equilibrium conditions. Here the temperature of the system is governed by the rate at which the thermal

link to the bath can release heat originated from the entropy changes. Under these conditions we have

$$\kappa(T(H) - T_0) = T \left( \frac{\partial S}{\partial H} \right)_T \frac{dH}{dt} \quad (3.4)$$

and by virtue of Maxwell relations

$$T(H) - T_0 = -\frac{T}{\kappa} \frac{dH}{dt} \left( \frac{\partial M}{\partial T} \right)_H \quad (3.5)$$

The temperature of the system will respond to the temperature dependence of magnetization as the field is swept. As such it will be sensitive to field-induced phase transitions or level crossings. The effect of sweeping upwards or downwards in field will only be reflected in the sign of  $\Delta T$ , and thus upsweeps and downsweeps will be the opposite of one another at a continuous phase transition. This may not be the case if the field induces some non-reversible change, as is the case in a first-order transition. Thus, MCE is an effective way to differentiate the order of a transition. As a final remark, the MCE data can be integrated to obtain the system entropy, magnetization and other thermodynamic potentials.

## 3.2 Dielectric measurements

The role of active dielectric degrees of freedom in a solid state system is reflected in its dielectric susceptibility  $\chi$ . In general, in a linear system it is defined from the polarization in response of the system to an electric field as

$$P_i = \epsilon_0 \chi_{ij} E_j, \quad (3.6)$$

where Einstein summation is assumed. Ferroelectric materials develop spontaneous electric polarization in the absence of an electric field (just as in ferromagnets) so (3.6) no longer holds. Knowing  $\chi$  and  $P$  provides complementary information on the dielectric behavior of a system. The former can usually be accessed directly from capacitance as described below. However, only relative changes in the latter can be measured [81] and thus we present the concept of pyroelectric currents, as a method to access ferroelectric polarizations.

### Complex capacitance

Accurate measurements of capacitance are used across many fields for a large variety of purposes. From accelerometers to magnetometers, understanding the changes in capacitance of a system can be extremely insightful. The most common capacitor geometry is that of a parallel plates, where

$$C = \epsilon \epsilon_0 \frac{S}{d} \quad (3.7)$$

where  $d$  the distance between plates and  $S$  their surface. If we leave the geometric component of it aside, capacitance gives access to the dielectric nature of the system between the plates, by probing directly its relative electric permittivity  $\epsilon$ , or equivalently its dielectric

permittivity as,  $\epsilon = 1 + \chi_e$ . Any dielectric phenomenon (relaxation, resonances, ferroelectric instabilities, etc.) leaves a trace in  $\epsilon$ . In addition, thanks to the magnetoelectric coupling that is present in many frustrated magnetic systems, it may also be sensitive to magnetic phenomena.

If capacitance is probed with a time-dependent AC electric field, it can be regarded as a complex quantity

$$C = C' + iC'' \quad (3.8)$$

where it is customary to refer as  $C'$  to the real component, and  $C''$  to the imaginary one. Thinking in terms of the complex admittance, the imaginary term can be understood as *dynamics* in the system, stemming from real currents or induced charge displacements.

$$\epsilon = \epsilon' + i\epsilon'' \quad (3.9)$$

Dielectric susceptibility is in fact a response function, since it relates an electric field applied to a system and the induced polarization. As such, it is subject to the principle of causality. This has the important consequence that real and imaginary components are not independent, and they must to obey the Kramers-Kronig relations. Such relations impose strong constraints to the existence of imaginary components in the complex response of a system.

In many quantum materials the coupling between lattice and spin degrees of freedom results in a significant magnetostriction, i. e., changes in the lattice constants induced by a magnetic field. If this is the case, a magnetic field may change both the permittivity and the geometry of a sample simultaneously, both with contributions in capacitance. Disentangling changes in permittivity from changes in geometry on capacitance is complex and often may require of complementary techniques.

## Pyroelectric currents

A ferroelectric material is characterized by the onset of spontaneous ferroelectric polarization. It is the result of a long-range-ordered arrangement of electric dipoles within a polarizable system. The presence of the ferroelectric moment  $P$  generates a certain electric charge density on the surface of the material given by

$$\sigma = \mathbf{P} \cdot \hat{\mathbf{n}} \quad (3.10)$$

where  $\hat{\mathbf{n}}$  is the vector normal to the surface. If placed between capacitor plates, this creates an induced charge density (see Fig. 3.2). However, no potential drop is measured between the plates, as the charge imbalance becomes perfectly compensated.

One of the smoking-gun evidences for a ferroelectric state is the occurrence of *pyroelectric currents*. In short, as the temperature of a ferroelectric system is raised, the polarization is reduced. This entails a redistribution of charge inside the solid, which effectively translates as an electric current. The reduction of sample charge density induces also a current between the capacitor plates which can be measured with a sensitive ammeter. Assuming a fixed parallel-plate capacitor geometry:

$$I_{pyro} = \frac{dQ}{dt} = S \frac{dT}{dt} \frac{\partial \mathbf{P}}{\partial T} \cdot \hat{\mathbf{n}} \quad (3.11)$$

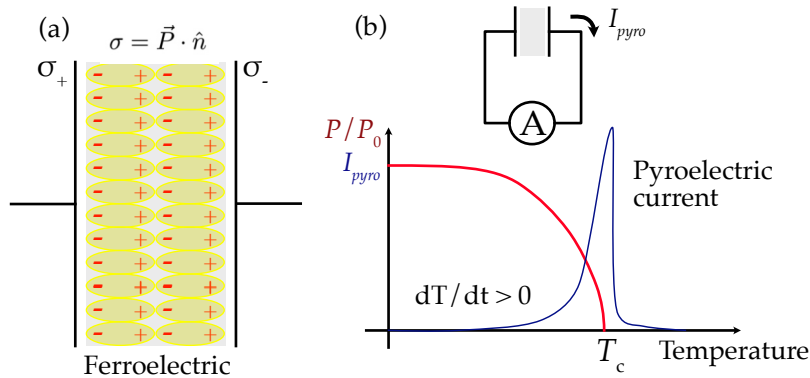


**Figure 3.2:** (a) A ferroelectric material shows long-range order of electric dipoles. This creates a charge density on the surface of the material. (b,c) Depolarizing the bulk by rising the temperature induces a *pyroelectric current*, that may be measured with sensitive amperemeters.

where  $S$  is the surface of the capacitor plates. Integration of the pyroelectric current results on the ferroelectric polarization.

Common in ferroelectric materials (as in ferromagnetic ones) is the spontaneous formation of domains with different polarization directions, in order to minimize the Coulomb dipole interaction energy globally. If one measures in cooling down, no pyroelectric current will be observed as the domain structure will give a net zero electric moment. To prepare for pyroelectric currents, samples are customarily cooled under a strong poling electric field that favors the formation of a single ferroelectric domain well below the ordering temperature. Measuring while warming, a non-zero current can be observed. Importantly, in a ferroelectric system the direction of the applied poling field determines that of the induced polarization. Measurements of sign-switching of polarization and currents are customary when characterizing a ferroelectric.

### 3.3 Neutron scattering

The neutron is one of the fundamental constituents of all matter that surrounds us. This particle possesses a mass of  $m_n = 1.675 \cdot 10^{-27}$  kg, is electrically neutral and carries a small magnetic moment  $\mu_n = -9.66 \cdot 10^{-27}$  J/T. In virtue of particle-wave duality, neutrons may interact with matter in a wave-like manner, giving rise to diffraction, interference and other phenomena.

The versatility of the neutron as a probe in many areas of physics arises as a consequence of its fundamental properties. Being an electrically neutral particle, the neutron is insensitive to the atomic electron clouds, thus allowing it to penetrate well within condensed matter, as opposed to X-rays or electrons. As a nucleon, the neutron is subject to the strong nuclear force which allows it to interact with the atomic nuclei. Interacting through strong force gives it sensitivity to different isotopical species. In addition, its magnetic moment allows it to interact with unpaired electrons in magnetic atoms. The neutron can react to magnetization densities *locally* and thus gives us a tool to study the *magnetism* in a system.

When it comes to thermal neutrons, their application in solid state systems is unparalleled. On the one hand, their wavelength matches that of inter-atomic spacing in solids, yielding structural information in e.g. diffraction experiments. On the other hand, their typical energies matches those of many condensed-matter excitations, making of them prime witnesses of interatomic interactions through inelastic scattering experiments.

The interaction of the neutron with the probed system results in an exchange of energy and momentum. By measuring the resulting energy and momentum of the neutron (by measuring it in a detector) one can access the details of the microscopic interaction. The

The central quantity of interest in a scattering experiment is the partial differential cross section  $d^2\sigma/d\Omega dE'$ . Assuming we irradiate a system with a certain flux of particles,  $\Phi$ , this quantity shows the number of scattered particles per unit time, into a small solid angle,  $d\Omega$ , in a particular direction of space with final energies between  $E'$  and  $E' + dE'$ . If we have an energy-discriminating neutron counter covering a solid angle  $d\Omega$ , this is precisely the quantity that we are measuring in an experiment.

Scattering theory allows us to relate the differential cross section to the scattering potential by virtue of Fermi's golden rule. Let us assume a neutron of energy  $E$  and momentum  $\mathbf{k}$  produces a change in the system under investigation from a state  $\lambda$  to  $\lambda'$ , thereby changing its energy and momentum to  $E'$  and  $\mathbf{k}'$ . The cross section of the process can be expressed as

$$\left(\frac{d^2\sigma}{d\Omega dE'}\right)_{\lambda \rightarrow \lambda'} = \frac{k'}{k} \left(\frac{m}{2\pi\hbar^2}\right)^2 |\langle \mathbf{k}'\lambda' | V | \mathbf{k}\lambda \rangle|^2 \delta(E_\lambda - E_{\lambda'} + E - E') \quad (3.12)$$

where  $V$  is the interaction potential. Note that total energy and momentum are conserved in the process. Plugging in the different interaction potentials between the neutron and the scattering system allows to create a link between microscopic interaction and macroscopic effects.

## Nuclear scattering

Its hadronic nature confers the neutron the potential to interact with the atomic nucleus via strong interaction. This interaction is extremely short ranged (typically  $\sim 10^{-15} - 10^{-14}$  m) and depends largely on the nuclear configuration of the target isotope. An exact mathematical description is extremely challenging. However, the effects can be very well approximated using *Fermi pseudopotentials*. The interaction potential is approximated by a delta well

$$V_n(\mathbf{r}) = \frac{2\pi\hbar^2}{m} b\delta(\mathbf{r}) \quad (3.13)$$

where  $b$  is the so-called scattering length. This parameter accounts for the scattering capabilities of different nuclei and has been tabulated for all stable isotopes [82]. Figure 3.3 shows the values for the first 75 elements of the periodic table. One of the practical consequences of the complex nucleus-neutron interaction is that the scattering length remains of the same order of magnitude across the whole periodic table. In that sense, the sensitivity of the neutron to a particular element is roughly independent of  $Z$ , unlike for X-rays where the scattering cross section increases strongly with  $Z$ , making the light atoms effectively transparent.

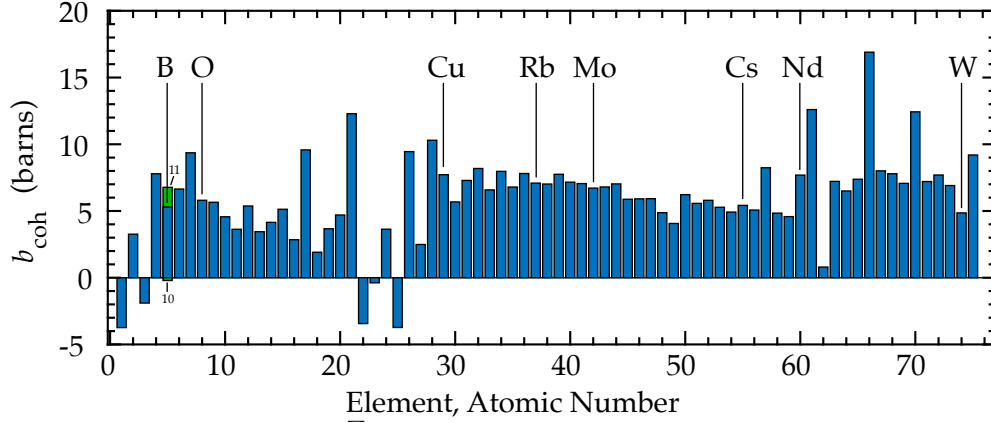


**Figure 3.3:** Coherent scattering length for the different elements in the periodic table, from [82]. In the case of several stable isotopes, the chart shows the (real) averaged value considering natural elemental concentrations. The elements present in the compounds used in this thesis are labeled. In the case of boron, scattering lengths of both stable isotopes  $^{10}\text{B}$  and  $^{11}\text{B}$  are shown along with natural boron.

If one considers an ensemble of scattering centers, one must distinguish two processes: coherent and incoherent ones. The former is the results of correlations between the positions of the same nucleus at different times, and on the correlation between the positions of different nuclei at different times. As such it gives rise to interference effects and are of key relevance in neutron crystallography and is the quantity given in Fig. 3.3. The latter depend only on the correlation between the positions of the same nucleus at different times and therefore does not contribute to interference.

Certain nuclides have a large affinity for neutrons and their interaction results in the capture of neutrons. This interaction is strongly dependent on the neutron energy, but in general negligible for thermal neutrons. This is represented as an imaginary component in the scattering length (not shown in Fig. 3.3). For some isotopes like  $^{113}\text{Cd}$  the absorption cross section is so high that makes it a perfect component for neutron shields. Another instance is that of boron, where  $^{10}\text{B}$  has a large capture likelihood. The presence of such nuclear species is generally unwanted in neutron scattering experiments.

Solid state systems generally possess a periodic structure in space, i.e. a lattice. Assuming such a periodic arrangement of nuclei in a crystal gives rise to the well known Bragg's law of diffraction. For elastic processes, macroscopic interference effect builds up space as reflected by

$$\left(\frac{d\sigma}{d\Omega}\right)_{\text{elastic}} = N \frac{(2\pi)^3}{v_0} \sum_{\tau} \delta(\kappa - \tau) |F_N(\kappa)|^2 \quad (3.14)$$

where  $\tau$  are elements of the reciprocal lattice,  $v_0$  is the unit cell size and  $|F_N(\kappa)|^2$  is the nuclear structure factor, that accounts for the nuclei contained in the unit cell. Constructive interference is only obtained when  $\tau = \kappa = \mathbf{k} - \mathbf{k}'$ . This is the basis for nuclear neutron diffraction.

The incoming neutron may also give energy to the system and create a fundamental lattice vibration, or take energy from it by absorbing it. Since phonons have a well defined

energy-momentum relation, for such process to happen (e.g. creation of a phonon) the scattering vector must match the momentum of the quasiparticle up to a reciprocal lattice vector  $\boldsymbol{\kappa} = \mathbf{k} - \mathbf{k}' = \boldsymbol{\tau} + \mathbf{q}$ , while the energy transfer matches that of the phonon  $E' - E = \hbar\omega(\mathbf{q})$ . Energy and momentum of thermal neutrons satisfy these conditions for a very broad range of momenta and energies. As a result studying such inelastic processes gives us access directly to the phononic spectrum of a system.

## Magnetic scattering

One key property of the neutron is its magnetic moment. As such it interacts with unpaired electrons through the following potential

$$-\boldsymbol{\mu}_n \cdot \mathbf{B} = -\frac{\mu_0}{4\pi} \gamma \mu_N 2\mu_B \sigma \left[ \underbrace{\nabla \times \left( \frac{\mathbf{s} \times \hat{\mathbf{R}}}{R^2} \right)}_{\text{Spin}} + \underbrace{\frac{1}{\hbar} \frac{\mathbf{p} \times \hat{\mathbf{R}}}{R^2}}_{\text{Orbital}} \right] \quad (3.15)$$

with  $\gamma$  the neutron gyromagnetic ratio and  $\mu_N$  the nuclear magneton. We identify two contributions, from orbital and spin degrees of freedom. Under this potential, the interaction of the neutron with the scattering system becomes spin-dependent and the cross section needs to be rewritten to account for this as:

$$\left( \frac{d^2\sigma}{d\Omega dE'} \right)_{\sigma\lambda \rightarrow \sigma'\lambda'} = \frac{k'}{k} \left( \frac{m}{2\pi\hbar^2} \right)^2 |\langle \mathbf{k}'\sigma'\lambda' | V_m | \mathbf{k}\sigma\lambda \rangle|^2 \delta(E_\lambda - E_{\lambda'} + \hbar\omega) \quad (3.16)$$

where  $\sigma$  ( $\sigma'$ ) is the spin state of the incoming (outgoing) neutron, and  $V_m$  the magnetic interaction potential. An evaluation of the matrix elements involved in the core of (3.16) shows that the scattering is only sensitive to the magnetization density *perpendicular* to the scattering vector  $\boldsymbol{\kappa}$ . Thus the cross section can be rewritten as

$$\left( \frac{d^2\sigma}{d\Omega dE'} \right)_{\sigma\lambda \rightarrow \sigma'\lambda'} = (\gamma r_0)^2 \frac{k'}{k} |\langle \sigma'\lambda' | \boldsymbol{\sigma} \cdot \mathbf{Q}_\perp | \sigma\lambda \rangle|^2 \delta(E_\lambda - E_{\lambda'} + \hbar\omega) \quad (3.17)$$

with  $\mathbf{Q}_\perp = \hat{\boldsymbol{\kappa}} \times (\mathbf{Q} \times \hat{\boldsymbol{\kappa}})$  and  $\mathbf{Q} = -\mathbf{M}(\boldsymbol{\kappa})/2\mu_B$  a component of the Fourier transform of the magnetization density at wavevector  $\boldsymbol{\kappa}$ . The constant  $r_0$  is the electron classical radius ( $2.82 \cdot 10^{-15} m$ ) and gives a rough scale for magnetic elastic scattering probability.

In transition metals of the 3d group the effect of crystal electric fields is to lift the orbital degeneracy fully, quenching the orbital angular momentum ( $L = 0$ ) and the magnetic scattering is only due to spin. In a crystal of such nature, the scattering cross section results

$$\begin{aligned} \frac{d^2\sigma}{d\Omega dE'} &= (\gamma r_0)^2 \frac{k'}{k} \sum_{\alpha\beta} (\delta_{\alpha\beta} - \hat{\kappa}_\alpha \hat{\kappa}_\beta) \sum_{l'd'} \sum_{ld} F_{d'}^*(\boldsymbol{\kappa}) F_d(\boldsymbol{\kappa}) \\ &\sum_{\lambda\lambda'} p_\lambda \langle \lambda | \exp(-i\boldsymbol{\kappa} \cdot \mathbf{R}_{l'd'}) S_{l'd'}^\alpha | \lambda' \rangle \langle \lambda' | \exp(i\boldsymbol{\kappa} \cdot \mathbf{R}_{ld}) S_{ld}^\beta | \lambda \rangle \delta(E_\lambda - E_{\lambda'} + \hbar\omega) \end{aligned} \quad (3.18)$$

where  $S_{ld}^\beta$  is the  $\beta$  spin component of ion  $d$  in cell  $l$ , corresponding to the nucleus sitting in  $\mathbf{R}_{ld}$ . The quantity  $F_d(\boldsymbol{\kappa})$  is the magnetic form factor and corresponds to the Fourier transform of the normalized density of unpaired electrons ( $s_d(\mathbf{r})$ ) for ion  $d$

$$F_d(\boldsymbol{\kappa}) = \int s_d(\mathbf{r}) \exp(i\boldsymbol{\kappa} \cdot \mathbf{r}) d\mathbf{r} \quad (3.19)$$

Considering elements where both spin and orbital degrees of freedom have nontrivial contributions involves a much more complex analysis. In the case of rare-earths, there is a useful approximation based on the large spin-orbit coupling. In the so called *dipolar approximation* the results in (3.18) can be used with a few modifications. Under LS coupling the magnetic ion state can be specified by its quantum numbers  $L, S, J$ . On the one hand, the spin operators  $S$  in (3.18) is to be substituted by the total angular momentum  $J$ . On the other hand, the magnetic form factor includes orbital and spin contributions and is rewritten as

$$\frac{1}{2}F_d(\boldsymbol{\kappa}) = \frac{1}{2}g_S\mathcal{J}_0(\boldsymbol{\kappa}) + \frac{1}{2}g_L[\mathcal{J}_0(\boldsymbol{\kappa}) + \mathcal{J}_2(\boldsymbol{\kappa})] \quad (3.20)$$

with

$$g = g_S + g_L; \quad g_S = 1 + \frac{S(S+1) - L(L+1)}{J(J+1)}; \quad g_L = \frac{1}{2} + \frac{L(L+1) - S(S+1)}{2J(J+1)} \quad (3.21)$$

and

$$\mathcal{J}_n = 4\pi \int_0^\infty j_n(\kappa r) s(r) r^2 dr \quad (3.22)$$

with  $j_n(\kappa r)$  the spherical Bessel function of order  $n$ . The values of  $\mathcal{J}_n$  as a function of  $\kappa$  are tabulated and can be accessed for example in [18].

All in all, 3.18 draws a connection between static magnetic correlations in a system and the scattering of neutrons interacting with it. In general any kind of correlation (structural or magnetic, static or dynamic, short or long ranged) can be measured through neutron scattering. Such give access to thermal averages of varied operators and thus provide key insight on the physical mechanisms at play in a scattering event. In full generality we have

$$\left( \frac{d^2\sigma}{d\Omega dE'} \right)_{coh} = \frac{\sigma_{coh}}{4\pi} \frac{k'}{k} NS(\boldsymbol{\kappa}, \omega) \quad (3.23)$$

The function  $S(\boldsymbol{\kappa}, \omega)$  is called the scattering function and it represents the Fourier transform in time and space of the time-dependent pair-correlation function, i.e.

$$S(\boldsymbol{\kappa}, \omega) = \frac{1}{2\pi\hbar} \int G(\mathbf{r}, t) \exp[i(\boldsymbol{\kappa} \cdot \mathbf{r} - \omega t)] d\mathbf{r} dt \quad (3.24)$$

The latter gives information (e.g. in the case of nuclear scattering in a crystal) of how positions of different atoms relate in space and time. Through this we may see that neutron scattering can also probe short-range and low-dimensional order, correlations in liquids and heavily damped excitations. All sorts of temporal or spatial correlations will be captured in the neutron scattering cross section.

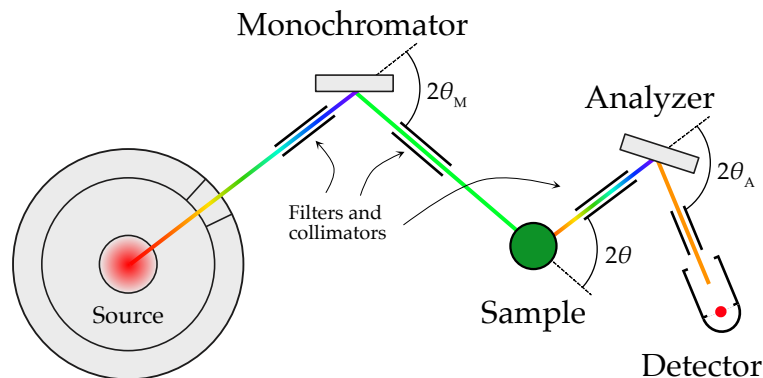


**Figure 3.4:** Schematic representation of the elements of a typical triple-axis neutron instrument. Its working principle is detailed in the text.

### Neutron technologies

In this final some insight is given on the production and measurement of neutron radiation. The complexity of generating neutron beams with high fluxes and the difficulty of steering them results in a small number of large scale facilities scattered around world where neutron techniques are available.

Traditionally the production of neutrons has relied in nuclear fission in the core of a nuclear reactor. When fissible nuclear material is hit with neutrons, the product is a large amount of energy and neutrons that may produce further fission. Such coupled processes generate a chain reaction, with a large neutron surplus. The resulting neutrons can be moderated until their energies match measurement requirements and then guided towards target samples. Nuclear reactor source generate continuous beams and can be found in facilities such as the Institut Laue-Langevin (ILL, Grenoble, France) or the High-Flux Isotope Reactor (HFIR, Oak Ridge, USA).

Modern approaches to neutron production have been developed on the base of nuclear spallation. High energy proton beams are made impact onto a heavy metal target (typically tungsten or mercury). The violent impact strips numerous neutrons off of the target material that may also be moderated to desired energies. Such sources usually work in a pulsed way, where protons are shot in bunches, as opposed to continuously, generating neutron bursts at definite time intervals. Facilities of this kind offer very high controllable fluxes. Examples of spallation sources include the Paul Scherrer Institute (PSI, Villigen, Switzerland), the Japan Proton Accelerator Research Complex (JPARC, Tokai, Japan) or the ISIS Neutron and Muon Source (Oxfordshire, UK).

Neutron instruments are adapted to the particular research goal and their neutron source. In this work, roughly two types of machine were used: double/triple axis and time-of-flight instruments. Historically, first instruments were double and triple axis machines on fission sources. Their functioning is rather similar and is schematized in Fig. 3.4. A polychromatic neutron beam is extracted from the source and guided towards a monochromator. A high purity single crystal (usually silicon cut along a (111) direction or pyrolitic graphite along (002)) selects a single wavelength via Bragg. This chooses the initial energy and momentum  $\mathbf{k}$ . The beam is collimated and guided onto the sample.

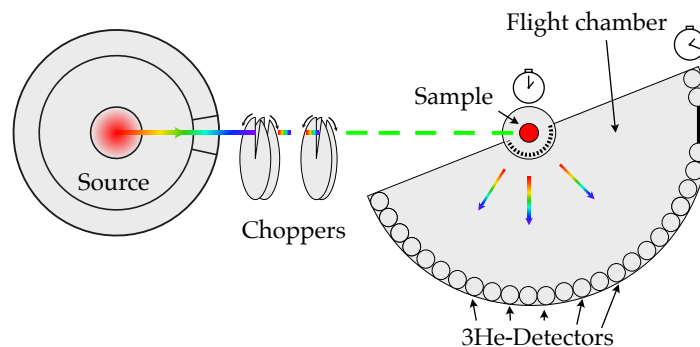


**Figure 3.5:** Schematic of a time-of-flight neutron spectrometer. A source (continuous or pulsed) produces a polychromatic neutron beam. A system of choppers shapes, cuts and monochromatizes the beam that is guided towards the sample. After each neutron bunch reaches the sample, neutrons scatter (elastically or inelastically) into the flight chamber. The time taken by each individual scattered neutron to reach the detector bank is measured. The  $^3\text{He}$  detectors are time and position sensitive, allowing a strong discrimination of the final neutron energies and momentum direction.

Scattering occurs, resulting in emission of neutrons in all directions and with different energies. The final energy and momentum are selected by the two last arms. An analyzer crystal is positioned following the direction  $\mathbf{k}'$  from the sample. The working principle of the analyzer is the same as the monochromator, Bragg-scattering neutrons with a particular energy. Setting a neutron counter downstream to the analyzer allows us to measure the intensity of the scattering process as a function of energy and momentum transfer. EIGER and TASP at PSI are of this type.

In a two-axis machine, the energy analyzer is omitted and the detector sits downstream the sample. The thermal neutron spectrometer D23 at ILL uses this principle. This approach is generally justified for diffraction, as the elastic scattering is around 100.000 times more likely than inelastic events. However, in some cases these may become comparable and triple axis machines are preferred for a proper separation of contributions.

The basic principle of time-of-flight (TOF) machines is measuring the time a neutron takes to travel from the sample to the detector. This time is related to the energy of the neutron and can be determined with extreme precision with modern electronics. The working principle is summarized in Fig. 3.5. A polychromatic neutron beam is extracted from the source. A series of choppers (rotating discs with thin apertures) prepare the beam by shaping, monochromatizing and removing harmonics. The resulting neutron bunch is scattered at the sample position. The time taken for the scattered neutrons to *fly* up to the detector is measured. The detector bank is typically composed of hundreds of position sensitive fixed single detector with a good time-detection resolution. The large size of the detector gives access to a large amount of scattered wave vectors and energies simultaneously.

The beam preparation depends on the source type and the experimental technique. In a TOF spectrometer, a high degree of monochromatization is preferred, in order to measure energy transfer processes with high energy resolution. Examples include IN5 at ILL, or DCS at NIST. On the contrary, Laue TOF diffractometers skip the monochromatization and a white beam hits the sample. The wide distribution of wavelengths allows to observe

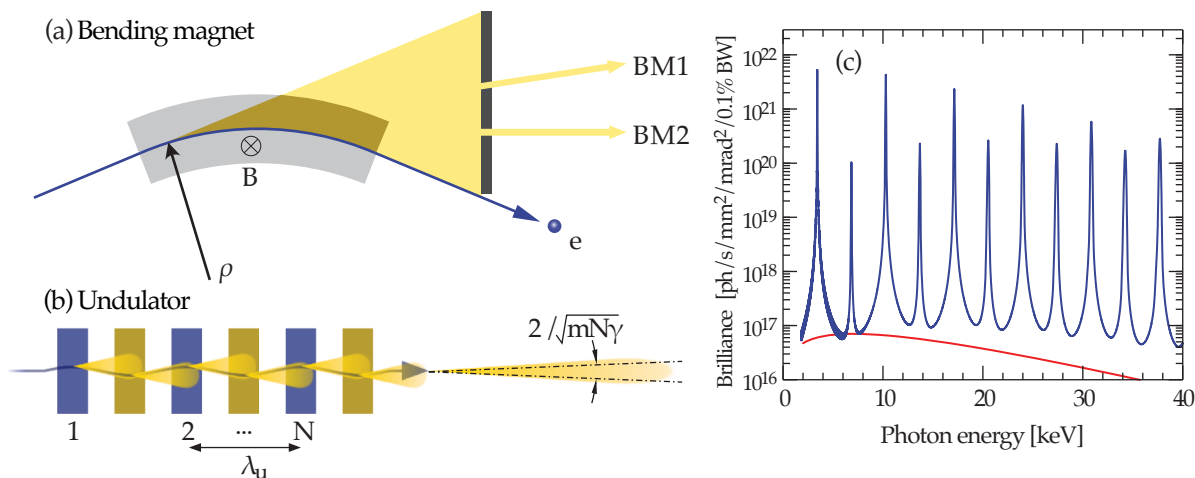


**Figure 3.6:** Schematic geometry of (a) a bending magnet and (b) an undulator insertion device. (a) A magnetic field is applied into the paper to curve the trajectory of an electron bunch. The resulting radiation can typically supply several beamlines. (b) The electron bunch is forced to *undulate* by a series of opposed magnetic dipoles arranged very close together. Blue and yellow represent up- and down-pointing magnetic fields. The angular deviation from the straight path is so small that the forward-emitted radiation interferes, giving rise to constructive conditions only for particular wavelengths. (c) Comparison of brilliances at a 3 GeV 4th generation synchrotron running at 400 mA between a U14 undulator and a bending magnet with  $B = 1.41$  T (red). The figure highlights the interference principle that rules undulator emission and the much higher brilliance that can be achieved in them.

a large volume of the reciprocal space simultaneously. An example of such machine is WISH at ISIS.

### 3.4 X-Ray scattering

In the previous section we have discussed the large applicability of the neutron a scattering probe in solid state systems. Nonetheless, the most widespread probe for diffraction and structural studies is X-rays. Their easy production allows X-ray diffractometers to be day-to-day equipment in any laboratory. The basics of diffraction techniques have been already discussed above. The largest differences here are the extremely large energy of photons compared to neutrons with similar wavelengths, and the fact that photons interact mainly with the electronic clouds. Here we want to discuss a particular source of X-rays that produces astoundingly large fluxes with unparalleled collimation: the synchrotron light source.

#### Synchrotron radiation

When a charged particle is accelerated, it emits radiation as described by the Hertzian dipole, in the direction perpendicular to its acceleration. If the particles are brought to relativistic speeds the resulting emitted power by bending its trajectory in a magnet rises rapidly with the Lorentz relativistic factor  $\gamma$ . At the same time, the emitted beam divergence is reduced as  $1/\gamma$  in the forward direction, resulting in an extremely large flux

on a very small cross section. In a synchrotron light source both effects are engineered in order to provide exceptional photon fluxes.

In a nutshell, a synchrotron machine is composed of a storage ring where electrons are made turn at relativistic speeds; insertion devices, where radiation is produced by deflecting those electrons; and resonant cavities, where energy is supplied to keep them running. Electrons in modern synchrotron facilities have energies of a few giga-electronvolts. The figure of merit for synchrotron emission is its *brilliance*. It is defined as

$$B = \frac{\phi}{4\pi^2\sigma_x\sigma_y\sigma_{x'}\sigma_{y'}\frac{d\omega}{\omega}} \quad (3.25)$$

where  $\phi$  is the photon flux (ph/s),  $\sigma_{x,y}$  is the linear source size and  $\sigma_{x',y'}$  the angular beam divergence, and  $d\omega/\omega$  is a relative bandwidth around a particular frequency value  $\omega$ . Fig. 3.6.(c) shows the extremely large brilliances that can be obtained in the newest generation of synchrotrons.

Synchrotron radiation is produced as a result of bending electrons trajectories. In early facilities this was mainly done in the bending magnets (BM) (called like that as they steer the electron trajectory in the ring). The resulting radiation is spread over wide areas and has a very uniform brilliance over a broad range of energies. The beams are collimated and monochromatized by complex optics arrangements and focusing single crystals. A schematic representation of a bending magnet is shown in Fig. 3.6.(a).

In modern synchrotron facilities, the straight parts of the storage rings are used to produce extremely bright and intense radiation using so-called insertion devices. These systems possess an alternating array of magnets that make the electron trajectory wiggle around a straight path. In each of this wiggles, a cone of light is emitted in the forward direction. The *undulator* geometry maximally exploits this emission by making the different light bunches overlap and interfere. Only certain wavelengths interfere constructively, and as a result the spectrum consists of a fundamental frequency plus a series of regularly spaced higher harmonics, all with extreme brilliances. A million-fold increase in brilliance can be obtained in undulators compared to bending magnet stations, as is represented in Fig. 3.6.(c). Part of this enhanced brilliance resides in the highly collimated beams. As a result, undulators generate extremely high photon fluxes with extremely low beam divergences, which provides for super high resolution in diffraction experiments.

Due to the very large photon flux, the sample environment at synchrotron sources is very versatile, allowing for example very low temperature cryostat stages without eliminating the beam intensity completely. Various synchrotron lines were used to examine the crystal structures of  $\text{Cs}_2\text{Cu}_2\text{Mo}_3\text{O}_{12}$  and  $\text{Rb}_2\text{Cu}_2\text{Mo}_3\text{O}_{12}$  at low temperatures, as presented in Chapter 5.

### 3.5 Magnetometry

It goes without saying that a key property of a magnet is its magnetization. Measurements of magnetization can bring relevant information on the nature of the ground state of a magnetic system, as well as on the interactions that are established on the atomic scale. In the following, three magnetometry techniques are outlined.

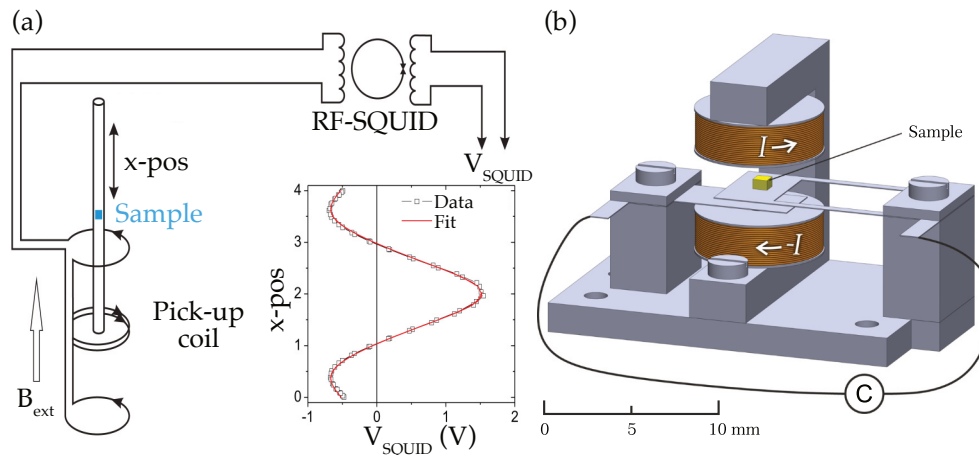


**Figure 3.7:** (a) Working scheme of a SQUID magnetometer, adapted from [83]. (b) Structure of the Faraday balance magnetometer, adapter from [84].

### Squid magnetometry

Possibly the most widespread technique to measure magnetization is based on Superconducting Quantum Interference Devices (SQUID). Based on the Josephson effect, they provide extreme sensitivity to very small magnetic fields.

A typical DC Squid magnetometer consists of three elements. First, a superconducting second-order gradiometer coil (as shown in Fig. 3.7.(a)) acts as pick-up coil. Sweeping a magnetic sample through the coil creates a current that is sensed by a SQUID ring, to which the first circuit is connected inductively. The quantization of magnetic flux in a ring with a Josephson junction provides an sensitive conversion of magnetic flux change to voltage. The voltage across the SQUID can be measured directly, or be coupled inductively to an amplifier and a data acquisition system. The whole system acts as a sensitive transducer from magnetic flux to voltage. The resulting signal can be fitted to the model of a magnetic dipole, resulting in sensitivities to bulk magnetic moments as small as  $5 \cdot 10^{-8} \text{ emu} = 5 \cdot 10^{-11} \text{ J/T}$  or roughly  $10^{12}$  Bohr magnetons in a sample.

### Torque magnetometry

As sensitive as SQUID magnetometers may be, they do not perform great when millikelvin temperatures are required. Their working principle based on the translation of samples across a sensitive coil generates excessive heat to cool the system below 1 K. Even if implementations with powerful  $^3\text{He}$  refrigerators exist, they are costly and cannot access the range below 300 mK. In this regard, capacitance-based measurements offer a great and simple solution that can be used down to dilution-fridge temperatures.

A magnetic moment in an inhomogenous magnetic field experiences a certain force and a torque. If we place a magnetic sample on a flexible cantilever, this will deflect under the action of the field. This deflection may be measured with extreme sensitivity if the cantilever is part of a parallel plate capacitor, reflected as changes in capacitance. The torque on a cantilever of length  $d$  (with  $\mathbf{d}$  the vector linking the fixed point of the

cantilever and the sample) can be expressed as

$$\mathcal{T} = \underbrace{\mathbf{M} \times \mathbf{H}}_{\parallel} + \underbrace{\mathbf{d} \times (\mathbf{M} \cdot \nabla)\mathbf{H}}_{\perp} \quad (3.26)$$

where the two terms are given by the magnetization components parallel ( $\parallel$ ) and perpendicular ( $\perp$ ) to the magnetic field [85]. Clearly, this technique is sensitive to any changes in the magnetization of a sample. It is generally unfeasible to perform an absolute calibration of the measurements. However, we have a tool to probe any magnetic phase transitions with high precision. Sudden changes in magnetization associated with phase transformations leave clear, sharp signatures in the torque dependence. Using soft cantilevers allows for extreme sensitivity to such phase transitions.

### Faraday balance

Even if we cannot calibrate our torque signals, we can still obtain quantitative information by using a differential method. Measurements are carried out in the compact magnetometer shown in Fig. 3.7.(b). More details can be found in [84].

By applying a controlled magnetic field gradient to the sample, we can determine the total longitudinal magnetization. The longitudinal force on a magnetic moment under a magnetic field is proportional to its gradient  $F_z = m_z \frac{\partial B_z}{\partial z}$ . In turn, for small field gradients, this force creates a slight deflection  $\delta \propto F_z$  on the cantilever. A uniform field gradient can be created by a pair of coils in anti-Helmholtz configuration where  $\frac{\partial B_z}{\partial z} \propto I$ . All in all, the resulting deflection is  $\delta \propto m_z I$ . Finally, assuming a parallel plate geometry the capacitance is inversely proportional to the plate distance, we obtain the following expression

$$\left. \frac{dC}{dI} \right|_{I=0} = m_z (C_{I=0})^2 \quad (3.27)$$

from which  $m_z$  can be obtained. Measurements of  $C$  with a field gradient given by  $+I$  and  $-I$  gives the left hand side of the equation as long as the current is small enough to provide a linear deflection. A value of magnetization can be derived up to a global scale factor. Finally, the scale factor (which only depends on the stiffness of the cantilever and is therefore roughly independent of temperature) to obtain absolute units can be extracted from a comparison to high temperature data obtained with other technique, like SQUID.

## 3.6 Crystal growth and sample synthesis

The advancement of research in condensed matter physics relies heavily on the synthesis and engineering of new quantum materials. Enormous efforts go towards conceiving physical realizations of systems with exotic properties. In this work, two families of materials were synthesized and grown as single crystals. On the one hand, the family of quasi-1D quantum antiferromagnets  $A_2\text{Cu}_2\text{Mo}_3\text{O}_{12}$ , with  $A = \text{Rb}, \text{Cs}$ . On the other hand, members of the family of purported kagome magnets  $R_3\text{BWO}_9$ , with  $R = \text{La}, \text{Pr}, \text{Nd}$ . In the following, the details of the synthesis and crystal growth of both families of materials are outlined.

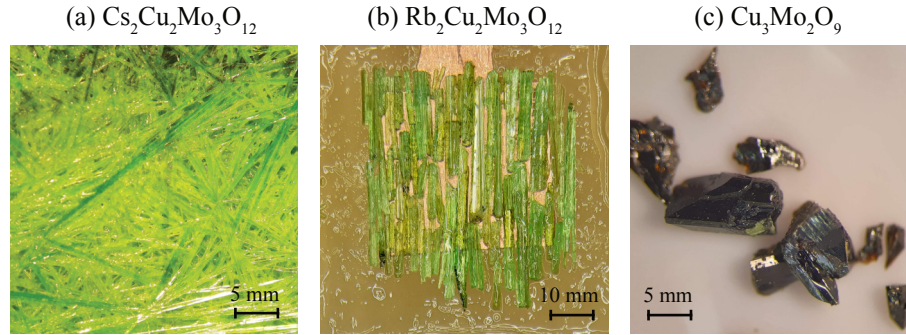
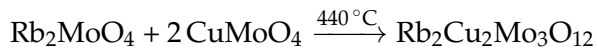
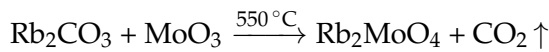
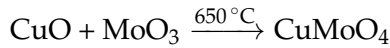


**Figure 3.8:** (a) Close-up picture of a batch of  $\text{Cs}_2\text{Cu}_2\text{Mo}_3\text{O}_{12}$ . Dark green single crystals are embedded in a waxy-looking light green flux. (b) A set of  $\text{Rb}_2\text{Cu}_2\text{Mo}_3\text{O}_{12}$  single crystals mounted on a capacitor. (c) Single crystals of  $\text{Cu}_3\text{Mo}_2\text{O}_9$  are found in the bottom of the crucibles during crystal growth.

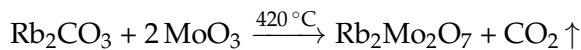
### $A_2\text{Cu}_2\text{Mo}_3\text{O}_{12}$

Both  $\text{Cs}_2\text{Cu}_2\text{Mo}_3\text{O}_{12}$  and  $\text{Rb}_2\text{Cu}_2\text{Mo}_3\text{O}_{12}$  were synthesized by means of solid state reactions from commercially available chemical precursors. Starting with  $\text{Rb}_2\text{Cu}_2\text{Mo}_3\text{O}_{12}$ , powders of this compound were synthesized in a three step process:



Each reaction involved several sintering steps at the indicated temperatures for times ranging from 12 h to 48 h. After each sintering round, the resulting material was thoroughly ground to a fine powder. In general, best results were obtained for two rounds of sintering for 12-18 h, followed by a final longer sintering for 36-48 h. Each intermediate compound is checked using powder X-ray to ensure quality and phase purity.

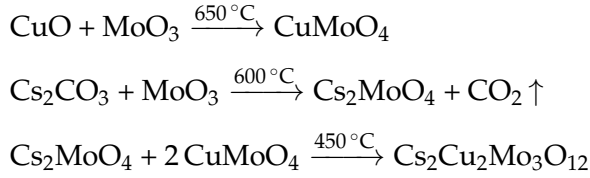
Single-crystal samples were grown using a flux method. A specifically synthesized flux is used for this process. For  $\text{Rb}_2\text{Cu}_2\text{Mo}_3\text{O}_{12}$ , the flux is  $\text{Rb}_2\text{Mo}_2\text{O}_7$  and is obtained in the following reaction:



This compound has a melting point between  $430^\circ\text{C}$  and  $440^\circ\text{C}$ . Powders of  $\text{Rb}_2\text{Cu}_2\text{Mo}_3\text{O}_{12}$  and the flux are mixed in a 1:2 molar proportion. The compounds are finely ground together and placed into an alumina crucible with a loose fitting lid. The mixture is then heated in a box furnace in air up to  $520^\circ\text{C}$  and kept at that temperature for 24 h. Then, a slow cooldown at a rate of  $2^\circ\text{C}/\text{h}$  is followed down to  $400^\circ\text{C}$ , after which the system is allowed to rapidly cool down to room temperature. Bright green single crystals appear on the surface of the flux and are extracted mechanically. No substance was found to dissolve the flux without harming the crystals. Typical shapes are thin needles with a sizes between 0.2 and 4 mm in length and 0.1 to 0.5 mm across

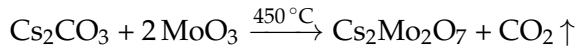
(Fig. 3.8.(b)). The resulting crystals are extremely fragile and break easily into smaller needles.

The process for  $\text{Cs}_2\text{Cu}_2\text{Mo}_3\text{O}_{12}$  is very similar. Again we followed a three step process:



with the same considerations.

Single crystals are grown also in a flux method, using  $\text{Cs}_2\text{Mo}_2\text{O}_7$  in this case as a flux:



Similarly,  $\text{Cs}_2\text{Cu}_2\text{Mo}_3\text{O}_{12}$  and flux are mixed in a 1:2 molar ratio. The same process is followed to treat the mixture, however with a dwelling maximum temperature of 510 °C. Green single crystals appear on the surface of the flux and are collected mechanically (Fig. 3.8.(a)).

Interestingly, in some batches we observe the crystallization of  $\text{Cu}_3\text{Mo}_2\text{O}_9$  in the bottom of the crucibles (Fig. 3.8.(c)). The significance of this will be discussed in Chapter 4.

### $R_3\text{BWO}_9$

Several members of the  $R_3\text{BWO}_9$  family were synthesized in powder form and grown in single crystals. These include the magnetic members  $\text{Nd}_3\text{BWO}_9$  and  $\text{Pr}_3\text{BWO}_9$ , and the non-magnetic  $\text{La}_3\text{BWO}_9$ . The synthesis of powder materials is very similar for all of them. We started from commercial precursors, including oxides of the target rare earth in trivalent oxidation state,  $R^{3+}$ . The following solid-state reaction was followed:



The powder precursors are mixed and placed in an alumina crucible, then brought to high temperature in a box furnace. Best results were obtained when the thermal treatment was repeated three times over 16 h/48 h/48 h. The product of each process is finely reground and checked for purity using powder X-ray diffraction (Fig. 3.9.(b)).

Single crystals are grown using a flux method, using lead monoxide (PbO) as a solvent. Here we follow a procedure close that in [86]. Powders of the target material and PbO are mixed in a molar ratio 1:40/3 and ground together finely. The mixture is placed into a platinum crucible with a loose fitting lid and brought to 1100 °C for 72 h in air. After that follows a slow cooling down to 900 °C over 96 h, to finish with a rapid cooling to room temperature. In the process, most PbO evaporates from the crucible.

Single crystals appear on the bottom of the crucible between the remains of PbO. These crystals are impervious to strong bases and therefore a concentrated solution of KOH is used to dissolve the remaining PbO flux. Crystals show vibrant purple (Nd) or green (Pr) colors (Fig. 3.9.(a)), or are transparent (La). They are elongated and show

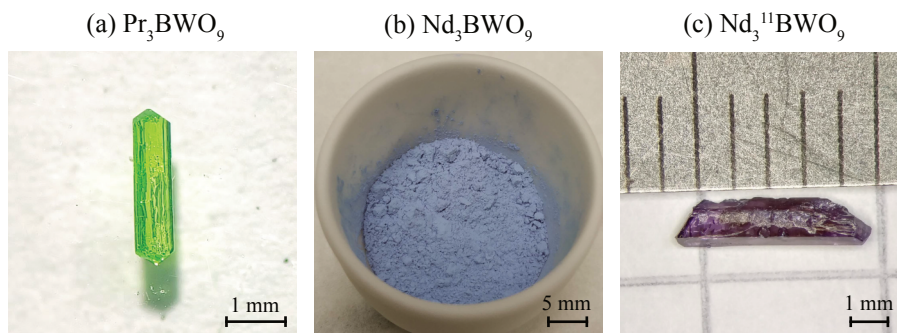


**Figure 3.9:** (a) A single crystal of  $\text{Pr}_3\text{BWO}_9$ . (b) Powders of  $\text{Nd}_3\text{BWO}_9$  prepared as described in the text. (c) A single crystal of  $^{11}\text{B}$ -enriched  $\text{Nd}_3\text{BWO}_9$  used in diffraction experiments.

well defined facets perpendicular to the hexagonal plane. Masses as large as 40 mg were obtained for a single crystal following this method.

As discussed above, some isotopes have a large affinity to capture neutrons. Materials have to be enriched in particular isotopes in order to be apt for neutron scattering experiments. One of the elements where this is the case is boron. Of the two stable isotopes, one shows an extremely large absorption cross section. For the neutron experiments shown in Chapter 6, we synthesized and grew  $^{11}\text{B}$ -enriched samples. The availability of isotope-enriched chemicals is quite limited, thus another process was used for the sample synthesis:



where  $\text{H}_3^{11}\text{BO}_3$  is enriched up to 99% in  $^{11}\text{B}$ . Single crystal growth was carried out using the same conditions as for natural boron (Fig. 3.9.(c)), with identical results in all the cases.



## Chapter 4

# Quantum multiferroicity and BEC criticality in $\text{Rb}_2\text{Cu}_2\text{Mo}_3\text{O}_{12}$

The results discussed in this chapter can also be found in the following reference:  
*S. Hayashida, L. Huberich, D. Flavián, Z. Yan, K. Yu. Povarov, S. Gvasaliya, and A. Zheludev. Critical dielectric susceptibility at a magnetic BEC quantum critical point. Phys. Rev. Research 3, 033053 (2021).*

**Summary of contributions.** Numerical studies were conducted by the author in collaboration with A. Valenti, L. Giobbi and Prof. S. Huber. Single crystal samples of  $\text{Rb}_2\text{Cu}_2\text{Mo}_3\text{O}_{12}$  were grown by S. Hayashida, with support from Z. Yan. High temperature measurements were carried out by the author. Low temperature measurements of capacitance were done by S. Hayashida with support of L. Huberich and the author. Pyroelectric currents were measured by the author and S. Hayashida. Theoretical interpretation of the results was developed by the author and S. Hayashida.

### 4.1 Introduction

Magnetic insulators have long served as experimental prototypes for fundamental studies of thermal and quantum phase transitions. These materials can often be carefully tuned to quantum QCPs, for example by an applied magnetic field. The fact that magnetic-field-induced transitions in spin systems may show dielectric anomalies is a well known phenomenon [87]. Pioneering work on determining the critical susceptibility at a magnetic QCP from electric permittivity measurements was performed at the saturation transition in  $\text{Ba}_2\text{CoGe}_2\text{O}_7$  [88]. Here, electric polarization is a primary order parameter, coupled linearly to staggered magnetization by means of spin-dependent p-d hybridization [89, 90]. The observed behavior is in excellent agreement with the Ising universality class [88], exhibiting the potential of using the dielectric channel to access magnetic quantum criticality.

BEC physics is often encountered in magnetic insulators as magnetic excitations become gapless, as was motivated in Chapter (2). In those systems the critical susceptibility associated to the order parameter adopts a concrete meaning (completely lacking in the original Bose gas theory), as the change in staggered magnetization under an equally

staggered field. Unfortunately, it still remains inaccessible, as there is no practical way to produce a measurement field that is modulated at the atomic length scale. At best, it can in principle be inferred from correlation functions measured in scattering experiments [91].

In this chapter, we use a similar gimmick to that in [88] and demonstrate how the critical susceptibility at a BEC QPT can be measured in a probe-response manner, by actually applying an electric excitation field and measuring the dielectric response. We study  $\text{Rb}_2\text{Cu}_2\text{Mo}_3\text{O}_{12}$ , a quantum magnetic material with a field-induced magnon BEC QPT, in which magnetoelectric coupling makes the uniform electric polarization a primary BEC order parameter. This allows us to directly measure the critical behavior of susceptibility at the quantum critical trajectory and extract BEC critical exponents.

### **$\text{Rb}_2\text{Cu}_2\text{Mo}_3\text{O}_{12}$ overview**

The peculiar magnetic and dielectric properties of the quasi-one-dimensional frustrated ferro-antiferromagnet  $\text{Rb}_2\text{Cu}_2\text{Mo}_3\text{O}_{12}$  have been studied for over a decade. It crystallizes in a monoclinic structure, with space group  $C2/c$  (No. 15) [92] with lattice parameters  $a = 27.675(5)$  Å,  $b = 5.094(7)$  Å,  $c = 19.264(5)$  Å, and  $\beta = 107.29(2)^\circ$  at room temperature. The magnetic properties are due to  $S = 1/2$   $\text{Cu}^{2+}$  ions.  $\text{CuO}_4$  units form a one-dimensional structures along the crystallographic  $b$  axis, well isolated by the bulky  $\text{Rb}^+$  ions. Powder samples have been heavily investigated by means of magnetic and dielectric measurements [93–100], high-pressure studies [101, 102], nuclear magnetic resonance [103, 104], neutron scattering [99, 100, 105], muon spin relaxation [99, 106], and electron spin resonance [98, 100]. The ground state is a gapped quantum paramagnet, with magnetic long-range order induced in a magnon BEC transition at  $\mu_0 H_{c1} \approx 2$  T. At zero field, the non-magnetic singlet features a spin gap of  $\sim 2$  K. The BEC “dome” extends up to  $\mu_0 H_{c2} \sim 13$  T, where the magnetic system becomes saturated. Magnetic long-range order is confined below  $T < 1.5$  K for any magnetic field orientation [97, 98]. The exchange interactions are highly frustrated, which spurred intensive studies of its ground state. Competing ferromagnetic nearest-neighbor  $J_1 = -138$  K and antiferromagnetic next-nearest-neighbor  $J_2 = 51$  K [93, 94] position  $\text{Rb}_2\text{Cu}_2\text{Mo}_3\text{O}_{12}$  in close proximity to the transition between ferromagnetism and helimagnetism (classically). In the quantum limit, many exotic phases are predicted to be stabilized in this point, including condensation of multipolar bound states [107, 108].

A comprehensive array of bulk measurements were carried out on single-crystals samples [98], bringing key findings into light. The entire field-temperature phase diagram was mapped out, resulting to be curiously anisotropic. The lower critical fields differ by up to 50% depending on the field direction, and the upper ones being almost the same in all geometries. Recent neutron scattering studies suggested an interplay of more complex interactions such as interchain and anisotropic couplings [100], describing  $\text{Rb}_2\text{Cu}_2\text{Mo}_3\text{O}_{12}$  as an extremely anisotropic, frustrated spin ladder. Note that a zero-field spin gap would be a natural consequence of spin-ladder physics [109–111].

The material generated a great deal of excitement when it was found to exhibit magnetic-field-induced ferroelectricity at temperatures much higher than magnetic ordering, already at  $T' = 8$  K [95, 96, 99, 100]. It was suggested that below  $T'$  the system is a chiral spin liquid, with no magnetic long-range order but with spontaneously chiral

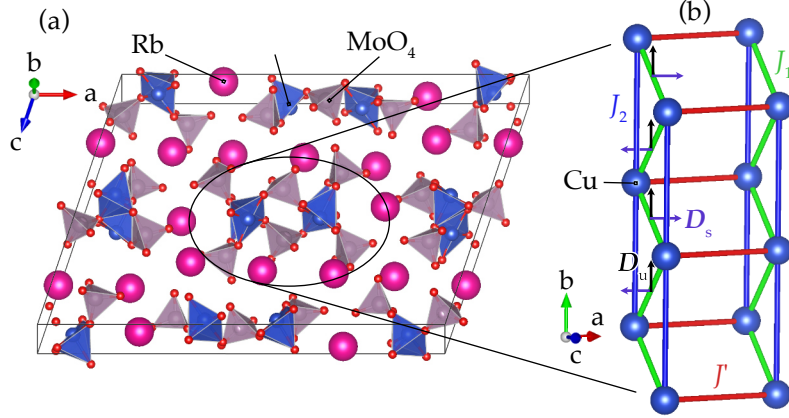


**Figure 4.1:** (a) Schematic crystal structure of  $\text{Rb}_2\text{Cu}_2\text{Mo}_3\text{O}_{12}$ . The magnetic spin ladder is highlighted. (b) Structure of a spin ladder, showing the exchange couplings that build the Hamiltonian in (4.2). The alternating DM vectors on the nearest-neighbor couplings is shown on the left leg of the ladder.

spin fluctuations [32]. A connection between ferroelectricity and such magnetic chiral state has not been established, though is the focus of theoretical effort. At much lower temperatures, another dielectric anomaly is detected which corresponds to the boundary of the BEC dome of order [99].

All previous studies were carried out on powder samples. This limits control over sample quality and is particularly dangerous for any measurements in an applied field, where any features in the data will be smeared out by the directional averaging of magnetic anisotropy. In contrast, our focus is on high-quality single crystals. In the course of this chapter, we show that the  $T' = 8$  K anomaly is actually spurious, as a result of impurities. Two magnetic-field-induced magnon BEC QPTs are experimentally accessible, one at the gap-closing field  $H_{c1}$  and another one at saturation field  $H_{c2}$ , that we use as a platform to access critical properties. We show that in the  $T \rightarrow 0$  limit, polarization is a primary BEC order parameter at the upper critical field but not at the lower one. We finally do what is in principle impossible in powders: measure the quantum scaling behavior of critical dielectric susceptibility at the  $H_{c2}$  magnon BEC QCP.

## 4.2 Refining the spin Hamiltonian

The goal to describe the physics of a magnetic system goes through finding a suitable spin Hamiltonian. In general, minimal models with a few couplings can capture most low energy phenomena thanks to the very short range of superexchange couplings. Attempts to finding such a model for  $\text{Rb}_2\text{Cu}_2\text{Mo}_3\text{O}_{12}$  span over 15 years. Initially conceived as a frustrated spin chain, the model did not fully capture the low-temperature physics, in particular the zero-field spin gap.

A more refined model was recently proposed, where  $\text{Rb}_2\text{Cu}_2\text{Mo}_3\text{O}_{12}$  is described as a spin ladder with significantly anisotropic interactions [100], in the form of Dzyaloshinskii-Moriya (DM) terms. The model reproduces well many experimental observations, however there is one caveat.

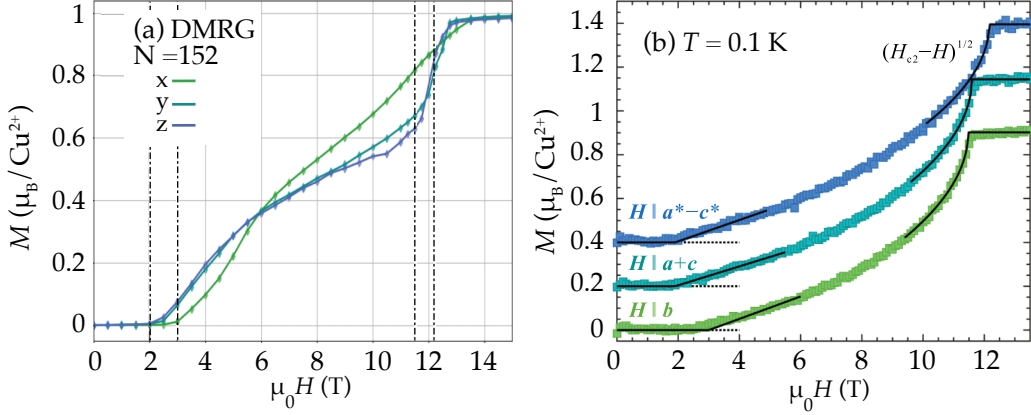


**Figure 4.2:** (a) Numerical calculation of magnetization as a function of field for the Hamiltonian in 4.3 using DMRG on a system of  $N = 152$  sites. Broken lines indicate critical fields as discussed in the text. (b) Measured magnetization on  $\text{Rb}_2\text{Cu}_2\text{Mo}_3\text{O}_{12}$  for three field orientations from [98]. Note that the data sets have an offset of 0.2 units for visibility.

Anderson’s theory of superexchange is based on virtual electron hopping between nearby magnetic ions. This theory can be extended to take into account the effect of spin-orbit interactions. Spin-orbit interaction binds spin- and real-space, but it does so isotropically, without breaking the  $\text{SU}(2)$  symmetry of a Heisenberg Hamiltonian. As a result, the exchange coupling becomes a tensor magnitude; its antisymmetric part being the origin of DM interactions. Note that these define a preferential direction given by the Dzyaloshinskii vector, and would break the rotational symmetry. This is precisely avoided by the symmetric part of the anisotropy tensor. For a single bond, this can be well described as

$$\mathcal{H}_{1,2} = J\mathbf{S}_1 \cdot \mathbf{S}_2 + \mathbf{D} \cdot (\mathbf{S}_1 \times \mathbf{S}_2) + \frac{1}{2J}(\mathbf{D} \cdot \mathbf{S}_1)(\mathbf{D} \cdot \mathbf{S}_2) - \frac{|\mathbf{D}|^2}{4J}\mathbf{S}_1 \cdot \mathbf{S}_2 \quad (4.1)$$

The first term in (4.1) is the Heisenberg Hamiltonian, the second the usual DM term and the last two terms come from the symmetric part of the interaction. This expression is fully symmetric under rotations, and importantly, the weight of all anisotropic terms is controlled by the vector  $\mathbf{D}$ . For multiple connected bonds, however, staggering and frustration of the  $\mathbf{D}$  vectors may still break spin rotation symmetry, defining preferential directions in space.

The reason why the symmetric part of the anisotropy is often ignored is that its weight, given by  $|\mathbf{D}|^2/4J$ , makes its effect negligible. However, for the case of [100] it is not the case. In fact, their fitted couplings suggest all terms in (4.1) must have the same weight, rendering their proposed Hamiltonian simply unphysical.

Using as a starting point the model in [100], we propose a Hamiltonian that captures

the anisotropy in  $\text{Rb}_2\text{Cu}_2\text{Mo}_3\text{O}_{12}$

$\mathcal{H} =$

$$\begin{aligned} \sum_l \sum_{\sigma=\pm} \left[ \left( J_1 - \frac{|\mathbf{D}_{\sigma,l}|^2}{4J_1} \right) \mathbf{S}_{\sigma,l} \cdot \mathbf{S}_{\sigma,l+1} + J_2 \mathbf{S}_{\sigma,l} \cdot \mathbf{S}_{\sigma,l+2} + \frac{J'}{2} \mathbf{S}_{+,l} \cdot \mathbf{S}_{-,l} \right. \\ \left. + \mathbf{D}_{\sigma,l} \cdot \mathbf{S}_{\sigma,l} \times \mathbf{S}_{\sigma,l+1} \right. \\ \left. + \frac{1}{2J_1} (\mathbf{S}_{\sigma,l} \cdot \mathbf{D}_{\sigma,l}) (\mathbf{S}_{\sigma,l+1} \cdot \mathbf{D}_{\sigma,l}) \right. \\ \left. - g\mu_B \mathbf{B} \cdot \mathbf{S}_{\sigma,l} \right] \end{aligned} \quad (4.2)$$

with

$$\mathbf{D}_{\sigma,l} = \sigma \left[ \mathbf{D}_u + (-1)^l \cdot \mathbf{D}_s \right] \quad (4.3)$$

where the index  $l$  runs along the ladder and  $\pm$  indicates either side of it, with the couplings being defined as in Fig. 4.1. The first line describes the isotropic interactions with corrections on the nearest neighbor coupling. The second and third lines describe the antisymmetric and symmetric part of the anisotropy, respectively. Finally, the fourth line adds the Zeeman energy from an external magnetic field. Anisotropic exchanges are only considered for the nearest neighbors, as the coupling is strongest. Note that due to the low symmetry of the system, no symmetry restrictions exist on the DM vectors for nearest neighbors. Two types of DM interactions are considered as reflected in (4.3): a uniform ( $\mathbf{D}_u$ ) and a staggered one ( $\mathbf{D}_s$ ).

Using a combination of exact diagonalization (ED) and density matrix renormalization group (DMRG) calculations we optimize the coupling constants in (4.2) to fit experimental data. In particular, constraints are imposed from critical fields and magnetization curves from [98]. The accurate determination of different critical fields allows for a fine tuning of the anisotropy. In addition, the couplings are modified such that the spectrum is consistent with spectroscopic measurements on powders in [100].

ED is used to explore the parameter space using a ladder with 16 sites. Due to the strong frustration in the system, finite-size effects are very significant on the obtained coupling constants. Further optimization of the parameters relies on DMRG on large systems, with up to 152 sites. Carefully extrapolating to the thermodynamic limit, we obtain a set of parameters that is consistent with several experimental observations. The optimized values result

$$J_1 = -126.4 \text{ K}; \quad J_2 = 39.0 \text{ K}; \quad J' = 22.7 \text{ K}; \quad D_u = 19.4 \text{ K}; \quad D_s = 40.5 \text{ K} \quad (4.4)$$

where we assumed  $\mathbf{D}_u = D_u \hat{z}$  and  $\mathbf{D}_s = D_u \hat{x}$ , directions in real space. This choice of directions seems consistent with the experimental data if  $\hat{x} \sim b$ ,  $\hat{y} \sim a^* - c^*$ , and  $\hat{z} \sim a + c$ . The resulting magnetization curves are shown in Fig. 4.2. Notably, our model reproduces well the anisotropy of the lower critical fields and the vanishing magnetic susceptibility in the gapped, low-field phase. Even though the model slightly underestimates the value of the saturation fields, it seems to capture their anisotropy. This may indicate an overestimation of the g-tensor, taken here to be  $g = 2.16$  as in [100].

Our model fails dramatically in reproducing the magnetization values at intermediate fields, when the system is only partially magnetized. However, this may be unsurprising since three dimensional coupling is being neglected. Note that it is precisely 3D coupling that generates the ordered dome in a gapped quantum magnet. This extra transverse coupling can be implemented in the form of a random-phase approximation (RPA). One would solve the model of individual 1D chains exactly and then couple the chains in three dimensions with a mean field approach. In doing so, the total system magnetic susceptibility ( $\chi$ ) for example becomes renormalized by transverse couplings ( $J_{\perp}$ ) as

$$\chi(\omega, \mathbf{q}) = \frac{\chi^{1D}(\omega, \mathbf{q})}{1 + 2J_{\perp} \cos(q_{\perp})\chi^{1D}(\omega, \mathbf{q})}. \quad (4.5)$$

This self consistent technique has been used for several 1D systems with successful results [53, 112, 113]. In addition, the coupling to lattice degrees of freedom and polarization is a natural way forward in the study. The magneto-electric coupling in  $\text{Rb}_2\text{Cu}_2\text{Mo}_3\text{O}_{12}$  may modify the anisotropic  $\mathbf{D}$  vectors in the proximity to the saturation field.

### 4.3 Dielectric measurements in $\text{Rb}_2\text{Cu}_2\text{Mo}_3\text{O}_{12}$

Motivated by the discovery of magnetic-field dependent electric polarization in the absence of magnetic ordering in  $\text{Rb}_2\text{Cu}_2\text{Mo}_3\text{O}_{12}$ , we conduct a thorough study of its magneto-electric response. We present in the following measurements of capacitance and electric polarization for a wide range of temperatures and magnetic fields, on a variety of samples. We clarify the origin of the 8 K anomaly reported in [95, 97, 99, 100] and show that  $\text{Rb}_2\text{Cu}_2\text{Mo}_3\text{O}_{12}$  is an excellent quantum multiferroic at low temperatures. Our electric susceptibility data bring a new perspective into the quantum critical regime around the QCPs in  $\text{Rb}_2\text{Cu}_2\text{Mo}_3\text{O}_{12}$ .

#### High-temperature dielectric properties

In order to understand the phenomena behind the  $T' = 8$  K transition that has been reported by several authors [95, 97, 99, 100], we carry out a study of the temperature and field dependence of capacitance of several kinds of samples of  $\text{Rb}_2\text{Cu}_2\text{Mo}_3\text{O}_{12}$ . These include: (1) sintered powder prepared as described in previous references and mounted in a capacitance cell; (2) a set of roughly 200 small crystals randomly aligned with their  $b$  axis preferentially in plane; (3) about 50 handpicked larger single crystals aligned with their  $b$  axes parallel (and randomly distributed in the perpendicular direction) in a capacitance cell; (4) a single-crystal sample of  $\sim 0.1$  mg on which we deposit silver paint electrodes; and (5) a powder produced by finely grinding small single crystals, which is also placed in a capacitance cell. Representative images of all these samples are shown in Fig. 4.3.(a-f). The capacitance cell consists of two parallel copper plates spaced by a Teflon frame. Samples (1), (2), (3), and (5) are measured using this cell.

The nature of the field-induced  $T'$  dielectric anomaly is revealed on the measurements in Fig. 4.4, that shows the temperature dependence of sample-cell capacitance for samples of types (1) - (5). In short, it develops only in sintered powder (Fig. 4.4.(a)) but is absent in all samples derived from single crystals (Fig. 4.4.(b-e)). The monotonic and featureless capacitance of the empty cell was measured separately and subtracted.

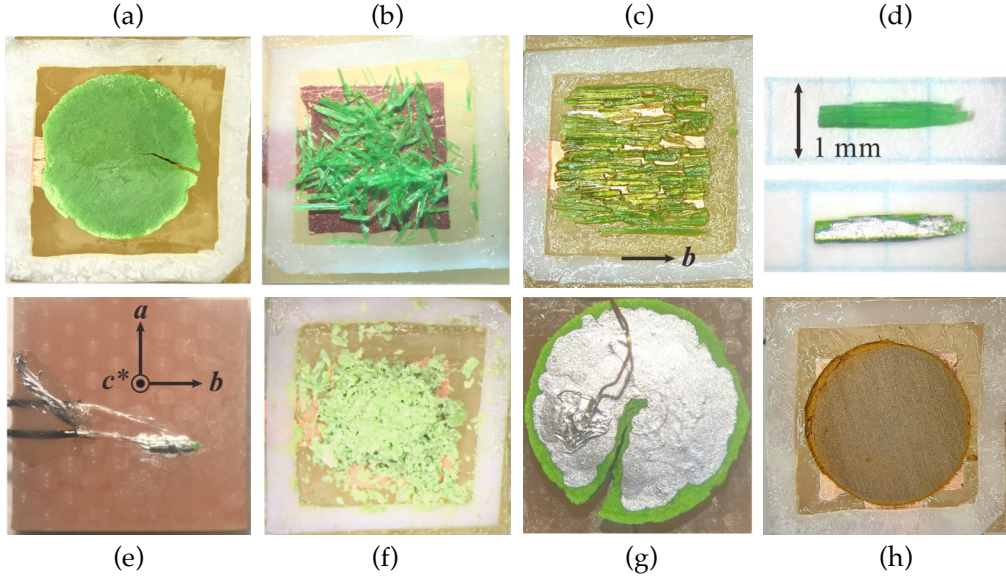


**Figure 4.3:** Photos of various  $\text{Rb}_2\text{Cu}_2\text{Mo}_3\text{O}_{12}$  samples used. (a) Sintered-powder sample. (b) Randomly assembled crystals, with their  $b$  axis preferentially in plane. (c) Coaligned crystals, only along  $b$ , disordered in the perpendicular direction. (d) Single-crystal sample without and with silver-paste contacts. (e) Sample assembled for single-crystal dielectric measurements. Coaxial cables are connected right up to the sample stage. (f) Finely ground crystals. (g) Pelletized sintered-powder sample with deposited silver electrodes. (h) Sintered and pelletized  $\text{Cu}_3\text{Mo}_2\text{O}_9$  powders.

In an applied magnetic field, the capacitance of the sintered-powder sample develops a peak of about 1.5 fF in the real part, as well as a distinct feature in the imaginary part at around  $T' = 8$  K [Fig. 4.4.(a)]. The observed features are very similar to the dielectric anomaly reported in Refs. [99, 100]. and clearly can be ascribed to the same ferroelectric anomaly. Strikingly, this peak in capacitance is completely absent in all the remaining samples, obtained from single crystals [see Fig. 4.4.(b-e)]. A geometry with  $\mathbf{H} \perp \mathbf{b}$  and  $\mathbf{H} \perp \mathbf{E}$  is used for the coaligned-crystals measurement in Fig. 4.4.(c). Similar data were obtained with  $\mathbf{H} \perp \mathbf{b}$ ,  $\mathbf{H} \parallel \mathbf{E}$  and  $\mathbf{H} \parallel \mathbf{b}$ ,  $\mathbf{H} \perp \mathbf{E}$ .

Data in Fig. 4.4.(d) are measured with a magnetic field perpendicular to the single-crystal  $\mathbf{b}$  axis and probing electric field perpendicular to  $\mathbf{c}^*$ . Measurements for magnetic fields along the  $\mathbf{b}$  direction are qualitatively very similar. Altogether, Fig. 4.4 shows that that the  $T'$  anomaly reported in Refs. [95, 96, 99, 100] is endemic to sintered powders and must be originate from an impurities. Note that the data in Fig. 4.4.(b) (random crystals) show a vague field-dependent variation of about 0.15 fF in  $\Delta C'$ , suggesting some residual impurity contamination may still be present in the sample.

The most likely culprit is a related compound, namely,  $\text{Cu}_3\text{Mo}_2\text{O}_9$ . This material displays a very large ferroelectric anomaly at its magnetic ordering transition, which occurs precisely at 8 K [114]. Its synthesis process [115] is similar to that in  $\text{Rb}_2\text{Cu}_2\text{Mo}_3\text{O}_{12}$  and  $\text{Cs}_2\text{Cu}_2\text{Mo}_3\text{O}_{12}$ . As described in Chapter 3 we found grains of this material in some batches of our crystal growth, and could extract enough material to create the sample in Fig. 4.3.(h). We measured the capacitance of  $\text{Cu}_3\text{Mo}_2\text{O}_9$  using the same capacitor cell.

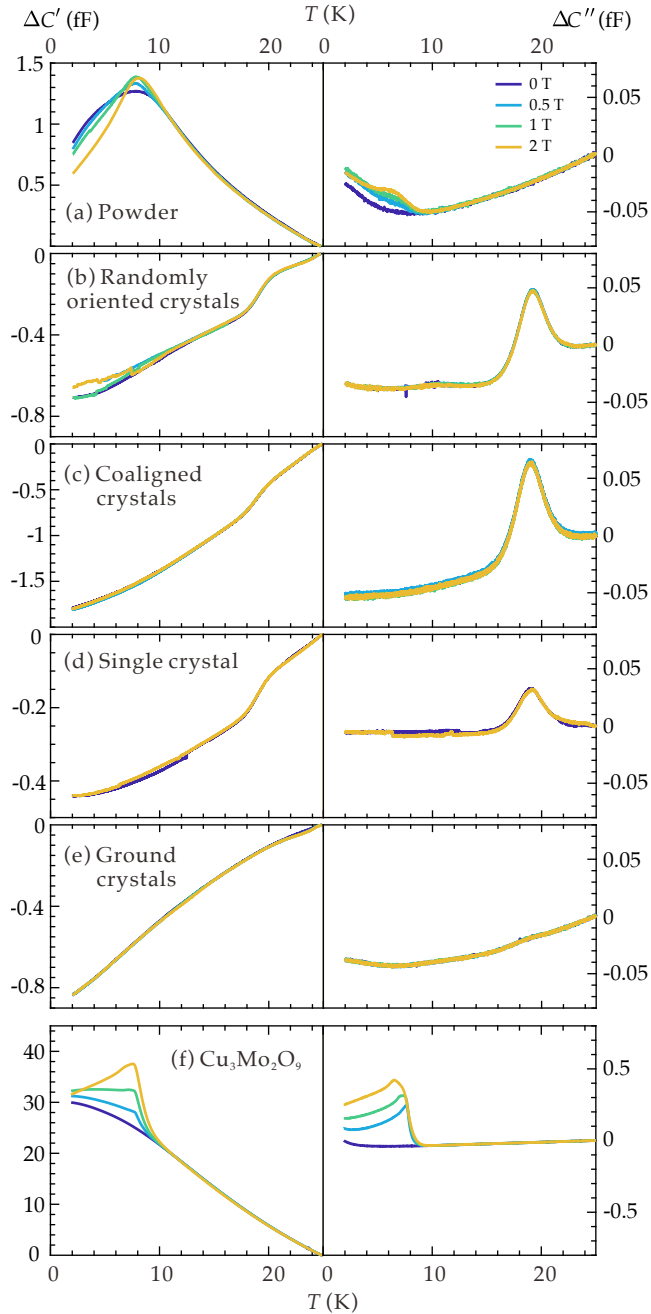


**Figure 4.4:** Temperature scans of the capacitance above 2 K for (a) sintered powder, (b) randomly oriented crystals, (c) coaligned crystals, (d) a single piece of the crystal, (e) powder produced from finely ground crystals, and (f)  $\text{Cu}_3\text{Mo}_2\text{O}_9$  powder. The labels of the left and right axes are the changes in the capacitance from 25-K  $\Delta C'$  and  $\Delta C''$ , respectively.

The results, shown in Fig. 4.4.(f), reveal a prominent anomaly at  $T' = 8$  K, which coincides with that seen in the sintered-powder sample of  $\text{Rb}_2\text{Cu}_2\text{Mo}_3\text{O}_{12}$ . The magnitude of this  $\Delta C'$  anomaly is about 50 times larger as in the sintered sample of  $\text{Rb}_2\text{Cu}_2\text{Mo}_3\text{O}_{12}$ . An impurity concentration of  $\text{Cu}_3\text{Mo}_2\text{O}_9$  as little as  $\sim 2\%$  would suffice to mimic the  $T'$  anomaly in  $\text{Rb}_2\text{Cu}_2\text{Mo}_3\text{O}_{12}$ . Importantly, such a small amount may go completely undetected by means of powder x-ray diffraction. In summary, all these results reveal one thing: The  $T'$  anomaly is not endemic to  $\text{Rb}_2\text{Cu}_2\text{Mo}_3\text{O}_{12}$ .

Having shown something that the  $T'$  anomaly is not present in single crystals, we note something that indeed is present. Fig. 4.4.(b-d) reveal a different dielectric anomaly at about 19 K. This anomaly is characterized by a step in real part, accompanied by a significant peak in the imaginary part of capacitance. The feature is, however, absent in the bulk material that is ground to a fine powder as shown in Fig. 4.4.(e). This feature is entirely field independent and is therefore of non-magnetic origin. Though not relevant to the discussion that follows in this chapter, its relevance will be later discussed in Chapter 5 terms of dielectric relaxation.

### An actual quantum multiferroic ground state

Having resolved that the purported high-temperature chiral spin liquid phase is related to sample impurities, we focus on the low temperature dielectric response of  $\text{Rb}_2\text{Cu}_2\text{Mo}_3\text{O}_{12}$ . We show how dielectric anomalies appear at the field-induced magnon BEC transition, related to the onset of a ferroelectric ground state.

We, thus, first attempt to determine the electric polarization associated to this state. Fig. 4.5.a shows the temperature dependence of the capacitance of the pelletized sintered-powder sample in Fig. 4.3.(g) measured in a magnetic field  $\mu_0 H = 11$  T. In capacitance, we observe a broad anomaly at 0.7 K, corresponding exactly to the phase boundary of the magnon BEC dome [98]. The random orientation of crystallites in the powder (with respect to the external field) leads to a broadening of the anomaly. This feature is consistent with a previous dielectric study below 6 T [99]. We measured a pyroelectric current when heating up the sample across this transition, as shown by the peak in  $I_p$  in Fig. 4.5.(b). This current may be integrated to result in electric polarization (Fig. 4.5.(c)). Current and the corresponding electrical polarization are completely switchable by the reversal of the poling electric-field. Therefore, spontaneous ferroelectric polarization is an inherent property of the magnon BEC phase, and this phase is in fact multiferroic.

As discussed in detail below, much higher quality and orientation-resolved data on the dielectric constant can be obtained from single crystals. However, due to their very reduced size we were unable to measure polarization in these samples. From to geometry considerations, the expected pyroelectric current from our single crystals must be 50-100 times smaller than that seen in Fig. 4.5.(b), the latter being close to the detection limit of our setup.

In the following, we will focus on measurements of capacitance as a function of magnetic field and temperature. Those will give us direct access to the dielectric susceptibility of our samples. In order to justify this, we invoke the scaling theory of phase transitions, according to which the free energy of a system can be expressed as the sum of analytical (slowly varying) and singular (rapidly varying at the phase transition) terms. We want to focus on the critical (diverging) contribution to dielectric susceptibility, which we hence-

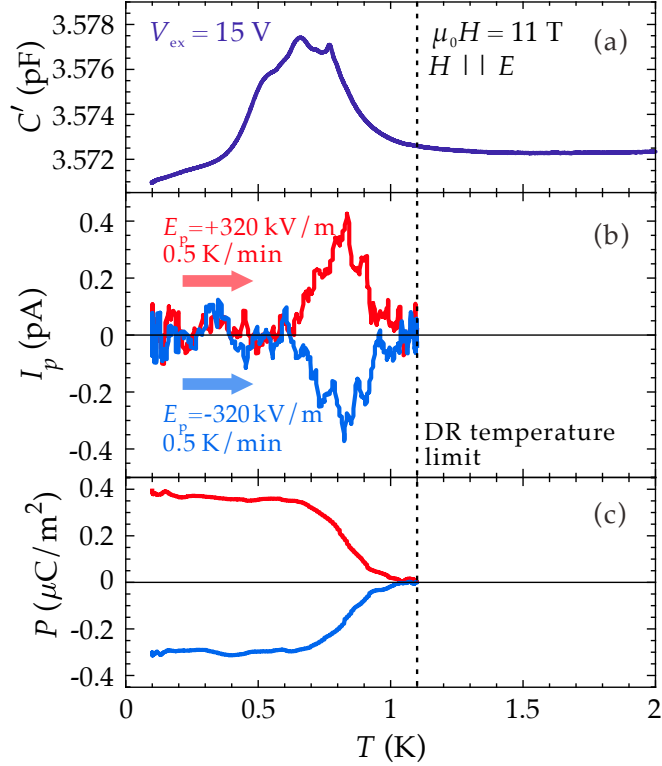


**Figure 4.5:** Temperature scans of (a) real capacitance  $C'$  and (b) pyroelectric currents  $I_p$  on pelletized  $\text{Rb}_2\text{Cu}_2\text{Mo}_3\text{O}_{12}$  sintered powder (as shown in Fig. 4.3.(g)). The magnetic field is applied parallel to the electric field. (c) Electric polarization  $P$  as obtained from the integration of the pyroelectric current over the measurement time. The dashed represents is the upper limit in temperature of the  $^3\text{He}$ - $^4\text{He}$  dilution refrigerator in its low-temperature, condensation mode.

forth denote as  $\chi$ . To do this and single out the critical terms, we assume that below  $T = 1$  K only this critical contribution shows any significant field dependence. A similar approach has been followed in [88] for example.

In our measurements we show the value of capacitance subtracting a baseline (non-critical) value, which is determined at 14 T for each temperature. This value of field is well removed from the critical regime, giving a value of roughly 0.24 pF. Note the diminutive changes in total capacitance; in all measurements  $\Delta C/C \lesssim 1\%$ . We further assume that the critical susceptibility  $\chi$  is proportional to the changes in capacitance,  $\Delta C$ . This approach is, admittedly, not without limitation. A separation between analytical and singular free energy contributions is not unambiguous to begin with. Indeed, the measured  $\Delta C$  shows some small variation between the gapped, ordered, and fully polarized phases even away from the critical regions of the field-induced phase transitions (see Fig. 4.6.(b)). This effect is rather significant in general, however for the  $\mathbf{H} \parallel \mathbf{c}^*$  geometry it is considerably smaller than the divergence in the immediate vicinity of the actual critical point.

Fig. 4.6 shows typical raw data as  $\Delta C(H, T) = C(H, T) - C(14 \text{ T}, T)$  for several temperatures and fields along three crystal directions. Pairs of sharp peaks are clearly observed below 1.4 K for  $H \parallel a$ , 0.9 K for  $\mathbf{H} \parallel \mathbf{b}$ , and 1 K for  $\mathbf{H} \parallel \mathbf{c}^*$ . Only the real part  $\Delta C'$  of

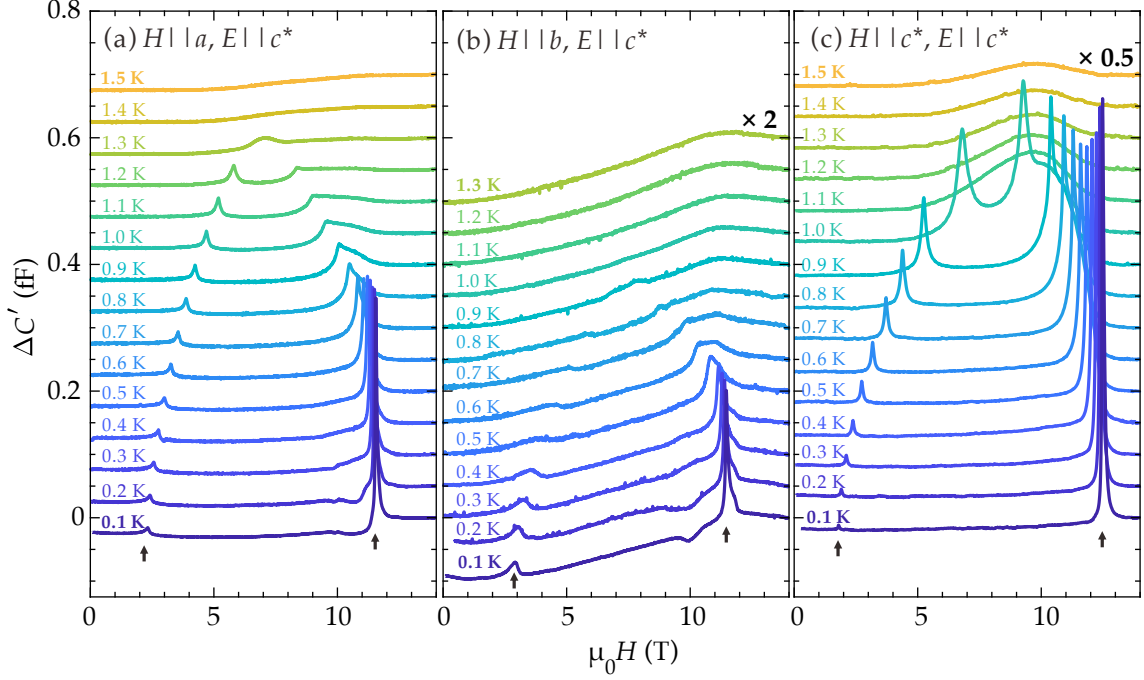


**Figure 4.6:** Typical capacitance  $\Delta C'$  data in applied magnetic fields along the (a) **a**, (b) **b**, and (c) **c\*** directions. The label of the vertical axis is the change in the capacitance from 14-T  $\Delta C'$ . For visibility, the scans are offset by 0.1 fF relative to one another. Note that the data in (b) and (c) were previously rescaled by 2 and 0.5, respectively, in order to unify the scale among all plots. Arrows indicate phase transitions as discussed in the text.

the measured capacitance is plotted. A small imaginary contribution is also measured, its relevance will be noted below. These anomalies are very similar to those found at ferroelectric transitions in different largely-studied magnon BEC compounds such as  $\text{TlCuCl}_3$  [25, 116]. The only difference is that our measurements on  $\text{Rb}_2\text{Cu}_2\text{Mo}_3\text{O}_{12}$  extend to higher fields closer to saturation.

Note that in our experiments the capacitor plates are directly deposited on the crystal surface. As long as the geometry of the capacitor does not change with the experimental conditions, we can associate the changes in capacitance to changes in dielectric constant. However, this association of  $\chi$  with  $\Delta C$  relies on the assumption that striction effects are negligible. In order to check to what extent this is the case, we measured the capacitance of the coaligned single crystals in Fig. 4.3.(c) loaded in a capacitance cell. In this setup the crystals are in contact with only the lower plate, while the upper plate remains free, sustained by a Teflon spacer. The expansion of Teflon is essentially zero at such low temperatures and, thus, the measured capacitance is entirely insensitive to striction. The susceptibility divergence using that setup is practically identical to that measured with electrodes mounted directly on the sample surface, validating our approach.

The bulk of our measurements are displayed in false-color plots in Fig. 4.7.(b,e,h). The phase boundaries (determined through the peak positions of the anomalies) are best revealed in the field-derivative of capacitance measured at a constant temperature,  $dC'/dH$ . Fig. 4.7.(c,f,i) show precisely this quantity. Circular symbols the

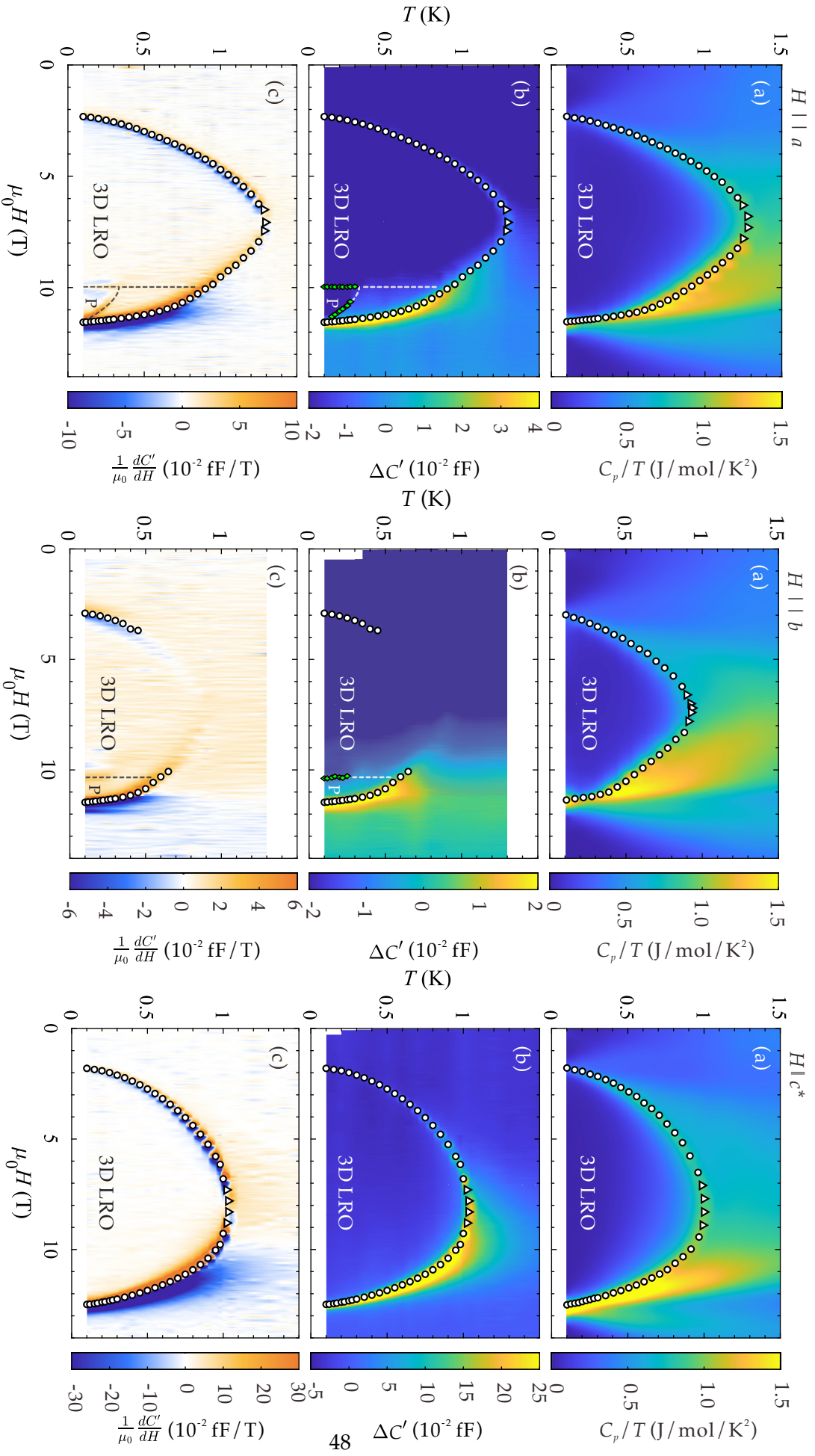


**Figure 4.7:** False-color plots of (a) specific heat  $C_p/T$ , (b) capacitance  $\Delta C'$ , and (c) field-derivative of capacitance. Circles and triangles indicate the transitions identified in the field and temperature scans, respectively, for both specific heat and capacitance. Green diamonds indicate extra features observed in the derivative of capacitance. The phase regions are labeled as the three-dimensional long-range order (3D LRO) and presaturation (P). Dashed lines are guides for the eye.

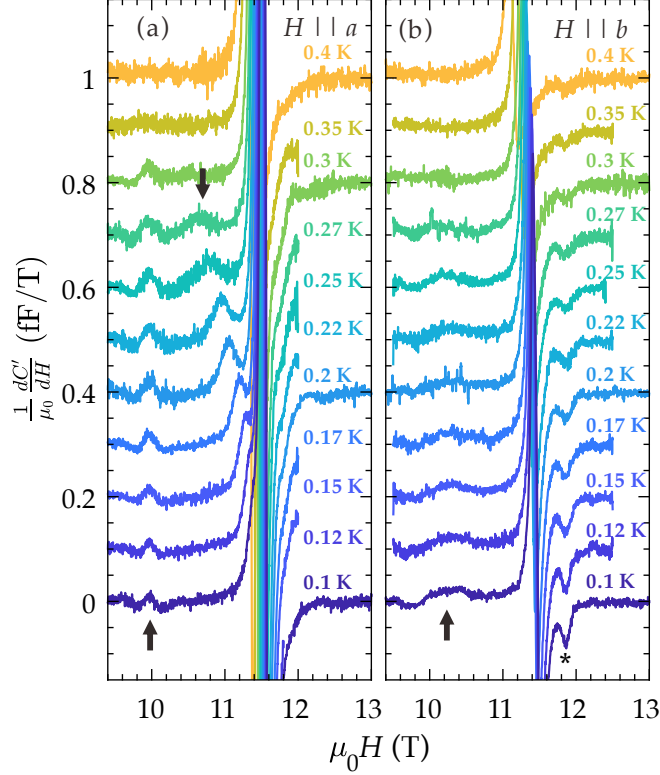


**Figure 4.8:** Derivative of the capacitance for (a)  $\mathbf{H} \parallel \mathbf{a}$  and (b)  $\mathbf{H} \parallel \mathbf{b}$ . Arrows and an asterisk indicate additional phase transitions as discussed in the text.

Fig. 4.7.(b,c,e,f,h,i) panels show where the derivative changes sign. Triangles are extracted from constant-field temperature scans across the transition, not shown here. Both symbols and are used to define the LRO phase limits.

A direct comparison to the calorimetric response highlights the dual nature of the phase transition. For that, we combine the  $\mathbf{H} \parallel \mathbf{b}$  specific heat data of Ref. [98] with additional measurements for  $\mathbf{H} \parallel \mathbf{a}$  and for  $\mathbf{H} \parallel \mathbf{c}^*$ , measured under identical conditions. All those complete the plots in Fig. 4.7.(a,d,g). Again, open circles mark the observed lambda anomalies in field scans, where triangles denote those in constant-field temperature scans. The latter coincide with the observed dielectric divergences and follow the same anisotropy pattern with regard to the magnetic-field direction. We conclude that the divergent dielectric constant is associated with the thermodynamic field-induced phase transition and the onset of magnetic order.

The dielectric signal for the  $\mathbf{H}, \mathbf{E} \parallel \mathbf{c}^*$  configuration is most pronounced. From this, we may exclude one possible microscopic origin of ferroelectricity: the reverse Dzyaloshinskii-Moriya mechanism [117, 118]. Electric polarization appears as a result of a planar helimagnetic structure. The resulting polarization vector is contained in the spin-rotation plane. A planar helix orients itself to be perpendicular to an applied magnetic field, excluding ferroelectricity in the  $\mathbf{H} \parallel \mathbf{E}$  setting.

Finally, note how additional phase transitions near the upper critical fields are revealed in our capacitance measurements, that completely are overlooked by specific heat.

Weak features in the dielectric response are found below  $H_{c2}$  for  $\mathbf{H} \parallel \mathbf{a}$  and  $\mathbf{H} \parallel \mathbf{b}$ . These features are best distinguished as anomalies in the  $dC'/dH$  curves in Fig. 4.8, and are highlighted by black arrows. Phase boundaries are sketched with dashed lines and small green diamonds in Fig. 4.7. Note how for  $\mathbf{H} \parallel \mathbf{b}$  there an additional feature at 11.9 T (asterisk in Fig. 4.8.(b)), lying above the saturation field for this crystallographic direction. Even though it cannot be excluded as a new phase transition, this is highly unlikely. The most feasible interpretation is the presence of a small misaligned crystalline grain in the sample, which is for example close to the  $\mathbf{H} \parallel \mathbf{c}^*$  orientation. While the peak for  $\mathbf{H} \parallel \mathbf{b}$  is the weakest of all the orientations, that for  $\mathbf{H} \parallel \mathbf{c}^*$  is significantly stronger at saturation, which exceeds 11.4 T. Consequently, even a tiny grain could generate the dip at 11.9 T for  $\mathbf{H} \parallel \mathbf{b}$ . On the other hand, notice that any features below the saturation field cannot be due to a similar contamination: other orientations simply show no strong features in that range of fields.

The nature of the observed presaturation phases cannot be further clarified at this point. However, the presence of presaturation phases in frustrated ferro-antiferromagnets have been discussed by a variety of theoretical works. Such phases include spin-nematic or spin density wave order [107, 108]. Given the proximity of the exchanges in  $\text{Rb}_2\text{Cu}_2\text{Mo}_3\text{O}_{12}$  to the classical ferromagnet-helimagnet transition [100, 119, 120] it would not be surprising to find this phenomenology in  $\text{Rb}_2\text{Cu}_2\text{Mo}_3\text{O}_{12}$ .

## 4.4 Criticality at a Bose-Einstein Condensation of magnons

The previous section shows how, in  $\text{Rb}_2\text{Cu}_2\text{Mo}_3\text{O}_{12}$ , antiferromagnetic and ferroelectric orders are linked, and this gives rise to dielectric anomalies at the phase boundaries. The goal of the current section is to show how we can use the dielectric channel to capture the critical susceptibility in the field-induced magnon BEC QCP. The measurements of critical quantities must be always done meticulously. As discussed above, discerning critical from non critical contributions can entail complications. This is only accentuated by the fact that the extent of the quantum critical region is at best only loosely defined. To avoid common mistakes, we carried out a few tests to establish a refined measurement and data treatment method.

### Optimizing the method

A likely risk is the use of a too large excitation voltage  $V_{ex}$  for our alternating current (ac) permittivity measurements. A large excitation voltage would maximize the signal to noise ratio, therefore increasing the sensitivity. However, it may lead to non-linearities in the system response. To test the influence of the excitation voltage, we scan the upper critical field in  $\mathbf{H} \parallel \mathbf{c}^*$  at the lowest accessible temperatures of  $T = 0.1$  K. In this setting, our system is most sensitive to any bias in our treatment. The results are shown in Fig. 4.9.(a), where a shift of the peak to slightly higher fields is observed upon reducing the excitation voltage from 15 to 7.5 V. This is likely due to a slight heating of the sample by the probing ac field, which in turn originates from a small dissipative component to capacitance, as noted below in more detail. This extrinsic heating is gone for  $V_{ex} \leq 3$  V. Indeed, an excitation voltage of 1.5 V produces practically identical data to those of 3 V.

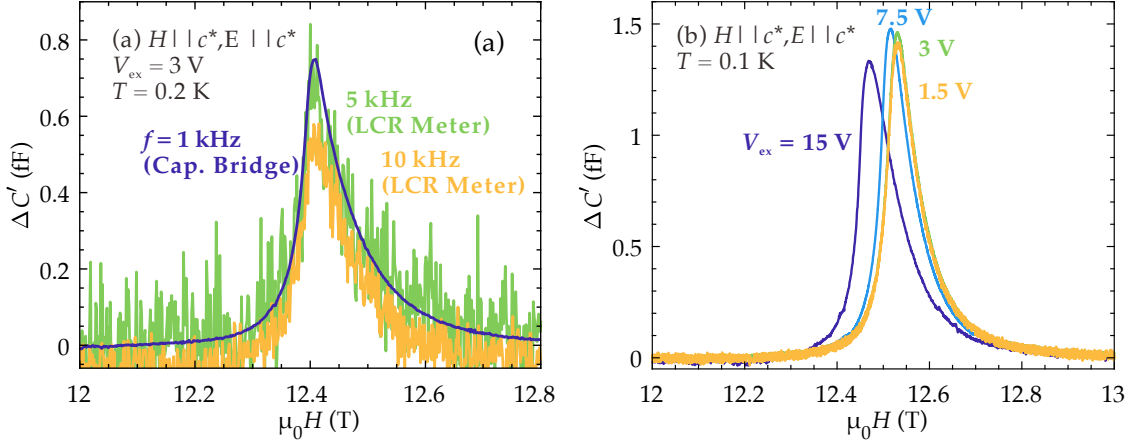


**Figure 4.9:** (a) Frequency variation of field scans of  $\Delta C'$  at 0.2 K measured with an excitation voltage of  $V_{ex} = 3$  V for  $\mathbf{H} \parallel \mathbf{c}^*$ . (b) Field scans of  $\Delta C'$  at 0.1 K with a series of excitation voltages for  $\mathbf{H} \parallel \mathbf{c}^*$ .

Further, it is our goal to measure the *static* critical susceptibility of the system. Different responses to probing fields can be obtained precisely as a function of the variation rate of the excitation [121]. The different regimes (static, intermediate, and adiabatic) are loosely defined by a characteristic relaxation time of the probed degree of freedom. Understanding this time scale is generally paramount. Therefore, it is necessary to verify that our selected frequency is low enough to probe the static limit of susceptibility.

For this purpose, we study the frequency dependence of the capacitance peak, again, at the upper critical field for  $\mathbf{H} \parallel \mathbf{c}^*$  at  $T = 0.2$  K. The capacitance bridge used for the bulk of the measurement has a native fixed frequency of 1 kHz. An LCR-meter was employed to access other frequencies, despite its much reduced sensitivity. Leaving aside the noise in the latter setup, no change in either peak shape or amplitude between 1 and 5 kHz is observed. Even though there are some small discernible deviations at 10 kHz, likely due again to sample heating (note dissipated power increases with frequency), a frequency of 1 kHz can clearly be regarded as “safe”.

Following our characterization of the measured response, the data discussed below were collected using  $V_{ex} = 3$  V and  $f = 1$  kHz.

### BEC universality class

If we want to measure the critical susceptibility via dielectric properties, we have to understand whether these in fact become critical at the QCP. Thus, we question whether the electric polarization  $P$  is indeed a primary order parameter in the quantum phase transition, i. e., as  $T \rightarrow 0$ . This is not a trivial issue, yet key to our analysis.

Early studies of the field-induced magnon BEC transition in the spin ladder compound  $\text{H}_8\text{C}_4\text{SO}_2 \cdot \text{Cu}_2\text{Cl}_2$  evidenced a diverging sharp peak in the dielectric constant of this material as a function of magnetic field [122]. However, it was found that the anomaly decreases drastically towards low temperatures, being eventually reduced to a finite small jump at the transition point at the QCP. This is clear evidence that at the QCP, the spon-

taneous electric polarization is merely a secondary order parameter. A similar scenario is found in the coupled spin-dimer system  $\text{TlCuCl}_3$ : the large dielectric divergence measured at finite temperature gradually gives way to a vanishingly small anomaly at the QCP. This behavior is captured by the reverse Dzyaloshinskii-Moriya mechanism [117, 118] responsible for ferroelectricity in both systems. In this mechanism, electric polarization linearly couples to the vector chirality of the magnetic manifold:

$$P \propto \mathbf{e}_{ij} \cdot \langle \mathbf{S}_i \times \mathbf{S}_j \rangle \quad (4.6)$$

where  $\mathbf{e}_{ij}$  is the vector linking sites  $i$  and  $j$ . Under a magnetic field, this chirality is proportional to the product of the field-induced uniform longitudinal magnetization  $\langle S_z \rangle$  and the spontaneous transverse staggered magnetization (BEC order parameter)  $\langle S_\perp \rangle$ , in short:

$$P \propto \langle S_z \rangle \langle S_\perp \rangle \quad (4.7)$$

At  $T = 0$ , and as a consequence of the finite spin gap,  $\langle S_z \rangle$  remains strictly zero up to  $H_{c1}$  and grows linearly above it [123]. This results in a vanishing bilinear coupling of polarization to the magnetic order precisely at the QCP. In this situation, quadratic and higher-order coupling terms may remain relevant, rendering  $P$  a secondary order parameter of the phase transition revealed as finite jump at  $H_{c1}$  of dielectric susceptibility.

It is only if the temperature is raised, that the situation changes due to thermally induced population of excited levels. The thermalized quantum magnet develops a non-vanishing magnetization  $\langle S_z \rangle$  in an external field. Then vector chirality becomes proportional to  $\langle S_\perp \rangle$ . As a result, electric polarization becomes linearly coupled to the magnetic primary order parameter, therefore turning itself into one.

Evidenced in Fig. 4.6, the same scenario takes place at the lower critical field in  $\text{Rb}_2\text{Cu}_2\text{Mo}_3\text{O}_{12}$ . The sharp dielectric divergence at finite temperature slowly loses weight and weakens as the temperature is lowered, almost vanishing at 100 mK. It therefore clear that at the quantum critical point the dielectric permittivity is not critical.

In stark contrast, the divergence found at the upper critical field becomes much stronger upon cooling and survives at the QCP for all field orientations. This difference to the lower critical field can be easily explained in the terms discussed above. At such high fields, we are dealing with an almost fully saturated magnet, and thus near  $H_{c2}$  the system has a large uniform magnetization regardless the temperature. Thus, by virtue of 4.7 vector chirality becomes linearly proportional to staggered magnetization, with a large and very slightly temperature dependent coefficient  $\langle S_z \rangle \sim 1/2$ . This shows that, even at the QCP, polarization and staggered magnetization become proportional to one another and thus the spontaneous electric polarization becomes an order parameter for this transition.

It must be noted, that in our discussion we used an illustration based on the inverse DM mechanism, even though we argued that it is unlikely that it is the origin of magnetoelectric coupling in  $\text{Rb}_2\text{Cu}_2\text{Mo}_3\text{O}_{12}$ . A similar argumentation holds, however, for other mechanisms such as the spin-dependent p-d hybridization mechanism [88].

Finally, we can do an easy test to check whether electric polarization is a primary order parameter at our QPT. This is based on the effect that a conjugate field to an order parameter has on its expectation value. If we are dealing with a secondary order parameter, the effect of its conjugate field may be to shift slightly the transition point.

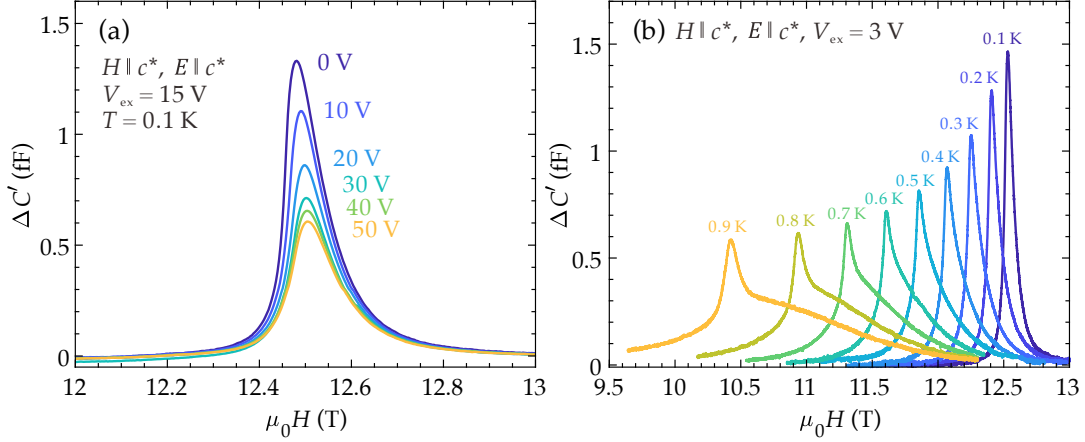


**Figure 4.10:** (a) Field scans of  $\Delta C'$  at 0.1 K with a series of bias DC voltages for  $\Delta C'$  measured with an excitation voltage of  $V_{ex} = 15$  V. (b) Field scans of  $\Delta C'$  measured with an excitation voltage of  $V_{ex} = 3$  V for  $H \parallel c^*$ .

However, it would have no effect on the actual transition happening, and therefore it must leave susceptibility divergence almost intact. On the contrary, if we are working on a primary order parameter, the effect of its conjugate field is to destroy the transition completely. The field breaks the transition symmetry explicitly, thereby hampering a spontaneous symmetry breaking that is key in second order transitions. As a result, the critical susceptibility no longer diverges, but is strongly suppressed and turned into a hump at the critical point. The latter scenario is very clearly represented in our measurements in Fig. 4.10.(a). Measurements of the strong peak  $H_{c2}$  for  $H \parallel c^*$  are measured under a biasing static uniform electric field at  $T = 0.1$  K. The increasing amplitude of the DC field leads to a strong suppression of the peak, showing that electric polarization is in fact a primary order parameter of the phase transition.

Note that a similar check could be performed for the other primary order parameter, that is the staggered magnetization. The limiting factor in that case is that the conjugate field is a magnetic field with the exact same staggering as the magnetization. This staggering is on the atomic scale, and is thus impossible to be realized experimentally.

Now that we understand which role the different order parameters play at the QCPs there is one more question to ask ourselves: to what extent these can be described under a BEC framework. Many magnetic systems do in fact show good realizations of field-induced transitions in the BEC universality class (see for example a comprehensive list in [56]). However, one factor that strongly limits this description is magnetic anisotropy. Its presence breaks explicitly the  $SU(2)$  symmetry involved in the BEC mechanism, breaking down this description. We have already noted in the previous sections how in  $Rb_2Cu_2Mo_3O_{12}$  the very important relevance of antisymmetric terms in the Hamiltonian, therefore anisotropy is a major concern. In fact, anisotropy is also quite apparent in our measurements (Fig. 4.7) where the shape of the domes of magnetic long-range order is strongly geometry-dependent, even giving rise to kinks in the shape as for  $H \parallel b$ .

We can gain some information on the influence of anisotropy on the QCP at  $H_{c2}$  by analyzing the details of these phase boundaries. These boundaries carry information on

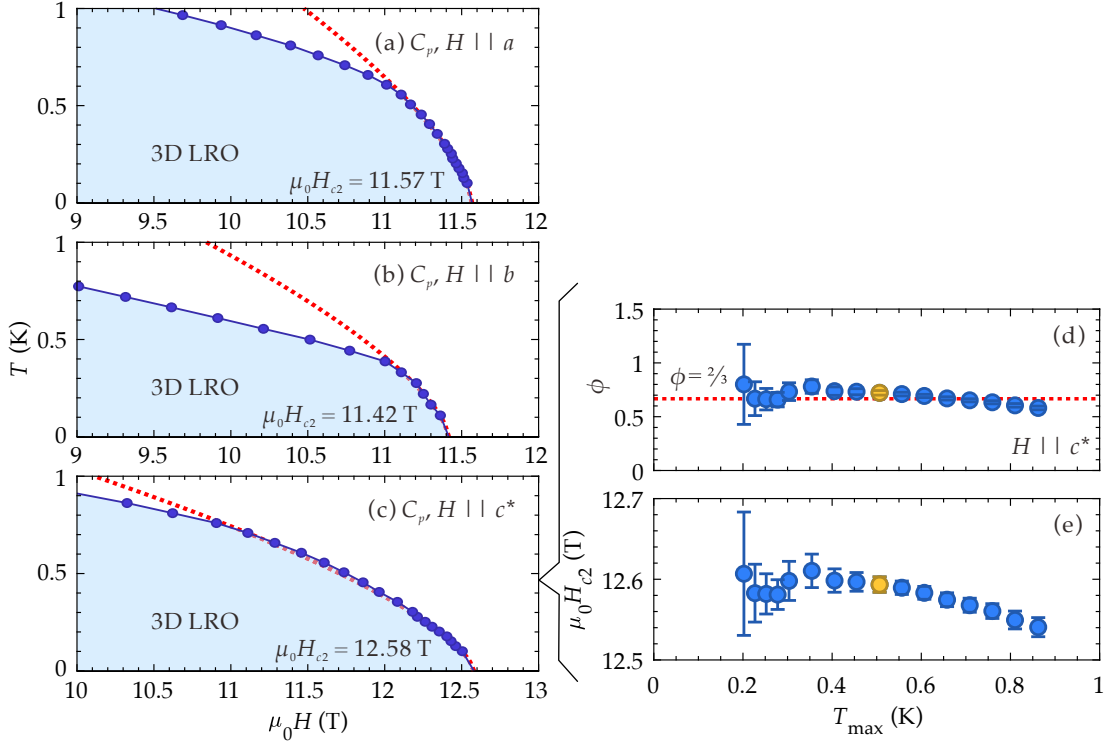


**Figure 4.11:** Phase diagram boundaries measured by specific heat in applied magnetic fields along the (a) **a**, (b) **b**, and (c) **c\*** directions. The dashed curves are power-law fits in the range of  $T = 0.35$  K, where the exponent is fixed to  $2/3$ . (d) and (e) Shrinking-fit-window analysis of the measured phase boundaries for  $\mathbf{H} \parallel \mathbf{c}^*$ . The plots show the least-squares fitted values of (d) the phase boundary exponent  $\phi$  and (e) the upper critical field  $H_{c2}$  vs the temperature range used for the fit. The dashed line is at  $\phi = 2/3$ .

the so-called crossover exponent  $\phi$ , which is defined as

$$|H - H_c| \propto T^{1/\phi} \quad (4.8)$$

in the limit  $T \rightarrow 0$ . There are concrete theoretical expectations for the value of this exponent. In particular, for a 3D BEC QCP, we expect  $\phi = 2/3$  [54–56]. Figures 4.11.(a-c) show a detail of the phase boundaries in the proximity to  $H_{c2}$  as extracted from lambda anomalies observed in the specific heat measurements shown in Fig. 4.7. A clear change of slope in the curves is evidenced for the geometries where  $\mathbf{H} \parallel \mathbf{a}$  and  $\mathbf{H} \parallel \mathbf{b}$ , suggesting a crossover between scaling regimes as a function of the magnetic field. Whether this is related to the presence of presaturation phases in these field configuration is unclear at this point. Either way, this crossover imposes a strong limitation on the extent of the critical regime that we can access close to the QCP and prevents any quantitative scaling analysis for these orientations, making these unsuitable to study BEC criticality.

By contrast, no anomalous change in slope is observed for  $\mathbf{H} \parallel \mathbf{c}^*$ , making this geometry a good candidate to observe BEC physics. A windowing analysis of the phase boundary provide a very good fit to a power-law phase boundary. Details of this analysis are displayed in Fig. 4.11.(d) and Fig. 4.11.(e), where the best fit is obtained for tempera-

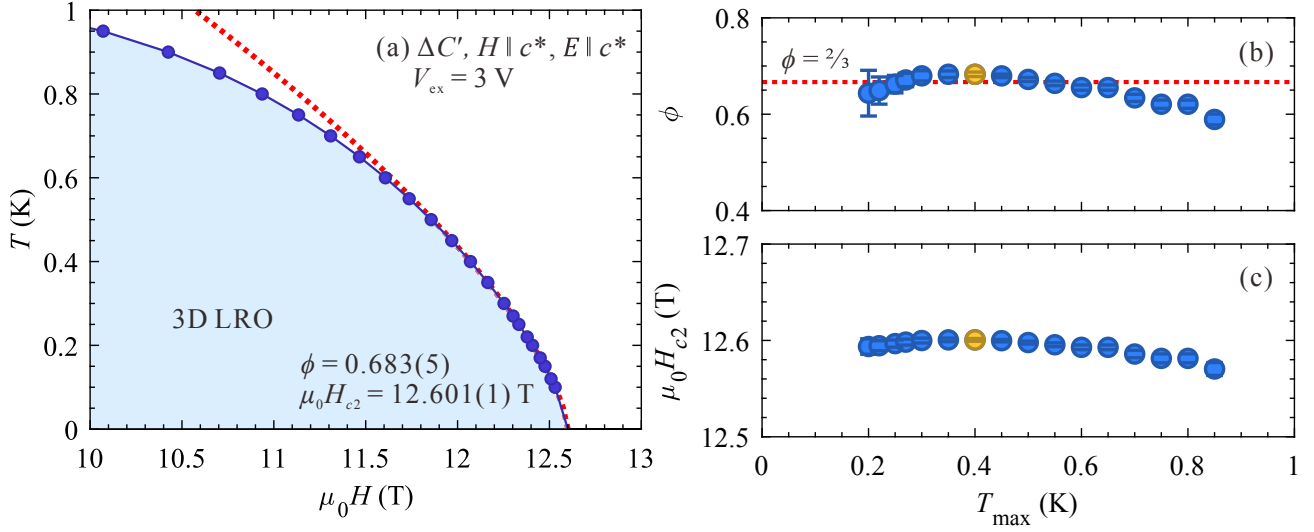


**Figure 4.12:** (a) Phase diagram boundary for  $\mathbf{H} \parallel \mathbf{c}^*$ . Circles are the transition points determined from the capacitance data. The solid curve is a guide for the eye. The dashed curve is (b,c) Windowing analysis of the measured phase boundaries. The plots show the least-squares fitted values of (b) the phase boundary exponent  $\phi$  and (c) the upper critical field  $H_{c2}$  vs the temperature range used for the fit. The dashed line is at  $\phi = 2/3$ .

tures up to  $T_{max} = 0.52$  K yielding a crossover exponent of  $\phi = 0.72(2)$ . In fact, the exact value of  $\phi = 2/3$  as predicted for BEC describes the data well up to 0.7 K (as shown in Fig. 4.11.(c)). For this particular geometry and those temperatures accessible in our experiments, the transition does indeed look very much like a BEC one.

We reach the same conclusions by analyzing the phase boundaries as determined by the positions of dielectric anomalies. For this we turn to our measurements with optimized experimental conditions ( $V_{ex} = 3$  V): typical constant temperature scans are shown in Fig. 4.10.(b) for reference. The resulting phase boundary can be found in Fig. 4.12.(a), showing again a smooth evolution of the phase boundary up to the highest measured temperatures. We repeat our windowing analysis (shown in Fig. 4.12.(b) and 4.12.(c)) which reveals an even more robust agreement with BEC theory. For the optimal fitting range below  $T_{max} = 0.4$  K, our analysis yields  $\phi = 0.683(5)$  and  $\mu_0 H_{c2} = 12.601(1)$  T. This substantial precision and agreement with predictions is based on the extreme sensitivity of our measurement technique to the phase boundary. The dielectric anomalies become strongly accentuated in the all-important lower-temperature region and show a very sharp and narrow peak. Note that, in contrast, due to fundamental reasons (Nernst's theorem or third law of thermodynamics) the specific heat of the system must become zero at zero temperature, and the lambda anomalies become small and hard to quantify as the temperature is reduced.

### The critical susceptibility

Our analysis so far shows that  $\mathbf{H} \parallel \mathbf{c}^*$  is a good geometry to observe quantum critical behavior. We therefore examine the divergence of electric susceptibility along the so-

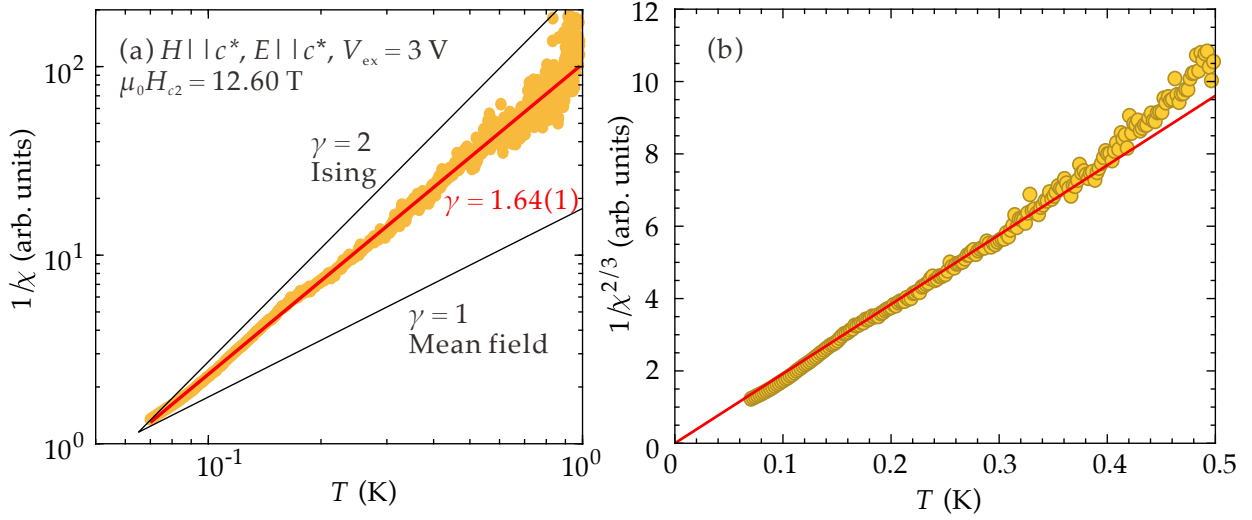


**Figure 4.13:** (a) A log-log plot of the inverse critical dielectric susceptibility,  $1/\chi$ . The red line is a power-law fit to the data. Black lines are power laws with exponents of  $\gamma = 1$  and  $\gamma = 2$ . (b) Inverse critical dielectric susceptibility  $1/\chi^{2/3}$  vs temperature  $T$  at  $H = H_{c2}$ . The data are binned by two successive points. The solid line is a guide for the eye.

called quantum critical trajectory, i. e., a measuring in temperature at the critical magnetic field  $\mu_0 H = \mu_0 H_{c2}$ . Fig. 4.12 provides us with a really good estimation of this value, which is crucial as we approach our base temperature. The results at 12.601 T are displayed in Fig. 4.13.

In order to ascribe the observed features to critical susceptibility it is important to note two points. First, is the presence of dissipation in our system. In these measurements the imaginary component of capacitance is well below 0.1% of the real component in absolute values. In addition, it never exceeds 11% of  $\Delta C'$ , allowing us to ignore this imaginary part and analyze the scaling of the real part alone. Second point is the presence of a little field dependence of the signal far from the critical regions. Figure 4.6 shows how capacitance is flat in the gapped low field phase and in the fully polarized state, however featuring a small increase in the intermediate phase. This behavior is particularly prominent for  $\mathbf{H} \parallel \mathbf{b}$ , and is likely a result of a slight magnetostriction in the system. This is only natural in a system where spin-orbit coupling plays a role. However, for the selected geometry with  $\mathbf{H} \parallel \mathbf{c}^*$  this effect is almost negligible, being its contribution to  $\Delta C'$  over two orders of magnitude smaller than that of the critical divergence. As a result, this effect can be disregarded in our further analysis.

Following our initial argumentation,  $\chi$  must be proportional to the change in capacitance. A log-log plot of  $1/\chi \propto 1/\Delta C'$  vs temperature shows in fact power-law behavior. (Fig. 4.13.(a)). This trend is robust over more than one decade in temperature, evidencing that the critical contribution is dominant in the extracted  $\chi$ . We can extract a critical exponent by a least-square fit to a power law, which yields  $\gamma = 1.64(1)$ . Note that this exponent is significantly different from trivial models such as the mean-field theory, where one expects a divergence with exponent  $\gamma = 1$ ; or more complex systems such as the 3D-Ising transition observed in  $\text{Ba}_2\text{CoGe}_2\text{O}_7$  [88] with  $\gamma = 2$ . In contrast, the fitted exponent is

in excellent agreement with the expectations for three-dimensional BEC quantum critical susceptibility,  $\gamma = 3/2$  [58, 88]. In addition, the divergence as  $T^{-3/2}$  of critical susceptibility exactly at the quantum critical point is explicitly displayed in Fig. 4.13.(b). There, inverse susceptibility is rescaled according to the BEC critical exponent, which reveals a trend towards zero (divergence) exactly at zero temperature. The solid line is not a fit, but simply a guide for the eye.

Notably, these constitute the first direct measurement of the critical susceptibility at a Bose-Einstein Condensation QCP in a magnetic system, in a transparent probe-response fashion.

Finally, in passing we came across an interesting dichotomy that is worth highlighting. The realization of Bose condensation requires the presence of  $U(1)$  symmetry, regarded as particle number conservation. In a magnet, this translates into axially symmetric Hamiltonians in order to show BEC of magnons. In  $\text{Rb}_2\text{Cu}_2\text{Mo}_3\text{O}_{12}$ , however, the large amount of experimental data do advocate for its very significant magnetic anisotropy. There is a large dependence on the direction of an external field and yet, anisotropy seems to not break the BEC picture down at all. While these two facts are sometimes reconciled by an incommensurate magnetic structure (the incommensuration effectively averages out the effect of anisotropy globally) we already discussed that the resulting electric polarization would be different to what our results show. Deeper analysis is needed to bring together these two disjoint perspectives.

## 4.5 Conclusions

$\text{Rb}_2\text{Cu}_2\text{Mo}_3\text{O}_{12}$  is an amazing quantum multiferroic, with a complex phase diagram where magnetism and ferroelectricity are two faces of the same coin. However, only single-crystal experiments could provide a complete picture of its magnetoelectric properties.

Our work shows that the ferroelectric anomalies that have been reported at 8 K, and ascribed to a chiral-spin-liquid behaviour, are actually due to a tiny amount of a ferroelectric impurity in polycrystalline samples, and thus completely spurious.

$\text{Rb}_2\text{Cu}_2\text{Mo}_3\text{O}_{12}$  is a rare species of quantum magnet with two experimentally accessible field-induced magnon BEC transitions. At the upper critical field, we observe the electric polarization is a primary order parameter at the quantum critical point. We argue how in any gapped quantum paramagnet (regardless of the microscopic origin of magnetoelectric coupling) this cannot be the case at the lower critical field.

Precisely because they are *both* primary order parameters, the bilinear coupling of electric polarization and the magnetic BEC order parameter enables breakthrough direct measurements of the critical BEC susceptibility. Its measured power-law divergence at the quantum critical point is in excellent agreement with long-standing theoretical predictions.

Modulation of dielectric permittivity reveal a presaturation phase in the dome of order, which may feature exotic order such as a spin-nematicity or spin density wave. All in all, this illustrates that electrometry can be an extremely sensitive experimental tool for quantum magnetism.



## Chapter 5

# Dielectric relaxation by quantum critical magnons in $\text{Cs}_2\text{Cu}_2\text{Mo}_3\text{O}_{12}$

The results discussed in this chapter can also be found in the following references:

*D. Flavián, S. Hayashida, L. Huberich, D. Blosser, K. Yu. Povarov, Z. Yan, S. Gvasaliya, and A. Zheludev.* Magnetic phase diagram of the linear quantum ferro-antiferromagnet  $\text{Cs}_2\text{Cu}_2\text{Mo}_3\text{O}_{12}$ . *Phys. Rev. B* **101**, 224408 (2020).

*D. Flavián, P. A. Volkov, S. Hayashida, K. Yu. Povarov, S. Gvasaliya, P. Chandra, and A. Zheludev.* Dielectric Relaxation by Quantum Critical Magnons. *Phys. Rev. Lett.* **130**, 216501 (2023).

**Summary of contributions.** Single crystals of  $\text{Cs}_2\text{Cu}_2\text{Mo}_3\text{O}_{12}$  were first grown by S. Hayashida. The author optimized the process and grew all samples used in this chapter. Thermodynamic and pyroelectric current measurements were carried out by the author. Measurements of capacitance were performed by the author with support from S. Hayashida in the sample assembly and K. Povarov for frequency dependence. A theoretical model was developed in collaboration with P. Volkov and P. Chandra. Finally, the detailed analysis of the crystal structure of  $\text{Cs}_2\text{Cu}_2\text{Mo}_3\text{O}_{12}$  (and  $\text{Rb}_2\text{Cu}_2\text{Mo}_3\text{O}_{12}$ , as described in the appendix) was done by the author with the support of S. Gvasaliya (ETH Zurich), D. Chernyshov (ESRF) and D. Allan (Diamond Light Source).

### 5.1 Introduction

Soft-magnon and saturation transitions in antiferromagnets may result in ferroelectric order in addition to magnetism thanks to magneto-electric coupling in quantum magnets. In most known examples, the electric polarization is merely a passive participant, reflecting the evolution of spin correlations and may be adequately described by purely magnetic microscopic Hamiltonians. We have seen in the previous chapter that this is likely the situation in the ground state of  $\text{Rb}_2\text{Cu}_2\text{Mo}_3\text{O}_{12}$ . However, there is no reason for this to always be the case.

The search for qualitatively new dielectric phenomena at magnetic QCPs and the so-called *multiferroic* quantum critical regime [124, 125] is gaining increasing attention. Whereas, multiferroics are mostly insulating materials studied towards specific room-

temperature functionalities, quantum criticality requires of suppression of conventional order and low temperatures to be found in all its glory. As a result, little is known about this rather unexplored regime.

This chapter explores the realization of one such phenomenon where both electric and magnetic degrees of freedom play non-trivial roles at a QCP: the dielectric relaxation induced by quantum critical magnons. Significant modulations of the electric permittivity of  $\text{Cs}_2\text{Cu}_2\text{Mo}_3\text{O}_{12}$  (a sister compound to  $\text{Rb}_2\text{Cu}_2\text{Mo}_3\text{O}_{12}$ ) are found at ultra-low temperatures. These are ascribed to electric degrees of freedom that experience a relaxation phenomenon, even when all other lattice degrees of freedom are well frozen out. The characteristic time of this relaxation shows Arrhenius activation with an energy scale that corresponds exactly to that of the magnons that softens at the QCP. The results reveal a framework where virtual magnons mediate this novel dielectric relaxation as a result of interaction between low-energy lattice and quantum-critical spin degrees of freedom.

### The magnetism of $\text{Cs}_2\text{Cu}_2\text{Mo}_3\text{O}_{12}$

Our subject of study,  $\text{Cs}_2\text{Cu}_2\text{Mo}_3\text{O}_{12}$ , has previously attracted attention as a frustrated ferro-antiferromagnetic  $S = 1/2$  quantum spin chain system [94, 126]. Structurally, it is very similar to  $\text{Rb}_2\text{Cu}_2\text{Mo}_3\text{O}_{12}$  [93, 94, 97, 98, 100, 127], crystallizing in a  $C2/c$  space group and with lattice parameters  $a = 27.922(4)$  Å,  $b = 5.126(5)$  Å,  $c = 20.259(5)$  Å, and  $\beta = 107.28(2)^\circ$  at room temperature. However, it develops three-dimensional magnetic order at zero field below  $T_N = 1.85$  K [126, 128]. Bulk magnetization reveals a small easy-axis anisotropy that suggest the structure may be close to a collinear one. However, the actual magnetic structure remains unknown to date, partially complicated by the unavailability of sufficiently large single crystals [128]. Preliminary unpublished powder neutron diffraction experiments hint towards a  $(0, 0, 0)$  magnetic propagation vector, which makes an accurate structural determination exceedingly challenging.

In applied magnetic fields  $\text{Cs}_2\text{Cu}_2\text{Mo}_3\text{O}_{12}$  displays a rather complex phase diagram with a cascade of phase transitions for fields applied along the chain direction. The spin achieves saturation at  $\mu_0 H_c \sim 7.3 - 8.7$  T (depending on field direction) via a magnon-BEC-type QCP [128]. Estimations of the exchange constants revealed strong competition between FM ( $J_1 = -93$  K) nearest neighbors and AFM ( $J_2 = 33$  K) next-nearest neighbors [94]. The presence of a presaturation phase regardless of field orientation awoke interest in relation to spin-nematic phases, which were predicted to occur right below the saturation transition. However, new results ([129] and our discussion below) seem to indicate conventional dipolar order.

## 5.2 The crystal structure of $\text{Cs}_2\text{Cu}_2\text{Mo}_3\text{O}_{12}$

The crystal structure of  $\text{Cs}_2\text{Cu}_2\text{Mo}_3\text{O}_{12}$  has been discussed in the literature by several authors [130–136]. Overall, it is assumed that the structure is equivalent to that of  $\text{Rb}_2\text{Cu}_2\text{Mo}_3\text{O}_{12}$ . However, an actual structure determination is (to the best knowledge of the author) lacking. In the original paper [137], no determination of the atomic coordinates is provided. The reason behind is likely the large structural unit, containing 19 atoms with little symmetry restrictions on the asymmetric unit; together with the challenge in obtaining single-crystal samples. We refined the crystal structure of several

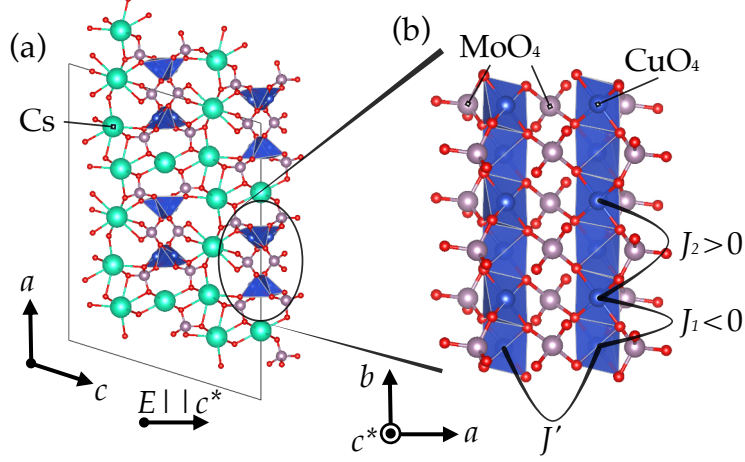


**Figure 5.1:** Schematic crystal structure of  $\text{Cs}_2\text{Cu}_2\text{Mo}_3\text{O}_{12}$  based on the 300 K refinement given in Appendix B. (a) The unit cell contains four pairs of copper chains that run parallel to the crystallographic  $b$  axis. The direction along which the electric field is applied in the single-crystal measurements ( $\mathbf{E} \parallel \mathbf{c}^*$ ) is indicated. (b) Detail view of the structure of pair of chains along the  $b$  axis. Three unit cells are depicted, as well as the three nearest magnetic exchange bonds.

samples of  $\text{Cs}_2\text{Cu}_2\text{Mo}_3\text{O}_{12}$  at different temperatures using single-crystal X-ray diffraction. The details of the data collection and subsequent refinement can be found in Appendix B.

The structure of  $\text{Cs}_2\text{Cu}_2\text{Mo}_3\text{O}_{12}$  and the expected superexchange pathways relevant to magnetism are shown in Fig. 5.1.  $\text{Cs}_2\text{Cu}_2\text{Mo}_3\text{O}_{12}$  and  $\text{Rb}_2\text{Cu}_2\text{Mo}_3\text{O}_{12}$  are extremely similar in their crystal structure, as interatomic angles and distances in Table 5.1 show. The differing lattice parameters are the result of the different ionic radii between  $\text{Cs}^+$  and  $\text{Rb}^+$  cations. As opposed to that the one-dimensional units of  $\text{CuO}_4$  tetrahedra (along with the bridging Mo atoms) show only the slightest differences in angles and distances. One important observation is that the nearest neighbor coupling links inequivalent  $\text{Cu}^{2+}$  ions and as a consequence the Cu-Cu distance is alternating along the  $b$  direction. This alternation translates into two possible superexchange parameters for nearest neighbors  $J_1$  and  $J'_1$ . Table 5.1 shows this alternation explicitly and compares it to that in  $\text{Rb}_2\text{Cu}_2\text{Mo}_3\text{O}_{12}$ , where it seems to be less accentuated. A discussion of the influence of this alternation can be found in [100, 138], where the authors argue that the difference in bonds is too small to have a significant effect on the magnetism. However, we would like to point out that different exchanges would break the translational symmetry of the magnetic lattice, lifting the frustration and favoring the dimerization of spins.

### 5.3 The dielectric response of $\text{Cs}_2\text{Cu}_2\text{Mo}_3\text{O}_{12}$

Inspired by the fact that the magnetic field-induced AF phase in  $\text{Rb}_2\text{Cu}_2\text{Mo}_3\text{O}_{12}$  is also ferroelectric (FE) as discussed in the previous chapter, we performed detailed dielectric permittivity studies of  $\text{Cs}_2\text{Cu}_2\text{Mo}_3\text{O}_{12}$  as a function of temperature ( $T$ ), magnetic field ( $H$ ) and probing frequency of the electric field ( $\omega$ ). An analysis of the response in the quantum

**Table 5.1:** Bond lengths and angles in  $\text{Cs}_2\text{Cu}_2\text{Mo}_3\text{O}_{12}$  involved in superexchange pathways.

$\text{Cs}_2\text{Cu}_2\text{Mo}_3\text{O}_{12}$		
	Bond distance (Å)	Bond angles (°)
$J_1$	3.0960(8)	$\phi(\text{Cu}_1-\text{O}_5-\text{Cu}_2) = 91.92(11)$ $\phi(\text{Cu}_1-\text{O}_1-\text{Cu}_2) = 101.45(14)$
$J'_1$	3.0710(8)	$\phi(\text{Cu}_2-\text{O}_3-\text{Cu}_1) = 89.52(14)$ $\phi(\text{Cu}_2-\text{O}_2-\text{Cu}_1) = 101.56(16)$
$J_2$	5.1265(4)	
$J'$	4.9166(9)	
$\text{Rb}_2\text{Cu}_2\text{Mo}_3\text{O}_{12}$		
	Bond distance (Å)	Bond angles (°)
$J_1$	3.0786(11)	$\phi(\text{Cu}_1-\text{O}_5-\text{Cu}_2) = 91.98(17)$ $\phi(\text{Cu}_1-\text{O}_1-\text{Cu}_2) = 101.56(19)$
$J'_1$	3.0729(11)	$\phi(\text{Cu}_2-\text{O}_3-\text{Cu}_1) = 89.85(19)$ $\phi(\text{Cu}_2-\text{O}_2-\text{Cu}_1) = 101.7(3)$
$J_2$	5.0947(3)	
$J'$	4.9070(13)	

critical regime around the upper critical field in  $\text{Cs}_2\text{Cu}_2\text{Mo}_3\text{O}_{12}$  is repeated almost verbatim, and shows very similar results to those reported for  $\text{Rb}_2\text{Cu}_2\text{Mo}_3\text{O}_{12}$ . Nevertheless, new features are unveiled in the field and temperature dependence of dielectric permittivity. All the new findings are captured in a model of dielectric relaxation mediated by virtual magnetic quantum fluctuations, showing a novel non-trivial interaction between spin and lattice excitations.

### A multiferroic ground state

As a first step towards understanding the coupling of dielectric and magnetic degrees of freedom, we show that the dome of long range order is in fact multiferroic just as in  $\text{Rb}_2\text{Cu}_2\text{Mo}_3\text{O}_{12}$ . Measurements of pyroelectric currents witness the existence of ferroelectric polarization in  $\text{Cs}_2\text{Cu}_2\text{Mo}_3\text{O}_{12}$  as shown in Fig. 5.2.(b,c). Fig. 5.2.(a) shows the capacitance of a cylindrical powder sample of roughly 5 mm in diameter and 0.3 mm in height at 7.5 T. We choose this field as the phase boundary is below 1.1 K (upper limit of refrigerator) and it can be crossed in a controlled way to monitor  $I_p$ .

The onset of long range order is indicated by a hump in real capacitance, corresponding to the boundary of the BEC of magnons. The broadening of this feature is due essentially to the anisotropy of the upper critical field in  $\text{Cs}_2\text{Cu}_2\text{Mo}_3\text{O}_{12}$ . Following the prescriptions described in the Chapter 3 a peak is found in pyroelectric current measured upon warming up at a constant magnetic field value (Fig. 5.2.(b)). Integration of this signal results in the electric polarization displayed in Fig. 5.2.(c). In order to increase

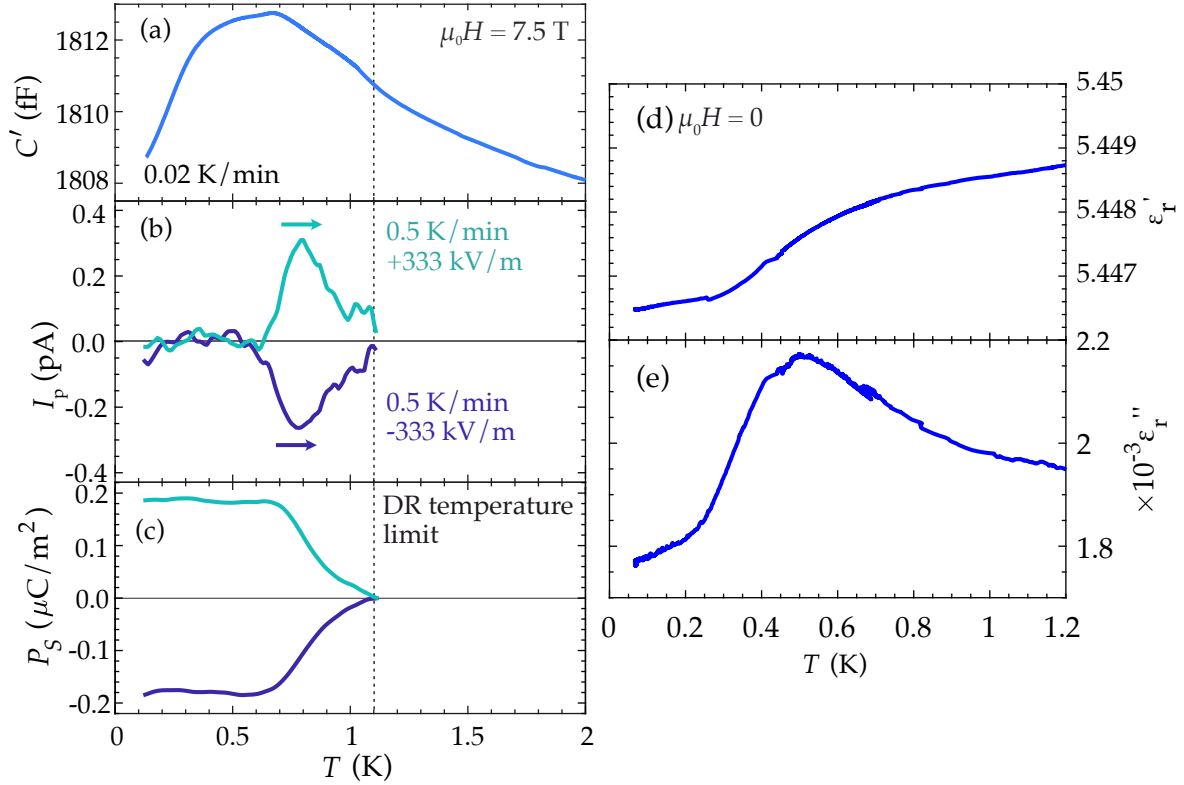


**Figure 5.2:** (a) Temperature dependence of capacitance in a polycrystalline sample at 7.5 T. The sweeping rate for this measurement is indicated in the figure. (b) Pyroelectric current measured as described in the text. The poling electric field during cooling is displayed. (c) Electric polarization of  $\text{Cs}_2\text{Cu}_2\text{Mo}_3\text{O}_{12}$ . A dashed vertical line in the figure denotes the maximum temperature of the Dilution refrigerator (DR) insert in its dilution mode. The temperature cannot be driven further up in a controlled way. (d,e) Relative complex dielectric permittivity ((d) real, and (e) imaginary components) of a polycrystalline sample of  $\text{Cs}_2\text{Cu}_2\text{Mo}_3\text{O}_{12}$  at low temperatures.

the statistical significance of the data and reduce the noise level, the measurement was repeated five times and the result of averaging is shown in the figure. The onset of an electric polarization is concomitant to the onset of magnetic order. Furthermore, it is completely sign-switchable by the reversal of the poling electric field, which proves that the system becomes indeed ferroelectric at the phase transition.

The values of polarization are comparable to those found in the sister compound  $\text{Rb}_2\text{Cu}_2\text{Mo}_3\text{O}_{12}$  [127]. The values of polarized moment is very reduced as compared to many multiferroics of spin origin, where typically moments one or two orders of magnitude larger are found [20]. Once again, the limited size of the single-crystal samples completely precludes the access to direction-resolved polarization measurements in  $\text{Cs}_2\text{Cu}_2\text{Mo}_3\text{O}_{12}$ .

In addition, we determine the relative complex permittivity of  $\text{Cs}_2\text{Cu}_2\text{Mo}_3\text{O}_{12}$  in large powder samples. We carry out measurements on a large powder sample where we had an optimal control of the sample dimensions. A sintering heat treatment is applied prior to measurement to compact the powder. The resulting sample of 5.16 mm in diameter

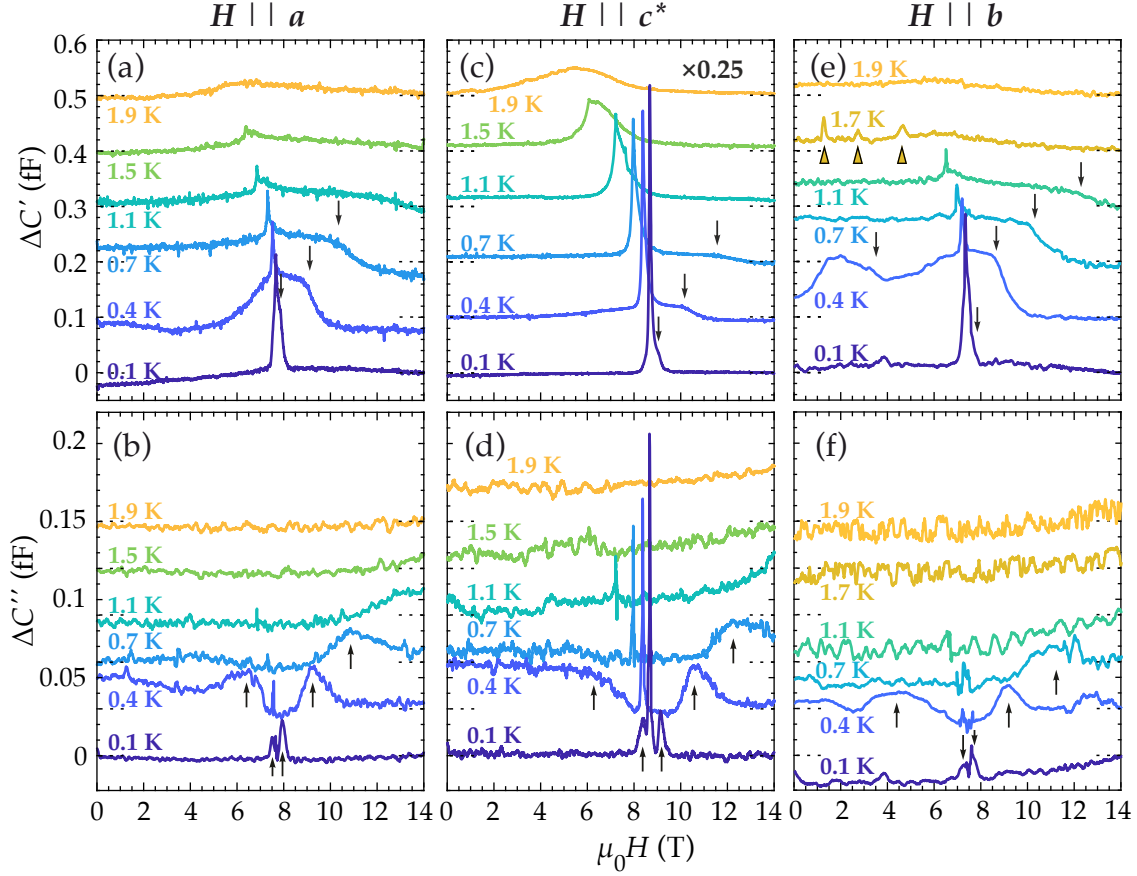


**Figure 5.3:** Typical raw field-scans of capacitance at constant temperature on a single-crystal sample of  $\text{Cs}_2\text{Cu}_2\text{Mo}_3\text{O}_{12}$ . Both the real ( $\Delta C'$ ) and imaginary ( $\Delta C''$ ) components of the measurement are shown. The probing electric field is always parallel to the  $c^*$  axis whereas the magnetic field is: (a,b)  $\mathbf{H} \parallel \mathbf{a}$ , (c,d)  $\mathbf{H} \parallel \mathbf{c}^*$ , and (e,f)  $\mathbf{H} \parallel \mathbf{b}$ . Data sets in (a,c,e) and (b,d,f) are offset for visibility by 0.1 fF and 0.05 fF, respectively. Note that data in (c) is multiplied by 0.25 to share the scale with (a,e). Black arrows indicate dissipative features as discussed in the text. Triangles in (e) show the presence of the boundary anomaly up to much higher temperatures and lower fields.

and 0.66 mm in height was used to measure the data displayed in Fig. 5.2.(d,e). Data in Fig. 5.2.(d) reveal a modest relative dielectric constant of  $\epsilon_r = 5.44$ . This value is similar to that reported for the Rb-based sister compound [100, 139].

Data in Fig. 5.2.(d,e) already anticipate some results that will be discussed in extensive detail below. A broad step in real part of permittivity is accompanied by a peak in dissipation (Fig. 5.2.(e)) at 0.5 K.

Our directional-dependent measurement power relies again on the changes of the dielectric constant as a function of an external magnetic field. Due to the shape of single crystals, our measurements are restricted to  $\mathbf{E} \parallel \mathbf{c}^*$ , but we have complete freedom to choose a geometry for the magnetic field. Raw capacitance data collected at  $\omega = 1$  kHz are presented in Fig. 5.3. In this case, we show explicitly both real ( $\Delta C'$ ) and imaginary ( $\Delta C''$ ) components, which are proportional to the respective components of the dielectric constant  $\epsilon'$  and  $\epsilon''$ . Just as in Fig. 4.6, a prominent feature dominates the data, corre-

sponding to the magnetic-ferroelectric long-range-order transition. As was argued for  $\text{Rb}_2\text{Cu}_2\text{Mo}_3\text{O}_{12}$ , the divergence of the capacitance implies that, along with any magnetic order, polarization is itself a primary order parameter of the transition, and is critical at the QCP at  $H_c$ . All the discussion in the previous chapter extends to present phase boundary anomaly, as it is the saturation transition of  $\text{Cs}_2\text{Cu}_2\text{Mo}_3\text{O}_{12}$ . Measurements of the imaginary component (Fig. 5.3.(b,d,f)) do show peaks at the phase transition, more pronounced at the lowest temperature where the real part of the anomaly is largest (in particular for  $\mathbf{H} \parallel \mathbf{c}^*$ ). Its origin can be ascribed to movement of ferroelectric domain walls. In any case, this contribution is always a small part of the total signal and does not alter our analysis.

The major new observation is an additional modulation of both  $\Delta C'$  and  $\Delta C''$  at low temperatures. As shown by arrows in Fig. 5.3 an extra feature with both significant real and imaginary components emerges in  $\text{Cs}_2\text{Cu}_2\text{Mo}_3\text{O}_{12}$ , that has no analog in  $\text{Rb}_2\text{Cu}_2\text{Mo}_3\text{O}_{12}$ . The manifestation in the real component is a step-like anomaly that moves away from the critical field as the temperature is raised, both above and below  $H_c$ . Correspondingly, a peak emerges in the imaginary component of capacitance where the step becomes steepest. The large imaginary component must be related to dissipation in the system as a result of a dynamical process. We henceforth refer as  $T^*$  to the temperature at which  $\Delta C''$  peaks. The origin of this anomaly and its intrinsic relevance to the physics of  $\text{Cs}_2\text{Cu}_2\text{Mo}_3\text{O}_{12}$  is investigated in detail below and understood in terms of dynamical relaxation. In spite of the very strong directional dependence of the phase-boundary divergence, this new feature shows a nearly isotropic behaviour. This is highlighted in Fig. 5.4.(a,b), where the scale of the anomalies around the QCP is directly compared for different field directions. Whereas the divergence at the phase boundary changes by an order of magnitude depending on the field direction, both real and imaginary components of the dissipative anomaly remain the same for all geometries.

Anisotropy in  $\text{Cs}_2\text{Cu}_2\text{Mo}_3\text{O}_{12}$  defines a spin easy axis and an almost collinear structure at zero field [128]. As a result, the system undergoes a spin-flop transition at 2 T, for fields parallel to the chain directions,  $\mathbf{H} \parallel \mathbf{b}$ . Interestingly, the presence of a spin-flop transition affects both kinds of anomalies. On the one hand, the feature at the phase boundary retains a significant weight as the magnetic field is lowered almost all the way down to zero field (triangles in Fig. 5.3.(e)). It is particularly prominent in the vicinity of the bicritical termination point found at 2 T and 1.4 K. On the other hand, the value of  $T^*$  is reduced around the spin-flop field, echoing the reduction of  $T_c$  (triangles in Fig. 5.7.(e)).

## BEC criticality

Data in Figure 5.3 evidence the relevance of two phenomena in the dielectric response in  $\text{Cs}_2\text{Cu}_2\text{Mo}_3\text{O}_{12}$ . In order to comprehend the nature of the new relaxing features, we need to understand to what extent the description of the QCP in  $\text{Cs}_2\text{Cu}_2\text{Mo}_3\text{O}_{12}$  in the framework of Bose-Einstein Condensation of magnons holds. For this purpose, the analysis that has been presented for  $\text{Rb}_2\text{Cu}_2\text{Mo}_3\text{O}_{12}$  is repeated verbatim for  $\text{Cs}_2\text{Cu}_2\text{Mo}_3\text{O}_{12}$ .

As a first step, the measurement conditions were validated following the same procedures (not shown). An excitation voltage of  $V_{ex} = 0.75$  V was chosen and used for the entirety of the measurements that are presented in this chapter. Further, a frequency

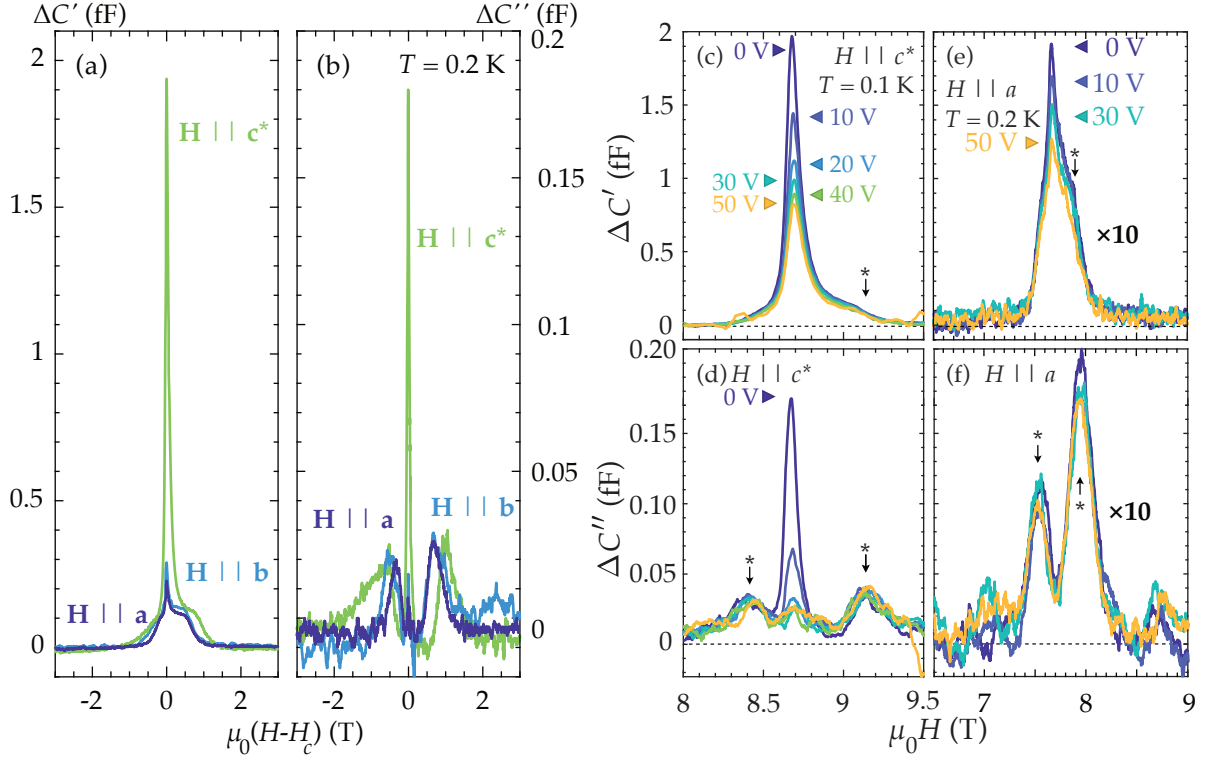


**Figure 5.4:** (a,b) Comparison of dielectric anomalies close to the QCP for all field geometries: (a) real and (b) imaginary components. All signals are shown to scale and the field axis shows the distance to the critical field. The sharp peaks at  $H_c$  show a stark directional dependence. In contrast, the amplitude of the broad anomalies besides it are completely isotropic. (c-f) Effect of a DC bias electric field along the crystallographic  $\mathbf{H}^*$  axis on the complex dielectric response of  $\text{Cs}_2\text{Cu}_2\text{Mo}_3\text{O}_{12}$  close to the QCP for: (c,d)  $\mathbf{H} \parallel \mathbf{c}^*$  and (e,f)  $\mathbf{H} \parallel \mathbf{a}$ . Magnetic field is  $\mathbf{H} \parallel \mathbf{a}$ . Note that data in (e,f) have been multiplied by 10 in order to match the scale in (c,d). Colors show field scans at a constant temperature of 200 mK and different bias fields from 0 to 250 kV/m, show in the labels. Only the diverging feature at the phase boundary is modified by a uniform electric field, as expected for a critical susceptibility. The broad dissipative features in (c-f) marked by asterisks are unchanged.

of 1 kHz is optimal to probe critical properties at the QCP and it is used for the majority of measurements. However, as it will be shown below, the new anomalies found in  $\text{Cs}_2\text{Cu}_2\text{Mo}_3\text{O}_{12}$  show a frequency dependence even in the very slow limit that we are considering.

With the details of the experiment method out of the way, we confirm that electric polarization is indeed a primary order parameter at the QCP. This is done again by observing how a bias uniform DC field destroys the phase transition by explicitly breaking the system  $SO(2)$  symmetry. This is reflected in a suppression of the divergence of dielectric susceptibility at the QCP as is shown in Fig. 5.4.(c-f). Here we investigate the action of such DC field on the geometry with the largest and the smallest anomalies:  $\mathbf{H} \parallel \mathbf{c}^*$  (Fig. 5.4.(c,d)) and  $\mathbf{H} \parallel \mathbf{a}$  (Fig. 5.4.(e,f)) respectively.

Measurements around at  $H_c$  at 0.1 K for  $\mathbf{H} \parallel \mathbf{c}^*$  and 0.2 K for  $\mathbf{H} \parallel \mathbf{a}$  display a

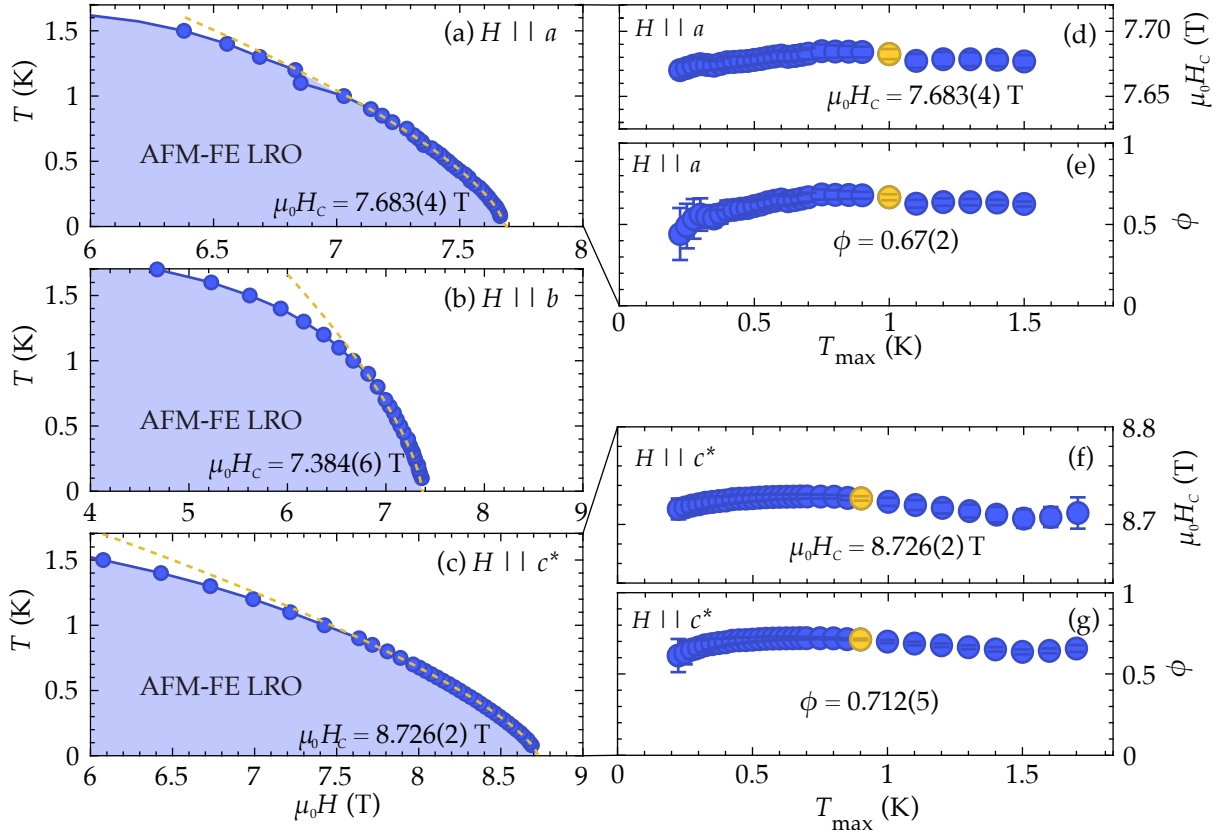


**Figure 5.5:** Phase boundaries in  $\text{Cs}_2\text{Cu}_2\text{Mo}_3\text{O}_{12}$  obtained from dielectric anomalies under applied magnetic fields along the (a)  $a$ , (b)  $b$ , and (c)  $c^*$  directions. The dashed curves are best power-law fits in the range given in Table 5.2. (d-g) Shrinking-fit-window analysis of the measured phase boundaries for (d,e)  $\mathbf{H} \parallel a$  and (f,g)  $\mathbf{H} \parallel c^*$ . The plots show the least-squares fitted values of (d,f) the phase boundary exponent  $\phi$  and (e,g) the upper critical field  $H_{c2}$  vs. the temperature range used for the fit.

reduction of the real divergent peak as the external DC field is increased, just as was found in  $\text{Rb}_2\text{Cu}_2\text{Mo}_3\text{O}_{12}$ . The effect is particularly strong on the imaginary component (Fig. 5.4.(d,f)), where a modest field reduces the anomaly well below the sensitivity of our method. This component of dielectric permittivity is associated with ferroelectric domain-wall dynamics. A static field suppresses creeping and thereby the imaginary part of the response. This confirms again that both staggered magnetization and electric polarization are primary order parameters for the QPT.

Surprisingly, the additional dissipative features besides the main peak (asterisks in Fig. 5.4.(c-f)) are completely unaffected by the presence of an external DC field. No representative change can be observed in either real or imaginary component of this anomaly for any of the presented geometries.

To determine the applicability of BEC theory to the observed QCPs we examine the long-range-order phase boundaries close to  $H_c$ . The boundaries are extracted from the maxima of capacitance in Fig. 5.3 for each magnetic field geometry and plotted in Fig. 5.5.(a-c). Once again, a shrinking-window analysis is performed to fit the boundaries

**Table 5.2:** Critical fields and boundary exponents extracted from best fits in the range given by  $T_{max}$  around the QCP for the investigated field geometries.

	$\mu_0 H_c$	$\phi$	$T_{max}$ (K)
<b>H</b>    <b>a</b>	7.683(4)	0.67(2)	1.00
<b>H</b>    <b>b</b>	7.384(4)	0.68(3)	0.90
<b>H</b>    <b>c*</b>	8.726(5)	0.712(5)	0.90

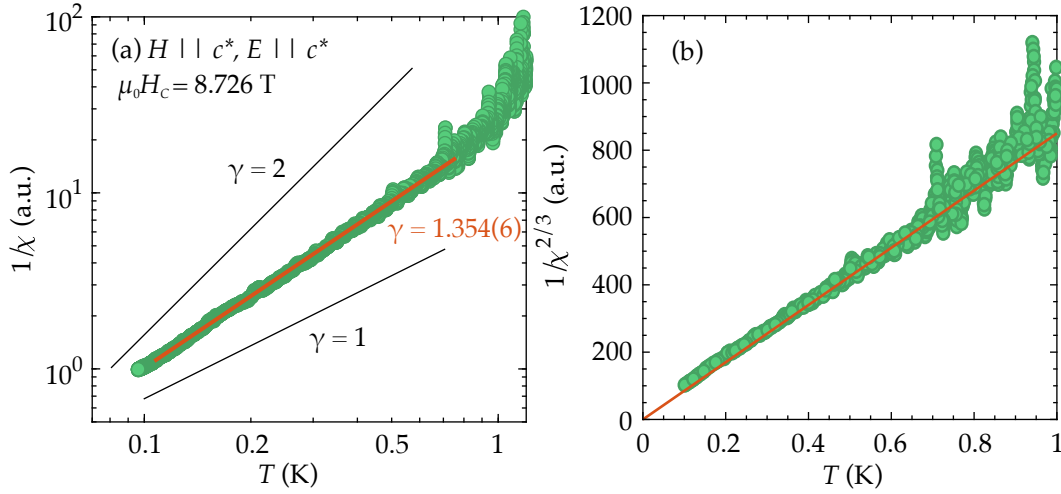


**Figure 5.6:** Scaling of the critical dielectric susceptibility in  $\text{Cs}_2\text{Cu}_2\text{Mo}_3\text{O}_{12}$  ( $\chi \propto \Delta C'$ ) along the critical trajectory (fixed  $\mu_0 H_c = 8.726$  T). (a) A double logarithmic plot shows indeed power-law behavior below 1 K and down to the lowest measured temperatures. Best fit to a power-law trend is shown as a solid thick line, along with the obtained critical exponent. Solid thin lines are guides to the eye representing mean-field ( $\gamma = 1$ ) and 3D-Ising ( $\gamma = 2$ ) results. (b) Susceptibility rescaled as  $\chi^{-2/3}$  shows a divergent trend towards zero temperature, highlighting the fact that this quantity is *quantum* critical.

to a power-law and extract the boundary exponents. As opposed to  $\text{Rb}_2\text{Cu}_2\text{Mo}_3\text{O}_{12}$ , in this case the phase boundaries show a smooth evolution away from  $H_c$ , up and above 1 K. The results of the windowing analysis are exemplified in Fig. 5.5.(d-g) and summarized in Table 5.2. Figure 5.5.(a-c) also shows the best fits for each individual field geometry.

The fitted boundary exponents are in a remarkable agreement with the expected critical exponent  $\phi = 2/3$  for a 3D BEC QCP. In addition, the resulting uncertainties are very low thanks to the high signal-to-noise ratio of capacitance measurements. Note that  $\text{Cs}_2\text{Cu}_2\text{Mo}_3\text{O}_{12}$  shows very clean realizations of the BEC criticality for all geometries: **H** || **a**, **H** || **b** and **H** || **c\***. This is in contrast to kinks found in  $\text{Rb}_2\text{Cu}_2\text{Mo}_3\text{O}_{12}$ , and suggests that the magnetic interaction in  $\text{Cs}_2\text{Cu}_2\text{Mo}_3\text{O}_{12}$  is more isotropic than in  $\text{Rb}_2\text{Cu}_2\text{Mo}_3\text{O}_{12}$ .

Having determined the critical fields we can finally turn to study the critical susceptibility,  $\chi$ , at  $H = H_c$ . We remind again our assumption that the main contribution to  $\Delta C'$  is from the critical (divergent) part of electric susceptibility. Following the above argumentation, the same picture as for  $\text{Rb}_2\text{Cu}_2\text{Mo}_3\text{O}_{12}$  must hold and we can access it as

$\chi \propto \Delta C'$ . Figure 5.6 shows data for  $\mathbf{H} \parallel \mathbf{c}^*$  along the critical trajectory at  $\mu_0 H_c = 8.726$  T. The log-log scale in Figure 5.6.(a) shows a robust power-law trend for  $\chi$  over a decade in temperature and down to the lowest accessible values. Least-squares fit to a power-law function, results in a critical exponent  $\gamma = 1.354(6)$ , remarkably close to the expected value of  $\gamma = 3/2$  for BEC. Once more, the measured susceptibility does indeed show a divergent behavior as  $T \rightarrow 0$  as evidenced by Fig. 5.6.(b). Together with the phase boundary analysis, these results confirm that the QCP in  $\text{Cs}_2\text{Cu}_2\text{Mo}_3\text{O}_{12}$  is a good realization of a 3D BEC of magnons.

Note that we have restricted our analysis of  $\chi$  to  $\mathbf{H} \parallel \mathbf{c}^*$ . Unlike for the phase boundary, where only the peak position matters, here the amplitude of the signal is crucial for the results. In this geometry the real part of the diverging anomaly is much larger than that of the dissipative anomaly, and the latter can be neglected. On the contrary, for  $\mathbf{H} \parallel \mathbf{a}$  and  $\mathbf{H} \parallel \mathbf{b}$  the amplitude of both anomalies is comparable. The relaxing feature will be shown to have its own temperature dependence, which makes it not challenging to isolate each contribution to the total capacitance.

All in all, our data supports the description of the QPTs in  $\text{Cs}_2\text{Cu}_2\text{Mo}_3\text{O}_{12}$  in the 3D BEC universality class. Crucially, the presence of an additional phenomenon on top of the divergence of susceptibility at the QCP does not modify this description (beyond hampering our analysis as discussed in the previous paragraph). The two contributions to dielectric susceptibility are therefore independent, as will be further justified below, and can be treated independently. However, it will be further clarified that both contributions are intimately linked and ruled by one single entity, the magnon that softens at the QCP.

## 5.4 Dielectric relaxation by quantum critical magnons

The current section focus on the omnipresent low-temperature broad features in  $\text{Cs}_2\text{Cu}_2\text{Mo}_3\text{O}_{12}$  and that were absent in the isostructural  $\text{Rb}_2\text{Cu}_2\text{Mo}_3\text{O}_{12}$ .

Figure 5.7 provides a clear picture of the field and temperature dependence of the dissipative new feature, specially in comparison to the divergence at the boundary. Unlike the divergence, the additional features show virtually no difference in magnitude between measurements under different magnetic field orientations (as was already evidenced in Fig. 5.4.(a,b)). Moreover, their magnitude is not particularly field-dependent, and they persist even in the absence of applied field. Note that in our discussion of the origin of the boundary anomaly we argue the need for a non-zero field induced magnetization. Obviously, their origin must be entirely different. Yet, both effects must be intimately linked, as they both coalesce and become critical at the QCP. The values of  $T^*$  at different fields are explicitly displayed in Fig. 5.12 (triangles) and Fig. 5.15.

Several simple scenarios for the origin of the  $T^*$  feature can be readily ruled out. First, the feature must be a bulk-, rather than a surface- or finite-size-effect, since a comparable anomaly at the same  $T^*$  is also observed in polycrystalline samples (Fig. 5.2.(d,e)). While this feature is broadened by the powder-nature of the sample, it shows that relaxation is not happening at the surface of the material but is rather an intrinsic bulk effect of  $\text{Cs}_2\text{Cu}_2\text{Mo}_3\text{O}_{12}$ . Second, there is no thermodynamic phase transition at these temperatures [128]. In any case, such a large dissipation is not something that one would expect at a thermodynamic phase transition. This is in contrast to  $\text{Rb}_2\text{Cu}_2\text{Mo}_3\text{O}_{12}$  [127], where

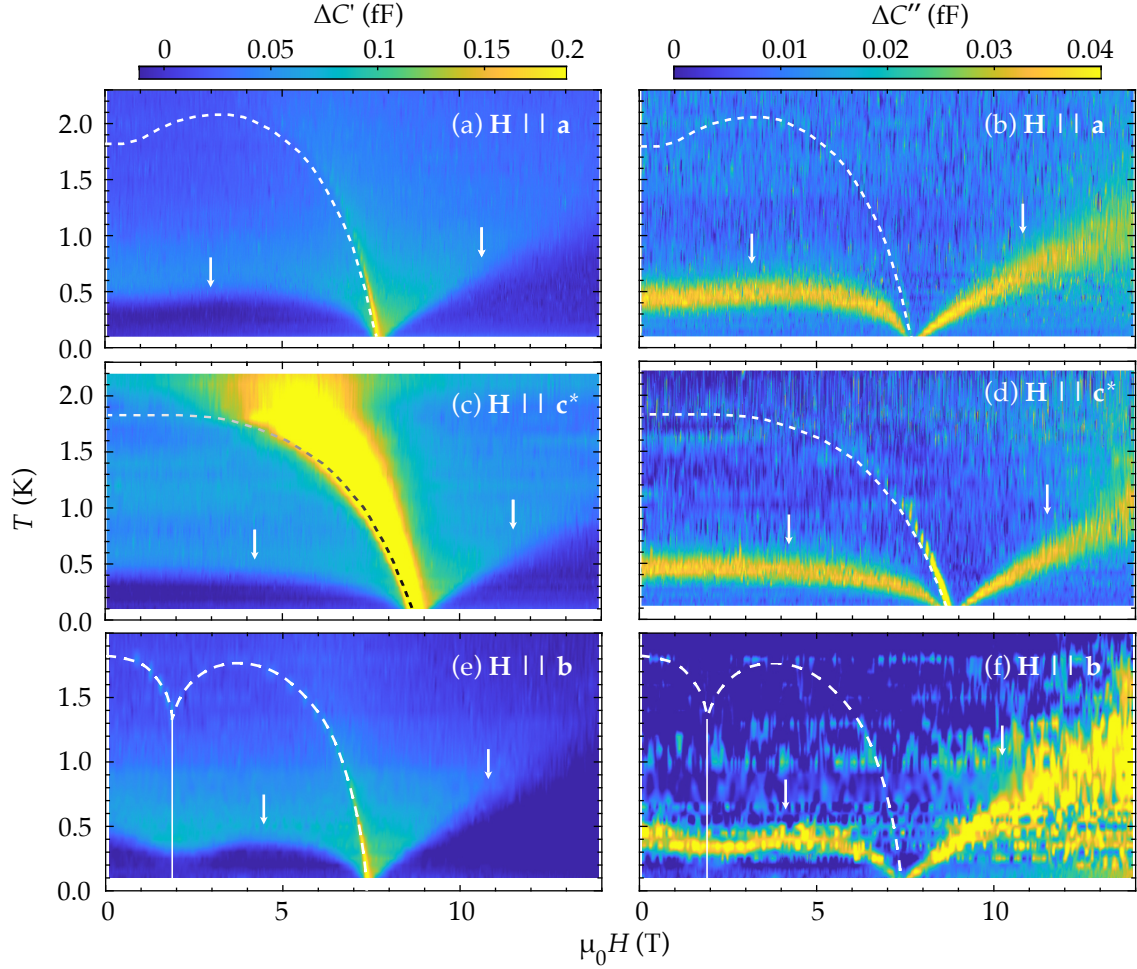


**Figure 5.7:** False color plots of complex capacitance  $\Delta C = \Delta C' + i\Delta C''$ . The electric field is applied parallel to the  $\mathbf{c}^*$  axis. The magnetic field is applied along three mutually orthogonal crystallographic directions: (a,b)  $\mathbf{H} \parallel \mathbf{a}$  and (c,d)  $\mathbf{H} \parallel \mathbf{c}^*$ , and (e,f)  $\mathbf{H} \parallel \mathbf{b}$ . The color scale is shared across (a)/(c)/(e), and (b)/(d)/(f), respectively. It has been chosen to highlight the novel low temperature anomalies (arrows). As a result some stronger peaks at the magnetic phase boundary (dashed line, Ref.[128]) are blown out. A solid line in (e,f) represents the first-order spin-flop transition.

the only dielectric anomaly observed corresponds precisely to the thermodynamic phase transition. A glass-like freezing transition at  $T^*$  is also unlikely, due to the absence of any hysteresis or history-dependence in our measurements.

Step-like behavior of  $\epsilon'$  above a magnetic field-induced saturation QCP has been reported previously in another quantum magnet  $\text{Ba}_2\text{CoGe}_2\text{O}_7$  [88]. There it was attributed to the fluctuations of the AF order, the characteristic energy/ temperature of the anomaly coinciding with that of the field-induced single-magnon Zeeman gap  $g\mu_B\mu_0(H - H_c)$ . This interpretation can not be carried over to  $\text{Cs}_2\text{Cu}_2\text{Mo}_3\text{O}_{12}$ . In our material, above  $H_c$  the scale of  $T^*$  is roughly *ten times smaller* than the Zeeman gap (triangles vs. the dashed line in Fig. 5.15). A different mechanism must be at play.

Since the data shown were collected at finite frequency of 1 kHz, one could suspect a proximity of a mechanical resonance in the measurement setup that couples to our probe. Frequency-dependent measurements firmly rule that out: while some mechanical resonances are indeed detected, none are found in the immediate neighborhood of 1 kHz (see Fig. 5.13 and the discussion below). Also, all appear to be excited by Lorentz forces in the connecting wires, and therefore vanish in the absence of an applied magnetic field, very much unlike the feature under discussion. The final suspicion is that slow dielectric relaxation may arise from trapping of charge carriers [140]. In our case this seems unlikely, as  $\text{Cs}_2\text{Cu}_2\text{Mo}_3\text{O}_{12}$  is a good insulator and is transparent in bulk at room temperature.

## Debye relaxation

The origin of the  $T^*$  feature is revealed in a quantitative analysis of the data in terms of dielectric relaxation electric dipoles. The model that captures the dynamics of finite electric dipoles is that of *Debye relaxation*. When a DC electric field is applied to a polar material, a certain electric polarization builds up. This process is not instantaneous and in fact, the polarization buildup follows an exponential law with a characteristic time  $\tau$ . This quantity is called the *relaxation time* and it is an intrinsic property of the dielectric system. If the applied field is instead an alternating one, the response of the system will try to follow that of the external field but the finite value of  $\tau$  will result in a dephasing. As a result, the response becomes complex depending on the frequency of the driving field. In a dielectric, the relation between polarization and electric field is given by the electric permittivity, and the effect of relaxation is captured in the Debye equations:

$$\epsilon(\omega) = \epsilon_\infty + \frac{\epsilon_s - \epsilon_\infty}{1 + i\omega\tau} \quad (5.1)$$

Note that this is a complex relation.  $\epsilon_s$  is the *static* limit of permittivity and corresponds to the situation where the driving field is much slower than the characteristic time  $\omega \ll \tau^{-1}$ . In contrast,  $\epsilon_\infty$  shows the permittivity in the limit where the probing frequency is so large that the system cannot respond to the external field. The lineshape from 5.1 is shown in Fig.5.8. A peak in the imaginary component of  $\epsilon$  is found when the frequency of the excitation field matches  $\omega = \tau^{-1}$ . In general, the value of the characteristic time varies with external parameters such as temperature.

The observation of Debye relaxation requires the presence of a single relaxation time, a condition which is hardly ever met in solid state systems [141, 142]. In real materials, the presence of vacancies, impurities or dislocations gives rise to local deviations from the single relaxation time, resulting in a *distribution* of characteristic times. Interac-

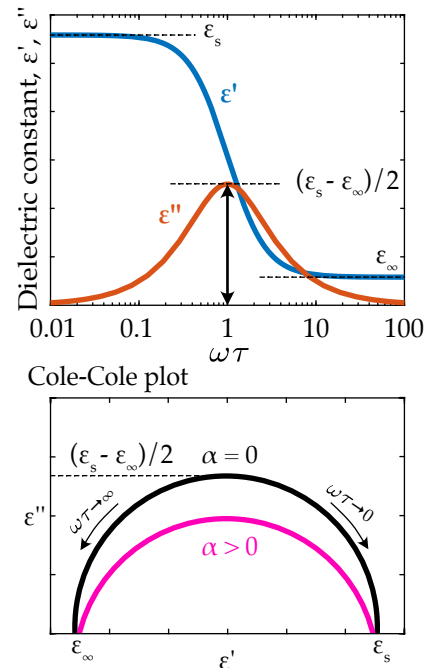


**Figure 5.8:** (Above) Characteristic real and imaginary components of a the Debye relaxation response. (Below) The Cole-Cole plot is a key tool to understand the presence of a distribution of relaxation times ( $\alpha \neq 0$ ) in a system.

tion between electric dipoles may also contribute to this effect, due to their large density in solids. As a result of such extended distribution of relaxation times, the peak in  $\epsilon''$  will smear in frequency and its maximum amplitude will be reduced. An empirical model to capture this phenomenology was proposed by Cole and Cole,

$$\epsilon(\omega) = \epsilon_\infty + \frac{\epsilon_s - \epsilon_\infty}{1 + (i\omega\tau)^{1-\alpha}} \quad (5.2)$$

where the distribution width is encoded into a phenomenological parameter  $\alpha < 1$ . Note that the exponent  $\alpha = 0$  corresponds to the Debye relaxation model with a single relaxation time [143].

It can be shown that on the complex plane given by  $\epsilon'$  and  $\epsilon''$ , the response of a material showing Debye relaxation is a semicircle. The radius of this curve is exactly  $(\epsilon_s - \epsilon_\infty)/2$ , it is centered around  $((\epsilon_s - \epsilon_\infty)/2, 0)$  and each point represents a different frequency of the probing field. The effect of a distribution of relaxation times as in (5.2) is to shift the center of the circumference in the vertical axis (as shown in Fig.5.8). This plot is therefore a useful tool in determining the degree of dispersion of relaxation times and is referred to as the Cole-Cole plot. Any deviations from Debye relaxation become apparent through this plot.

Possibly the simplest system in which Debye relaxation can be found is the bistable model of a dipole. A double-well potential describes the potential landscape of a polar molecule, where each of the stable positions at the bottom of the wells represent two states of an electric dipole (e.g.  $\vec{p}$  and  $-\vec{p}$ ). The two states are separated by a potential barrier  $\Delta$ , and the state is subject to fluctuations that may drive it over the barrier. If an imbalance is created (for example by applying an electric field), the system will *relax* towards the lower energy state. Overall, the transition probability shows Arrhenius behaviour given by

$$w = Ae^{-\Delta/k_B T} \quad (5.3)$$

for a deep well, where  $A$  is a constant denoting the number of attempts per second to jump over the barrier classically. Macroscopically, the relaxation time  $\tau$  is given by the reciprocal of  $w$ . This simplistic model can reproduce the temperature dependence of numerous relaxation processes and will be relevant to the physics of  $\text{Cs}_2\text{Cu}_2\text{Mo}_3\text{O}_{12}$ .

## Relaxation in $\text{Cs}_2\text{Cu}_2\text{Mo}_3\text{O}_{12}$

Debye-like relaxation is a process that relies on the existence of persistent electric dipoles. We build a model of relaxation for  $\text{Cs}_2\text{Cu}_2\text{Mo}_3\text{O}_{12}$  based on two hypothesis, that will be supported by our comprehensive data set.

1. Low-energy electric dipoles exist in  $\text{Cs}_2\text{Cu}_2\text{Mo}_3\text{O}_{12}$  and are free to undergo relaxation down to the ultra-low temperatures at which the relaxing features are found.
2. The only interaction of the electric dipoles with a external magnetic field is reflected in their relaxation rate. The relaxation time thus becomes a function of temperature and magnetic field.

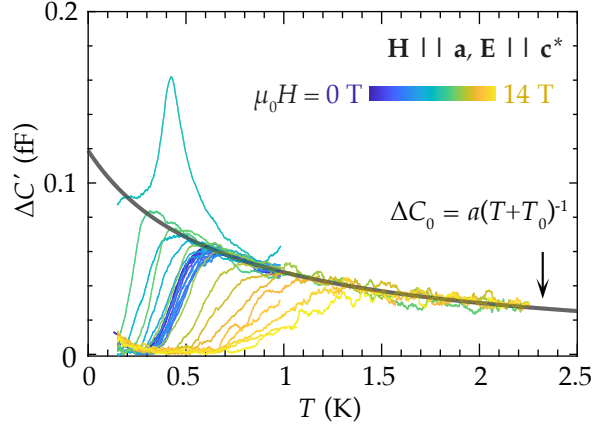


**Figure 5.9:** The static response of  $\text{Cs}_2\text{Cu}_2\text{Mo}_3\text{O}_{12}$  shows no field dependence. Regardless of the applied field, all capacitance curves collapse on a single line (solid black line) at elevated temperatures. Data correspond to the geometry of Fig. 5.7.(a). A phenomenological fit to the data is shown by a bold black line. The large peak at 0.4 K corresponds to the anomaly at the phase boundary.

Under these conditions, we want to describe our capacitance data around  $T^*$  with the following equation

$$\Delta C = \frac{\Delta C_0(T)}{1 + (i\omega\tau(T, H))^{1-\alpha}}. \quad (5.4)$$

where,  $\Delta C_0$  is the static response. This response is independent of the existence of relaxation, and as per our second hypothesis, it should be independent of the magnetic field. We focus our analysis on the geometry where  $\mathbf{H} \parallel \mathbf{a}$  where the dielectric anomaly at the boundary is smallest and the contribution from relaxation is dominant. All data discussed below are collected with  $\mathbf{H} \parallel \mathbf{a}$  and  $\mathbf{E} \parallel \mathbf{c}^*$ .

Qualitatively, relaxation can be expected to occur faster at high temperature, and so  $\tau(T)$  is expected to decrease with increasing temperature. Higher temperatures promote thermal fluctuations that increase the likelihood of a dipole to hop between states. Therefore, at high enough temperatures,  $\Delta C$  (5.4) should simply reduce to the static dielectric constant. In Fig. 5.9 we demonstrate that most of the measured  $\Delta C'$  curves *collapse on a single, field-independent, line at  $T \gtrsim T^*$* . The only exception is the data close to the QCP, where the sharp dielectric anomaly at the transition overwhelms the background. The resulting universal curve  $\Delta C'_0(T)$  is well-fitted by the form  $a(T + T_0)^{-1}$  ( $T_0 = 0.68(1)$  K, Fig. 5.9). The lack of a field-dependence of  $\Delta C'_0(T)$  implies that this contribution is unrelated to magnetism and is entirely due to the crystal lattice. One could suspect the origin to be a yet undetected nearby structural transition. However, a lattice-driven ferroelectric transition is unlikely, due to the modest absolute value of the dielectric constant in  $\text{Cs}_2\text{Cu}_2\text{Mo}_3\text{O}_{12}$  ( $\epsilon \approx 5.5$ , Fig. 5.2.(d)). Moreover, the relative change in the dielectric constant due to the temperature-dependent background is smaller than 1%. We conclude that  $\Delta C'_0(T)$  is due to some yet to be identified *persistent low-energy electric dipole degrees of freedom in  $\text{Cs}_2\text{Cu}_2\text{Mo}_3\text{O}_{12}$* .

With  $\Delta C'_0(T)$  characterized, the parameter  $\alpha$  in (5.1) can be determined from the plots of the real vs. imaginary parts of  $\Delta C$  (Cole-Cole plots). Figure 5.10 display the Cole-Cole

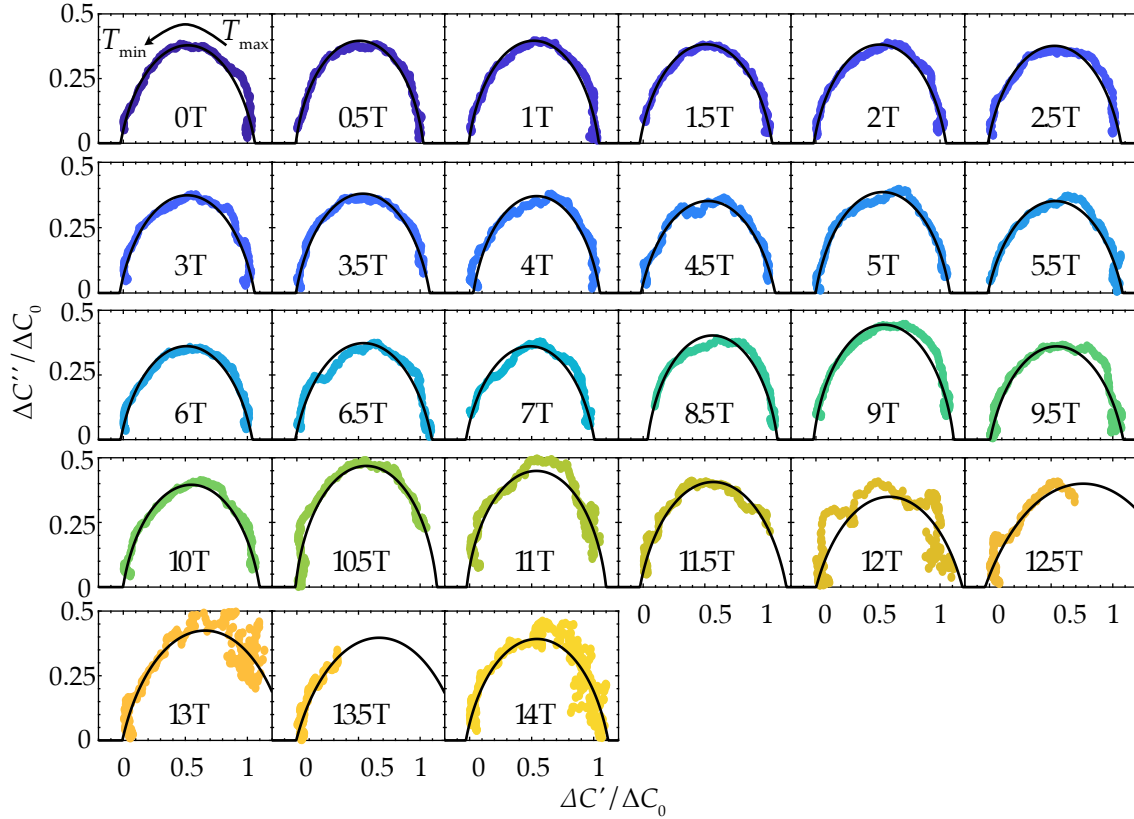


**Figure 5.10:** Cole-Cole plots for data collected with  $\mathbf{H} \parallel \mathbf{a}$  with a probing frequency of 1 kHz. Axes are shared across all subplots. Black solid lines represent the best fit to a semi-circumference as expected for the Cole-Cole model. The extracted values for  $\alpha$  are summarized in Fig. 5.11.

diagram for 27 values of magnetic field, all distant enough from the QCP. A semicircular shape can be readily identified for all field values. Note a small particularity about these plots. As discussed above, each point in the Cole-Cole plot represents a different *frequency*. Then sweeping frequency the semicircle is drawn. Our measurements are, however, carried out at a constant frequency of 1 kHz, and what we show in Fig. 5.10 is the evolution as a function of *temperature*. We have already argued how the relaxation time picks up a certain temperature dependence, thus sweeping temperature is roughly equivalent to sweeping frequency, from the static limit at high temperatures to the infinite limit at the lowest.

The data in Fig. 5.10 are well fitted to the Cole-Cole model of (5.4) at a constant frequency. Independent fits are performed for each value of magnetic field and the results are summarized in Fig. 5.11.(a). Note that no assumption on the functional dependence of  $\tau$  is needed for these fits. Especially at low fields the data show little variation around the average value of  $\alpha_{avg} = 0.20$ . This value shows a good agreement to all data sets and is selected as a global parameter. The higher discrepancy in the high-field data is mainly due to the restricted temperature coverage of the data sets preventing access to the full circumference.

The only remaining fit parameter not determined globally is the characteristic time

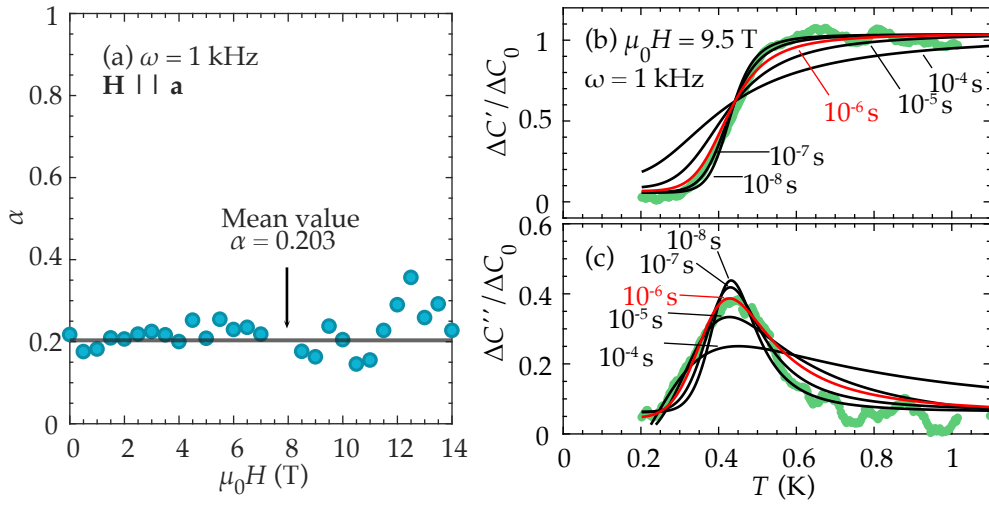


**Figure 5.11:** a Phenomenological  $\alpha$  parameter extracted from the best fit of data in Fig. 5.10 to (5.1). The average value, used in the global fit in the main text is shown as a solid line. (b,c) The goodness of fit to (5.1) strongly depends on the attempt time,  $\tau_0$ . The panels show the (b) real and (c) imaginary components of an instance of the best simultaneous fits with a fixed attempt time, displayed next to the curves. The best fit with  $\tau_0 = 10^{-6}$  s is highlighted in red.

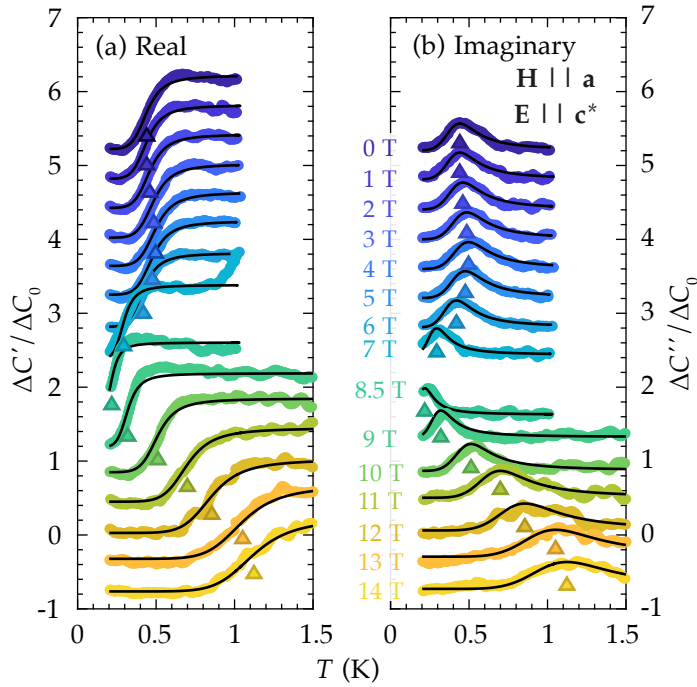


**Figure 5.12:** Constant-field measurements of complex capacitance. Data shown in (b)- real part and (c)- imaginary part are normalized by the “background”  $\Delta C_0$  in Fig. 5.9. Same colors correspond to same magnetic field values, also shared with Fig. 5.9. An offset of 0.4 units has been added between sets for visibility. Black solid lines show the best fit to the Cole-Cole model of (5.4). Both panels show the same scale and units. Triangles (▲) denote the position of  $T^*$ .

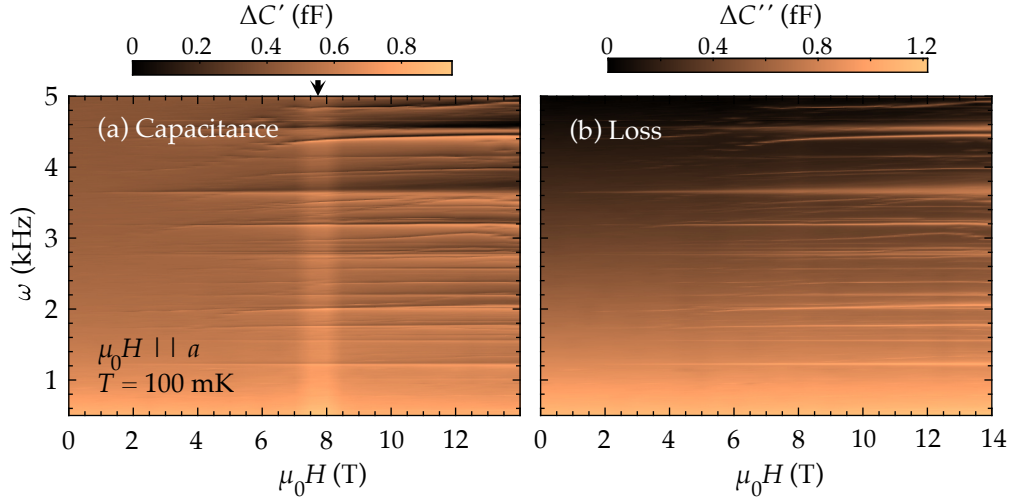


**Figure 5.13:** Complex capacitance scans at 100 mK at different magnetic fields and frequencies: (a) real component, (b) imaginary component. Resonant features can be identified at a variety of frequencies, whose strength grows as does the magnetic field ( $\mathbf{H} \parallel \mathbf{a}$ ). In (a), a faint vertical stripe represents the peak at the critical field (black arrow), which gives an idea of the relative strength of the resonances with respect to the signal measured from the sample.

scale  $\tau(T, H)$ . Except for the close vicinity of the QCP, at each value of magnetic field, an excellent agreement with experiment is obtained assuming an activated behavior

$$\tau(T, H) = \tau_0 \exp[\Delta(H)/k_B T]. \quad (5.5)$$

In this expression  $\Delta(H)$  is the “barrier height” and  $\tau_0$  the “attempt time”. This assumption brings about very naturally the fact that temperature plays a similar role to frequency in tuning the system from static to relaxing. Note that this assumption crystallizes our second model hypothesis, namely the effect of a magnetic field is to modify the value of the energy barrier for relaxation. Activated or Arrhenius behavior is very common among relaxation processes and can be found in a broad variety of systems, from polar liquids, to polymers and crystalline insulators [141, 144, 145].

The resulting least-squares fits are shown in Fig. 5.12. A *single field- and temperature-independent*  $\tau_0 \approx 10^{-6}$  s was found to be sufficient to capture the data quantitatively. The final model has therefore one single free parameter per magnetic field, and two globally fitted parameters. We have checked that other values of  $\tau_0$  notably reduce the fit quality as is illustrated in Fig. 5.11.(b). This very simple model captures all the observed features in the data with just a few parameters.

Note that both the real and imaginary parts are reproduced simultaneously using the same values of  $\Delta(H)$  for all temperatures. In contrast, if we were dealing with glassy behavior, relaxation times would be expected to show a divergent behavior at a finite temperature [146, 147]. This is yet another argument against strong disorder effects and glassiness, despite the distribution of relaxation scales indicated by  $\alpha = 0.2$ .

## The frequency dependence

Equation (5.1) implies a very specific form of frequency dependence. To further test the robustness of our model to different probing frequencies we characterize the system dielectric constant as a function of field and frequency. The observed system response is extremely complicated and full of features as is shown in Fig. 5.13.

Fig. 5.13 shows a complex landscape of anomalies at the base temperature of 100 mK. The values of frequency at which these anomalies appear are rather insensitive to the magnetic field, while their amplitude is strongly magnetic field dependent. The figure exemplifies the response between 0.5 kHz and 5 kHz, but our measurements were extended up to 20 kHz.

These features do not correspond to our sample at all. All of them correspond to electro-mechanical resonances in our measurement setup and we are able to understand their resonant shape in terms of a simple toy model. The system under study can be simplistically thought of as composed of a pair of capacitor plates held at the cold finger of a dilution refrigerator refrigerator. In order to measure capacitance, long, high-fidelity coaxial cables connect the sample to the measurement device, though leaving a small exposed piece of cabling that creates effectively a coil, immersed in the magnetic field. The cold finger is subject to vibrations that shake the coil in the field, generating in it a small electric current by induction. This effect is enhanced when the probing frequency of the electric field matches one of the mechanical normal modes of the cold finger system, giving rise to resonant behavior via Lorentz forces.

As resonances, the real and imaginary part of the response function (here  $\Delta C'$  and  $\Delta C''$ , respectively) must be related via Kramers-Kronig relations. This fact was confirmed for the most prominent features at a variety of fields, confirming their resonant nature. The amplitude of these features grows almost linearly proportional to the strength of the magnetic field, pointing to a linear coupling to it.

Some observations from the pattern of resonances are to be noted. First, the resonance frequency is essentially field and temperature independent for the majority of observed features. An unchanged pattern is measured up to temperatures as high as 100 K. Secondly, the landscape of resonances can be altered by changing the mass of the cold finger. Upon repeating the measurements in Fig. 5.13 with added weights to our sample stage, the resonance frequencies changed dramatically, further highlighting that these are sample-independent. Finally, there is no normal modes below 1.2 kHz. This shows that our measurements at 1 kHz are protected from these mechanical resonances.

These modes are rather strong in comparison with the dielectric signal from the sample. The anomaly corresponding to the saturation field ( $\mu_0 H_a = 7.66$  T) is visible as a vertical stripe in the data set in Fig. 5.13.(a). From this we obtain an amplitude ratio of up to 10:1 between the additional resonances and the saturation transition peak. These modes, though completely extrinsic and unrelated to the physics of  $\text{Cs}_2\text{Cu}_2\text{Mo}_3\text{O}_{12}$  cannot be avoided, as they are a result of the geometry of the experiment. It is for this reason that measuring magnitudes against frequency is not advisable in our experiment, and we choose temperature scans at constant frequencies. Notably, the resonances are absent in the absence of an external field and zero-field measurements are unaffected by extrinsic resonances. The resonance landscape is completely stable once the system is cooled down. Therefore, data in Fig. 5.13 allows us to find frequency windows that are

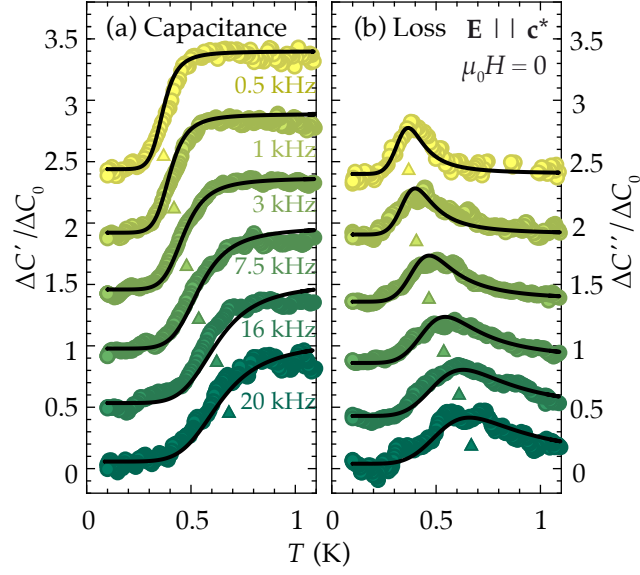


**Figure 5.14:** Frequency dependence of complex capacitance at zero magnetic field, (a)-real and (b)-imaginary parts. The excitation frequency is consistently color-coded in the two panels. An offset of 0.5 units has been added for clarity. Black lines show the evaluation of (5.1) with parameters fixed from Fig. 5.12, not a fit. Triangles represent the corresponding values of  $T^*$  at different frequencies.

far enough from extrinsic resonances, where we can study the frequency dependence in an applied magnetic field.

Having understood how to tune frequency, we study its effect on the dielectric response of  $\text{Cs}_2\text{Cu}_2\text{Mo}_3\text{O}_{12}$ . Fig. 5.14 shows a set of measurements at zero field under different excitation frequencies. The range in frequencies covers nearly two decades. With a fixed barrier height, an evaluation of (5.1) gives the expected temperature dependence of relaxation which is overlaid on the data sets. Fig. 5.14 demonstrates that the parameters extracted from the 1 kHz data also describe the capacitance measured at other frequencies *without any additional fitting*. The conclusion is that the relaxation time  $\tau(T, H)$  is *independent of probing frequency and is an intrinsic property of  $\text{Cs}_2\text{Cu}_2\text{Mo}_3\text{O}_{12}$* . Note on the other hand that the value of  $T^*$ , as defined above by the maximum in  $\Delta C''$ , is dependent on the measurement frequency and not a property of the material.

### Dielectric relaxation by quantum critical magnons

The combined results of our Cole-Cole analysis are borne out in Fig. 5.15. The activation energy  $\Delta(H)/k_B T$  is shown alongside with the temperature of long range ordering  $T_c$  [128] and  $T^*$ . Strikingly, for  $H > H_c$ ,  $\Delta(H)$  coincides with the single-magnon Zeeman gap  $g\mu_B\mu_0(H - H_c)$ , where the  $g$ -factor is taken as  $g = 2.16$  [98, 100]. This strongly suggests that the  $T^*$  feature arises from the relaxation of low-energy structural dipole moments (the ones responsible for the background dielectric constant as discussed above) by single magnons. The isotropy of  $T^*$  with respect to the field orientation naturally follows from the very isotropic  $g$ -factor and saturation magnetization [128]. In the ordered phase,  $T^*$

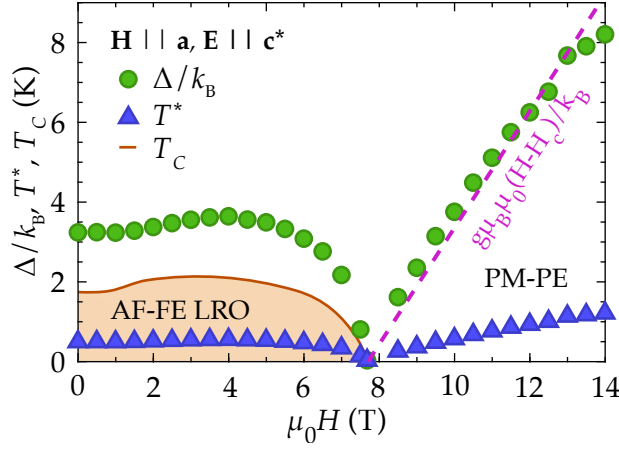


**Figure 5.15:** Characteristic energy barrier extracted from Cole-Cole model (circles). Above the QCP, it follows the Zeeman energy of a single magnon, given by a pink dashed line. Triangles represent the position of  $T^*$ , at which the relaxing dissipative anomaly is observed. For completeness, the phase boundary is depicted, showing the PM-PE (paramagnetic-paraelectric) and AF-FE phases (shadowed) [128].

does not change much at low fields, but goes to zero as  $H \rightarrow H_c$ . This behavior is also consistent with a single-magnon process within the ordered phase.

To put our findings in perspective, exponentially activated relaxation times are often observed in ferro- and paraelectrics [148–150]. In those cases, the activation energy usually corresponds to that of a longitudinal optical phonon [151] - an excitation carrying a finite dipole moment. In our case though, the dielectric relaxation can be instead attributed to a magnon. This conclusively demonstrates that individual *magnons can carry electric dipole moment* in  $\text{Cs}_2\text{Cu}_2\text{Mo}_3\text{O}_{12}$ . Unlike the other cases of magnons showing electric behavior [26–28, 152–155], the effects we observed persist beyond the ordered phase into the field polarized region  $H > H_c$  and are detected at remarkably low temperatures and frequencies.

The obtained value of  $10^{-6}$  s for the attempt time  $\tau_0$  in  $\text{Cs}_2\text{Cu}_2\text{Mo}_3\text{O}_{12}$  is striking. It corresponds to a very low attempt frequency of 1 MHz. For most of the field range explored, the magnon frequency is of the order 0.1 THz, i.e. five orders of magnitude higher. This is in stark contrast to other polar insulators [148–150] where  $\Delta\tau_0\hbar \sim 0.01 - 0.1$ . The key difference is that in  $\text{Cs}_2\text{Cu}_2\text{Mo}_3\text{O}_{12}$  the low- $T$  dielectric response is likely coming from the lattice, while the relaxation is occurring by the spin excitations. Therefore,  $\tau_0$  is determined by the strength of the spin-lattice coupling, which is expected to be much weaker than the phonon interactions in the ferroelectric case.

The insensitivity of this effect to a DC field is easy to understand in the proposed framework. The energy of the magnon is unaffected by a uniform electric field, and since this dictates the only relevant energy scale for relaxation, the effect remains unchanged.

The presented results show that a single magnon is condensing at the QCP in  $\text{Cs}_2\text{Cu}_2\text{Mo}_3\text{O}_{12}$ . Condensation of bound magnon states has been discussed as the origin of the presaturation phases [128, 129]. However, bound magnon states would show a much larger Zeeman gap close to the QCP (e.g. twice as large for a 2-magnon bound state). This shows that the presaturation phases in  $\text{Cs}_2\text{Cu}_2\text{Mo}_3\text{O}_{12}$  must host some form

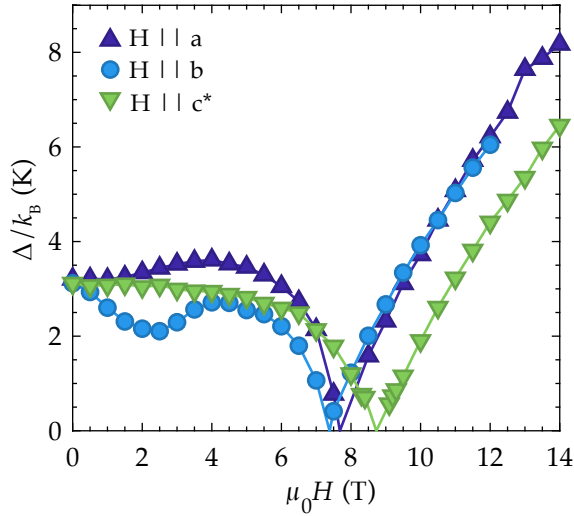


**Figure 5.16:** Characteristic energy barriers  $\Delta$  for each direction of the applied magnetic field. Solid lines are a guide to the eye.

of conventional dipolar order.

Finally we extend our analysis to the whole set of data that is available. We can repeat the same procedure for each of the field directions shown in Fig. 5.7 and obtain the corresponding activation energy for relaxation. The results are summarized in Fig. 5.16 showing a completely equivalent scenario for all investigated geometries. The magnon energy is exactly the barrier to relaxation, for every direction of a magnetic field. Fig. 5.16 is also a witness of the nearly isotropic  $g$ -tensor in  $\text{Cs}_2\text{Cu}_2\text{Mo}_3\text{O}_{12}$ , as was suggested from bulk magnetization measurements [128]. As was anticipated above, the presence of a spin-flop transition for  $\mathbf{H} \parallel \mathbf{b}$  influences the barrier for relaxation, reducing  $\Delta$  at 2 T, and indicating that relaxation is linked to the magnetic structure in the long-range ordered phase.

The proposed relaxation phenomenon can describe the entirety of the comprehensive set of dielectric measurements in  $\text{Cs}_2\text{Cu}_2\text{Mo}_3\text{O}_{12}$ . The magnon energy is clearly given by the Zeeman energy above the QCP, as described in the BEC theory. Spectroscopy measurements may reveal what magnon modes are responsible for the relaxation within the long-range ordered regions.

## 5.5 Are $\text{Rb}_2\text{Cu}_2\text{Mo}_3\text{O}_{12}$ and $\text{Cs}_2\text{Cu}_2\text{Mo}_3\text{O}_{12}$ different?

The proposed model of dielectric relaxation is extremely successful in describing all the low temperature features observed in the dielectric response of  $\text{Cs}_2\text{Cu}_2\text{Mo}_3\text{O}_{12}$ . However, a lingering question is why of the two very similar compounds  $\text{Cs}_2\text{Cu}_2\text{Mo}_3\text{O}_{12}$  and  $\text{Rb}_2\text{Cu}_2\text{Mo}_3\text{O}_{12}$ , both of which show ferroelectricity at the magnetic phase boundary mediated by the same mechanism, only the former displays the broad low-temperature relaxation features discussed above. One possible explanation would be qualitative structural differences at the lowest temperatures. Indeed,  $\text{Rb}_2\text{Cu}_2\text{Mo}_3\text{O}_{12}$  has an additional

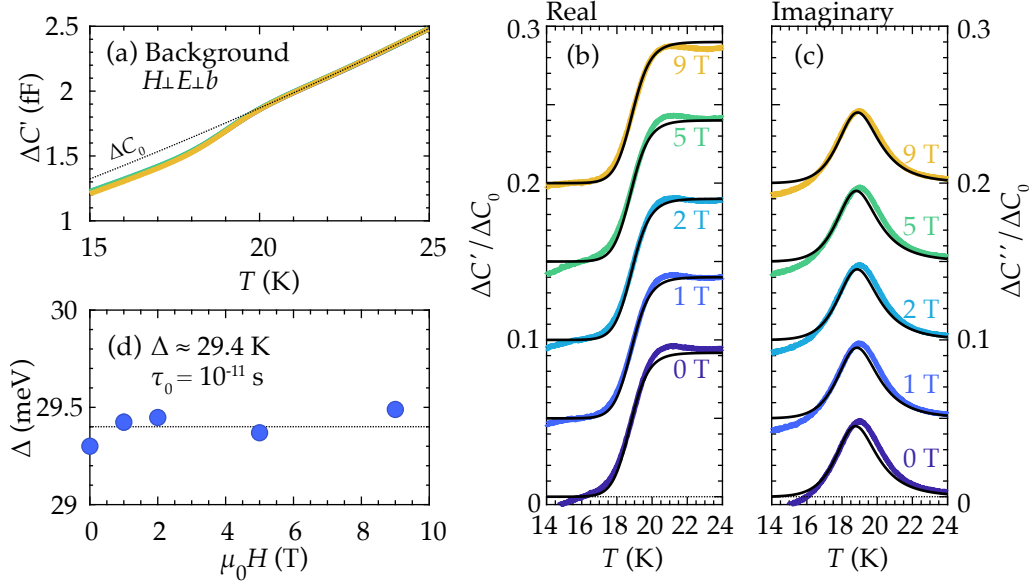


**Figure 5.17:** a) Capacitance measured on  $\text{Rb}_2\text{Cu}_2\text{Mo}_3\text{O}_{12}$  at zero magnetic field as reported in [127]. A phenomenological background ( $\Delta C_0$ ) is determined from the high-temperature capacitance signal. (b) The reduced real and imaginary components of the signal show good agreement with a Cole-Cole model, as described in the text. The extracted energy gap and attempt time are consistent with optical phonon activity.

yet unexplained dielectric anomaly unrelated to magnetism at about 20 K, which may indicate a structural phase transition absent in  $\text{Cs}_2\text{Cu}_2\text{Mo}_3\text{O}_{12}$ .

In order to tackle this question, we study the crystal structure of both materials in detail. Synchrotron radiation is used to observe the temperature evolution of the lattice parameters of  $\text{Cs}_2\text{Cu}_2\text{Mo}_3\text{O}_{12}$  and  $\text{Rb}_2\text{Cu}_2\text{Mo}_3\text{O}_{12}$  down to cryogenic temperatures. Details of the analysis can be found in Appendix B. Our measurements do not find indications of structural phase transitions or differences in the crystallography of these materials at low temperature.

Having clarified it does not come from a phase transition, we evaluate the high-temperature anomaly of  $\text{Rb}_2\text{Cu}_2\text{Mo}_3\text{O}_{12}$  in terms of dielectric relaxation. This analysis gives insight on the possible origins of relaxation in both sister compounds.

### Relaxation in $\text{Rb}_2\text{Cu}_2\text{Mo}_3\text{O}_{12}$

We revisit the single crystal capacitance data of  $\text{Rb}_2\text{Cu}_2\text{Mo}_3\text{O}_{12}$  in Fig. 4.4. The anomaly at 19 K shows a typical relaxation profile like those discussed above in this chapter, however at a much higher temperature. The temperature dependence of capacitance shows a step in its real part, coinciding with a peak in the imaginary component (Fig. 5.17.(a)). This is as well reminiscent of a relaxation process and can be modeled using Eq.5.1, following the procedure outlined above. At such high temperatures the lattice expansion is no longer negligible and the total capacitance has a strong contribution from volume expansion, that translates into change in the geometry of the capacitor plates (area and distance). Disentangling geometry and the changes in dielectric permittivity cannot be

easily carried out, and a background signal is obtained assuming a phenomenological second order polynomial for  $\Delta C_0$ , as shown in Fig. 5.17.(a). It is clear from the data that a magnetic field has a negligible influence on the dielectric response at this temperature. Data measured from 0 T to 9 T in a configuration where  $\mathbf{H}$ ,  $\mathbf{E}$ , and the crystallographic  $\mathbf{b}$  axis are all mutually orthogonal.

A good fit to Eq.5.1 of both real and imaginary components can be obtained with  $\alpha = 0$  and is displayed in Fig. 5.17.(b,c) for the range of magnetic fields. The extracted barrier height is shown in Fig. 5.17.(d), where once again a single attempt time was optimized globally. This fit reveals a completely different situation to that found in  $\text{Cs}_2\text{Cu}_2\text{Mo}_3\text{O}_{12}$ . The obtained attempt time is  $\tau_0 \approx 10^{-11}\text{s}$  (or approximately a frequency of 0.1 THz) and a characteristic energy barrier of  $\Delta/k_B = 29.4$  meV. These values (both energy scale and frequency) are consistent with activity of optical phonons (with typical frequencies in the THz range).

It has been argued that such relaxing features are commonly the result of defects in the crystal structure of a material. Relaxation anomalies have been reported at low temperature (30 K to 50 K) in a variety of polar insulating systems, including well known oxide perovskites as  $\text{KTaO}_3$  and  $\text{BaTiO}_3$  [156] and have been linked to relaxation of localized polarons around residual defects [157]. Typical values of  $\tau_0$  were found to be around  $10^{-14}$  s [156, 158], independent of sample composition and textures, differing from  $\text{Rb}_2\text{Cu}_2\text{Mo}_3\text{O}_{12}$  by three orders of magnitude and making this scenario unlikely.

A more likely mechanism is one involving an optical phonon. Such low temperature dielectric relaxation has been observed in  $\text{SrTiO}_3$  as a collection of dielectric and ultrasound anomalies between 8 K and 67 K [150, 151]. The energy barrier and attempt time in that system is more consistent with our result for  $\text{Rb}_2\text{Cu}_2\text{Mo}_3\text{O}_{12}$ , suggesting that similar physics may be involved, while the presence of oxygen vacancies is almost assured. However, quantitative discussion about the origin needs to rely on a careful examination of the phonon spectrum and normal modes in the system.

In summary, there seems to be no differences between  $\text{Cs}_2\text{Cu}_2\text{Mo}_3\text{O}_{12}$  and  $\text{Rb}_2\text{Cu}_2\text{Mo}_3\text{O}_{12}$ . They share the same crystal structure and both display dielectric relaxation. The findings in  $\text{Rb}_2\text{Cu}_2\text{Mo}_3\text{O}_{12}$  bring some insight on the origin of low-energy dipolar degrees of freedom in  $\text{Cs}_2\text{Cu}_2\text{Mo}_3\text{O}_{12}$ , suggesting that crystallographic vacancies are responsible for localized electric dipoles. This scenario would naturally explain the isotropy of the effect found in  $\text{Cs}_2\text{Cu}_2\text{Mo}_3\text{O}_{12}$  and the insensitivity of the lattice response to magnetic fields. The coupling of vacancies to phonons has been thoroughly studied and is responsible for relaxation processes. However, the reasons why these may couple to magnons instead of phonons in  $\text{Cs}_2\text{Cu}_2\text{Mo}_3\text{O}_{12}$  remains a mystery.

## 5.6 Conclusion

Despite its apparent simplicity as an antiferromagnet,  $\text{Cs}_2\text{Cu}_2\text{Mo}_3\text{O}_{12}$  displays captivating phenomena at low temperatures. Not only it realizes a cascade of phase transitions in applied fields, also we were able to find the same phenomenology as in  $\text{Rb}_2\text{Cu}_2\text{Mo}_3\text{O}_{12}$ , namely a quantum multiferroic ground state where magneto-electric coupling gives access to magnetic quantum critical properties. However, our most significant discovery is

that electric activity of magnetic excitations can couple to dielectric degrees of freedom. We have demonstrated the relaxation of dielectric degrees of freedom mediated by virtual soft magnons in  $\text{Cs}_2\text{Cu}_2\text{Mo}_3\text{O}_{12}$ . Our data highlight the tunability of the coupling: The applied magnetic field becomes a convenient ‘knob’ for tuning interactions between the polarizable lattice and spins due to proximity to a magnetic quantum critical point.

Delving into the differences between the isostructural  $\text{Rb}_2\text{Cu}_2\text{Mo}_3\text{O}_{12}$  and  $\text{Cs}_2\text{Cu}_2\text{Mo}_3\text{O}_{12}$ , we found dielectric relaxation is a shared property, though the responsible in  $\text{Rb}_2\text{Cu}_2\text{Mo}_3\text{O}_{12}$  seems to be an optical phonon. Yet, one question remains still unanswered: what is the microscopic origin of electric dipoles in these magnets? And even more importantly, why is relaxation in  $\text{Cs}_2\text{Cu}_2\text{Mo}_3\text{O}_{12}$  mediated by magnons and not by the more conventional processes observed in the case of  $\text{Rb}_2\text{Cu}_2\text{Mo}_3\text{O}_{12}$ ?

The coupling of magnetic and dipolar degrees of freedom furnishes an extremely versatile tool to study quantum criticality and probing new forms of quantum phases. The findings presented in this chapter sit truly on the boundary of two very disparate fields, namely those of quantum magnetism and ferroelectrics. They directly relate to the novel and much-celebrated concept of multiferroic quantum criticality, constituting one of the first instances of a phenomena where both dielectric and magnetic degrees of freedom play non-trivial roles next to a quantum critical point. Theoretical effort is necessary now to understand the physics governing this exotic phenomenon.



## Chapter 6

# Unveiling the magnetism of the quantum antiferromagnet $\text{Nd}_3\text{BWO}_9$

The results discussed in this chapter can also be found in the following reference:  
*D. Flavián, J. Nagl, S. Hayashida, M. Yan, O. Zaharko, T. Fennell, D. Khalyavin, Z. Yan, S. Gvasaliya, and A. Zheludev*. Magnetic phase diagram of the breathing-kagome antiferromagnet  $\text{Nd}_3\text{BWO}_9$ . *Phys. Rev. B* **107**, 174406 (2023).

**Summary of contributions.** Single crystal samples of  $\text{Nd}_3\text{BWO}_9$  were first grown by S. Hayashida. Then the growth procedure was optimized by the author, who grew all of the samples discussed in this chapter, with the exception of the sample for the IN5 experiment, which had a large contribution from J. Nagl. Bulk measurements were measured by the author, with the support of M. Yan, J. Nagl and S. Hayashida. The experiment on EIGER was carried out by the author with S. Hayashida and M. Yan, with support from T. Fennell (PSI) and a strong input from J. Nagl in building a theoretical CEF model. Neutron scattering experiments on ZEBRA, HRPT (appendix), IN5 and D23 were carried out by the author and J. Nagl. The refinement of the magnetic structures was developed by the author with support from E. Ressouche (ILL).

### 6.1 Introduction

Strongly frustrated quantum antiferromagnets (AFM) are known to realize a panoply of magnetic states due to the delicate equilibrium between the magnetic interactions. In the presence of magnetic fields, the large ground state degeneracy is lifted in subtle and diverse ways, which leads to extremely rich phase diagrams. Realization of spin-density waves [159], magnetization plateaus [160, 161] commensurate-incommensurate transitions [162], and even more exotic order like spin nematicity [163, 164] is not rare, particularly in quasi-low-dimensional systems.

An archetypal model in 2D frustrated magnetism is the kagome lattice Heisenberg  $S = 1/2$  AFM (KHAF). The impossibility of satisfying all magnetic interactions in this lattice results in a macroscopic degeneracy of the ground state already at a classical level [165]. Turning to  $S = 1/2$  spins promotes the quantum fluctuations on the ground state giving rise to highly non-trivial phases [59]. Arguably, the most intriguing state is the hypothe-

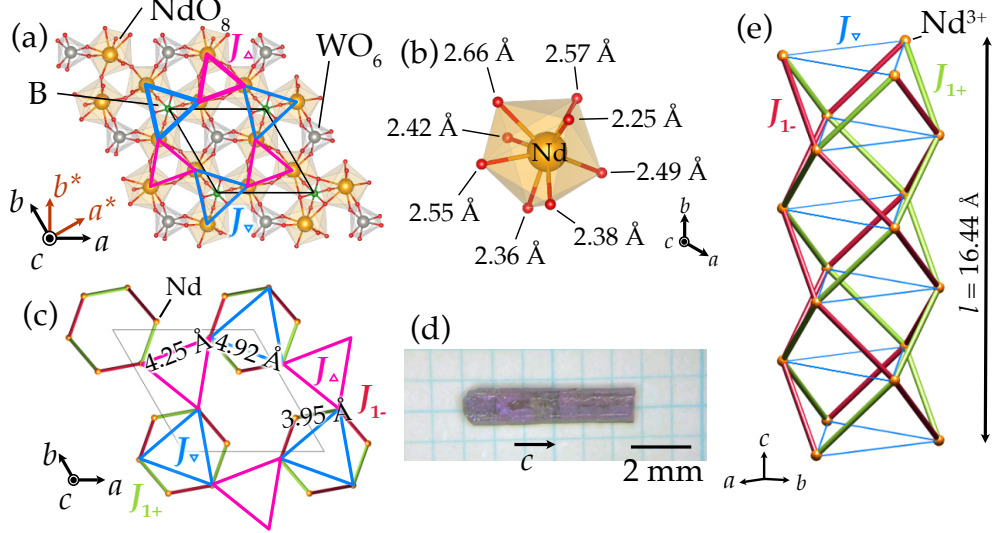


**Figure 6.1:** Crystal structure and superexchange topology in  $\text{Nd}_3\text{BWO}_9$ . (a) Schematic structure reflecting the purported kagome interaction in the crystallographic  $ab$  plane. Only atoms with  $0 \leq z \leq 0.5$  are shown here. There is an additional kagome plane in the unit cell, displaced by half-lattice parameter along the  $c$  crystallographic direction. (b) The environment of neodymium has very low symmetry, resulting in a  $C_1$  point group for the magnetic ion. Nd-O distances of the eight surrounding oxygen ions are indicated. (c) The shortest superexchange Nd-O-Nd bond links neodymium atoms in different kagome planes, forming isolated *spin tubes* along the  $c$  axis arranged in a triangular lattice. The kagome bonds are shown for reference along with bond distances. (d) A typical single-crystal sample of  $\text{Nd}_3\text{BWO}_9$ . Clear crystal facets appear perpendicular to the kagome  $ab$  plane. (e) Structure of a single spin-tube, showing the counterrotating nearest-neighbor interactions  $J_{1+}$  (green) and  $J_{1-}$  (red). Despite covering the same Nd-Nd distance, the different exchange pathways imply differing interactions, potentially of opposing sign.

sized Quantum Spin Liquid (QSL) [62] ground state. The prediction of fractionalization of quasiparticles in a 2D system triggered extensive effort from both theory and experimental perspectives [61, 64]. Nevertheless, the QSL phase remains experimentally elusive [68] as it constitutes a very fragile state. One of the main instabilities of the QSL states is the presence of terms in the Hamiltonian that lift the ground state degeneracy [166, 167]. The many different ways to lift this degeneracy have led to a flurry of magnetic structures [168–171]. However, occasionally deviations from a putative KHAF tend to stabilize QSL phases. In particular, the so called *breathing* anisotropy has been predicted to favor a resonance valence bond solid ground state for a wide range of coupling parameters [77, 172].

In this context, the recently discovered family  $R_3\text{BWO}_9$  of rare-earth antiferromagnets is an optimal platform for the search of spin-liquid candidates [173]. Here  $R^{3+}$  is a trivalent rare-earth element and the large difference in size of the constituent atoms prevents anti-site chemical disorder. All of the members of the family realize a breathing kagome lattice in their basal plane and show no sign of magnetic ordering down to 2 K. The strong spin-orbit coupling in combination with crystal electric field effects opens the possibility of realizing effective  $J_{\text{eff}} = 1/2$  magnetic moments.

Among all compounds in the family, the most promising is  $\text{Nd}_3\text{BWO}_9$ . A large Weiss

temperature [173] has been reported and the total angular momentum of  $\text{Nd}^{3+}$  ( $J = 9/2$ ) makes it a Kramers-doublet system. No magnetic long-range order has been found in previous studies down to 1.8 K. However, little is known so far about its magnetism.

We investigate the low temperature properties of single crystals of  $\text{Nd}_3\text{BWO}_9$  in order to uncover its magnetism. A detailed and methodical study of the material is laid out throughout this chapter. We revisit the crystal structure of  $\text{Nd}_3\text{BWO}_9$  to identify the relevant exchange couplings in a spin Hamiltonian. We find that crystal electric field lifts the single ion degeneracy, leaving an isolated doublet ground state with a strong Ising character. Using a combination of thermodynamic probes, we find a complex ground state with static magnetic long-range order below 0.3 K. Magnetizing the system with an external field results in fractional magnetization plateaux, regardless the orientation of the field. Finally, using neutron diffraction we determine the structure of the ordered phases. The magnetic structures along with bulk thermodynamic data suggests a three dimensional network of exchange interactions, with dominant quasi-1D couplings.

## 6.2 The crystal structure of $\text{Nd}_3\text{BWO}_9$

$\text{Nd}_3\text{BWO}_9$  crystallizes in a hexagonal structure with space group  $P6_3$  (No.173). The magnetic rare-earth  $\text{Nd}^{3+}$  ions occupy general  $6c$  Wyckoff positions in the unit cell. Thus, one finds six symmetry-related magnetic ions per unit cell.

Reports on the atomic positions in the unit cell show significant differences in the positions of the light ions [86, 173, 174]. All previous studies were performed using X-Ray diffraction, which is sensitive to the atomic electronic density. As a result, oxygen and boron are completely invisible to X-Rays in the presence of the much heavier tungsten and neodymium and their positions cannot be accurately refined. As will be discussed in detail below, the exact position of the oxygen atoms determines the nature of the CEF splitting, and with it all the low temperature physics of  $\text{Nd}_3\text{BWO}_9$ . An actual determination of  $\text{O}^{2-}$  coordinates is thus paramount.

We resort to neutron diffraction on powder samples to overcome this issue. The large scattering length of light atoms make neutron diffraction the ideal technique for this purpose. Data and results can be found in Appendix C. The model captures the position of oxygen and boron accurately and those positions are used in the following data analysis.

The purported breathing kagome structure is shown in Fig. 6.1(a). Unequal Nd-Nd distances and Nd-O-Nd angles result in inequivalent exchange parameters for neighboring corner-sharing triangles [173], resulting in breathing. This is represented by the exchange constants  $J_\Delta$  and  $J_\nabla$ , respectively.

However, the interaction between adjacent kagome planes cannot be neglected. Due to the short distances between kagome planes, the topology of the exchange interaction in  $\text{Nd}_3\text{BWO}_9$  is three dimensional. The bonds up to the four nearest neighbors is provided in Table 6.1, along with Nd-O-Nd angles for the relevant superexchange pathway. In fact, the shortest superexchange Nd-O-Nd bridges (nearest neighbors,  $J_1$ ) link rare-earth ions belonging to different kagome planes [Fig. 6.1(c)]. These couplings are arranged into isolated twisted 3-legged *spin tubes*, one-dimensional structures that extend perpendicular to the kagome planes [see Fig. 6.1(e)].

**Table 6.1:** Bond lengths and angles in  $\text{Nd}_3\text{BWO}_9$  involved in the possible superexchange pathways. The bonds are sorted by increasing Nd-Nd distance. Only angles for actual Nd-O-Nd bridges are given.

Bond	Bond distance ( $\text{\AA}$ ) $d_{\text{Nd-Nd}}$	Bond angles ( $^\circ$ )		
		Nd-O <sub>1</sub> -Nd	Nd-O <sub>2</sub> -Nd	Nd-O <sub>3</sub> -Nd
$J_{1+}$	3.94	103.4	-	114.6
$J_{1-}$	3.94	105.0	102.7	-
$J_{\Delta}$	4.25	-	115.8	-
$J_3$	4.38	-	124.9	-
$J_{\nabla}$	4.90	143.2	-	-

Superexchange interactions are strongly dependent on the angles of the covalent bonds between magnetic ions and intermediary ligands. Goodenough-Kanamori rules provides approximate rules to predict the sign of the interactions depending on this angle [175, 176]. Angles close to 180 degrees give antiferromagnetic couplings, whereas angles near 90 degrees usually result in ferromagnetic correlations. The case of the nearest neighbor interaction is rather particular. The couplings winding clockwise around the tubes ( $J_{1+}$ ) and those winding counterclockwise ( $J_{1-}$ ) stem from different superexchange pathways, even though the Nd-Nd distances are the same due to symmetry (Fig. 6.1.(e)). As a result, two different nearest neighbor couplings are possible. Even more so, the angles that we find are roughly between 100 and 110 degrees, which puts them in a marginal case where both ferromagnetism or antiferromagnetism could be realized, depending on the detailed geometry of the overlapping orbitals.

In case of having both nearest neighbors antiferromagnetic, the resulting spin tubes form a bipartite lattice (thus unfrustrated). The system becomes frustrated by the action of further neighbor couplings. On the other hand, if the nearest-neighbor couplings have opposite sign, the structure becomes frustrated on the first neighbor level, and becomes further frustrated by further neighbors.

Finally, the minimal symmetry environment around the  $\text{Nd}^{3+}$  ions result in a trivial  $C_1$  point symmetry. As a result, the degeneracy of the total angular momentum levels ( $J = 9/2$ ) is lifted completely into five Kramers doublets as is discussed in detail below.

### 6.3 The single-ion perspective

In rare-earth ions, a clear hierarchy in energy scales dictates the physics of the ground state. Spin-orbit coupling and Hund rules determine the angular momentum of electronic states in a free ion. A multiplet of constant total angular momentum  $J = 9/2$  builds the ground state of free  $\text{Nd}^{3+}$  ions. However, immersed in a crystal, the electrostatic interactions (which can be accurately treated as a small perturbation) split the degeneracy of this state, determining the character of low energy physics. The low-temperature magnetism of  $\text{Nd}_3\text{BWO}_9$  is given by the lowest energy CEF multiplet, in this case a doublet that allows a Hamiltonian description in terms of effective  $j_{\text{eff}} = 1/2$  degrees of freedom.

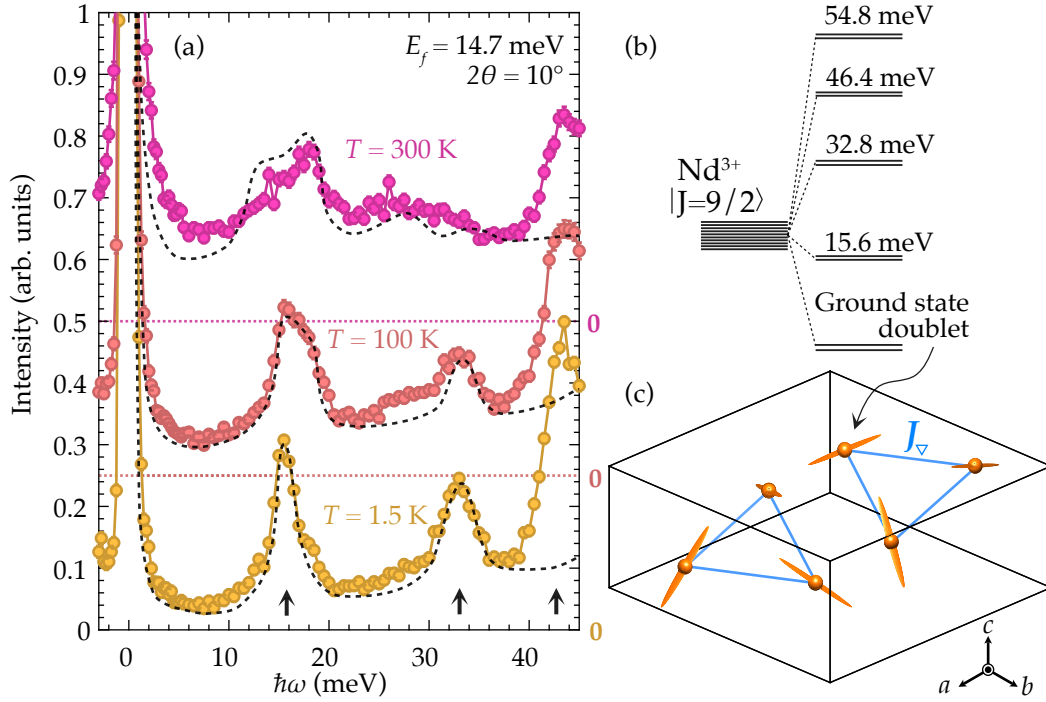


**Figure 6.2:** (a) Inelastic neutron scattering intensity at a constant scattering angle for three different temperatures. The final energy of  $E_f = 14.7$  meV was fixed and incident energy varied, fixing a  $10^\circ$  scattering angle. Possible CEF resonances are indicated by black arrows. An offset of 0.25 and 0.50 units was added for visibility, a dashed line indicates the reference zero for those data sets. (b) CEF spectrum as calculated from point-charge calculations. (c) Pictorial representation of the  $g$ -tensor at each individual  $\text{Nd}^{3+}$  position. The axes of the ellipsoids are proportional to the  $g_{ii}$  components in the diagonalized form.

## Measuring the CEF levels

The splitting of single-ion energy levels can be probed by means of inelastic neutron scattering. Within a given multiplet, the neutron scattering cross section is proportional to

$$\frac{d^2\sigma}{d\Omega dE'} \propto p_n |\langle \Gamma_m | J_\perp | \Gamma_n \rangle|^2 \delta(\hbar\omega + E_n - E_m) \quad (6.1)$$

where  $\Gamma_n$  represent the CEF eigenvectors within a total  $J$  multiplet. Thus, the transition probability is proportional to the matrix elements between different states within the multiplet, weighted by their thermally excited population,  $p_n$ .

The inelastic neutron scattering spectra for three different temperatures are shown in Fig. 6.2.(a). Data is measured in a triple-axis geometry at a fixed scattering angle  $2\theta$ . The analyzer is set to measure a final energy  $E_f = 14.7$  meV, while scanning in incident energy. Large intensity at zero-energy transfer corresponds to quasielastic scattering. Three resonances are identified at 15.9, 32.8, and 43.7 meV. The first two are ascribed to CEF induced levels, consistently to the CEF model that we develop below. The last one is consistent with high-order harmonic scattering in monochromator/analyzer and is likely spurious, thus its insensitivity to changes in temperature. Importantly, no resonance is

**Table 6.2:** Refined CEF Hamiltonian parameters in (6.3) for Nd<sub>3</sub>BWO<sub>9</sub>.

$B_l^m$ ( $\mu\text{eV}$ )	$l$		
	2	4	6
+6	-	-	-0.2
+5	-	-	-2.5
+4	-	-14.6	-0.9
+3	-	-45.9	-0.2
+2	372.1	-6.3	0.1
+1	-1051.9	-19.3	0.0
$m$ 0	134.9	6.1	0.0
-1	-8.8	38.5	-0.6
-2	166.5	3.1	0.3
-3	-	19.2	0.2
-4	-	-15.2	-0.6
-5	-	-	-1.4
-6	-	-	-0.6

found below 15.9 meV. Since the total angular momentum  $J = 9/2$  of the free Nd<sup>3+</sup> is expected to be fully split into five Kramers doublets, this shows that the low temperature physics of Nd<sub>3</sub>BWO<sub>9</sub> can indeed be described in terms of the lowest-laying doublet, well separated from the excited states above  $\Delta = 15.9$  meV  $\approx$  180 K. The highest energy doublet lies just above the upper range of the measurement, as is shown in the CEF model that is detailed below. In order to gain some insight on the nature of the ground state doublet, we use a point-charge approach to model the level splitting.

### CEF Hamiltonian from electrostatics

As already discussed, the strongest energy scale (besides electron-electron Coulomb interaction) in rare-earth ions is that of spin-orbit coupling, which fixes the total angular momentum of the valence electron shell,  $J$ . Combined with the fact that  $4f$  electrons lie well inside the atomic electronic cloud, the effect of an external crystal electric field on trivalent rare-earths can be treated as a small perturbation to the lowest energy  $J$  multiplet. The effect of such CEF is to split the degeneracy, by mixing the  $|J, J^z\rangle$  states and creating energy gaps of the order of tens of meV. From symmetry considerations one can determine the remaining degeneracy of the resulting states. For example, the presence of time reversal symmetry in a Kramers doublet ion, as Nd<sup>3+</sup>, implies that each state is at least doubly degenerate. The  $C_1$  local symmetry in Nd<sub>3</sub>BWO<sub>9</sub> means no further constraint, and the multiplet is split in 5 doublets. However, we may go beyond and calculate exactly the energy splittings and the actual wave functions under the CEF influence. The strong localization of  $4f$  electrons allows us to assume that the charges that create the CEF sit well outside of the space that the magnetic ion occupies. Thus we can define a region in space empty of free charges (besides of course that of the magnetic ion) where the CEF electric potential obeys Laplace's equation and can thus be expanded in a series

of spherical harmonics:

$$V(\mathbf{r}) = \sum_{l,m} A_l^m Y_{lm}(\hat{\mathbf{r}}) = \sum_{l=0,2,4,6} \sum_{m=-l}^l A_l^m Y_{lm}(\mathbf{r}) \quad (6.2)$$

The second equation stems from the  $4f$  nature of the electrons. As such the angular momentum is  $l = 3$ , which restricts the spherical harmonic expansion up to  $l = 6$  terms. In addition, due to orthogonality relations of the spherical harmonics, also all terms with odd  $l$  vanish. We therefore describe the crystal electric field with a small set of parameters. Finally, by virtue of the Wigner-Eckart theorem, within a given total- $J$  multiplet we may replace the  $x$ ,  $y$  and  $z$  coordinates by the angular momentum operators  $\hat{J}_x$ ,  $\hat{J}_y$  and  $\hat{J}_z$  and arrive to the crystal field Hamiltonian for rare-earth ions

$$\mathcal{H}_{CEF} = \sum_{l=0,2,4,6} \sum_{m=-l}^l B_l^m O_l^m(\hat{\mathbf{J}}) \quad (6.3)$$

Here, the so called *Stevens operators* ( $O_l^m$ ) are polynomials in  $\hat{J}_x$ ,  $\hat{J}_y$  and  $\hat{J}_z$ , which are tabulated and can be found e. g. in [177, 178]. Local point symmetry around the magnetic ion further restricts the possible operators that enter the sum. However, in the case of  $\text{Nd}_3\text{BWO}_9$  the exceedingly low  $C_1$  symmetry implies that all 27 parameters are allowed.

In short, the electrostatic potential around the magnetic ion fixes the energy of the angular momentum states within a  $J$  multiplet. Thus, a precise understanding of the crystal structure should allow for a direct calculation of (6.3). This was explicitly shown in [178] and is the seed for the software `PyCRYSTALFIELD` [179]. An approximate CEF Hamiltonian can be calculated from electron Coulomb repulsion by treating the surrounding ligands within a *point-charge* model. Under that approximation, the coefficients in (6.3) are expressed as

$$B_l^m = -\gamma_{nm} q C_{nm} \langle r^n \rangle \theta_n \quad (6.4)$$

where  $\gamma_{nm}$  is calculated from the electric potential environment expressed as tesseral harmonics,  $q$  is the magnetic ion charge,  $C_{nm}$  are the normalization factors in the spherical harmonics,  $\langle r^n \rangle$  is the average radial value of the electron wavefunction (as given e.g. in [180]) and  $\theta_n$  are some ion-dependent multiplicative factors. The package `PyCRYSTALFIELD` takes a crystal structure and (respecting the ion's point symmetry) calculates all the  $B_l^m$  coefficients.

This approach, though powerful, is not free of pitfalls. One strong limitation is precisely the assumption of localized point charges. In real systems, ligand ions possess valence  $p$  orbitals. This results in an anisotropic charge distribution, deviating from the idealized point charge [181]. One way to alleviate such effect is to allow for charge transfer between point charges, and fit effective charges for each ion individually.

Knowing the system eigenstates and their energies, the neutron excitation CEF spectrum can be calculated, and is precisely displayed against the experimental data in Fig. 6.2.(a), where the instrumental resolution is calculated using the library `RESLIB`. As discussed above, the effective charges of the  $\text{O}^{2-}$  ligands are optimized to match the experimental results. In addition, we may calculate bulk properties, like magnetic susceptibility, from this single-ion perspective and compare them with measurements. These will

**Table 6.3:** Nd<sup>3+</sup> wavefunctions of the groundstate CEF doublet in the global frame.

Global frame		
	$ \psi_+\rangle$	$ \psi_-\rangle$
$ +9/2\rangle$	0.351	0.005 - 0.012i
$ +7/2\rangle$	0.515 - 0.200i	-0.002 + 0.092i
$ +5/2\rangle$	0.471 - 0.197i	0.091 - 0.006i
$ +3/2\rangle$	0.401 + 0.064i	-0.133 + 0.052i
$ +1/2\rangle$	0.219 + 0.126i	0.203 - 0.056i
$ -1/2\rangle$	0.203 + 0.056i	-0.219 + 0.126i
$ -3/2\rangle$	0.133 + 0.052i	0.401 - 0.064i
$ -5/2\rangle$	0.091 + 0.006i	-0.471 - 0.197i
$ -7/2\rangle$	0.002 + 0.092i	0.515 + 0.200i
$ -9/2\rangle$	0.005 + 0.012i	-0.351

likely be good approximations as long as the thermal energy scale is much larger than the exchange couplings, on the order of a few kelvin as estimated from the Curie-Weiss temperature. These results are shown below in Fig. 6.3.

All in all, the optimized CEF parameters are summarized in Table 6.2. Calculations are performed in a global  $xyz$  frame with  $x$  and  $z$  along the crystallographic axes  $\mathbf{a}$  and  $\mathbf{c}$  respectively, with  $y$  perpendicular to both and parallel to  $\mathbf{b}^*$ . Diagonalization of the CEF Hamiltonian provides the energy spectrum shown in Fig. 6.2 and the resulting eigenstates for the lowest energy doublet are given in Table 6.3. Due to the low symmetry, all  $B_m^l$ s carry weight and the lowest doublet eigenfunctions are a combination of all possible free-ion states  $|J = 9/2, J^z\rangle$ . From these, one can additionally determine the local g-tensor for each ion:

$$g = \begin{pmatrix} 4.53 & 0.52 & -2.48 \\ 0.52 & 0.17 & -0.41 \\ -2.48 & -0.41 & 2.03 \end{pmatrix} \quad (6.5)$$

It has a complicated form, again due to low symmetry. As it is customary in e.g. spin-ice materials, the effect of a CEF is to define some *local* anisotropy axes. We can determine those by diagonalizing  $g$  as follows

$$g = \begin{pmatrix} 0.52 & 0 & 0 \\ 0 & 0.08 & 0 \\ 0 & 0 & 6.13 \end{pmatrix} \quad (6.6)$$

We can determine the reference frame where the g-tensor is diagonal and refer it to the global one by a series of rotations. Using the Euler-angle  $zyz$  convention from this, the resulting rotations are described by the three angles (10.1°, 52.2°, 5.3°) for Nd<sub>1</sub>. This not only provides a local coordinate frame which simplifies the understanding of CEF, but crucially reveals the dominant Ising-like anisotropy for the single ion. The Ising single-ion character is further revealed if one rewrites  $|\psi_+\rangle$  and  $|\psi_-\rangle$  in the local coordinate frame. The resulting wave functions are given in 6.4, which show that to a very good approximation, locally we may write  $|\psi_+\rangle \sim |+9/2\rangle$  and  $|\psi_-\rangle \sim |-9/2\rangle$ .

**Table 6.4:**  $\text{Nd}^{3+}$  wave functions of the ground state CEF doublet in the local frame, as defined by the local anisotropy axes obtained from the g-tensor. In the local frame it is clear that the lowest-energy doublet can be seen as an Ising spin with  $|\psi_+\rangle \sim | +9/2\rangle$  and  $|\psi_-\rangle \sim | -9/2\rangle$ .

Local frame		
	$ \psi_+\rangle$	$ \psi_-\rangle$
$  +9/2\rangle$	0.959	-0.001
$  +7/2\rangle$	$0.020 + 0.033i$	$0.035 + 0.003i$
$  +5/2\rangle$	$0.108 - 0.133i$	$0.054 - 0.011i$
$  +3/2\rangle$	$0.076 - 0.172i$	$0.011 - 0.007i$
$  +1/2\rangle$	$0.020 + 0.031i$	$0.041 - 0.080i$
$  -1/2\rangle$	$0.041 + 0.080i$	$-0.020 + 0.031i$
$  -3/2\rangle$	$-0.011 - 0.007i$	$0.076 + 0.172i$
$  -5/2\rangle$	$0.054 + 0.011i$	$-0.108 + 0.133i$
$  -7/2\rangle$	$-0.035 + 0.003i$	$0.020 - 0.033i$
$  -9/2\rangle$	-0.001	-0.959

This strong anisotropy strongly confines the magnetic moments to one direction in space. The rotational symmetry of the crystal structure relates the different anisotropy axes for the six  $\text{Nd}^{3+}$  ions in the unit cell. The local anisotropy axes in the unit cell are depicted in Fig. 6.2.(c).

One must finally bear in mind that, even if the obtained results come from a very accurately known crystal structure, the current fit is strongly underconstrained. While the qualitative findings are robust and  $\text{Nd}_3\text{BWO}_9$  can be seen as an Ising system, the quantitative predictions from point-charge calculations may not be as accurate. One inherent limitation of the model is the very assumption of point charges. Charge distribution in real materials does show a certain spacial distribution that the model cannot account for. In addition, hybridization and chemical binding further modify the effective charges around the magnetic ions. This is precisely the reason why experimentally fittable data are key in providing a correct CEF description. However, in low symmetry scenarios like it is the case here, the lack of independent data gives large freedom in the choice of  $B_l^m$  parameters, with similar physical predictions.

## 6.4 Bulk measurements

We carry out a thorough study of bulk properties in  $\text{Nd}_3\text{BWO}_9$  to gain insight on its magnetic ground state. In particular, we report magnetic susceptibility, specific heat, magnetocaloric effect, magnetization and magnetic torque.

### Magnetic susceptibility

Figure 6.3 shows inverse susceptibility measurements for probing fields applied along the crystallographic directions  $\mathbf{a}^*$ ,  $\mathbf{b}$  and  $\mathbf{c}$ . Down to the lowest accessible temperature of 1.8 K, these data show no sign of magnetic ordering.

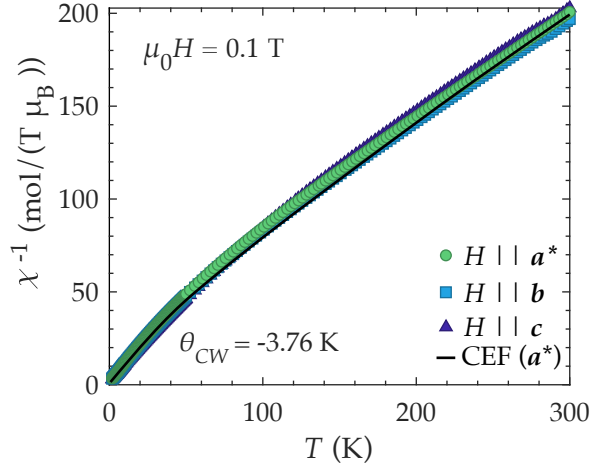


**Figure 6.3:** Inverse magnetic susceptibility on single crystals. Data show measurements for three field orientations. A small probing field of 0.1 T was used for all measurements. Curie-Weiss model is in good agreement with data below 60 K, with the Weiss temperatures and effective moment parameters given in Table 6.5. A black line represents the prediction from CEF model in (6.3) for  $\mathbf{H} \parallel \mathbf{a}^*$ . Fits for the other axes are nearly overlapped and are now shown for clarity.

**Table 6.5:** Fitting parameters from the Curie-Weiss model for data shown in Fig. 6.3.

	$20 \text{ K} \leq T \leq 60 \text{ K}$	
	$\theta_{CW} \text{ (K)}$	$\mu_{eff} \text{ (}\mu_B\text{)}$
$\mathbf{H} \parallel \mathbf{a}^*$	-3.78	2.94
$\mathbf{H} \parallel \mathbf{b}$	-3.82	2.90
$\mathbf{H} \parallel \mathbf{c}$	-3.68	2.91

A fit of the experimental data to a Curie-Weiss model for data above 130 K shows good agreement, with a large, negative Weiss temperature. However, the obtained values are an effect of the population of the different crystal electric field (CEF) levels. Such an analysis is heavily affected by the partial population of excited multiplets and lead to an overestimation of exchange parameters and exchange couplings.

Below 130 K a clear deviation from the high temperature fit is observed. This is consistent with the existence of a first crystal electric field level at 15.9 meV, signaling the total depletion of the population of the first excited state (Fig. 6.2). An additional fit to a Curie-Weiss law for a temperature range far enough from the CEF resonance has been performed. The results for temperatures in the range between 20 K and 60 K are summarized in Table 6.5, as well as the effective magnetic moments extracted from the Curie constants as  $C = N_A \mu_0 \mu_{eff}^2 / (3k_B)$ . Our results are consistent with those reported in [173] on polycrystal samples.

The resulting Weiss temperatures are much reduced compared to the high temperature fit [173]. However, they still reflect a predominant antiferromagnetic interaction

in Nd<sub>3</sub>BWO<sub>9</sub>. The effective magnetic moments are as well reduced with respect to the expectation for a free Nd<sup>3+</sup> ion:  $\mu_{eff} = g_J \sqrt{J(J+1)} \mu_B = 3.6 \mu_B$ , also as a result of the crystal field.

Susceptibility data show little dependence on the direction of the magnetic field, which suggests that the resulting magnetic anisotropy may remain small. However, from single-ion properties we understand that the system is in fact very anisotropic, with an almost perfect Ising-like character for Nd<sup>3+</sup> ions. The apparent isotropy is the result of rotational symmetry as will be discussed later in detail. In fact, the simple single-ion model reproduces quite well the temperature dependence of magnetic susceptibility over the whole measurement range (Fig. 6.3).

## Specific heat

Specific heat as a function of temperature and magnetic field is used to unveil the magnetic phase diagram of Nd<sub>3</sub>BWO<sub>9</sub> at ultra-low temperatures. Data obtained at zero field are shown in Fig. 6.4. Nd<sub>3</sub>BWO<sub>9</sub> shows an upturn in specific heat below 4 K with two clearly distinct features [Fig. 6.4.(a)]. Around 1 K, a hump in specific heat suggests the onset of short-range magnetic correlations [182]. At  $T_N = 300$  mK we found a sharp lambda anomaly representing the transition into magnetic long range order. Below  $T_N$  the specific heat signal remains large down to the lowest accessible temperatures in our setup, likely due to nuclear specific heat from the rare-earth ions. In order to understand exactly the nature of the magnetic specific heat, we have examined the different contributions and subtracted them from the measured total specific heat.

To estimate the phononic contribution, we synthesized the non-magnetic isostructural material La<sub>3</sub>BWO<sub>9</sub> and measured its specific heat in the same range of temperatures. This is shown in Fig. 6.4.(a) and represents the lattice contribution,  $C_L$ , in Fig. 6.4.(b).

An accurate estimation of the nuclear contribution to specific heat is usually much more complicated, as a variety of effects has to be considered. These include dipole and quadrupolar splitting, or hyperfine coupling between nuclei and electrons (which can be quite significant in magnetically ordered materials). Neodymium has two isotopes with nonzero dipolar and quadrupolar momenta, out of its 7 stable isotopes. In rare earth magnets, the leading term in the nuclear hamiltonian is the hyperfine coupling. Considering a nuclear species with total spin  $I$  and also quadrupolar splitting the resulting hamiltonian is:

$$H_{hf} = a' I_z + P \left[ I_z^2 - \frac{1}{3} I(I+1) \right] \quad (6.7)$$

where  $a' = a \langle J_z \rangle$ ,  $a$  is the contact hyperfine term and  $P$  the electric quadrupole constant. Values for  $a$  and  $P$  can be found in the literature and are observed to be roughly independent of the nuclear environment. The quadrupolar moment in Nd is small and can be neglected. However, the value of  $a'$  depends on  $\langle J_z \rangle$ , which in the case of Nd-based magnets is strongly modified from its maximum value due to CEF effects. Following the reasoning in Ref. [183], we assume all the nuclei couple equally to the electron density and the value of  $A_{Hyp}$  is approximated as that in Nd metal [48, 184]. The nuclear

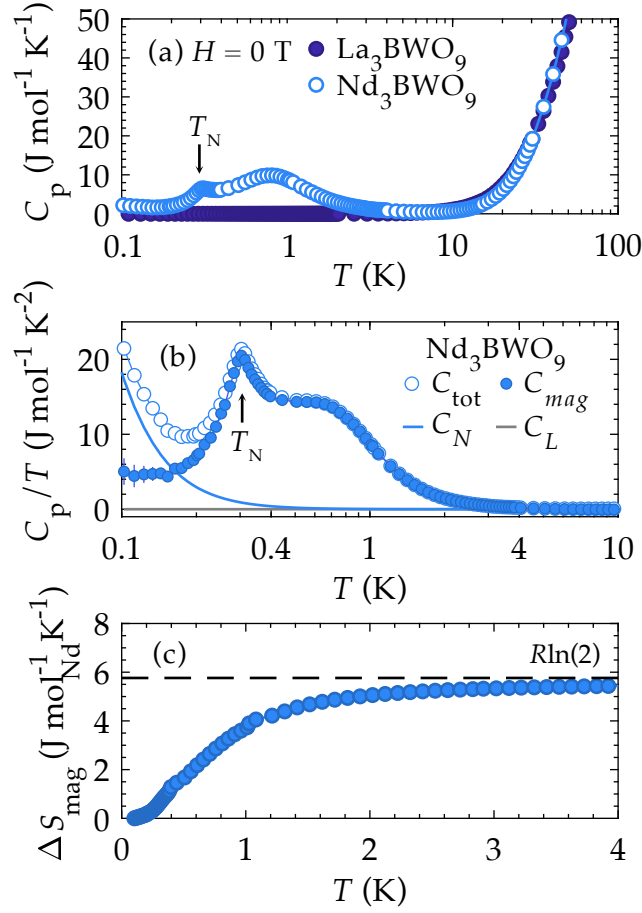


**Figure 6.4:** (a) Total specific heat at zero magnetic field for  $\text{Nd}_3\text{BWO}_9$  and the nonmagnetic isostructural compound  $\text{La}_3\text{BWO}_9$ .  $\text{Nd}_3\text{BWO}_9$  shows a substantial magnetic contribution to specific heat below 3 K. (b) Total specific heat (open circles) and magnetic specific heat (filled circles) after subtraction of lattice and nuclear degrees of freedom. The estimations of lattice ( $C_L$ ) and nuclear ( $C_N$ ) contribution are estimated as discussed in the text. A lambda anomaly can be found at  $T_N = 0.30$  K, signaling the onset of long-range magnetic order. (c) The magnetic entropy per  $\text{Nd}^{3+}$  ion saturates above 3 K. A dashed line represents the expected value for a two-level system at infinite temperature.

contribution to heat capacity is calculated as a multi-gap Schottky anomaly:

$$C_{\text{hf},\alpha} = \frac{R}{T^2} \frac{\sum_{i,j} (\Delta_i^2 - \Delta_i \Delta_j) \exp(-(\Delta_i + \Delta_j)/T)}{\sum_{i,j} \exp(-(\Delta_i + \Delta_j)/T)} \quad (6.8)$$

where  $k_B \Delta_i = i a'_\alpha$ , with  $i = -7/2, \dots, 7/2$  (both  $^{143}\text{Nd}$  and  $^{145}\text{Nd}$  are  $I = 7/2$ ) and  $\alpha$  runs over the different isotopes (the index  $\alpha$  is omitted in (6.8) for clarity). To calculate the total nuclear specific heat the contribution from each isotope is weighted depending on its isotopical abundance. This model with no free parameters is in good agreement with the lowest temperature data, as shown in Fig. 6.4.(b).

Having modeled the nuclear specific heat, the magnetic specific heat can be extracted by subtraction and is displayed in Fig. 6.4.(b). The magnetic specific heat was subsequently integrated to obtain the temperature dependence of magnetic entropy, depicted in Fig. 6.4.(c). The high temperature trend of this quantity approaches the value of  $R \ln(2)$ , the expected value of a two-level system.

The contact hyperfine interaction creates a large effective magnetic field at the nucleus position. It can be estimated as  $\mu H_{eff} = a'I/k_B$ , where  $\mu$  is the nuclear magnetic moment of  $^{143}\text{Nd}$  and  $^{145}\text{Nd}$ . In  $\text{Nd}_3\text{BWO}_9$ , this effective field is as large as 330 T, more than two orders of magnitude larger than the applied fields in this study. Consequently, the nuclear contribution to specific heat is insensitive to the externally magnetic field. A quantitative determination of this effect under magnetic fields is beyond the scope our study.

The observed nuclear anomaly in specific heat is, as expected, insensitive to the external field up to the pseudospin saturation. Yet, above the saturation field, the nuclear contribution to specific heat vanishes, as observed in the data sets at 150 mK in Fig. 6.5. This apparent contradiction can be explained analyzing the coupling of different degrees of freedom and how one probes them in a relaxation heat capacity experiment. An external source of heat may excite the electronic and lattice degrees of freedom. However, nuclear degrees of freedom may only be excited through their coupling to the former, and not directly by the heat source [185, 186]. Therefore, our ability to probe nuclear specific heat depends on the existence of magnetic fluctuations at temperatures comparable with the nuclear gaps. At sufficiently large magnetic fields, the magnon Zeeman gap that opens at saturation is large compared to the thermal energy in the system. Thus, above 2 T magnetic fluctuations are strongly suppressed and nuclei can no longer be probed. Remarkably, the reduction of the nuclear signal against the increasing field (an artifact as nuclear degrees of freedom get decoupled from the magnetic ones) gives most likely rise to the kink-like feature indicated with an asterisk in Fig. 6.5.(b).

The evolution of the specific heat of  $\text{Nd}_3\text{BWO}_9$  under magnetic fields is shown in Fig. 6.5 for fields along two different crystallographic directions. The total heat capacity is displayed here, without subtraction of lattice or nuclear degrees of freedom. Typical-field scans show a number of anomalies that are consistent with the existence of three different phases with static magnetic order at low temperatures.

Three distinct features can be observed for  $\mathbf{H} \parallel \mathbf{a}^*$  at the lowest temperature, at 0.45, 0.62 and 1.05 T and are marked with triangles in Fig. 6.5.(a). These features are rather broad in field, particularly at saturation. Such broad features are reminiscent of low-dimensional crossover behavior, rather than true phase transitions. However, the existence of thermodynamic transitions has been confirmed by neutron diffraction (as discussed below). The lowest field anomaly moves to zero field as temperature is increased. The two higher field anomalies merge at 0.25 K, the highest temperature of the ordered phase. Though the specific heat anomalies in Fig. 6.5.(a) are too broad for a precise estimation of the upper critical field, this can be deduced from magnetocaloric effect measurements (see below).

For fields orthogonal to the hexagonal plane ( $\mathbf{H} \parallel \mathbf{c}$ ) at the lowest temperature one finds anomalies at 0.5 T, 0.8 T, and a sharper one at 0.95 T. [Fig. 6.5.(b)] Notably, in this configuration the different anomalies appear narrower than for  $\mathbf{H} \parallel \mathbf{a}^*$ , especially at the saturation field. The first two anomalies move apart as the temperature is increased, while

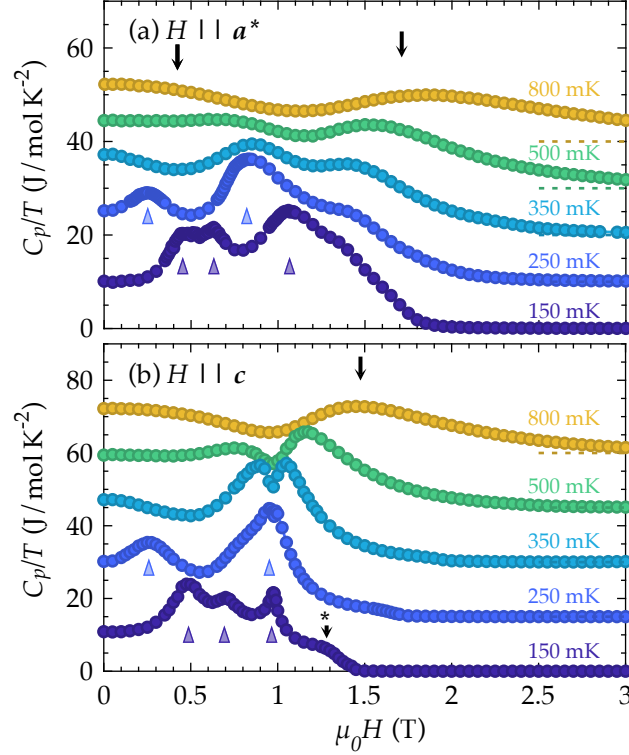


**Figure 6.5:** Typical field scans of specific heat measured at constant temperature in  $\text{Nd}_3\text{BWO}_9$  for (a)  $\mathbf{H} \parallel \mathbf{c}$  and (b)  $\mathbf{H} \parallel \mathbf{a}^*$ . An offset of 10 and 15  $\text{J/molK}^2$  is added for visibility between the scans for (a) and (b), respectively. Solid filled triangles show features associated with the phase transitions discussed in the main text. Black arrows signal the existence of broad double-hump features, described in the text. An asterisk shows a feature above the saturation transition which is argued to stem from nuclear specific heat.

the higher field anomaly barely shifts in position up to 0.2 K. The low field anomaly shifts towards zero field and disappears as  $T_N$  is reached. The two high-field anomalies merge at  $T = 0.2$  K. From the high field anomaly we extract an estimate of the saturation field of  $\mu_0 H_c = 0.975(3)$  T.

An estimation of the demagnetization field at saturation gives a value corresponding to roughly 1.2% of the saturation field. This value is based on the total magnetization at saturation and assuming an spherical sample. The small value suggests that demagnetizing fields have very little effect on the properties of the material close to saturation.

Finally, double-hump features can be observed above 0.3 K for both magnetic field configurations. These are significant up to the highest measured temperatures and particularly prominent around the saturation field (black arrows in Fig. 6.5). For  $\mathbf{H} \parallel \mathbf{c}$  the amplitude of these modulations is larger than in  $\mathbf{H} \parallel \mathbf{a}^*$ . Such features are often associated with a low-dimensional crossover from the zero field disordered phase to the fully polarized state without the occurrence of a phase transition [98, 128, 187, 188]. They can be understood in terms of models of hard-core bosons and are usually associated with quantum critical behaviour in one dimensional magnets [189, 190]. They have been observed in several quasi-1D antiferromagnets [187, 188], which hint towards the relevance

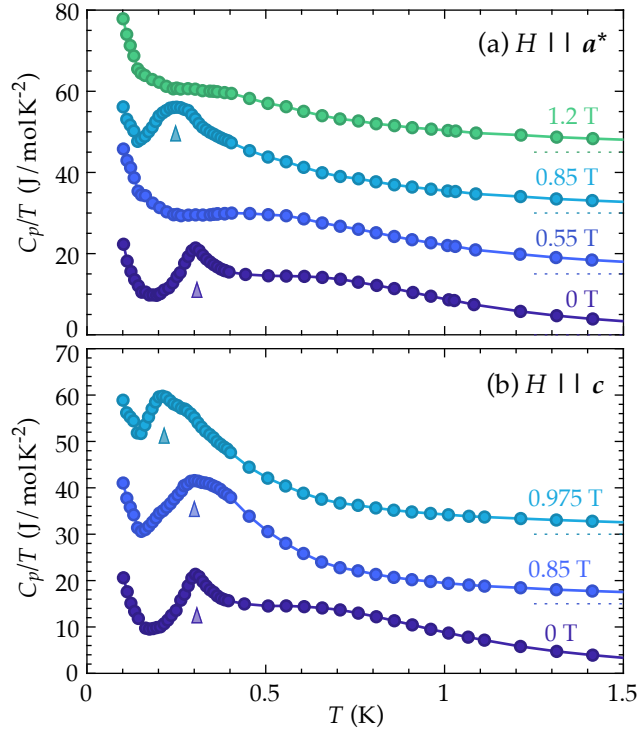


**Figure 6.6:** Typical temperature scans of specific heat for different fixed values of magnetic field applied along (a)  $\mathbf{H} \parallel \mathbf{c}$  and (b)  $\mathbf{H} \parallel \mathbf{a}^*$ . An offset of  $15 \text{ J/mol/K}^2$  has been added for visibility. Solid filled triangles show features associated with the phase transitions discussed in the main text.

of the tube couplings.

### Magnetocaloric effect

Magnetocaloric effect (MCE) measurements in  $\text{Nd}_3\text{BWO}_9$  provide key information on the nature of the various phase transitions found with other techniques [79, 191, 192]. Changes in the temperature of the magnetic sample have been measured while changing the magnetic field, and keeping the puck (reservoir) temperature constant. Representative temperature profiles are shown in Fig. 6.7.(a,b). Several crossings can be observed for both configurations. The observed anomalies are too broad to assign exactly a transition point. Due to the proximity of the thermodynamic transitions in the phase diagram, features corresponding to both transitions merge and overlap. In our measurements the field is swept slow enough as to ensure equilibrium conditions.

Data measured with  $\mathbf{H} \parallel \mathbf{a}^*$  show mostly symmetric features around the crossing points. Particularly, this suggests that the measured phase transitions are of second order. In contrast, the low temperature profiles for  $\mathbf{H} \parallel \mathbf{c}$  show two distinct behaviors. At  $0.6 \text{ T}$  one finds a roughly symmetric feature, suggesting again a second order phase transition. This is different at  $0.975 \text{ T}$ , where a very asymmetric feature appears, pointing to a first order or discontinuous transition.

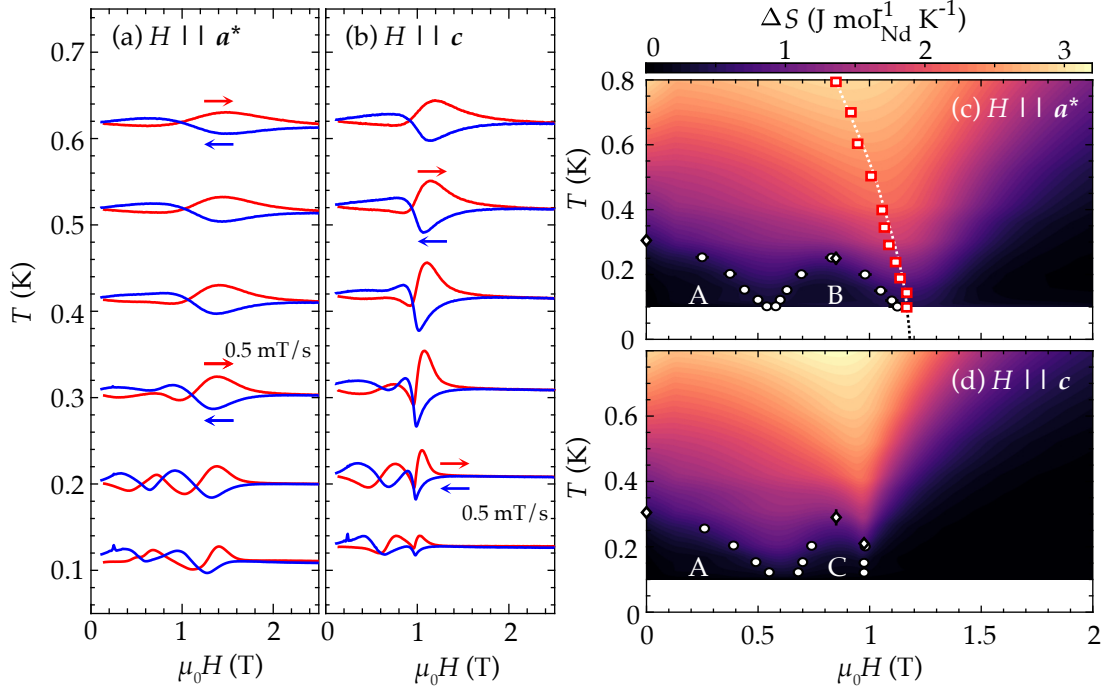


**Figure 6.7:** (a,b) Plots of the magnetocaloric effect in Nd<sub>3</sub>BWO<sub>9</sub> for different base temperatures and fields applied along (a)  $\mathbf{H} \parallel \mathbf{a}^*$  and (b)  $\mathbf{H} \parallel \mathbf{c}$ . For all the scans, red (blue) color represents data measured while driving the magnetic field up (down). A ramping rate of 0.5 mT/s was used throughout all the measurements. Small prominent features (especially at low fields) are spurious and the result of an unstable platform. (c,d) Entropy maps in false color for two magnetic field orientations. In false color plots, the change in entropy extracted from magnetocaloric data. Filled circles (diamonds) denote phase anomalies associated with phase transitions from specific-heat field (temperature) scans for (c)  $\mathbf{H} \parallel \mathbf{a}^*$  and (d)  $\mathbf{H} \parallel \mathbf{c}$ . In (c) red squares show the maxima of entropy at the measured temperatures. A white dashed line is a power-law fit to the data showing the best estimate for the upper critical field. The value of entropy is shown relative to that at 150 mK and 2.5 T ( $S_0$ , taken as reference).

No anomalies above the saturation field for  $\mathbf{H} \parallel \mathbf{c}$  are observed. The features observed in the fully polarized phase with specific, marked with an asterisk in Fig. 6.5.(b), leave no trace in the MCE data in the same configuration, which supports their origin in nuclear magnetism.

The MCE technique is based on the change of entropy in a magnetic system as it is driven through a phase transition, crossover, level crossing, etc. Consequently, one can retrieve the change in entropy in a system from the change in temperature against magnetic field [79]. Under equilibrium conditions, the entropy may be obtained as:

$$\Delta S = S(H) - S_0 = - \int \kappa \frac{T - T_{bath}}{T} dt \quad (6.9)$$

where  $\kappa$  is the thermal conductivity of the thermal link in the calorimeter,  $T$  is the sample temperature, and  $T_{bath}$  is the thermal bath temperature. Integration of the data in Fig. 6.7.(a,b) gives rise to the entropy maps displayed in Fig. 6.7.(c,d). The data above 0.2 K are a good picture of the entropy stored in the magnetic subsystem. However, for

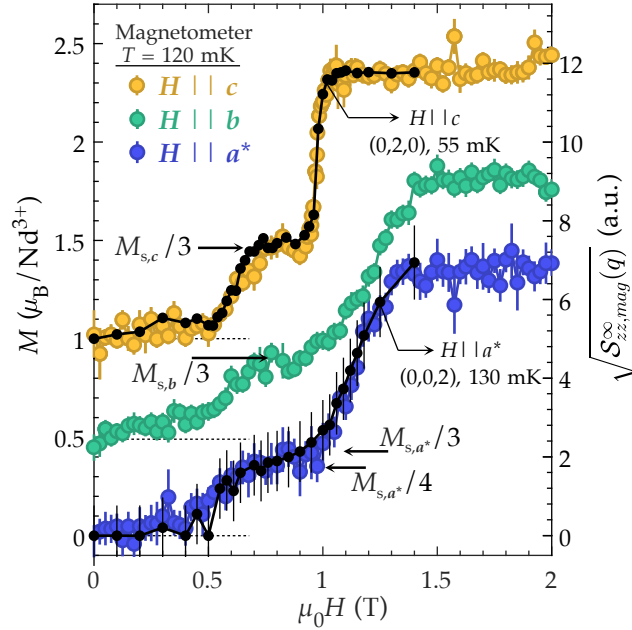


**Figure 6.8:** Magnetization per  $\text{Nd}^{3+}$  ion measured at 120 mK in  $\text{Nd}_3\text{BWO}_9$  for magnetic fields along the crystallographic directions  $a^*$ ,  $b$ , and  $c$  from bulk measurements (left axis). Magnetization extracted from neutron diffraction intensity of nuclear reflections is superimposed to the corresponding bulk data. Plotted is the rescaled square root of the static, magnetic structure factor  $\mathcal{S}_{z,z}^\infty(\mathbf{q})$  (right axis). The measured reflections ( $\mathbf{Q}$ ) are indicated in the figure. Two of the data sets have been offset vertically by 0.5 and 1.0 units to improve visibility (a dashed line indicates their respective zero). The magnetization value at 1/3 of saturation is indicated for each individual data set by an arrow next to the plateau state. For  $\mathbf{H} \parallel \mathbf{a}^*$  the fractional value 1/4 is also shown.

temperatures below 0.15 K imperfect equilibrium conditions prevent a reliable estimation of entropy. A strong accumulation of entropy is observed at the saturation field for both field configurations. The position of the peaks in entropy match the estimated position of the critical fields from specific heat. For  $\mathbf{H} \parallel \mathbf{a}^*$ , the maxima in entropy at different temperatures were used to obtain an accurate estimate of the upper critical field. A fit to the data provides  $H_{c,a^*} = 1.187(13)$  T. This value is consistent with the various probes used in this study.

### Magnetization and magnetic torque

The evolution of magnetization under a magnetic field at low temperature provides insight on the type of order in  $\text{Nd}_3\text{BWO}_9$ . Strikingly, a fractional magnetization plateau is observed for all measured configurations, as displayed in Fig. 6.8. The value of magnetization is consistent with a fractional  $M/M_s = m = 1/3$  plateau and spans a range of fields of 0.2 - 0.3 T for all orientations. In addition, the zero field phase shows zero magnetization for all applied fields, which suggests the realization of a gapped phase at  $T = 0$ . Magnetization data for inequivalent directions in the hexagonal plane show very similar behavior, but differ from the results perpendicular to the plane.

For  $\mathbf{H} \parallel \mathbf{a}^*$  and  $\mathbf{H} \parallel \mathbf{b}$  the zero magnetization phase extends up to 0.4 T. Above 0.5 T the system transitions into the fractional magnetization plateau state up to a marked limit at 1 T. The transition into the fully saturated phase is gradual between 1 T and 1.3 T. The fractional value of magnetization in this case is also consistent with a  $m = 1/4$ -plateau. While this value is less common in frustrated magnets, the neutron diffraction data that are presented below suggest this can be the case. Both  $m = 1/3$  and  $m = 1/4$  values are shown in Fig. 6.8, showing that our magnetization data cannot single out one of the cases.

In contrast, much sharper features are found when fields  $\mathbf{H} \parallel \mathbf{c}$  are applied. A non-magnetizable phase appears up to 0.5 T, above which the system jumps rapidly into the plateau state at 0.65 T. The observation of a  $1/3$  plateau is very solid in this geometry, other fractional values do not match our data. The plateau terminates in a first-order jump to saturation around 1 T. Notably, despite the presence of a first-order transition, our measurements did not show signatures of hysteresis across the saturation transition for  $\mathbf{H} \parallel \mathbf{c}$ .

Saturation fields extracted from magnetization data are consistent with those found in the specific heat data. The values for saturation magnetization show little anisotropy, finding  $1.34(6)\mu_B$ ,  $1.31(3)\mu_B$ , and  $1.35(4)\mu_B$  per magnetic ion for configurations  $\mathbf{a}^*$ ,  $\mathbf{b}$ , and  $\mathbf{c}$  respectively. It suggests a nearly isotropic g-tensor in the bulk. This in fact the case, despite the perfect Ising anisotropy of the local g-tensor. In fact, averaging (6.6) over the six  $\text{Nd}^{3+}$  positions provides an effective g-tensor

$$g = \begin{pmatrix} 2.35 & 0 & 0 \\ 0 & 2.35 & 0 \\ 0 & 0 & 2.03 \end{pmatrix} \quad (6.10)$$

This effective tensor is almost isotropic showing that the bulk isotropy comes from the rotational symmetry between the highly anisotropic local moments. In either case, the saturation magnetization is short of the total moment of Nd. A smaller magnetic moment at saturation compared to the effective moment extracted from susceptibility measurement is common in Nd-based rare-earth frustrated magnets [193–196]. In these systems, it is often understood in terms of strong Ising anisotropy as a consequence of the CEF scheme, as it is our case in  $\text{Nd}_3\text{BWO}_9$ . However, in some cases this reduction in fact reflects persistent fluctuations of the ordered moment [194]. The strong frustration in  $\text{Nd}_3\text{BWO}_9$  suggest fluctuations can have a strong influence.

Finally, low-temperature magnetization in the fully saturated pseudospin phase shows no increase up to the highest probed fields. The increase of magnetization may be a rough estimator of the eigenstate admixing due to anisotropies (via Van-Vleck terms). No appreciable change in magnetization is observed up to 2 T, indicating the total magnetization in the restricted pseudospin subspace is likely to be an approximately good quantum number. This reflects again our single-ion predictions, the eigenstate mixing is minimal and the moments are almost pure in a local basis.

Magnetic torque is arguably the most sensitive technique to magnetic phase transitions. Raw data are presented as the change in the measured capacitance  $\Delta C = C(H) - C(H = 0 \text{ T})$  as a function of magnetic field for each temperature (Fig. 6.9). The torque data show strong differences between the measurements in the basal plane and perpendicular to it, but the obtained results are very similar for both measurements within the

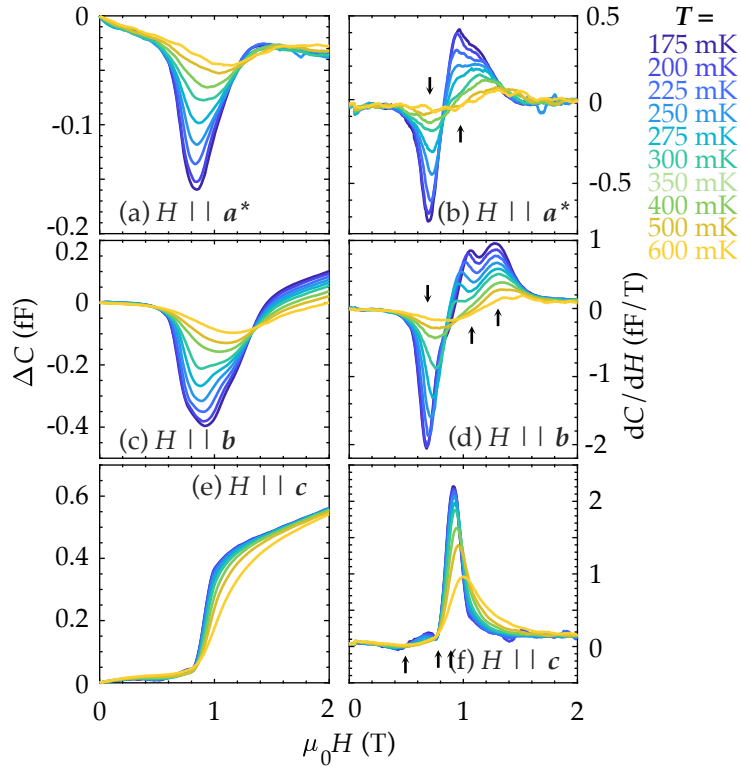


**Figure 6.9:** Magnetic torque ( $\Delta C$ ) and its field derivative measured at constant temperatures against magnetic field, for three field orientations: (a,b)  $\mathbf{a}^*$ , (c,d)  $\mathbf{b}$ , and (d,e)  $\mathbf{c}$ . For all data sets, a reference value of capacitance at zero field has been chosen and subtracted. Black arrows indicate features that may be identified with phase transitions.

plane. The raw data show some structure, but not sharp features as is customary in such measurements. Phase transitions are best captured in the first derivative of the raw data [Fig. 6.9.(b), 6.9.(d), and 6.9.(f)].

Field derivative data show features that correspond with transitions observed in the other techniques reported in this study. Direct comparison with the other data sets is necessary to pinpoint what anomalies represent real phase transitions. These features are indicated with arrows in the field derivative data [Fig. 6.9.(b), 6.9.(d), and 6.9.(f)]. For  $\mathbf{H} \parallel \mathbf{a}^*$  two distinct anomalies can be observed in the scan at 175 mK, at 0.68 T and at 0.99 T. These correspond to the lower and upper boundaries of the plateau phase. Data for  $\mathbf{H} \parallel \mathbf{b}$  show three anomalies at 0.68 T, 1.02 T and 1.28 T. The lower fields correspond again to the boundaries of the plateau phase. Notably, these two anomalies come together as the temperature is increased and disappear above 300 mK. The higher field anomaly, which is broader and less sharp, corresponds to the crossover into the fully saturated state. Finally, fields applied along the  $\mathbf{c}$  direction reveal a completely different structure. Three anomalies can be identified at 0.48 T, 0.71 T, and 0.95 T. The associated transitions in this case are the boundaries of the plateau for the high field features and the transition from the low field phase to paramagnet for the low field anomaly. The low field features, though weak, fade away as the transition temperature is overcome. The

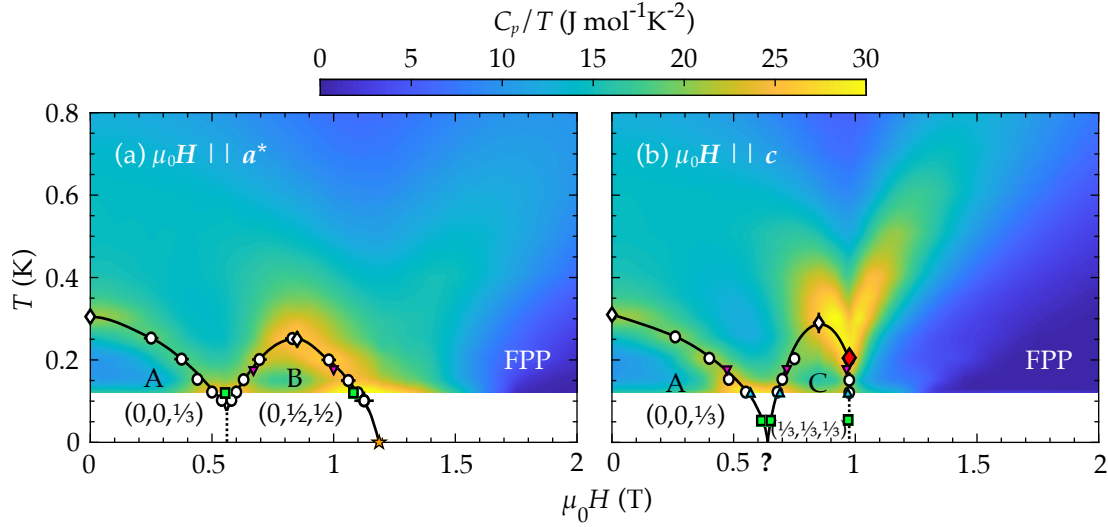


**Figure 6.10:** Magnetic phase diagram of Nd<sub>3</sub>BWO<sub>9</sub> in a magnetic field applied along the principal directions: (a)  $a^*$  and (b)  $c$ . The background depicts false color maps of  $C_p(H, T)$ , with a shared color scale. Symbols: white circles and diamonds represent transitions obtained from field and temperature scans of specific heat, respectively. Green squares represent the phase boundaries extracted from neutron diffraction data in Fig. 6.11. Upward-facing blue triangles show transitions extracted from bulk magnetization, downward facing pink triangles transitions from magnetic torque. A red diamond denotes the estimated position of the tricritical point for  $H \parallel c$ . An orange star shows the upper critical field estimated in Fig. 6.7. Solid and dashed lines are a guide to the eye, representing second and first order transitions, respectively. The different phases are labelled as: A, B, C and Fully Polarized Pseudospin (FPP). The ordered phases show their corresponding magnetic propagation vector, as discussed in the text.

high field anomaly remains up to the highest temperatures representing the crossover of the system into the fully polarized pseudospin.

### Magnetic phase diagram

We construct the phase diagram of Nd<sub>3</sub>BWO<sub>9</sub> using a combination of all bulk techniques. Using specific heat as false-color we display the low-temperature order in Fig. 6.10 for two orientations of the magnetic field. All outlined techniques are used to identify several regions of magnetic order. The system reveals complex behaviour, with two different domes of long-range order observed for each configuration. The zero field phase, A, is robust against fields applied along any direction, after which a plateau appears. For the remaining part, we will determine the magnetic order that is established in those phases, identifying quite complex magnetic structures.

## 6.5 Magnetic diffraction and magnetic structures

Magnetic ordering breaks time reversal symmetry in a magnetic system, but may as well break other spacial symmetries. One prime example is that of a simple Neel antiferromagnet, where the positive exchange couplings contribute to an enlargement of the magnetic

unit cells. As a result, understanding the type of order parameters and the structures that appear in the different phases can provide crucial information on the microscopic interaction taking place in a magnetic system. Particularly in frustrated systems, magnetic structures can be rather complex, consequence of the fine interplay of interactions.

Any magnetic structure can be described withing the propagation vector formalism. In this framework, the structure is characterized by how it changes from one unit cell to another, which is encoded in the *propagation vectors*,  $\mathbf{k}_i$ . The structure is defined by average magnetic moment on each ion, given by in the case of  $n_k$  propagation vectors by

$$\langle\langle \mathbf{m}_{\mathbf{l},j} \rangle\rangle = \sum_{i=1}^{n_k} \mathbf{m}_{i,j} \exp(i\mathbf{k}_i \cdot \mathbf{l}) + c.c. \quad (6.11)$$

where  $j = 1, \dots, n_c$  are the different magnetic ions in the unit cell,  $\mathbf{l}$  is the label of a crystallographic unit cell, and  $\mathbf{m}_{i,j}$  the complex amplitude vectors for all magnetic ions in the unit cell. Thus, a magnetic structure is a sum contributions of amplitudes at each propagation vector. For each  $k_i$  the corresponding contribution to the structure is specified by a  $(3 \times n_c)$  dimensional vector of the form

$$\vec{m}_i = (\mathbf{m}_{i,1}, \dots, \mathbf{m}_{i,n_c}) \quad (6.12)$$

specifying the magnetic components of each magnetic ion withing the unit cell. This vector must adhere to certain symmetry restrictions in the proximity to a second-order transition.

A propagation vector breaks certain symmetries of the crystal space group  $G$ . We define the little group of  $\mathbf{k}$ ,  $G_{\mathbf{k}}$ , as those remaining symmetries of  $G$  that leave the propagation vector invariant. In this point, the Landau theory of second-order phase transitions gives a key result. The order parameter of the ordered phase, as a result of a continuous phase transition, must belong to one of the irreducible representation of the symmetry group of the ordered structure [6]. In the case of magnetic structures this implies that the lowest energy  $\vec{m}_i$  will belong to one of the irreps of the little group  $G_{\mathbf{k}}$  [197]. Decomposing  $G_{\mathbf{k}}$  allows us to find a (generally small) set of basis vectors  $\psi_{\Gamma_k, j}$  that relate the components of  $\vec{m}_i$  withing an irrep  $\Gamma_k$  as

$$\vec{m} = \sum_{j=1}^{n_{\Gamma_k}} C_j \psi_{\Gamma_k, j} \quad (6.13)$$

where  $C_j$  are coefficients and the propagation vector coefficient ( $i$ ) is dropped for clarity. Nowadays, standard software can carry out the symmetry decomposition and find those basis vectors, in this work we used BASIREPS [198]. Performing such an analysis for each propagation vector is not only necessary to respect the crystal symmetries, but greatly simplifies the problem of finding a magnetic structure from.

We employ single-crystal neutron diffraction to investigate the magnetic structures realized in the low temperature ordered phases of  $\text{Nd}_3\text{BWO}_9$ . We start by finding the propagation vectors of all phases using a combination of techniques. The evolution of order parameters with field and temperature is in perfect agreement with the thermodynamic data. Results from a time-of-flight spectrometer reveal the presence of short-range order above true magnetic ordering, and the existence of multi- $\mathbf{k}$  structures. Using large collections of magnetic reflections we succeed in finding magnetic structures of phases A and C.

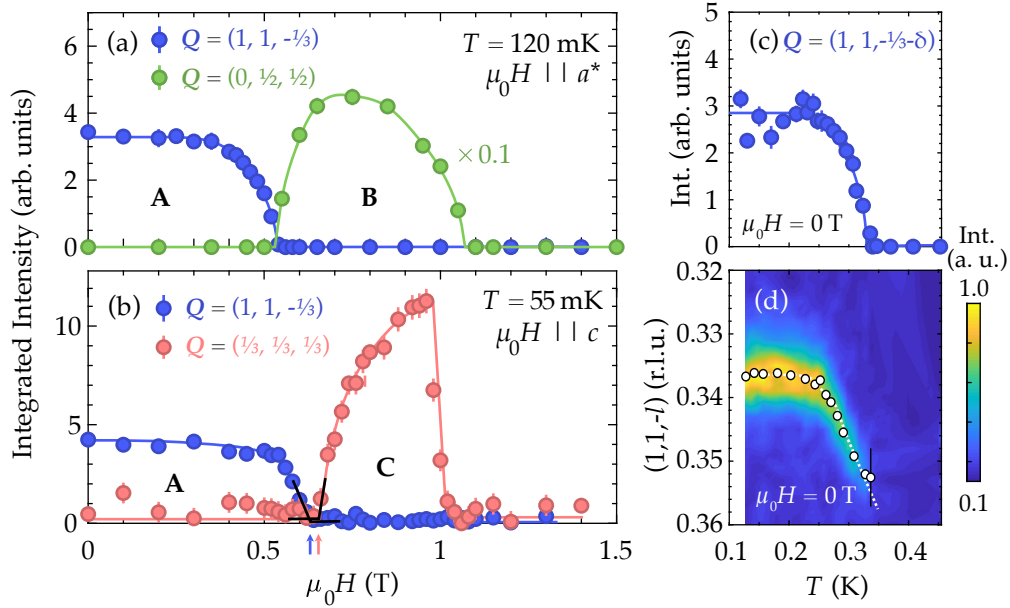


**Figure 6.11:** Results from single crystal magnetic neutron diffraction. (a,b) Field dependence of the integrated neutron intensity at the magnetic propagation vectors for: (a)  $\mathbf{H} \parallel \mathbf{a}^*$  (ZEBRA, PSI) and (b)  $\mathbf{H} \parallel \mathbf{c}$  (WISH, ISIS). Note that in (a) the intensity of the  $(0,1/2,1/2)$  reflection has been rescaled by  $\times 0.1$ . In (b) the limits of the ordered phases are highlighted and shown with arrows. (c) Evolution of the integrated intensity of the reflection  $(1,1,-1/3)$  with temperature at zero magnetic field. (d) Incommensuration of the propagation vector at zero field against temperature, shown as a shift in the peak position of the  $(1,1,l)$  reflection.

## Probing magnetic order

Magnetic order can be characterized by the decomposition of the magnetization density in Fourier components  $\mathbf{M}(\mathbf{q})$ . The propagation vectors,  $\mathbf{q}$ , can be identified in neutron diffraction as a result of the modulation of the magnetization density, giving rise to magnetic Bragg peaks.

A series of experiments on a 40 mg single crystal unveil the order of the magnetic phases. Zero field data show a commensurate phase with propagation vector  $\mathbf{k} = (0, 0, 1/3)$ . Fig. 6.11.(a) and Fig. 6.11.(b) show that magnetic reflection  $(1,1,-1/3)$  is present throughout phase A for both field orientations. The phase is consistent with commensurate order, which leads to the appearance of a magnetic supercell, as shown in Fig. 6.1.(d). Integrated intensity of reflection  $(1,1,-1/3)$  drops at the intermediate transition field, above which a different type of order is found depending on the direction of the magnetic field. For phase B ( $\mathbf{H} \parallel \mathbf{a}^*$ ) we found magnetic reflections  $(0,1/2,1/2)$  and  $(1/2,0,1/2)$ . These reflections vanish at fields slightly below saturation. Finally, phase C ( $\mathbf{H} \parallel \mathbf{c}$ ) has been found to realize order with propagation vector  $k_+ = (1/3, 1/3, 1/3)$ . Magnetic reflection  $k_- = (1/3, 1/3, -1/3)$ , which is inequivalent to the former, has also been found. Fig. 6.11.(b) shows an abrupt drop in the intensity of reflection  $(1/3, 1/3, 1/3)$  at a field of 0.99 T, consistent with a first order transition to saturation.

Note that phase B is characterized by a quadrupling of the unit cell in the  $ab$  plane as

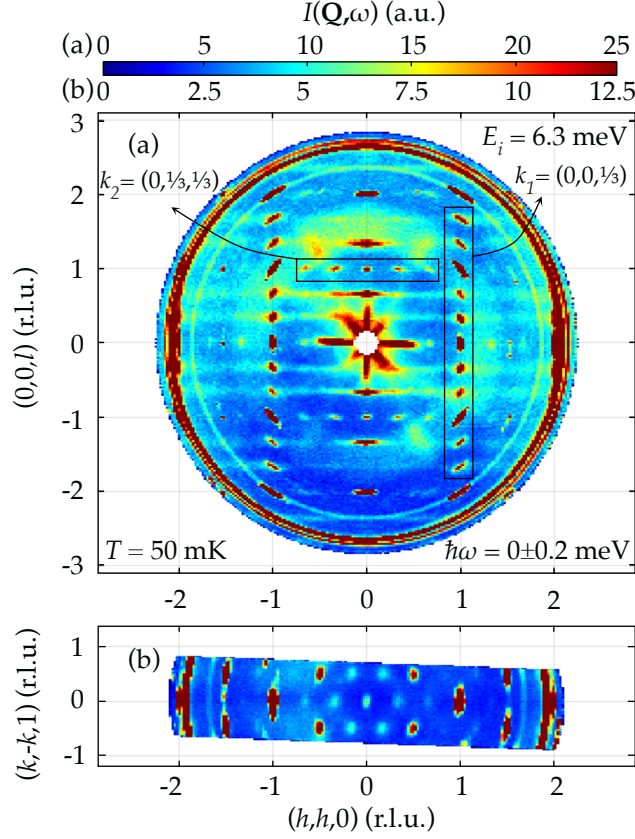


**Figure 6.12:** Neutron diffraction signal of  $\text{Nd}_3\text{BWO}_9$  with an incident wavelength of  $3.6 \text{ \AA}$  at  $50 \text{ mK}$  from the time-of-flight machine IN5 (ILL, France). (a)  $hhl$  plane. (b)  $(hh0)-(k,-k,1)$  plane. Magnetic reflections corresponding to propagation vectors  $\mathbf{k}_1 = (0, 0, 1/3)$  and  $\mathbf{k}_2 = (1/3, 1/3, 0)$  can be identified and are highlighted in the figure. Data are integrated in energy, in a range corresponding to the resolution  $\hbar\omega = 0 \pm 0.2 \text{ meV}$ . The color scale is not shared between (a) and (b) to highlight the weak Bragg peaks, both scales are given next to the colorscale.

a result of its propagation vector  $\mathbf{k} = (0, 1/2, 1/2)$ . For this reason, the existence of a  $m = 1/4$  fractional magnetization plateau can be more natural than a  $m = 1/3$  fraction. This is indeed also suggested by [199] where the authors extend magnetization measurements to lower temperatures.

An external magnetic field induces a ferromagnetic component in every lattice site that gives rise to the bulk magnetization. This produces extra scattering proportional to the square of the induced magnetic momentum at the position of each nuclear peak. Fig. 6.8 shows the uniform magnetization density extracted from two nuclear reflections: (020) for  $\mathbf{H} \parallel \mathbf{a}^*$  and (200) for  $\mathbf{H} \parallel \mathbf{c}$ . We selected reflections where nuclear contribution is minimal while a measurable magnetic intensity can be observed. The zero-field integrated intensity is subtracted from the data in a field to obtain the corresponding magnetic scattering. Longitudinal magnetization is then plotted as the square root of magnetic intensity. The agreement with bulk measurements is remarkable and further highlights the existence of magnetization plateaus regardless of field orientation.

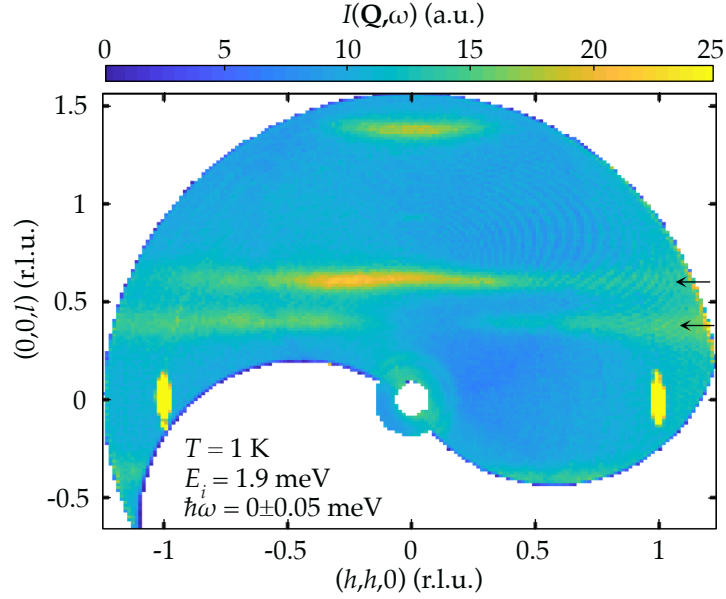


**Figure 6.13:** Elastic scattering in  $\text{Nd}_3\text{BWO}_9$  at 0.5 K in the  $(hhl)$  plane. Nuclear reflections are found at  $(-1,-1,0)$  and  $(1,1,0)$ . Structured diffuse scattering is observed at  $l = 0.41$  r.l.u. and  $l = 0.59$  r.l.u. (black arrows) for an extended range of  $h$  as a result of incommensurate short-range correlations in the spin-tubes. The intensity is modulated along  $h$ , which shows the relevance of in-plane interactions.

Zero field neutron diffraction reveals an incommensurate state between the low temperature ordered phase and the paramagnetic phase. The onset of incommensurate magnetic order appears around 0.34 K at the wavevector  $\mathbf{k}_{1\delta} = (0, 0, 1/3 + \delta)$ . Temperature dependence of the intensity around the  $(1,1,l)$  reflection in Fig. 6.11.(d), where the peak position is superimposed, shows this incommensuration. Reduction of the temperature leads to a change in the incommensurate propagation vector roughly linearly with temperature. At 0.26 K the propagation vector locks into the commensurate  $\mathbf{k}_1 = (0, 0, 1/3)$ , as observed for the low temperature structure. The robustness of this evolution to commensuration has been verified for several additional magnetic reflections.

Single crystal diffraction on a much larger sample reveals the presence of an additional propagation vector in the zero-field phase (Fig. 6.12). These results come from roughly 340 coaligned crystals (amounting to 1.6 g) measured at a time-of-flight spectrometer. Magnetic reflections corresponding to a propagation vector  $k_2 = (1/3, 1/3, 0)$  appear at a temperature of 50 mK as is evidenced in Fig. 6.12. The intensity of the Bragg peaks associated to this propagation vector show a much smaller intensity than those for  $k_1$ . The resulting magnetic structure at zero field is a multi-k one. This extra propagation vector likely arises at the locking-transition that is observed at 0.26 K and cants the spin to resolve the frustration from in-plane triangular couplings.

In addition to the extra propagation vector, Fig. 6.12 reveals that  $\text{Nd}^{3+}$  moments are not fully ordered in the ground state. Very significant magnetic diffuse scattering is observed for all non-integer  $l = n/3$  positions, with  $n$  integer. This diffuse scattering extends perpendicular to the  $c$  direction creating Bragg plates (two dimensional equiva-

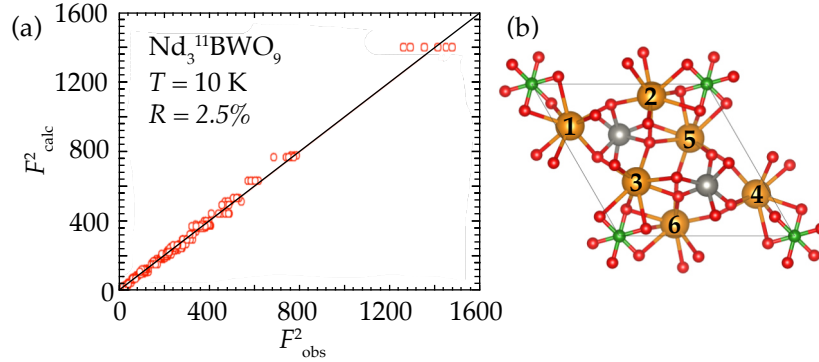


**Figure 6.14:** (a)  $|F_o|^2$  vs.  $|F_c|^2$  plot for the nuclear refinement of  $Nd_3^{11}BWO_9$ . The model includes a total of 21 parameters as described in the text, including a merohedral twin  $(k, h, -l)$ . A solid line is a guide to the eye where  $|F_c|^2 = |F_o|^2$ . (b) Crystal structure obtained from the nuclear refinement, showing the convention of label used for the magnetic ions in the text.

lent to Bragg rods). The existence of this extra scattering shows that part of the magnetic moment fluctuates strongly, even deep in the long range ordered phase. Notably, no extra scattering associated to the  $k_2$  propagation vector is observed, which suggest the fluctuations are strongly bound within the magnetic spin-tubes.

Additional measurements of magnetic diffuse scattering at high temperature evidence the onset of magnetic correlations well above the transition temperature. In Fig. 6.13 we show the scattering signal measured at 500 mK, a temperature almost twice  $T_N$ . The diffuse scattering is very similar to that found in the low temperature phase, though this time no magnetic Bragg peaks are found. The presence of this scattering evidences that the spin-tubes develop short-range 1-D order (there is no long-range order in 1D at finite temperature) at a much higher temperature, and correlation between tubes gradually sets in as the temperature is lowered, finally giving away true 3D order at  $T_N$ . In-plane interactions are likely responsible for the modulation in intensities along the disks. Finally, position of the disks of diffuse scattering is shifted away from  $l = n/3$  positions to  $l = n/3 \pm \delta$ . This shows that the incommensuration shown in Fig. 6.11 survives to higher temperatures and stems from the short-range correlations within the tubes. A value of  $\delta \sim 0.08$  (in relative lattice units, r.l.u.) is measured (disks at  $l = 0.41$  and  $l = 0.59$ ) at 500 mK.

## Nuclear structure

In order to determine the magnetic structures that  $Nd_3BWO_9$  realizes in the long-range ordered phases, a refinement of the nuclear structure of the material is in order. We collected 318 nuclear reflections at a temperature of 10 K on a single crystal sample of 40 mg in a lifting-counter diffractometer. Scattering intensity is integrated as omega-scans through the expected peak positions.

As stated above,  $Nd_3BWO_9$  crystallizes in the  $P6_3$  space group, which is polar. This means that there is no center of inversion in the crystal structure with two important consequences. (i) The  $z$  component of each nuclear positions is determined only relative to other nuclei. There is freedom for an arbitrary shift in  $z$  of all nuclei in the unit cell. In

**Table 6.6:** Results of fits of magnetic components in zero field for the different irreps in Eq. 6.14.

Irrep	$R_F$	Irrep	$R_F$
$\Gamma_{DT1}$	38 %	$\Gamma_{DT4}$	36 %
$\Gamma_{DT2}$	17 %	$\Gamma_{DT5}$	34 %
$\Gamma_{DT3}$	31 %	$\Gamma_{DT6}$	25 %

this case, we fix the Boron to lie at position (0 0 0). (ii) There is the possibility to generate crystal twins by merohedry. In the case of  $\text{Nd}_3\text{BWO}_9$ , every crystal is twinned, where each twin is the image by inversion of the other. In practice, that means that for each  $(hkl)$  contribution (both nuclear and magnetic) there is another  $(kh\bar{l})$  contribution from the twin. A reasonable fit has to include the presence of both in the form of several scale factors.

A refinement of the nuclear structure performed with 2 scale factors (one for each twin), 13 nuclear positions (B and W are in a high symmetry position, and we fix B z-component), and 6 isotropic thermal displacements, a total 21 parameters. The goodness of the refinement is reflected in a very low  $R_F$  factor of 2.54 % and graphically in Fig. 6.15. Interestingly, the ratio of twins is 1.99(2) to 1, in agreement with 2 to 1. This ratio is used through the rest of the analysis of the magnetic components.

### Zero-field magnetic structure

The magnetic structure in the zero field phase of  $\text{Nd}_3\text{BWO}_9$  is a multi-k structure with propagation vectors  $k_1 = (0, 0, 1/3)$  and  $k_2 = (1/3, 1/3, 0)$ . Integrated intensity of magnetic reflections belonging to both propagation vectors show that the magnetic moment has a predominant contribution from  $k_1$ , being the contributions from  $k_2$  a small correction. In the following, we determine the contribution from  $k_1$  to the magnetic structure, which is a good approximation of the actual structure.

Decomposition of the magnetic representation of the magnetic little group with propagation vector  $k = (0, 0, 1/3)$  is as follows:

$$\Gamma_{DT} = 3\Gamma_{DT1}(1) \oplus 3\Gamma_{DT2}(1) \oplus 3\Gamma_{DT3}(1) \oplus 3\Gamma_{DT4}(1) \oplus 3\Gamma_{DT5}(1) \oplus 3\Gamma_{DT6}(1) \quad (6.14)$$

There are 6 one-dimensional irreducible representations, that enter 3 times each in the full representation. A explicit description of the associated basis vectors can be found in Appendix D. The  $\text{Nd}^{3+}$  ions are sitting in a general Wyckoff position, therefore existing 6 magnetic moments per unit cell. All of the irreps allow full freedom to the direction and size of the moment of the ion sitting in position 1 (according to our reference) and fix the moment in the remaining by symmetry. In order to determine which irrep is realized in the magnetic structure, we perform a fit of the magnetic intensities within each irrep. The fit is based on positions extracted from nuclear refinement and includes three free parameters, the Cartesian coordinates of the magnetic moment in position 1:  $(u, v, w)_1$ . The refinement is based on 248 individual magnetic reflections. The results of such a fit for each irrep are summarized in Table 6.6. The best results are obtained in the  $\Gamma_{DT2}$  irrep, with a final agreement of  $R_F = 17\%$ . The corresponding basis vectors for each atom in the crystallographic unit cell are indicated in Table 6.7.

**Table 6.7:** Basis vectors of irrep  $\Gamma_{DT2}$  that gives the best agreement to the neutron reflections associated with  $k = (0, 0, 1/3)$ , as described in the text.

IR	BV	Atom	BV components		
			$m_{\parallel a}$	$m_{\parallel b}$	$m_{\parallel c}$
	$\psi_4$	1	1	0	0
		2	$-\frac{1}{2} + i\frac{\sqrt{3}}{2}$	0	0
		3	0	$-\frac{1}{2} - i\frac{\sqrt{3}}{2}$	0
		4	0	1	0
		5	$\frac{1}{2} - i\frac{\sqrt{3}}{2}$	$\frac{1}{2} - i\frac{\sqrt{3}}{2}$	0
		6	$\frac{1}{2} + i\frac{\sqrt{3}}{2}$	$\frac{1}{2} + i\frac{\sqrt{3}}{2}$	0
$\Gamma_{DT2}$	$\psi_5$	1	0	1	0
		2	0	$-\frac{1}{2} + i\frac{\sqrt{3}}{2}$	0
		3	$\frac{1}{2} + i\frac{\sqrt{3}}{2}$	$\frac{1}{2} + i\frac{\sqrt{3}}{2}$	0
		4	0	-1	-1
		5	$-\frac{1}{2} + i\frac{\sqrt{3}}{2}$	0	0
		6	$-\frac{1}{2} - i\frac{\sqrt{3}}{2}$	0	0
	$\psi_6$	1	0	0	1
		2	0	0	$\frac{1}{2} - i\frac{\sqrt{3}}{2}$
		3	0	0	$-\frac{1}{2} - i\frac{\sqrt{3}}{2}$
		4	0	0	-1
		5	0	0	$-\frac{1}{2} + i\frac{\sqrt{3}}{2}$
		6	0	0	$\frac{1}{2} + i\frac{\sqrt{3}}{2}$

The refined magnetic structure is shown in Fig. 6.15. The ordered moment is 1.54 Bohr's magnetons, showing that a large part of the magnetic moment is fluctuating. The refined magnetic moment of  $\text{Nd}_1$  is  $m_1 = (0.99(5), 0.66(5), 0.97(4))\mu_B$  in the global XYZ frame. The corresponding spherical coordinates  $\theta = 58.3^\circ$  and  $\phi = 31.6^\circ$ , are very close to those given by single-ion g-tensor principal axes in (6.6).

A *spin-density wave* propagating along the tube direction appears, creating a modulation of the amplitude magnetic moments. The modulation gives rise to a *UddUdd* or *DuuDuu* structure along the direction of propagation for each atom in the unit cell, where *U* represents a magnetic moment with its *w* component positive (pointing 'up' along *c*) and *D*, one with negative *w* (pointing 'down' along *c*). In addition lower case represents a moment amplitude half of that of the upper case ( $\mu = 0.77\mu_B$  vs.  $\mu = 1.54\mu_B$ ), giving rise to a compensated structure with zero net moment. Notably, the SDW structure is a result of the symmetry alone, all irreps of this space group with propagation vector  $k_1 = (0, 0, 1/3)$  result in a modulation of the magnetic moment along the *c* direction.

Strikingly, the resulting magnetic structure is in perfect agreement with expectations from single-ion physics. On the one hand, without constraints on the direction of the magnetic moment, the fitted moment direction for each  $\text{Nd}^{3+}$  ion matches the directions

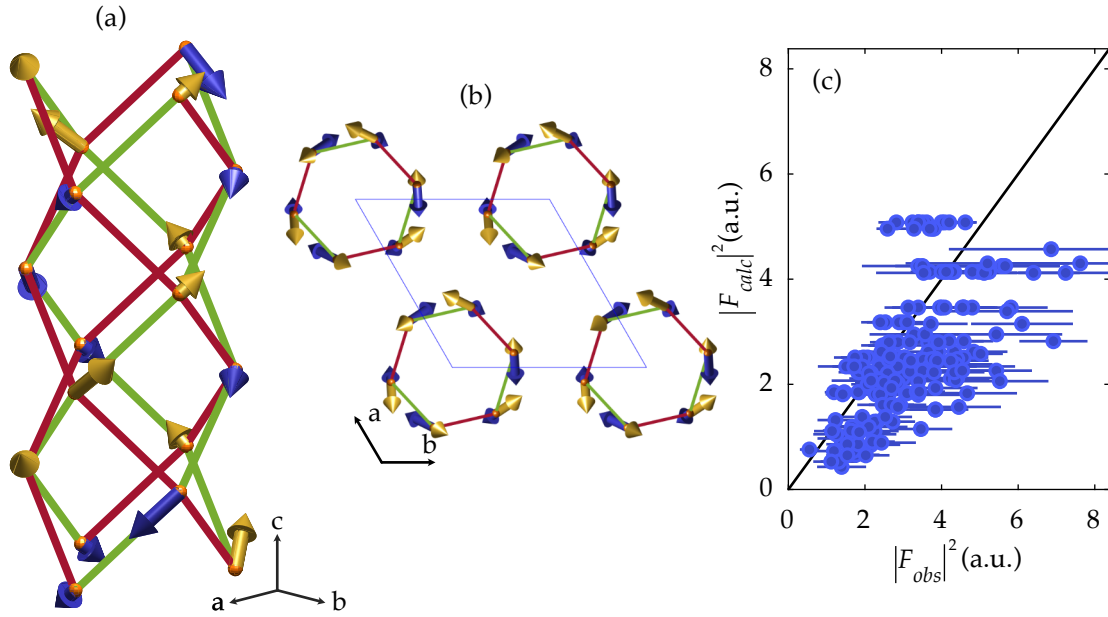


**Figure 6.15:** Magnetic structure of  $\text{Nd}_3\text{BWO}_9$  at zero field. (a) Structure along a single spin tube, showing the magnetic supercell. The depicted structure only considers the propagation vector  $\mathbf{k}_1 = (0,0,1/3)$ . (b) Zenith view of the kagome plane showing several spin tubes. (c)  $|F_c|^2$  vs.  $|F_o|^2$  plot of magnetic reflections. The model includes 3 free parameters as described in the text. A solid line is a guide to the eye where  $|F_c|^2 = |F_o|^2$ .

of Ising-axes obtained from single-ion CEF and shown in 6.2.(c). On the other hand, the arrangement of 'up' and 'down' pointing moments optimize the exchange energy assuming *opposite signs for nearest neighbor couplings*: ferromagnetic counter-clockwise coupling ( $J_{1+}$ ) and antiferromagnetic clockwise coupling ( $J_{1-}$ ), as depicted in Fig. 6.1.(e) and here. Following any of the ferromagnetic paths (green) the spin arrangement can be schematically described as  $uUuDdD$  within the magnetic supercell, which minimizes the ferromagnetic energy. Analogously, following an antiferromagnetic path (red) gives either  $UDUDUD$  or  $ududud$  arrangements, minimizing the energy of the antiferromagnetic links. In addition to that, in the plane (Fig. 6.15.(b)) every set of three spins in the corners of a  $J_\Delta$  triangle form an out of plane 120 degree structure, which also optimizes the antiferromagnetic interaction.

Note that the competition between FM  $J_{1+}$  and AFM  $J_{1-}$  gives naturally a way to a tripling of the unit cell. The winding repeats itself every three unit cells, supporting a structure with the same periodicity.

All in all, the refined magnetic structure is excellently consistent with local anisotropy and exchange geometry, while giving a good agreement to diffraction intensities. A comparison of calculated and observed structure factors for all measured reflections is shown in Fig. 6.15.(c). The data do not fall well on a line (as should be expected from this plot) and the dispersion is notable. It must be noted that the dispersion is quite symmetric with respect to the central line and that error bars are rather large. The small size of the sample and the complex sample environment used in the measurements (dilution refrigerator

**Table 6.8:** Results of fits of magnetic components in zero field for the different irreps in Eq. 6.15.

Irrep	$R_F$
$\Gamma_{P1}$	38 %
$\Gamma_{P2}$	40 %
$\Gamma_{P3}$	<b>16 %</b>

stick plus magnet) result in rather low magnetic signal intensities. As a consequence the relative uncertainty of the data is significant and the final agreement between model and observation is restricted by this. Therefore, the large agreement factors and the dispersion found in Fig. 6.15.(c) are a consequence of low counting statistics, and not an inaccurate model for the magnetic structure.

### Plateau phase for $\mathbf{H} \parallel \mathbf{c}$

The magnetic structure in the plateau phase for  $\mathbf{H} \parallel \mathbf{c}$  was investigated under a magnetic field of 0.85 T at a base temperature of 50 mK. Propagation vectors  $k_+ = (1/3, 1/3, +1/3)$  and  $k_- = (1/3, 1/3, -1/3)$  were identified and a number of magnetic reflections corresponding to both were measured, 104 and 80 respectively. The star of the propagation vector  $k = (1/3, 1/3, 1/3)$  indeed contain two elements, namely  $k_+$  and  $k_-$ . The corresponding contributions to the magnetic structure are analyzed independently.

The magnetic unit cell is a  $3 \times 3 \times 3$  extension of the nuclear unit cell, and contains 162  $\text{Nd}^{3+}$  ions. However, an analysis of the symmetry does constrain the free parameters greatly. The decomposition of the magnetic representation of the space group with propagation vector  $k_+ = (1/3, 1/3, +1/3)$  is as follows:

$$\Gamma_P = 6\Gamma_{P1}(1) \oplus 6\Gamma_{P2}(1) \oplus 6\Gamma_{P3}(1) \quad (6.15)$$

the decomposition contains three one-dimensional irreps that enter 6 times each. Naturally, the decomposition for  $k_-$  is the same, as all the vectors in the star of  $k$  are of the type  $P$ , i.e.  $(1/3, 1/3, u)$ , in the Brillouin zone. Therefore the following analysis is completely equivalent for both  $k_+$  and  $k_-$ . The propagation vector splits the Nd sites into two independent atomic orbits, giving two independently refinable magnetic moments:  $\text{Nd}_1$  and  $\text{Nd}_4$ . Antiunitary symmetry allows these irreducible representations to come together to form the same coirreducible representation (corep). This means that for each orbit we have the same three-dimensional irrep, however with independent parameters to refine. Each irrep allows the moments of two Nd ions to be refined with no constraints, i.e.  $(u, v, w)_1$  and  $(u, v, w)_4$ . The first orbit corresponds to ions  $\text{Nd}_1, \text{Nd}_2,$  and  $\text{Nd}_3$ , while the second corresponds to  $\text{Nd}_4, \text{Nd}_5,$  and  $\text{Nd}_6$ , in our convention.

In order to account for single-ion physics, we impose one constraint in our model. We assume that the Ising axis for  $\text{Nd}_1$  and  $\text{Nd}_4$  has to be completely equivalent, and therefore the refined moment for both orbits has to be related. We do so by imposing that  $(v, -u - v, -w)_4 = (u, v, w)_1$ , so that the paramagnetic symmetry between  $\text{Nd}_1$  and  $\text{Nd}_4$  is preserved. Our final model has therefore three refinable parameters, again the Cartesian components of the magnetic moment of  $\text{Nd}_1$ . In order to identify the irrep that is realized, we fit the different models to the measured magnetic intensities. The results for  $k_+ = (1/3, 1/3, +1/3)$  are summarized in Table 6.8 and show that  $\Gamma_{P3}$  gives the best

**Table 6.9:** Basis vectors of irrep  $\Gamma_{P3}$  that gives the best agreement to the neutron reflections associated with  $k = (1/3, 1/3, 1/3)$ , as described in the text.

IR	BV	Atom	BV components		
			$m_{\parallel a}$	$m_{\parallel b}$	$m_{\parallel c}$
$\Gamma_{P3}$	$\psi_7$	1	1	0	0
		2	0	$-\frac{1}{2} - i\frac{\sqrt{3}}{2}$	0
		3	$\frac{1}{2} - i\frac{\sqrt{3}}{2}$	$\frac{1}{2} - i\frac{\sqrt{3}}{2}$	0
	$\psi_8$	1	0	1	0
		2	$\frac{1}{2} + i\frac{\sqrt{3}}{2}$	$\frac{1}{2} + i\frac{\sqrt{3}}{2}$	0
		3	$-\frac{1}{2} + i\frac{\sqrt{3}}{2}$	0	0
	$\psi_9$	1	0	0	1
		2	0	0	$-\frac{1}{2} - i\frac{\sqrt{3}}{2}$
		3	0	0	$-\frac{1}{2} + i\frac{\sqrt{3}}{2}$

agreement to the data, with an agreement factor  $R_F = 16\%$ . The corresponding basis vectors are given in Table 6.9. Note that only atoms of the first orbit are explicitly given, the ones of the second orbit can be calculated by symmetry, taking the imposed constraint into account.

The fitted magnetic moment on  $\text{Nd}_1$  is  $m_1 = (0.99(4), 0.88(4), 1.18(7)) \mu_B$ , a total moment of 1.78 Bohr's magnetons. The magnetic moment amplitude corresponding to this Fourier component is modulated, just as in the zero field phase. The amplitude of the magnetic moments at this propagation vector is shown in Fig. 6.16. A modulation of amplitudes in a spin-density wave fashion along the  $c$  axis gives rise to similar  $Udd$  and  $Duu$  structures as discussed above, where the notation used is equivalent. As in the case of the zero field structure, the best fit is obtained when the magnetic moments sit in the directions dictated by the single-ion Ising axis. Looking at individual tubes, the corresponding arrangement of spins optimizes the exchange couplings. In this case, following the ferromagnetic paths (green) we follow three distinct series:  $UuUuUu$ ,  $DdDdDd$ , and  $ududud$ . In turn, looking at the antiferromagnetic paths we find the sequence  $UududD$  for all. The tubes can be seen as units that repeat in the rest of the large unit cell. In the plane, the effect of the propagation vector is to rotate the individual spin-tube structure by 120 degrees between adjacent neighbors. Importantly, this spin texture shows no global magnetization. In fact all three irreps give a perfectly compensated antiferromagnetic structure with zero net magnetic moment. Therefore, there must be an additional  $k = (0, 0, 0)$  component that may account for the finite magnetization exerted along the  $c$  axis. A symmetry analysis of all possible irreps with  $k = (0, 0, 0)$  is also performed. The decomposition of the magnetic representation gives four different irreps as:

$$\Gamma_{GM} = 3\Gamma_{GM1}(1) \oplus 3\Gamma_{GM2}(1) \oplus 3\Gamma_{GM3}(2) \oplus 3\Gamma_{GM4}(2) \quad (6.16)$$

where two of the irreps are one-dimensional and other two are two-dimensional.

Measuring magnetic scattering with a  $k = (0, 0, 0)$  propagation vector is usually quite complicated. At this propagation vector there is an interference with nuclear scattering

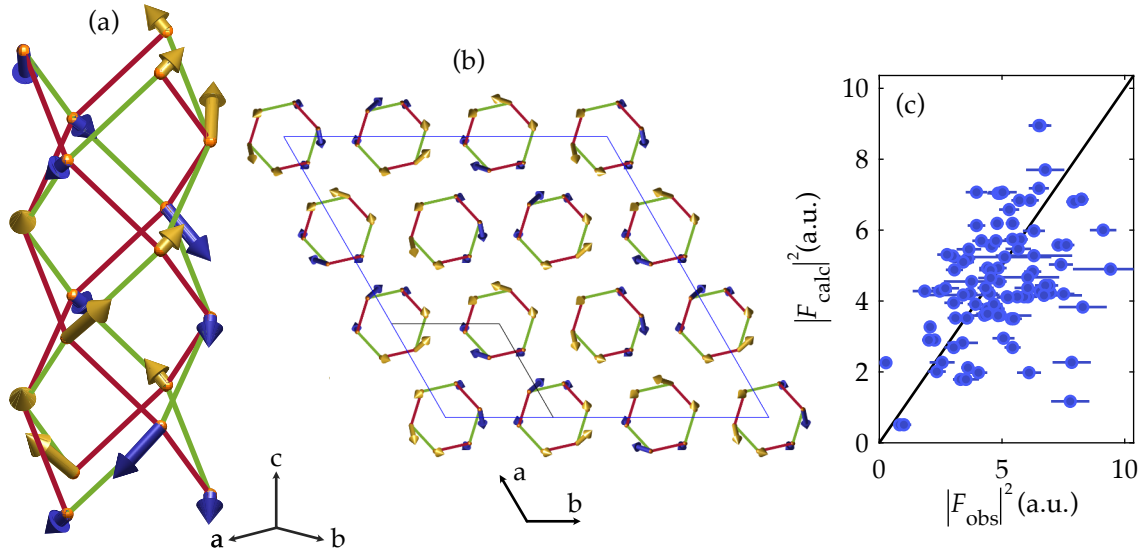


**Figure 6.16:** Magnetic Fourier component corresponding to  $\mathbf{k}_+ = (1/3, 1/3, 1/3)$  under a magnetic field of 0.85 T along the  $c$  crystallographic direction. (a) Magnetic moments ( $\mathbf{F}(\mathbf{Q})$ ) along a single spin tube. (b) Magnetic moments in the kagome plane, showing a projection of the large magnetic supercell. (c)  $|F_o|^2$  vs.  $|F_c|^2$  plot of magnetic reflections. The model includes 3 free parameters as described in the text. A solid line is a guide to the eye where  $|F_c|^2 = |F_o|^2$ .

and special techniques such as spin-polarized neutron diffraction are used to tell both contributions apart. However, a simple check of the overall magnetic moment for each irrep may directly indicate which one is involved in the magnetic structure. In fact, only  $\Gamma_{GM1}$  provides a net moment in the  $c$  direction, whereas  $\Gamma_{GM2}$  and  $\Gamma_{GM3}$  are compensated and  $\Gamma_{GM4}$  provides a net moment in the plane. Therefore we choose  $\Gamma_{GM1}$  to account for the  $k = (0, 0, 0)$  component. In this irrep, as was the case previously  $\Gamma_{DT2}$  and  $\Gamma_{P3}$ , the Cartesian coordinates of the magnetic moment on  $\text{Nd}_1$ ,  $(u, v, w)_1$ , can be independently chosen. Lacking a set of magnetic reflections to perform a fit, we follow an argumentation based on physics to fix the amplitude of this component. CEF fixes the dominant energy scale confining the spins to their Ising-axis. The direction of the moment in  $\text{Nd}_1$  is chosen to be parallel to that obtained from the fit of  $k_+ = (1/3, 1/3, 1/3)$ . Due to the symmetry of the irrep, automatically this axis is propagated to the remaining  $\text{Nd}^{3+}$  ions. Therefore, the effect of the ferromagnetic component is to modulate the amplitudes of the magnetic moments obtained in the refinement, leaving their spacial orientation intact.

In order to fix the amplitude of the ferromagnetic component, we may use the results of bulk magnetometry. One would make the  $(0, 0, 0)$  component such that the resulting magnetic moment along the  $c$  direction matches that of the plateau in the bulk. Another way to fix this is to realize that by adding a  $(0, 0, 0)$  component with the amplitude of a  $u$  moment (as defined above) the resulting magnetic structure automatically features  $1/3$  of the maximum magnetization (assuming the maximally magnetized would show all the moments with the maximum value of a  $u + U$  moment). Adding this component the individual moments change as follows:  $D \rightarrow d$ ,  $d \rightarrow 0$ ,  $u \rightarrow U$  and  $U \rightarrow U + u = \hat{U}$ . This gives a maximum moment for each ion of  $\hat{U} = 2.68 \mu_B$ .

**Table 6.10:** Basis vectors of irrep  $\Gamma_{GM1}$  describing a ferromagnetic component induced by the field in the high field phase for  $H \parallel c$ .

IR	BV	Atom	BV components		
			$m_{\parallel a}$	$m_{\parallel b}$	$m_{\parallel c}$
$\Gamma_{GM1}$	$\psi_1$	1	1	0	0
		2	-1	0	0
		3	0	1	0
		4	-1	-1	0
		5	1	1	0
		6	0	-1	0
	$\psi_2$	1	0	1	0
		2	0	-1	0
		3	-1	-1	0
		4	1	0	0
		5	-1	0	0
		6	1	1	0
	$\psi_3$	1	0	0	1
		2	0	0	1
		3	0	0	1
		4	0	0	1
		5	0	0	1
		6	0	0	1

The resulting magnetic structure is plotted in Fig. 6.17 and does indeed optimize the exchange energy in the system while showing 1/3 of the maximum magnetization. The resulting moment for  $\text{Nd}_1$  is  $m_1 = (1.49(8), 1.33(5), 1.78(5))\mu_B$ , corresponding to spherical angles  $\phi = 41.6^\circ$  and  $\theta = 48.4^\circ$ , showing a small deviation from the single-ion predictions. Interestingly, the magnetic moment in some atomic positions vanishes as the ferromagnetic component is added. Looking at the ferromagnetic paths (green) we observe the following sequences:  $U\hat{U}U\hat{U}U\hat{U}$ ,  $U0U0U0$ , and  $d0d0d0$ . The antiferromagnetic paths (red) do only show one sequence:  $0d\hat{U}U0U$ , which evidences that the total magnetization is 1/3 of the maximum. In the plane, the energy associated with the triangular couplings is also minimized, having either 120 degree arrangements of  $ddd$  and  $UUU$ , or having  $00\hat{U}$  that do not contribute to the overall energy.

A refinement of the magnetic moment components for the reflections associated with  $k_- = (1/3, 1/3, -1/3)$  yields very similar results in the same irrep ( $\Gamma_{3p}$ ). It is an extremely complex problem to differentiate whether the presence of  $k_+$  and  $k_-$  propagation vectors means a multi-k structure, where both propagation vectors coexist in the same structure, or the presence of magnetic domains, where the systems chooses (at random) one of the symmetry equivalent  $k$ 's. A superposition of the components from both  $k_+$  and  $k_-$  would give unreasonably large magnetic moments in the magnetic ions. We assume the presence of magnetic domains and that the actual magnetic structure is the composition of either  $k_+$  or  $k_-$ , and a ferromagnetic component, as described above. The resulting structure in

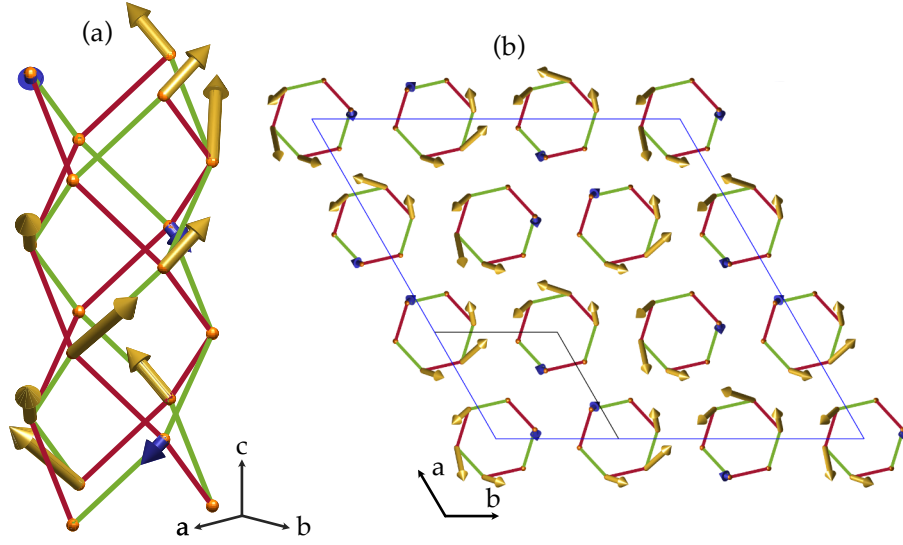


**Figure 6.17:** Magnetic structure of  $\text{Nd}_3\text{BWO}_9$  under a magnetic field of 0.85 T along the  $c$  crystallographic direction: (a) in one single spin tube, (b) in the plane, showing a slice of the magnetic supercell. The structure includes a  $\mathbf{k}_+ = (1/3, 1/3, 1/3)$  propagation vector and a ferromagnetic component as given in the text. Notice how one third of the magnetic moments vanishes.

the  $k_-$  domain is plotted in Fig. 6.18.

## 6.6 Discussion

The physics of  $\text{Nd}_3\text{BWO}_9$  is that of Ising spins with a complex network of exchange couplings. Our data reveals a complex phase diagram with highly structured magnetic structures as a result of the variety of local Ising axes. The zero field ordered phase is a complex multi- $k$  one that survives up to roughly 0.6 T for all field directions. Strikingly, the order realized in the plateau is completely different when fields are applied in the basal  $ab$  plane or perpendicular to it. Both high field phases (B and C) seem to give rise to magnetic domains, as a result of non-trivial stars of their propagation vectors.

Plateaux in the magnetically ordered sector are a hallmark of frustrated magnets. The existence of magnetization plateaux (and particularly at  $1/3$  of saturation) has been predicted for both kagome antiferromagnets [200, 201], as well as for a model of isolated antiferromagnetic spin tubes with a weak triangular rung interaction (see Fig. 6.1.(c)) [202–204]. The presence of magnetization plateaux independent of the orientation of the applied magnetic field suggests an stabilizing interplay between frustration mechanisms.

The boundaries between the different order phases also suggest complex physics playing a role at the phase transitions. For  $\mathbf{H} \parallel c$  we find the existence of a tricritical point (at 0.98 T and 0.22 K) where a second-order and a first-order transitions come together. This shows a significant spin-lattice interaction or magnetostriction in  $\text{Nd}_3\text{BWO}_9$ . The transition to saturation can be prematurely precipitated via an ‘order by distortion’ [205] mechanism. A gain in magnetic energy compensates a small loss in elastic energy, leading to a first order transition to saturation. Though our neutron diffraction data show

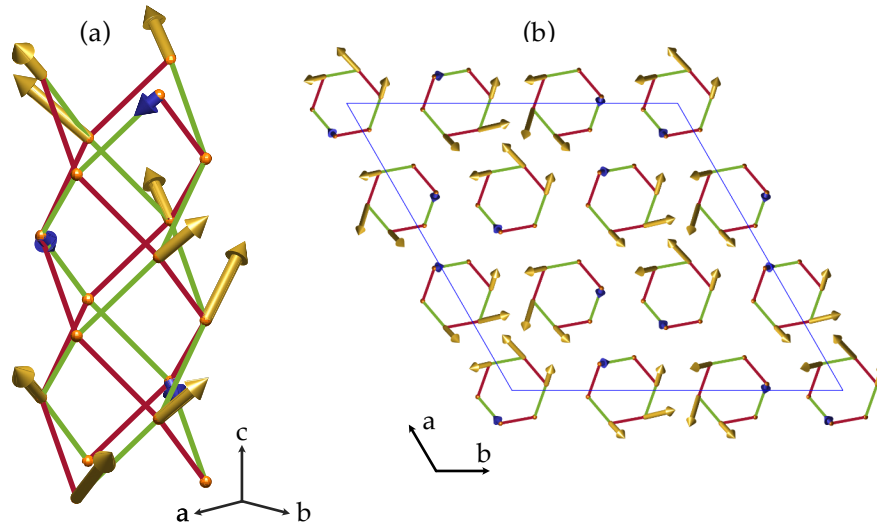


**Figure 6.18:** Magnetic structure of  $\text{Nd}_3\text{BWO}_9$  under a magnetic field of 0.85 T along the  $c$  crystallographic direction: (a) in one single spin tube, (b) in the plane, showing a slice of the magnetic supercell. The structure includes a  $\mathbf{k}_- = (1/3, 1/3, -1/3)$  propagation vector and a ferromagnetic component as given in the text. Notice how one third of the magnetic moments vanishes.

no evident change in the space group or lattice parameters in the high field phase, a detailed study would be necessary to discard this possibility. Note that this magneto-elastic coupling may result in a small change in the crystal electric field around the magnetic ions. The lack of symmetry of the CEF environment of the  $\text{Nd}^{3+}$  ions makes it extremely susceptible to perturbations. It is thus quite likely that the principal anisotropy axes in the A and C phases are slightly different.

Phases A and B appear to merge below 100 mK at 0.56 T. A first order phase transition is speculated between A and B, with a termination bicritical point where all phase boundaries meet. Neutron diffraction data in Fig. 6.11.(a) indicate the phases will likely merge slightly below 120 mK. Recent measurements follow this phase boundary down to lower temperatures and suggest an intermediate phase between A and B may take place [199].

Interestingly, between A and C the phase boundaries seem to develop smoothly down to the lowest measured temperatures and converge at  $T = 0$ . Neutron data at 55 mK show the phases are still separated by paramagnetism at this temperature Fig. 6.11.(b). A highly non-trivial order-to-order continuous quantum phase transition may take place between A and C at zero temperature (indicated with a question mark in Fig. 6.10). Order-to-order transitions of the second order are not allowed within the general Landau theory of phase transitions. However, extended models have predicted such transitions in a framework of deconfined quantum criticality [206, 207]. The presence of such QCPs has also been discussed in the field of heavy-fermion systems in the context of quantum bicriticality [208]. The applicability of either formalism requires more theoretical work. Precise measurements in the vicinity of these phase transitions would provide important insight on their nature. However, the strong signal from nuclear degrees of freedom and the extremely low temperatures involved prevent further investigation.

A discussion of the relevant couplings is in order.  $\text{Nd}_3\text{BWO}_9$  has been proposed in the as a kagome-lattice Heisenberg antiferromagnetic and promising QSL candidate [173]. However, the vast majority of our data point against the 2D-planar interactions being dominant. Instead, a model of 1D magnetism seems a better fit for this quantum magnetic material. Magnetic diffuse scattering further supports this model, showing significant short-range correlations only along the direction of the magnetic tubes in an extended temperature range. Heat capacity reveals double-hump features, typical of quasi-1D magnets [187, 188]. Also, all the magnetic structures can be described as a set of coupled spin tubes, with competing ferro- and antiferromagnetic nearest neighbor couplings. This is precisely the case also in the sister compound  $\text{Pr}_3\text{BWO}_9$ . Our recent spectroscopic data reveal a that the magnetic interaction in this system is not that of a kagome lattice, but in fact composed of weakly coupled 1D spin tubes. These tubes have the exact same structure that we propose for  $\text{Nd}_3\text{BWO}_9$ : ferromagnetic nearest-neighbor coupling winding counterclockwise around the tube, and antiferromagnetic coupling for the clockwise winding bonds [209]. These findings prompt a reevaluation of the proposed models for the family  $R_3\text{BWO}_9$  [210, 211].

Finally we comment on the structures that are found in the ordered phases. Even though spin-density waves are rather common in metallic systems as a result of Fermi surface nesting [212], they constitute one of the least classical ordered structures to be found in a magnetic insulator [213]. Most SDW models are based on the physics of the one-dimensional Tomonaga-Luttinger spin liquid (TLSL), to which a direct mapping exists from an antiferromagnetic quantum spin-1/2 chain. SDW structures have been found in partially magnetized states in quantum magnets as a result of stabilization of longitudinal incommensurate correlations. In  $\text{BaCo}_2\text{V}_2\text{O}_8$  [214, 215] and  $\text{SrCo}_2\text{V}_2\text{O}_8$  [216], it is Ising anisotropy that does the job; in  $\text{YbAlO}_3$  the result of anisotropic Ising-like interchain interactions [217–219]. In  $\text{Cs}_2\text{CoBr}_4$  a combination of mechanisms seems to be the origin of SDWs [220]. However, what all these SDWs have in common is that they only appear under a magnetic field, as this one is responsible to induce incommensurate correlations [221–223]. The resulting incommensurability is, as a result, controlled by the field. In contrast, in  $\text{Nd}_3\text{BWO}_9$  the SDW state appears at zero field and the magnetic field seems to have no effect on it. The lowest temperature state is the result of a lock-in transition, and stabilized by the onset of an additional  $\mathbf{k}_2$  propagation vector, probably to reduce the frustration in the interaction between single spin tubes which we disregard. However, an incommensurate ordered state does survive above 0.26 K for a narrow range in temperatures.

On the other hand, the origin of the observed incommensurate-commensurate (IC-C) transition may be due to dipolar coupling. Dipolar interactions are not uncommon in the study of rare-earth based magnets due to their large magnetic moments [224]. Their stabilizing role on incommensurate structures at temperatures above commensurate order has been argued in several systems with hexagonal structure [225–227]. Note that an incommensurate state with propagation vector along  $\mathbf{c}$  has also been proposed in the sister compound  $\text{Sm}_3\text{BWO}_9$  [211], showing incommensurability may be inherent to the tube structure. The peculiar competition between FM and AFM interactions on the spin-tube structures induces a natural explanation of the tripling of the unit cell. However, the relevance of the TLSL model in explaining the SDW states in this quasi-one-dimensional  $j_{eff} = 1/2$  Ising magnet deserves further exploration.

## 6.7 Conclusion

The low temperature magnetism of  $\text{Nd}_3\text{BWO}_9$  is extremely rich, realizing exotic magnetic phases and complex transitions between them. The presence of fractional magnetization plateaux highlight the frustrated nature of the magnetic interaction. The CEF gives rise to Ising spins with their moments along low symmetry directions. Notably, due to the rotational symmetry that relates the six magnetic ions in the unit cell, the extremely anisotropic single ion physics is disguised in almost isotropic bulk properties. Accurate knowledge of the CEF ground state is essential to disentangle the magnetic properties of rare-earth magnets.

Neutron diffraction reveals a complex ground state at zero field, with a multi-k magnetic structure realizing exotic spin-density-wave structures. Notably, the spin texture suggests two types of nearest-neighbor interaction with opposing signs, just as has been found in the sister compound  $\text{Pr}_3\text{BWO}_9$ . The origin of such structures is not known at the moment and deserves further investigation. The structure of the fractional  $m = 1/3$  magnetization plateau is also determined, showing as well a SDW state.

All of our data show that  $\text{Nd}_3\text{BWO}_9$ , and likely every other member of the whole family of frustrated magnets  $\text{R}_3\text{BWO}_9$ , are not 2D-kagome magnets but rather networks of weakly coupled 1D spin-tubes with competing ferro-antiferromagnetic interactions. Spectroscopic measurements are vital to understand the actual magnetic model realized in these systems.

## Chapter 7

# Conclusions and outlook

The study of emergent phenomena in condensed matter systems continually unveils new insights in physics. Quantum magnets, with their simplicity and tunability of spin Hamiltonians, represent a particularly fertile ground for exploration. By adjusting a few parameters, a wide array of phases and effects can be realized. In this thesis, we have delved into several low-dimensional magnets, where spin-orbit coupling unlocks exotic behaviors. We explored two avenues to emergent phenomena: the magneto-electric coupling on the  $A_2\text{Cu}_2\text{Mo}_3\text{O}_{12}$  family and the complex rare-earth frustrated magnetism in  $\text{Nd}_3\text{BWO}_9$ . Here we summarize the main conclusions and potential future research directions.

On the one hand, the quasi-1D family of magnets  $A_2\text{Cu}_2\text{Mo}_3\text{O}_{12}$  is a fantastic ground to study the interaction between electric and magnetic degrees of freedom in the proximity to quantum critical points. Magnetic frustration channels the realization of magnetic QCPs at laboratory-accessible magnetic fields in these strongly interacting systems. As a result of magneto-electric coupling, a entire range of phenomenal results are obtained, where magnetic field becomes a convenient tuning parameter.

First, we demonstrated how measurements of the dielectric properties of a system are an extremely powerful tool to its magnetism. With large versatility in experimental conditions, our measurements provide huge sensitivity to magnetic phase transitions, providing a very accurate tool to investigate QPTs.

Second, the magneto-electric coupling provide us with a new channel to access quantum criticality. As was demonstrated in both  $\text{Rb}_2\text{Cu}_2\text{Mo}_3\text{O}_{12}$  and  $\text{Cs}_2\text{Cu}_2\text{Mo}_3\text{O}_{12}$ , the particular coupling that emerges at the saturation QCPs opens a novel gateway to the critical susceptibility at a Bose-Einstein condensation. We are able to directly measure critical exponents in fantastic agreement with theory.

Third, we are able to uncover new phenomena. Electric dipoles in  $\text{Cs}_2\text{Cu}_2\text{Mo}_3\text{O}_{12}$  can relax mediated by virtual quantum magnons at low temperatures. The magnon mediating this process is precisely the one that softens at the QCP, making the relaxation itself go critical at saturation. This strikingly shows that magnons in  $\text{Cs}_2\text{Cu}_2\text{Mo}_3\text{O}_{12}$  are endowed with an electric dipole moment, regardless of the nature of the ground state. The origin of free dipoles, as well as the absence of this effect in  $\text{Rb}_2\text{Cu}_2\text{Mo}_3\text{O}_{12}$ , still remains a mystery.

While our data provide clear proof of a novel mechanism, further investigation is essential to fully elucidate this phenomenon. One remaining task is the determination

of the magnetic structure in the ground state of  $\text{Cs}_2\text{Cu}_2\text{Mo}_3\text{O}_{12}$ . An accurate magnetic structure knowledge can pinpoint the mechanism giving rise to ferroelectricity and the origin of electric activity of magnetic excitations.

Understanding the phonon spectrum is important to identify the origin of relaxing degrees of freedom in the both  $\text{Cs}_2\text{Cu}_2\text{Mo}_3\text{O}_{12}$  and  $\text{Rb}_2\text{Cu}_2\text{Mo}_3\text{O}_{12}$ . As was done in other systems like  $\text{SrTiO}_3$ , accurate knowledge of the phonon frequencies revealed that relaxation processes belong to particular lattice normal modes. The large amount of atoms in the unit cell, together with its low symmetry complicate the phonon spectrum greatly, making the problem almost intractable for *ab initio* techniques like Density functional theory.

Chemical substitution can give rise to QCPs, where the tuning parameter is the concentration of a certain element,  $x$ . This is for example the case in systems like  $\text{Rb}_x\text{Cs}_{1-x}\text{FeCl}_3$ , where the chemically induced QPT separates a quantum paramagnetic state ( $x = 0$ ) and a long-range ordered state ( $x = 1$ ). Investigating the substitution series  $\text{Rb}_x\text{Cs}_{2-x}\text{Cu}_2\text{Mo}_3\text{O}_{12}$  could bring insight on the mechanism behind the different magnetic ground states in  $\text{Rb}_2\text{Cu}_2\text{Mo}_3\text{O}_{12}$  and  $\text{Cs}_2\text{Cu}_2\text{Mo}_3\text{O}_{12}$ . Additionally, it may help pinpoint the origin of the electric dipoles of magnons and whether it is intrinsic only to  $\text{Cs}_2\text{Cu}_2\text{Mo}_3\text{O}_{12}$ .

Relaxation by quantum critical magnons likely extends beyond  $\text{Cs}_2\text{Cu}_2\text{Mo}_3\text{O}_{12}$  to other already known quantum magnets with strong magneto-electric coupling. Revisiting their low-temperature dielectric response for similar physics may prove fruitful. However, dielectric permittivity measurements at millikelvin temperatures are rare, as most magneto-electric phenomena occur at higher temperatures. Developing theoretical models of coupled magnetic and electric degrees of freedom is essential for uncovering the microscopic mechanism behind this new phenomenon.

Lastly, we highlight how an external magnetic field provides a fine-tuned regulation of the interaction between soft magnetic excitations and lattice degrees of freedom. Our findings may open new routes to quantum critical multifunctionality and potentially to coupling magnetic, electric, and optical degrees of freedom in hybrid quantum circuits.

On the other hand, our investigation into the quantum magnet  $\text{Nd}_3\text{BWO}_9$  has unveiled a series of intriguing phenomena, underscoring its rich and complex nature. Geometrically frustrated interactions and a complex crystal-electric field effects intertwine to create complex magnetism leading to several fractional magnetization plateaux and possibly non-trivial phase transitions beyond standard Landau theory.

Although much attention was brought to it being conceived as a good kagome-lattice antiferromagnet, our research highlights the importance interactions perpendicular to the kagome planes. In fact, there is solid evidence that the magnetism in  $\text{Nd}_3\text{BWO}_9$  can be understood in terms of 1D spin-tubes *perpendicular* to the kagome planes. A careful analysis of the crystallographic structure and allowed magnetic interactions is a pivotal point in modeling spin Hamiltonians. The key role of neutron spectroscopy as a technique in magnetism is emphasized by this case. Spectroscopic data are the only way to identify the relevant magnetic interactions that define the magnetic model in a material. This further urges to revisit other proposed magnetic Hamiltonians for low-dimensional magnetism.

Bulk magnetic properties show a nearly isotropic behavior. However, the single-ion anisotropy extracted from an analysis of the crystal electric field effect reveals an almost

perfect Ising anisotropy locally. The bridge between these two findings is built by the rotational symmetry of the crystal and highlights how in rare-earth magnets knowledge of the single-ion perspective is key to understand the whole physical picture.

The complex exchange patterns in  $\text{Nd}_3\text{BWO}_9$  lead to the realization of exotic SDW and multi-k ground states. Analyzing the stability of these phases against a magnetic field may contribute to find understand the nature of the different phase transitions. In particular, it can be insightful to understand the stability of phases B and C under tilted magnetic fields and whether there is a phase transition between them. In addition, the whether the transition between A and C happens actually at zero temperature is a key question that would reveal new QCPs.

Even if  $\text{Nd}_3\text{BWO}_9$  is not a kagome antiferromagnet, a study of the magnetic excitations can reveal interesting phenomena in such a quasi-1D spin-tube system. Knowing the eigenstates of the lowest energy crystal field doublets, one can build an effective Hamiltonian that describes the excitation spectrum and identify the relevant magnetic couplings.

Finally, talking about dielectric phenomena it is worth noticing that the crystal structure of  $\text{Nd}_3\text{BWO}_9$  has no inversion symmetry, thus allowing for a ferroelectric moment along its 6-fold rotation axis. While no evidence of phase transitions have been detected below 300 K, it would be interesting to determine whether a transition into a ferroelectric state happens at higher temperatures and how it may relate to the inherent twinning that we observed.

Competition between different different energy scales brings out the most interesting features of condensed matter systems. Perfectly balanced interactions prevent simple order to realize, promoting by contrast extremely correlated phases to come into light.

Frustration Is All You Need.

\* \* \*



# List of publications

D. Flavián, S. Hayashida, L. Huberich, D. Blosser, K. Yu. Povarov, Z. Yan, S. Gvasaliya, and A. Zheludev. *Magnetic phase diagram of the linear quantum ferro-antiferromagnet  $\text{Cs}_2\text{Cu}_2\text{Mo}_3\text{O}_{12}$* . Phys. Rev. B **101**, 224408 (2020).

S. Hayashida, L. Huberich, D. Flavián, Z. Yan, K. Yu. Povarov, S. Gvasaliya, and A. Zheludev. *Critical dielectric susceptibility at a magnetic BEC quantum critical point*. Phys. Rev. Research **3**, 033053 (2021).

D. Flavián, P. A. Volkov, S. Hayashida, K. Yu. Povarov, S. Gvasaliya, P. Chandra, and A. Zheludev. *Dielectric Relaxation by Quantum Critical Magnons*. Phys. Rev. Lett. **130**, 216501 (2023).

D. Flavián, J. Nagl, S. Hayashida, M. Yan, O. Zaharko, T. Fennell, D. Khalyavin, Z. Yan, S. Gvasaliya, and A. Zheludev. *Magnetic phase diagram of the breathing-kagome antiferromagnet  $\text{Nd}_3\text{BWO}_9$* . Phys. Rev. B **107**, 174406 (2023).

J. Nagl, D. Flavián, S. Hayashida, K. Yu. Povarov, M. Yan, N. Murai, S. Ohira-Kawamura, G. Simutis, T. J. Hicken, H. Luetkens, C. Baines, A. Hauspurg, B. V. Schwarze, F. Husstedt, V. Pomjakushin, T. Fennell, Z. Yan, S. Gvasaliya, A. Zheludev, *Excitation Spectrum and Spin Hamiltonian of the Frustrated Quantum Ising Magnet  $\text{Pr}_3\text{BWO}_9$* , Phys. Rev. Research **6**, 023267 (2024).



# Appendix A

## Experimental details

The details of the experiments that have been carried out in this work are described in the following. For clarity, the experiments belonging to each chapter are described in a separate sections.

### A.1 Chapter 4: Quantum multiferroicity and BEC criticality in $\text{Rb}_2\text{Cu}_2\text{Mo}_3\text{O}_{12}$

Comparative dielectric measurements on  $\text{Rb}_2\text{Cu}_2\text{Mo}_3\text{O}_{12}$  at high temperature were carried using samples of types (1) - (3) and (5) (see Fig. 4.3), placed in a capacitance cell with plate size  $6 \times 6 \text{ mm}^2$  and spacing of 0.2 mm. For single-crystal measurements, we used silver-paste contacts directly deposited on opposing (001) surfaces of a  $0.3 \times 1.8 \times 0.2 \text{ mm}^3$  single crystal, as displayed in Fig. 4.3. For pyroelectric current measurements, we deposited silver-paste contacts on the surface of a sintered-powder sample that was pelletized by baking at  $440 \text{ }^\circ\text{C}$  for 60 h. The pellet area was  $27 \text{ mm}^2$ , and the thickness was 0.78 mm.

Capacitance was measured using an Andeen-Hagerling 2550A capacitance bridge at a frequency of 1 kHz. We measured both real,  $C'$ , and imaginary,  $C''$ , parts of the capacitance. An excitation voltage between 1.5 and 15 V was applied. We used 15 V to map out the phase diagram with as high as possible signal-to-noise ratio and used 3 V to measure critical susceptibility in a linear response regime as discussed in the text. Frequency variation of capacitance was measured by a Keysight E4980A Precision LCR meter. A Keithley 6517A electrometer is used to provide direct current (DC) bias voltage of up to 50 V. Pyroelectric currents  $I_p$  were measured using the same device.

All measurements were carried out in a Quantum Design Physical Property Measurement System (PPMS) with a maximum magnetic field of 14 T. Low-temperature data down to  $T = 0.1 \text{ K}$  were taken with a  $^3\text{He}$ - $^4\text{He}$  dilution refrigerator PPMS insert.

For capacitance measurements, the temperature and magnetic field were swept continuously with minimum sweeping rates of 0.01 K/min and 2.5 Oe/s, correspondingly. For measurements of ferroelectric polarization, a voltage of  $\pm 250 \text{ V}$ , corresponding to an electric field of 0.32 kV/mm over the width of the sample, was applied when cooling the sample from 1.1 to 0.1 K at 11 T to avoid ferroelectric domain formation. The poling electric field was applied parallel to the magnetic field. After turning off the poling field

at 0.1 K, we waited for about 10 minutes until any extrinsic currents had disappeared.  $I_p$  was measured while warming up the sample at a steady sweeping rate of 0.5 K/min. Electric polarization  $P$  is obtained from the time integral of the  $I_p$ .

Heat capacity data for  $\mathbf{H} \parallel \mathbf{a}$  and  $\mathbf{H} \parallel \mathbf{c}^*$  were collected on a 0.12-mg single-crystal sample using a standard Quantum Design relaxation calorimetry option as measured in [98].

## A.2 Chapter 5: Dielectric relaxation by quantum critical magnons in $\text{Cs}_2\text{Cu}_2\text{Mo}_3\text{O}_{12}$

A detailed investigation of the chemical structure of  $\text{Cs}_2\text{Cu}_2\text{Mo}_3\text{O}_{12}$  is still lacking in the literature. A study of the structure, given in B, is carried out on single-crystal samples using a Bruker APEX-II instrument, equipped with a nitrogen blower that provides good temperature stability down to 95 K.

Complex permittivity measurements have been carried out on single-crystal samples. The crystal growth is detailed in Chapter 3. Silver paste electrodes were deposited on opposing faces of a crystal of dimensions  $2.4 \times 0.24 \times 0.1 \text{ mm}^3$  to build a capacitor with  $\mathbf{E} \parallel \mathbf{c}^*$ . The sample was then mounted on a sapphire substrate to ensure a good thermal exchange with the heat bath at low temperatures.

Bulk measurements were carried out using a  $^3\text{He}$ - $^4\text{He}$  dilution refrigerator insert for the Quantum Design Physical Property Measurement System (PPMS). Measurements of capacitance were performed with two different setups. Data at 1 kHz were measured on a Andeen-Hagerling AH 2550A Ultra-precision Capacitance Bridge (optimized for measurements at 1kHz). Measurements as a function of probing frequency were carried out in the Andeen-Hagerling AH 2700A Ultra-precision Capacitance Bridge. Due to the small amplitude of the measured signals, the data were taken always at constant frequency as the temperature and magnetic field were modified continuously. Typically, a rate of 0.01 K/min was chosen for the temperature scans. For field scans the ramping rate was optimized in order to minimize spurious heating due to eddy currents. A rate of 2.5 Oe/s was chosen below 0.25 K, 5 Oe/s between 0.25 K and 0.40 K and 10 Oe/s for all measurements above 0.40 K. In order to maximize the signal to noise ratio while keeping the self-heating minimal an excitation signal of  $V_{ex} = 0.75 \text{ V}$  was used for all the measurements.

Measurements of ferroelectric polarization as well as relative permittivity were performed on polycrystalline samples. Powders were synthesized in a solid state reaction. The powder was then compressed using a hydrostatic pressure of 80 kbar and subsequently sintered for 24 h at  $500^\circ\text{C}$ . Flat cylindrical pellets were prepared and finally silver electrodes were deposited on opposing faces.

Pyroelectric currents were measured using a Keithley 6517A electrometer as follows. At 8.5 T and 1.1 K a poling DC voltage of +300 V or -300 V was applied. Poling field is applied parallel to the magnetic field. Then the magnetic field was gradually reduced to 7.5 T and subsequently the sample was chilled to 0.1 K to avoid the formation of ferroelectric domains. Once the base temperature had been reached, the electric field was turned off and we waited for about 10 min until disappearance of extrinsic currents. The pyroelectric current was measured as the sample was warmed up to 1.1 K at a rate of 0.5 K/min. Electric polarization was obtained from the integration of the pyroelectric current

signal over the heating time. A Keithley 6517A electrometer was also used to provide a DC electric field on DC bias measurements on single crystals, always such that  $E \parallel c^*$ .

Synchrotron radiation was used to study the evolution of the lattice parameters of  $Rb_2Cu_2Mo_3O_{12}$  and  $Cs_2Cu_2Mo_3O_{12}$  as a function of temperature. The beamline BM01 [228] at the European Synchrotron Radiation Facility (ESRF, France) was used to measure powder diffractograms from 5 K to 300 K. The beamline is equipped with a Pilatus 2M two-dimensional detector. Powder samples were loaded in 200  $\mu\text{m}$ -diameter glass capillaries and installed in a He-flow cryostat with a base temperature of 4 K. The wavelength of choice was  $\lambda = 0.72479 \text{ \AA}$  for all measurements. In the case of  $Rb_2Cu_2Mo_3O_{12}$  an electronic detection threshold was imposed to filter out rubidium fluorescence. The samples were left to thermalize at the lowest attainable temperature for several hours before starting the measurements with increasing temperature. The refrigerator shrouds restrict the rotation of the samples to a few degrees, so powder diffraction patterns were collected keeping the samples in a still position. Detector images were processed using the Bubble suite. Powder diffractograms were collected with 1 K steps and fitted using Rietveld refinement implemented in the FullProf suite [198]. Single-crystal diffraction patterns were also measured with the same setup and experimental conditions. The reciprocal space coverage was strongly restricted and data were obtained as omega scans spanning 20 degrees. Integration of single detector images was done using CrysAlis-Pro.

Single-crystal diffraction on  $Cs_2Cu_2Mo_3O_{12}$  was performed in EH2 of the I19 instrument [229] at the Diamond Synchrotron facility (UK). A wavelength of  $\lambda = 0.48590 \text{ \AA}$  (silver  $K_\alpha$ ) was chosen to maximize the reciprocal space coverage. Single crystal samples of approximately  $50 \times 50 \times 100 \mu\text{m}^3$  in size were installed at the tip of the cold finger of a closed-cycle He refrigerator with a base temperature of 5 K. The samples are covered with a beryllium shroud to allow the evacuation of the sample space. The presence of the refrigerator restricts the diffractometer movement. Data sets were collected as phi rotations of approximately 300 degrees, keeping the remaining diffractometer angles fixed. The beamline is equipped with a single photon counter Eiger 4M CdTe two-dimensional detector, allowing a large coverage of reciprocal space. Integration of the detector images was performed using DIALS [230] as contained in the xia2 system [231].

### A.3 Chapter 6: Unveiling the magnetism of the quantum antiferromagnet $Nd_3BWO_9$

Single crystal samples of  $Nd_3BWO_9$  were grown by spontaneous crystallization using a flux method as described in [86]. Purple transparent single crystals with well defined facets were obtained. Typical masses range from a few micrograms to 40 mg and different samples were used in this study, depending on the technique. The chemical structure of the different single-crystal samples used in this study was validated using single-crystal X-ray diffraction on a Bruker APEX-II instrument, and was found to be in agreement with previous reports [173]. Powder samples of  $Nd_3BWO_9$ , as well as of the non-magnetic  $La_3BWO_9$ , were synthesized by a solid state reaction. The correct chemical structure and the quality of the powders was checked with powder X-ray diffraction in a Rigaku MiniFlex diffractometer. Boron-11 enriched samples (both powder and single crystals) were also prepared for their use in neutron scattering experiments as described in § 3.

Measurements of heat capacity, magnetocaloric effect (MCE), magnetization and magnetic torque were carried out using a  $^3\text{He}$ - $^4\text{He}$  dilution refrigerator insert for the Quantum Design Physical Property Measurement System (PPMS). A sample of mass 0.131 mg was used for both heat capacity and MCE measurements. Heat capacity data were collected using a standard relaxation method from Quantum Design for temperatures  $100 \text{ mK} < T < 4 \text{ K}$  in applied fields of  $0 \text{ T} < \mu_0 H < 3 \text{ T}$ . The magnetic field was applied along the crystallographic  $a^*$ , and  $c$  directions. In zero field, data were collected from 100 mK to 300 K. Heat capacity data of  $\text{La}_3\text{BWO}_9$  were measured down to 2 K and extrapolated to lower temperatures from an empirical fit to a  $T^3$ -power law. MCE data were measured using the same puck as for heat capacity. The change of temperature of the sample was recorded as the magnetic field was swept up and down at a constant rate. In order to avoid self heating of the puck, the field change rate was optimized and a value of 0.5 mT/s was selected. In the terminology of MCE measurements, our experiment was conducted under *equilibrium* conditions.

Magnetization was measured using an in house made Faraday-balance capacitive magnetometer [84] at 120 mK and 2 K and magnetic fields applied along three orientations:  $a^*$ , and  $b$ , and  $c$ . Additional measurements of magnetization carried out in the MPMS system at 2 K were used to calibrate the low temperature data and obtain absolute units (not shown here). Using the same setup, magnetic torque was measured up to 3 T and for temperature from 120 mK to 600 mK. The torque data correspond to the deflection of a small cantilever on which the sample is mounted. The magnetic field sweeping rate was also optimized to minimize heating due to eddy currents.

Magnetic susceptibility was measured using the Quantum Design Magnetic Property Measurement System (MPMS) SQUID Magnetometer. The temperature range from 1.8 K to 300 K was probed using a small polarizing field applied along three crystal directions:  $a^*$ , and  $b$ , and  $c$ . The probing field was  $\mu_0 H = 0.1 \text{ T}$ , where  $\mu_0$  denotes the permeability of vacuum.

Inelastic neutron scattering was used to investigate the crystal electric field induced scheme of total angular momentum states using the thermal neutron triple-axis-spectrometer EIGER at PSI. A powder sample of 11.1 g of  $\text{Nd}_3^{11}\text{BWO}_9$  was sealed in an aluminum can and installed in a standard  $^4\text{He}$  orange cryostat. A final wavelength of  $k_f = 2.66 \text{ \AA}^{-1}$  ( $\lambda = 2.36 \text{ \AA}$ ) was chosen, using a pyrolytic graphite filter to eliminate higher-order neutrons without further collimation. Data were measured at constant scattering angle,  $2\theta$ . The background was investigated to select the optimal value for the scattering angle, sufficiently far from the direct beam and low enough to have good counting and small decay in the signals due to magnetic structure factors. A value of  $2\theta = 10^\circ$  was chosen, and the incident energy was scanned at three different temperatures: 1.5 K, 100 K and 300 K.

Neutron single crystal diffraction was used to investigate the magnetic structures in the ordered phases. A single crystal sample of 18 mg in mass of  $\text{Nd}_3^{11}\text{BWO}_9$  and  $5.5 \times 1.4 \times 0.8 \text{ mm}^3$  was studied using two different instruments. Measurements with  $\mathbf{H} \parallel a^*$  were carried out at the Thermal Single Crystal Diffractometer ZEBRA at the Swiss Spallation Neutron Source, SINQ, in the Paul Scherrer Institut (PSI, Switzerland). The diffractometer was used in conjunction with a  $^3\text{He}$ - $^4\text{He}$  dilution refrigerator and a 6 T magnet. The crystal was aligned with its  $a^*$  axis vertical, the same direction as the applied magnetic field. Neutron wavelengths of  $\lambda = 2.314 \text{ \AA}$  and  $1.383 \text{ \AA}$  were selected, provided

by the PG(002) and Ge(220) monochromators. Additional measurements with  $\mathbf{H} \parallel \mathbf{c}$  were carried out in the time-of-flight diffractometer WISH at the ISIS facility in the Rutherford Appleton Laboratory, in the United Kingdom. The sample was mounted with its  $c$  axis vertical and parallel to the magnetic field. A  $^3\text{He}$ - $^4\text{He}$  dilution refrigerator and a 10 T magnet were used to access the ordered states in  $\text{Nd}_3\text{BWO}_9$ .

Neutron diffraction on powder samples is carried out at the High-Resolution Powder Diffractometer (HRPT) for Thermal Neutrons at PSI. 12 grams of  $\text{Nd}_3^{11}\text{BWO}_9$  is loaded with 10 bar of He gas in a copper can, for good thermal exchange. Diffraction data with a neutron wavelength of  $\lambda = 1.494 \text{ \AA}$  are collected for 8 h at a constant temperature of 700 mK. Refinement of the crystal structure is carried out with the Rietveld procedure using Fullprof, assuming 100 %  $^{11}\text{B}$  content.

Time-of-flight neutron diffraction data were measured on the disk chopper spectrometer IN5 at the Institut Laue-Langevin (Grenoble, France). A set of 340 single crystals (with total mass of 1.6 g) are coaligned in a copper sample holder and installed in a dilution-refrigerator stick with a base temperature of 50 mK. The crystals have their  $\mathbf{a}^*$  axis vertical. Neutron wavelengths of  $\lambda = 3.6 \text{ \AA}$  and  $\lambda = 6.5 \text{ \AA}$  are used to provide good coverage of reciprocal space and good resolution, respectively. Data are measured rotating the sample by 1 degree steps and counting an average time of 2 min per slice at 50 mK (360 degrees with  $\lambda = 3.6 \text{ \AA}$ , higher flux) and 5 min at 500 mK (250 degrees with  $\lambda = 6.5 \text{ \AA}$ ).

Large collections of magnetic reflections were measured at the thermal-neutron two-axis diffractometer D23 at ILL. A single crystal sample of 40 mg in mass (same as for ZEBRA and WISH above) is mounted on a copper holder with its  $c$  axis vertical, and installed in a dilution-refrigerator stick with a base temperature of 60 mK. To provide a magnetic field, a vertical 10 T cryomagnet with wide windows is used. A wavelength of  $\lambda = 1.283 \text{ \AA}$ , from a Cu (200) monochromator, is used to provide ample coverage in reciprocal space. A refinement of the nuclear unit cell is based on 318 nuclear reflections collected at 10 K. Afterwards, 248 magnetic reflections consistent with  $\mathbf{k} = (0, 0, 1/3)$  order are measured at zero field and 60 mK. Finally, we measure at 0.85 T and 60 mK 104 and 80 magnetic reflections corresponding to propagation vectors  $\mathbf{k}_+ = (1/3, 1/3, +1/3)$  and  $\mathbf{k}_- = (1/3, 1/3, -1/3)$ , respectively.



## Appendix B

# The crystal structures of $\text{Cs}_2\text{Cu}_2\text{Mo}_3\text{O}_{12}$ and $\text{Rb}_2\text{Cu}_2\text{Mo}_3\text{O}_{12}$

### B.1 Crystal structure of $\text{Cs}_2\text{Cu}_2\text{Mo}_3\text{O}_{12}$

The crystal structure of  $\text{Cs}_2\text{Cu}_2\text{Mo}_3\text{O}_{12}$  has never been properly determined in the literature. Here we provide such a refinement on single crystals at 300 K and at 100 K. Our results confirm the expected crystal structure ( $C2/c$  space group, similar to  $\text{Rb}_2\text{Cu}_2\text{Mo}_3\text{O}_{12}$ ) at both temperatures and show no change in symmetry down to 100 K.

The structure was solved using a prismatic crystal with approximate dimensions  $30 \times 10 \times 10 \mu\text{m}^3$  in a Bruker APEX-II instrument. Preliminary cell parameters were determined. A subsequent data collection was carried out to refine the crystal parameters and identify the chemical structure. An elevated number for redundancy of the measured reflections was selected to allow for an automated correction for X-ray absorption. Reflection intensities were analyzed and transformed into structural amplitudes using the suites SHELXL-2014.

After a few rounds of refinement the structure converged to a space group  $C2/c$  with the correct chemical composition. Some of the oxygen ions needed to be fixed in place manually to improve convergence. The final structure yielded a good agreement  $R = 5.6\%$ . The inclusion of anisotropic thermal parameters for all atoms give a final refinement of  $R = 4.3\%$ . The fractional coordinates for all atoms from the refinement are summarized in table B.3, alongside with the equivalent isotropic thermal parameters. Note that, having a monoclinic structure, these are calculated as

$$U_{eq} = (U_{11} + U_{22} \sin^2 \beta + U_{33} + 2U_{23} \cos \beta) / 3 \sin \beta \quad (\text{B.1})$$

A refinement of the structure at  $T = 100$  K was carried out on the same sample. The high temperature structure was taken as a starting point for the refinement of the low temperature data. A good refinement was readily obtained, with  $R = 5.4\%$ . Further inclusion of anisotropic thermal factors yields a final agreement factor of  $R = 3.1\%$ .

Our refinements are in agreement with the structure reported in [137]. Importantly, they show that the complex structure can correctly be described in a  $C2/c$  space group and that the structure remains unchanged down to 100 K. The refined space group is centrosymmetric. The presence of inversion center therefore forbids the spontaneous

**Table B.1:** Summary of X-ray refinements of the chemical structure of  $\text{Cs}_2\text{Cu}_2\text{Mo}_3\text{O}_{12}$  at 100 K and 300 K.

Characteristics	$T = 100$ K	$T = 300$ K
Crystal system	Monoclinic	Monoclinic
Space group	$C2/c$	$C2/c$
$a$ , Å	27.625(6)	27.9224(18)
$b$ , Å	5.121(2)	5.1265(3)
$c$ , Å	20.123(4)	20.2592(13)
$\beta$ , deg	106.88(3)	107.280(2)
$V$ , Å <sup>3</sup>	2724.1(14)	2769.1(3)
$Z$	8	8
$d_{calc}$ , g/cm <sup>3</sup>	4.23	4.18
$2\theta_{max}$ , deg	56.082	62.822
Measured reflections	44340	68466
Independent reflections	3304	4578
Refined parameters	174	174
R	0.031	0.043

appearance of a ferroelectric dipole moment. Cooling down from 300 K to 100 K is mainly reflected in a shortening of the crystallographic  $a$  axis, while the other axes remain almost unchanged.

## B.2 Low temperature crystal structures

Synchrotron radiation is used to monitor the crystal structure of both  $\text{Cs}_2\text{Cu}_2\text{Mo}_3\text{O}_{12}$  and  $\text{Rb}_2\text{Cu}_2\text{Mo}_3\text{O}_{12}$  down to base temperatures of 5 K. We present a combination of powder and single-crystal diffraction measurements that show no indications of structural phase transitions.

The powder-diffraction line BM01 at ESRF (France) provides an optimal setup to investigate the temperature dependence of the crystal structures. Powder diffraction patterns for both  $\text{Rb}_2\text{Cu}_2\text{Mo}_3\text{O}_{12}$  and  $\text{Cs}_2\text{Cu}_2\text{Mo}_3\text{O}_{12}$  have been measured in an extensive range of temperatures. The temperature evolution of the unit cell parameters is displayed for  $\text{Cs}_2\text{Cu}_2\text{Mo}_3\text{O}_{12}$  in Fig. B.1.(a-c). Similarly, temperature dependence is shown for  $\text{Rb}_2\text{Cu}_2\text{Mo}_3\text{O}_{12}$  in Fig. B.1.(d-f).

Data in Fig. B.1.(a-c) are refined based on the atomic positions extracted from single crystal measurements on  $\text{Cs}_2\text{Cu}_2\text{Mo}_3\text{O}_{12}$ , as given in above. Lattice parameters were refined using the Rietveld method, obtaining agreement factors of  $\chi < 2$  and  $R_F < 5\%$  in the whole temperature range. Unit parameters in Fig. B.1 show a smooth evolution from

**Table B.2:** Fractional coordinates and equivalent isotropic thermal parameters of the atomic basis of  $\text{Cs}_2\text{Cu}_2\text{Mo}_3\text{O}_{12}$  at 100 K.

Atom	$x/a$	$y/b$	$z/c$	$U_{eq}$
Cs(1)	0	0.17359(11)	0.75	0.01222(14)
Cs(2)	0.32191(2)	0.18638(8)	0.23093(2)	0.01217(12)
Cs(3)	0.25	0.25	0.5	0.01542(15)
Mo(1)	0.01712(2)	0.23496(9)	0.06894(3)	0.00728(14)
Mo(2)	0.18263(2)	0.25394(9)	0.10717(3)	0.00780(14)
Mo(3)	0.11275(2)	0.25156(9)	0.36754(3)	0.00736(14)
Cu(1)	0.42254(3)	0.24693(13)	0.04626(4)	0.00758(17)
Cu(2)	0.40071(3)	0.256883(13)	0.04204(4)	0.00767(18)
O(1)	0.5562(16)	0.4806(9)	0.6241(2)	0.0147(9)
O(2)	0.4972(15)	0.0545(9)	0.6213(2)	0.0128(9)
O(3)	0.44633(14)	0.9437(8)	0.4757(2)	0.0090(8)
O(4)	0.4586(14)	0.4494(8)	0.5188(2)	0.0090(8)
O(5)	0.30031(17)	0.6361(9)	0.3084(2)	0.0139(9)
O(6)	0.26170(17)	0.7837(8)	0.4161(2)	0.0145(10)
O(7)	0.34640(16)	0.0640(8)	0.3916(2)	0.0140(9)
O(8)	0.35953(15)	0.5446(8)	0.4561(2)	0.0118(8)
O(9)	0.4218(15)	0.1071(9)	0.7905(2)	0.0119(8)
O(10)	0.3266(17)	0.2921(8)	0.6389(3)	0.0123(9)
O(11)	0.4141(16)	0.5632(8)	0.6247(2)	0.0129(9)
O(12)	0.3836(15)	0.0487(8)	0.5567(2)	0.0097(8)

300 K down to 5 K, suggesting a consistent crystal structure in all the temperature range. There is a significant change in volume from 50 K upwards, which is mainly reflected in expansion of the  $a$  and  $c$  axes. In contrast, the length of the  $b$  axis starts to stagnate below 110 K, likely as a result of the onset of one-dimensional magnetic correlations. Interestingly, this axis shows a negative expansion coefficient below 50 K, and there is a significant expansion as temperature is lowered from 50 K to 5 K.

Data in Fig. B.1.(d-f) were obtained in a similar manner, obtaining agreement factors of  $\chi < 2.5$  and  $R_F < 5.5\%$  for each temperature. Lattice volume shows an almost linear temperature dependence almost down to the lowest measured temperature. In addition, in this system the crystallographic  $b$  axis is completely frozen below 138 K within the experimental resolution, as can be seen in Fig. B.1.(b). A small jump in unit cell volume is found at  $T = 13$  K, as shown with an arrow in Fig. B.1.(a). This jump is mostly reflected

**Table B.3:** Fractional coordinates and equivalent isotropic thermal parameters of the atomic basis of  $\text{Cs}_2\text{Cu}_2\text{Mo}_3\text{O}_{12}$  at 300 K.

Atom	$x/a$	$y/b$	$z/c$	$U_{eq}$
Cs(1)	0	0.17028(9)	0.75	0.02962(12)
Cs(2)	0.32211(2)	0.18822(7)	0.22993(2)	0.03142(10)
Cs(3)	0.25	0.25	0.5	0.04041(15)
Mo(1)	0.01705(2)	0.24338(7)	0.06900(2)	0.01479(9)
Mo(2)	0.18110(2)	0.24739(7)	0.10722(2)	0.01687(10)
Mo(3)	0.11195(2)	0.24560(6)	0.36868(2)	0.01471(9)
Cu(1)	0.42334(2)	0.25615(9)	0.04620(3)	0.01479(12)
Cu(2)	0.40146(2)	0.24091(9)	0.04231(3)	0.01536(12)
O(1)	0.55577(13)	0.4778(7)	0.62348(18)	0.0269(7)
O(2)	0.49819(13)	0.0508(7)	0.62106(18)	0.0271(7)
O(3)	0.44687(11)	0.9397(6)	0.47625(16)	0.0170(6)
O(4)	0.45907(11)	0.4475(6)	0.51933(16)	0.0170(6)
O(5)	0.30076(15)	0.6362(7)	0.30905(18)	0.0314(8)
O(6)	0.26433(16)	0.7868(8)	0.4158(2)	0.0367(10)
O(7)	0.34876(13)	0.0594(6)	0.39121(18)	0.0284(8)
O(8)	0.36040(11)	0.5398(6)	0.45536(17)	0.0213(6)
O(9)	0.42211(13)	0.1022(7)	0.70804(18)	0.0280(7)
O(10)	0.32795(13)	0.2901(7)	0.6372(2)	0.0266(7)
O(11)	0.41481(13)	0.5589(6)	0.62353(16)	0.0239(7)
O(12)	0.38478(11)	0.0439(6)	0.55657(16)	0.0179(6)

in a discontinuity in the crystallographic  $c$  axis, and a reduction of the monoclinic angle,  $\beta$ . Some light can be shed on the question whether this jump is associated with an actual phase transition from single-crystal diffraction.

Single crystal diffraction maps are also measured at BM01 for  $\text{Rb}_2\text{Cu}_2\text{Mo}_3\text{O}_{12}$  and  $\text{Cs}_2\text{Cu}_2\text{Mo}_3\text{O}_{12}$  are shown in Fig.B.2.(a,b) and Fig.B.2.(c,d), respectively. Both data set show a comparison of the diffraction spots in the  $(h0l)$  plane at two different temperatures. The small coverage of reciprocal space is due to the strong geometrical constraints associated to the helium refrigerator.

For  $\text{Rb}_2\text{Cu}_2\text{Mo}_3\text{O}_{12}$  a set of 168 reflections is collected for both temperatures in the range  $0 \leq h \leq 18$ ,  $-1 \leq k \leq 3$ ,  $-14 \leq l \leq 1$ . Reflections are integrated and indexed, resulting in both cases in a  $C2/c$  space group with a final  $R_{int} = 2.4\%$  for  $T = 170$  K (Fig.B.2.(c)) and  $R_{int} = 2.6\%$  for  $T = 5$  K (Fig.B.2.(d)). The data show no indications for

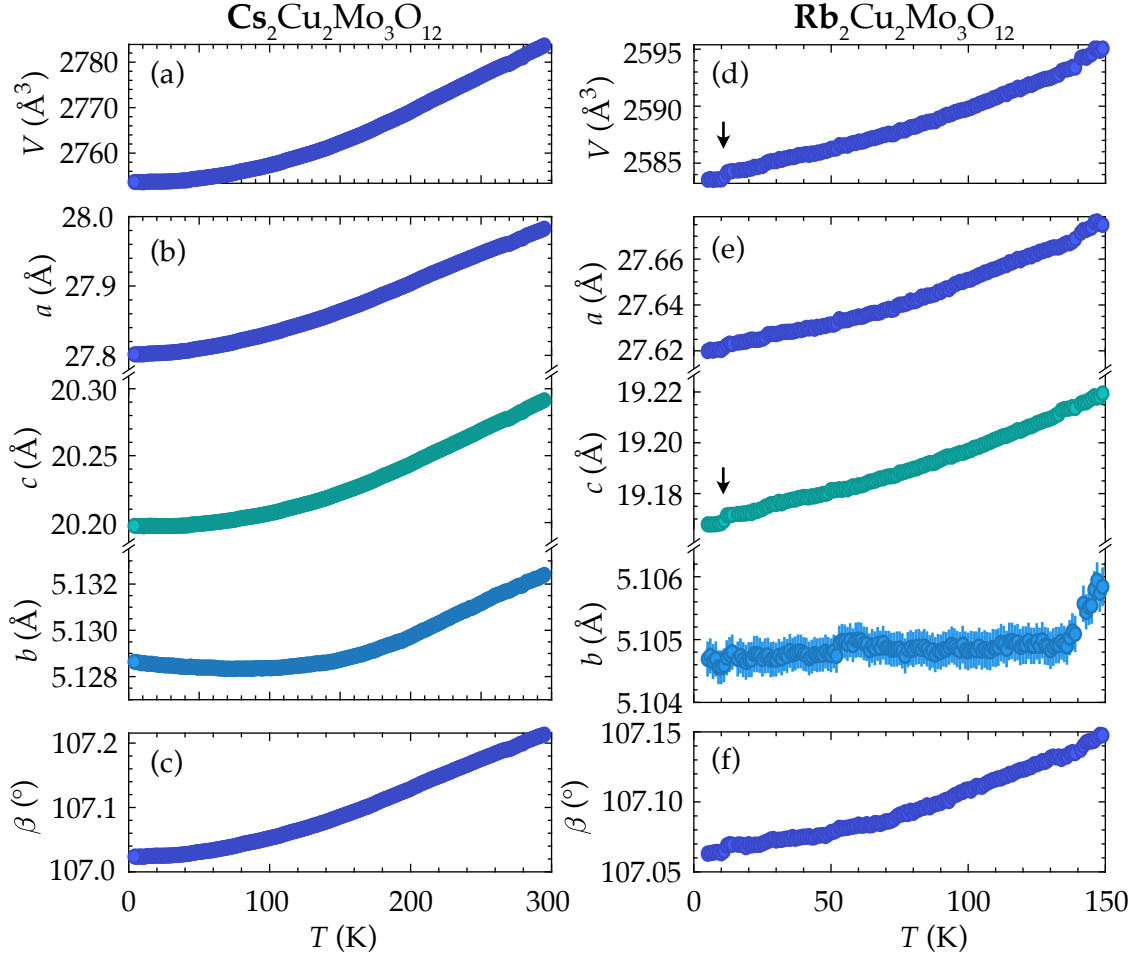


**Figure B.1:** Temperature dependence of unit cell parameters in  $\text{Cs}_2\text{Cu}_2\text{Mo}_3\text{O}_{12}$  (left, a-c) and  $\text{Rb}_2\text{Cu}_2\text{Mo}_3\text{O}_{12}$  (right, d-f) from powder diffraction. (a,d) Unit cell volume. (b,e) Lattice parameters  $a$ ,  $b$ , and  $c$ . Note the different scales for each of the axes. (c,f) Evolution of the monoclinic angle  $\beta$ .

additional reflections in the low temperature set.

For  $\text{Cs}_2\text{Cu}_2\text{Mo}_3\text{O}_{12}$  a set of 166 reflections is collected for both temperatures in the range  $0 \leq h \leq 10$ ,  $-3 \leq k \leq 1$ ,  $-4 \leq l \leq 8$ . Reflections are integrated and indexed, resulting in both cases in a  $C2/c$  space group, however with larger statistical R-factors:  $R_{int} = 34\%$  for  $T = 170$  K (Fig.B.2.(a)) and  $R_{int} = 40\%$  for  $T = 5$  K (Fig.B.2.(b)). While the data set shows a certain inconsistency with the expected space group, it shows no trace of new unindexed reflections, thus suggesting that no transition takes place.

A dedicated single-crystal experiment on  $\text{Cs}_2\text{Cu}_2\text{Mo}_3\text{O}_{12}$  was carried out on the single-crystal diffraction beamline I19 at the Diamond Light Source, which sits downstream a U21 undulator (21 dipole periods). We collected 17966 reflections at a base temperature of  $T = 11$  K using a very short wavelength ( $\lambda = 0.4959$   $\text{\AA}$ ) to have optimal access to reciprocal space. The integrated intensities show  $C2/c$  symmetry, resulting in an agreement factor  $R_{int} = 3\%$ . While a refinement of the structure is ongoing at the

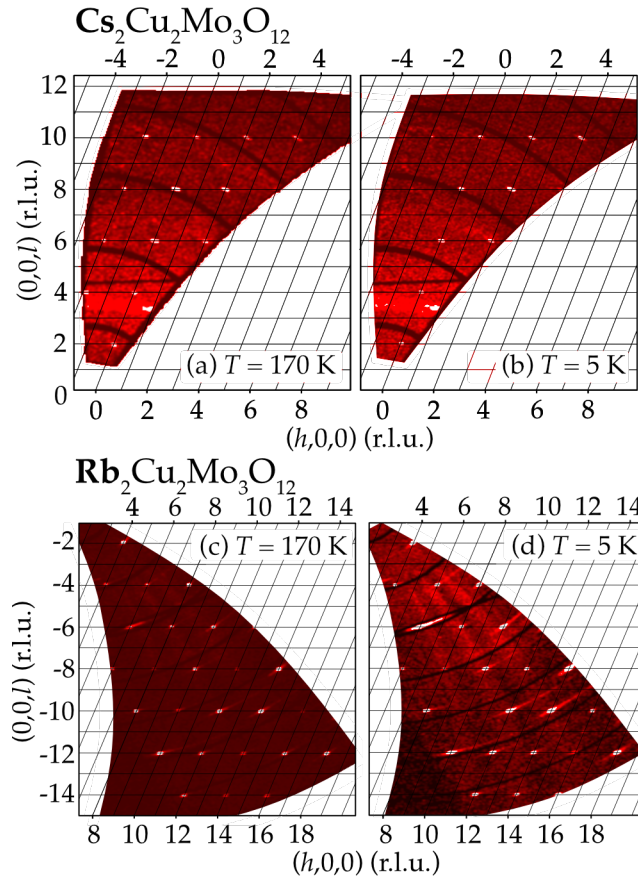


**Figure B.2:** Single crystal diffraction maps in the  $(h0l)$  plane of  $\text{Cs}_2\text{Cu}_2\text{Mo}_3\text{O}_{12}$  at (a) 170 K and (b) 5 K; and of  $\text{Rb}_2\text{Cu}_2\text{Mo}_3\text{O}_{12}$  at (c) 170 K and (d) 5 K. Solid lines show the unwarped lattice from indexation of the peaks, for reference. No new peaks are found in the low temperature data for either material.

moment, the low temperature set does not show evidence of a change in symmetry in  $\text{Cs}_2\text{Cu}_2\text{Mo}_3\text{O}_{12}$ . On a side note, the pattern on the cover of this text shows one typical measurement on I19. The figure shows a three-dimensional reconstruction of reciprocal space from single images, where each point represents one intense peak. Indexed peaks belonging to the sample are shown in orange, after being separated from the large mass of peaks coming from the sample environment (in blue).

In summary, the presented measurements shown no indication of a structural phase transition in either  $\text{Cs}_2\text{Cu}_2\text{Mo}_3\text{O}_{12}$  or  $\text{Rb}_2\text{Cu}_2\text{Mo}_3\text{O}_{12}$  down to  $\sim 5$  K. Structural determination of both structures at low temperatures will give a solid starting point to model these systems using numerical techniques, such as density functional theory.

## Appendix C

# The crystal structure of $\text{Nd}_3\text{BWO}_9$

The low-temperature structure of the quantum antiferromagnet  $\text{Nd}_3\text{BWO}_9$  is refined using neutron diffraction on a powder sample of 5 g. A fully substituted  $^{11}\text{B}$  sample is prepared on purpose of this purpose. The sample is placed in a copper can to ensure good thermal coupling and thermalization. Figure C.1 shows a powder diffraction pattern measured at  $T = 700$  mK with a wavelength  $\lambda = 1.494$  Å. Such a short wavelength provides access to a large range of reciprocal vectors.

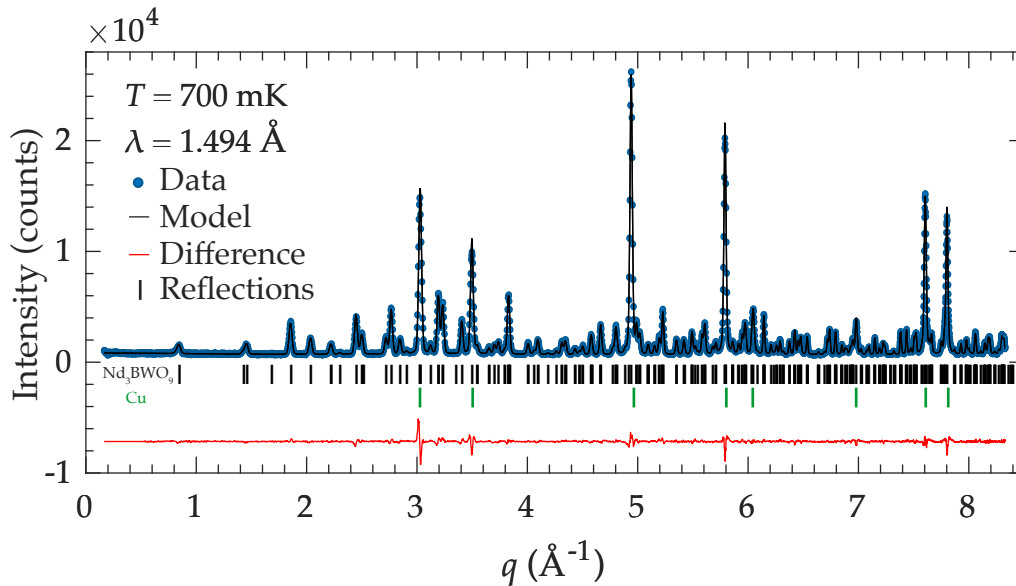


**Figure C.1:** Neutron powder diffraction pattern of  $\text{Nd}_3^{11}\text{BWO}_9$  at 700 mK and  $\lambda = 1.494$  Å. Data is fitted to the crystallographic model using Rietveld refinement. More prominent peaks come from the copper can in which the powder is installed for the measurement.

In the  $P6_3$  space group there is no inversion symmetry. As a result the  $z$  component of each nuclear position is determined only relative to other nuclei. There is freedom for an arbitrary shift in  $z$  of all nuclei in the unit cell. In this case, we fix the Boron to lie at position (0 0 0).

**Table C.1:** Atomic coordinates in  $\text{Nd}_3\text{BWO}_9$  from the refinement of data in Fig. C.1

Atom	$x$	$y$	$z$	$B_{iso}$
Nd	0.0837(3)	0.7230(3)	0.3437(11)	0.02(5)
B	0	0	0	1.90(14)
W	1/3	2/3	0.882(2)	0.67(15)
O <sub>1</sub>	0.0454(4)	0.8666(4)	0.9928(11)	0.33(8)
O <sub>2</sub>	0.1393(5)	0.5188(5)	0.1097(10)	0.71(9)
O <sub>3</sub>	0.1931(4)	0.4742(3)	0.6761(11)	0.13(8)

The data is fitted using the Rietveld method with two phases,  $\text{Nd}_3\text{BWO}_9$  and Cu. A good fit to the data is obtained with an agreement factor  $R_F = 4.1\%$  and given in Table C.1.

## Appendix D

# Details on the symmetry analysis of the magnetic structures in $\text{Nd}_3\text{BWO}_9$

In this appendix the details of the analysis of the symmetry, the irreducible representation decomposition and the associated basis vectors is provided based on the crystallographic space group  $P6_3$ . The decomposition of the magnetic representation and the corresponding basis vectors have been obtained from BasIrreps and the Bilbao Crystallographic Server.

### D.1 Basis vectors for $\mathbf{k} = (0,0,1/3)$

The decomposition of the magnetic representation gives 6 one-dimensional irreps, each entering the decomposition three times. The irreps are labeled as follows:

$$\Gamma_{DT} = 3\Gamma_{DT1}(1) \oplus 3\Gamma_{DT2}(1) \oplus 3\Gamma_{DT3}(1) \oplus 3\Gamma_{DT4}(1) \oplus 3\Gamma_{DT5}(1) \oplus 3\Gamma_{DT6}(1) \quad (\text{D.1})$$

where the number in brackets indicates the dimension of the irrep and the label  $DT$  refers to propagation vectors of the form  $(0,0,u)$  in the hexagonal system to which the space group belongs. The associated basis vectors for a general Wyckoff position for each irrep are given in the following tables.

### D.2 Basis vectors for $\mathbf{k} = (1/3,1/3,1/3)$

The decomposition of the magnetic representation with a propagation vector  $k_{P+} = (1/3,1/3,1/3)$  gives 3 one-dimensional irreps, each entering the decomposition six times. The irreps are labeled as follows:

$$\Gamma_P = 6\Gamma_{P1}(1) \oplus 6\Gamma_{P2}(1) \oplus 6\Gamma_{P3}(1) \quad (\text{D.2})$$

where the number in brackets indicates the dimension of the irrep and the label  $P$  refers to propagation vectors of the form  $(1/3,1/3,u)$  in the hexagonal system to which the space group belongs. The associated basis vectors for a general Wyckoff position for each irrep are given in the following tables. Note that the propagation vector  $k_{P-} = (1/3,1/3,-1/3)$  is inequivalent to  $k_{P+}$ , but admits an equal decomposition in terms of irreps.

IR	BV	Atom	BV components		
			$m_{\parallel x}$	$m_{\parallel y}$	$m_{\parallel z}$
$\psi_1$	1	1	1	0	0
	2	$-\frac{1}{2} + i\frac{\sqrt{3}}{2}$	0	0	0
	3	0	1	0	0
	4	0	$-\frac{1}{2} + i\frac{\sqrt{3}}{2}$	0	0
	5	-1	-1	0	0
	6	$\frac{1}{2} - i\frac{\sqrt{3}}{2}$	$\frac{1}{2} - i\frac{\sqrt{3}}{2}$	0	0
$\Gamma_{DT1}$	1	0	1	0	0
	2	0	$-\frac{1}{2} + i\frac{\sqrt{3}}{2}$	0	0
	3	-1	-1	0	0
	4	$\frac{1}{2} - i\frac{\sqrt{3}}{2}$	$\frac{1}{2} - i\frac{\sqrt{3}}{2}$	0	0
	5	1	0	0	0
	6	$-\frac{1}{2} + i\frac{\sqrt{3}}{2}$	0	0	0
$\psi_3$	1	0	0	1	0
	2	0	0	$\frac{1}{2} - i\frac{\sqrt{3}}{2}$	0
	3	0	0	1	0
	4	0	0	$\frac{1}{2} - i\frac{\sqrt{3}}{2}$	0
	5	0	0	1	0
	6	0	0	$\frac{1}{2} - i\frac{\sqrt{3}}{2}$	0

### D.3 Basis vectors for $\mathbf{k} = (0,0,0)$

The decomposition of the magnetic representation for the with a ferromagnetic propagation vector  $k_{GM} = (0,0,0)$  gives 2 one-dimensional and 2 two-dimensional irreps, each entering the decomposition three times. The irreps are labeled as follows:

$$\Gamma_{GM} = 3\Gamma_{GM1}(1) \oplus 3\Gamma_{GM2}(1) \oplus 3\Gamma_{GM3}(2) \oplus 3\Gamma_{GM4}(2) \quad (\text{D.3})$$

where the number in brackets indicates the dimension of the irrep and the label  $GM$  refers to a ferromagnetic propagation vector of the form  $(0,0,0)$  in the hexagonal system to which the space group belongs. The associated basis vectors for a general Wyckoff position for each irrep are given in the following tables.

IR	BV	Atom	BV components		
			$m_{\parallel a}$	$m_{\parallel b}$	$m_{\parallel c}$
$\Gamma_{DT2}$	$\psi_4$	1	1	0	0
		2	$-\frac{1}{2} + i\frac{\sqrt{3}}{2}$	0	0
		3	0	$-\frac{1}{2} - i\frac{\sqrt{3}}{2}$	0
		4	0	1	0
		5	$\frac{1}{2} - i\frac{\sqrt{3}}{2}$	$\frac{1}{2} - i\frac{\sqrt{3}}{2}$	0
		6	$\frac{1}{2} + i\frac{\sqrt{3}}{2}$	$\frac{1}{2} + i\frac{\sqrt{3}}{2}$	0
	$\psi_5$	1	0	1	0
		2	0	$-\frac{1}{2} + i\frac{\sqrt{3}}{2}$	0
		3	$\frac{1}{2} + i\frac{\sqrt{3}}{2}$	$\frac{1}{2} + i\frac{\sqrt{3}}{2}$	0
		4	0	-1	-1
		5	$-\frac{1}{2} + i\frac{\sqrt{3}}{2}$	0	0
		6	$-\frac{1}{2} - i\frac{\sqrt{3}}{2}$	0	0
	$\psi_6$	1	0	0	1
		2	0	0	$\frac{1}{2} - i\frac{\sqrt{3}}{2}$
		3	0	0	$-\frac{1}{2} - i\frac{\sqrt{3}}{2}$
		4	0	0	-1
		5	0	0	$-\frac{1}{2} + i\frac{\sqrt{3}}{2}$
		6	0	0	$\frac{1}{2} + i\frac{\sqrt{3}}{2}$

IR	BV	Atom	BV components		
			$m_{\parallel a}$	$m_{\parallel b}$	$m_{\parallel c}$
$\Gamma_{DT3}$	$\psi_7$	1	1	0	0
		2	$-\frac{1}{2} + i\frac{\sqrt{3}}{2}$	0	0
		3	0	$-\frac{1}{2} + i\frac{\sqrt{3}}{2}$	0
		4	0	$-\frac{1}{2} - i\frac{\sqrt{3}}{2}$	0
		5	$\frac{1}{2} + i\frac{\sqrt{3}}{2}$	$\frac{1}{2} + i\frac{\sqrt{3}}{2}$	0
		6	-1	-1	0
	$\psi_8$	1	0	1	0
		2	0	$-\frac{1}{2} + i\frac{\sqrt{3}}{2}$	0
		3	$\frac{1}{2} - i\frac{\sqrt{3}}{2}$	$\frac{1}{2} - i\frac{\sqrt{3}}{2}$	0
		4	$\frac{1}{2} + i\frac{\sqrt{3}}{2}$	$\frac{1}{2} + i\frac{\sqrt{3}}{2}$	0
		5	$-\frac{1}{2} - i\frac{\sqrt{3}}{2}$	0	0
		6	1	0	0
	$\psi_9$	1	0	0	1
		2	0	0	$\frac{1}{2} - i\frac{\sqrt{3}}{2}$
		3	0	0	$-\frac{1}{2} + i\frac{\sqrt{3}}{2}$
		4	0	0	$\frac{1}{2} + i\frac{\sqrt{3}}{2}$
		5	0	0	$-\frac{1}{2} - i\frac{\sqrt{3}}{2}$
		6	0	0	-1

IR	BV	Atom	BV components		
			$m_{\parallel a}$	$m_{\parallel b}$	$m_{\parallel c}$
$\Gamma_{DT4}$	$\psi_{10}$	1	1	0	0
		2	$\frac{1}{2} - i\frac{\sqrt{3}}{2}$	0	0
		3	0	1	0
		4	0	$\frac{1}{2} - i\frac{\sqrt{3}}{2}$	0
		5	0	-1	-1
		6	0	$-\frac{1}{2} + i\frac{\sqrt{3}}{2}$	$-\frac{1}{2} + i\frac{\sqrt{3}}{2}$
	$\psi_{11}$	1	0	1	0
		2	0	$\frac{1}{2} - i\frac{\sqrt{3}}{2}$	0
		3	0	-1	-1
		4	0	$-\frac{1}{2} + i\frac{\sqrt{3}}{2}$	$-\frac{1}{2} + i\frac{\sqrt{3}}{2}$
		5	1	0	0
		6	$\frac{1}{2} - i\frac{\sqrt{3}}{2}$	0	0
	$\psi_{12}$	1	0	0	1
		2	0	0	$-\frac{1}{2} + i\frac{\sqrt{3}}{2}$
		3	0	0	1
		4	0	0	$-\frac{1}{2} + i\frac{\sqrt{3}}{2}$
		5	0	0	1
		6	0	0	$-\frac{1}{2} + i\frac{\sqrt{3}}{2}$

IR	BV	Atom	BV components		
			$m_{\parallel a}$	$m_{\parallel b}$	$m_{\parallel c}$
	$\psi_{13}$	1	1	0	0
		2	$\frac{1}{2} - i\frac{\sqrt{3}}{2}$	0	0
		3	0	$-\frac{1}{2} - i\frac{\sqrt{3}}{2}$	0
		4	0	-1	0
		5	$\frac{1}{2} - i\frac{\sqrt{3}}{2}$	$\frac{1}{2} - i\frac{\sqrt{3}}{2}$	0
		6	$-\frac{1}{2} - i\frac{\sqrt{3}}{2}$	$-\frac{1}{2} - i\frac{\sqrt{3}}{2}$	0
$\Gamma_{DT5}$	$\psi_{14}$	1	0	1	0
		2	0	$\frac{1}{2} - i\frac{\sqrt{3}}{2}$	0
		3	$\frac{1}{2} + i\frac{\sqrt{3}}{2}$	$\frac{1}{2} + i\frac{\sqrt{3}}{2}$	0
		4	1	1	0
		5	$-\frac{1}{2} + i\frac{\sqrt{3}}{2}$	0	0
		6	$\frac{1}{2} + i\frac{\sqrt{3}}{2}$	0	0
	$\psi_{15}$	1	0	0	1
		2	0	0	$-\frac{1}{2} + i\frac{\sqrt{3}}{2}$
		3	0	0	$-\frac{1}{2} - i\frac{\sqrt{3}}{2}$
		4	0	0	1
		5	0	0	$-\frac{1}{2} + i\frac{\sqrt{3}}{2}$
		6	0	0	$-\frac{1}{2} - i\frac{\sqrt{3}}{2}$

IR	BV	Atom	BV components		
			$m_{\parallel a}$	$m_{\parallel b}$	$m_{\parallel c}$
$\Gamma_{DT6}$	$\psi_{16}$	1	1	0	0
		2	$\frac{1}{2} - i\frac{\sqrt{3}}{2}$	0	0
		3	0	$-\frac{1}{2} + i\frac{\sqrt{3}}{2}$	0
		4	0	$\frac{1}{2} + i\frac{\sqrt{3}}{2}$	0
		5	$\frac{1}{2} + i\frac{\sqrt{3}}{2}$	$\frac{1}{2} + i\frac{\sqrt{3}}{2}$	0
		6	0	1	1
	$\psi_{17}$	1	0	1	0
		2	0	$\frac{1}{2} - i\frac{\sqrt{3}}{2}$	0
		3	$\frac{1}{2} - i\frac{\sqrt{3}}{2}$	$\frac{1}{2} - i\frac{\sqrt{3}}{2}$	0
		4	$-\frac{1}{2} - i\frac{\sqrt{3}}{2}$	$-\frac{1}{2} - i\frac{\sqrt{3}}{2}$	0
		5	$-\frac{1}{2} - i\frac{\sqrt{3}}{2}$	0	0
		6	-1	0	0
	$\psi_{18}$	1	0	0	1
		2	0	0	$-\frac{1}{2} + i\frac{\sqrt{3}}{2}$
		3	0	0	$-\frac{1}{2} + i\frac{\sqrt{3}}{2}$
		4	0	0	$-\frac{1}{2} - i\frac{\sqrt{3}}{2}$
		5	0	0	$-\frac{1}{2} - i\frac{\sqrt{3}}{2}$
		6	0	0	1

IR	BV	Atom	BV components		
			$m_{\parallel a}$	$m_{\parallel b}$	$m_{\parallel c}$
$\Gamma_{P1}$	$\psi_1$	1	1	0	0
		2	0	$-\frac{1}{2} + i\frac{\sqrt{3}}{2}$	0
		3	$\frac{1}{2} + i\frac{\sqrt{3}}{2}$	$\frac{1}{2} + i\frac{\sqrt{3}}{2}$	0
	$\psi_2$	1	0	1	0
		2	$\frac{1}{2} - i\frac{\sqrt{3}}{2}$	$\frac{1}{2} - i\frac{\sqrt{3}}{2}$	0
		3	$-\frac{1}{2} - i\frac{\sqrt{3}}{2}$	0	0
	$\psi_3$	1	0	0	1
		2	0	0	$-\frac{1}{2} + i\frac{\sqrt{3}}{2}$
		3	0	0	$-\frac{1}{2} - i\frac{\sqrt{3}}{2}$

IR	BV	Atom	BV components		
			$m_{\parallel a}$	$m_{\parallel b}$	$m_{\parallel c}$
$\Gamma_{P2}$	$\psi_4$	1	1	0	0
		2	0	1	0
		3	-1	-1	0
	$\psi_5$	1	0	1	0
		2	-1	-1	0
		3	1	0	0
	$\psi_6$	1	0	0	1
		2	0	0	1
		3	0	0	1

IR	BV	Atom	BV components		
			$m_{\parallel a}$	$m_{\parallel b}$	$m_{\parallel c}$
$\Gamma_{P3}$	$\psi_7$	1	1	0	0
		2	0	$-\frac{1}{2} - i\frac{\sqrt{3}}{2}$	0
		3	$\frac{1}{2} - i\frac{\sqrt{3}}{2}$	$\frac{1}{2} - i\frac{\sqrt{3}}{2}$	0
	$\psi_8$	1	0	1	0
		2	$\frac{1}{2} + i\frac{\sqrt{3}}{2}$	$\frac{1}{2} + i\frac{\sqrt{3}}{2}$	0
		3	$-\frac{1}{2} + i\frac{\sqrt{3}}{2}$	0	0
	$\psi_9$	1	0	0	1
		2	0	0	$-\frac{1}{2} - i\frac{\sqrt{3}}{2}$
		3	0	0	$-\frac{1}{2} + i\frac{\sqrt{3}}{2}$

IR	BV	Atom	BV components		
			$m_{\parallel a}$	$m_{\parallel b}$	$m_{\parallel c}$
$\Gamma_{GM1}$	$\psi_1$	1	1	0	0
		2	-1	0	0
		3	0	1	0
		4	-1	-1	0
		5	1	1	0
		6	0	-1	0
	$\psi_2$	1	0	1	0
		2	0	-1	0
		3	-1	-1	0
		4	1	0	0
		5	-1	0	0
		6	1	1	0
	$\psi_3$	1	0	0	1
		2	0	0	1
		3	0	0	1
		4	0	0	1
		5	0	0	1
		6	0	0	1

IR	BV	Atom	BV components		
			$m_{\parallel a}$	$m_{\parallel b}$	$m_{\parallel c}$
$\Gamma_{GM2}$	$\psi_4$	1	1	0	0
		2	1	0	0
		3	0	1	0
		4	-1	-1	0
		5	-1	-1	0
		6	0	1	0
	$\psi_5$	1	0	1	0
		2	0	1	0
		3	-1	-1	0
		4	1	0	0
		5	1	0	0
		6	-1	-1	0
	$\psi_6$	1	0	0	1
		2	0	0	-1
		3	0	0	1
		4	0	0	1
		5	0	0	-1
		6	0	0	-1

IR	BV	Atom	BV components		
			$m_{\parallel a}$	$m_{\parallel b}$	$m_{\parallel c}$
$\Gamma_{GM3}$	$\psi_7$	1	1	0	0
		2	-1	0	0
		3	0	-1/2	0
		4	0	1/2	1/2
		5	0	-1/2	-1/2
		6	0	1/2	0
	$\psi_8$	1	0	1	0
		2	0	-1	0
		3	1/2	1/2	0
		4	-1/2	0	0
		5	1/2	0	0
		6	-1/2	-1/2	0
$\psi_9$	1	0	0	1	
	2	0	0	1	
	3	0	0	-1/2	
	4	0	0	-1/2	
	5	0	0	-1/2	
	6	0	0	-1/2	
$\psi_{10}$	1	0	0	0	
	2	0	0	0	
	3	0	1	0	
	4	1	1	0	
	5	-1	-1	0	
	6	0	-1	0	
$\psi_{11}$	1	0	0	0	
	2	0	0	0	
	3	-1	-1	0	
	4	-1	0	0	
	5	1	0	0	
	6	1	1	0	
$\psi_{12}$	1	0	0	0	
	2	0	0	0	
	3	0	0	1	
	4	0	0	-1	
	5	0	0	-1	
	6	0	0	1	

IR	BV	Atom	BV components		
			$m_{\parallel a}$	$m_{\parallel b}$	$m_{\parallel c}$
$\Gamma_{GM4}$	$\psi_{13}$	1	1	0	0
		2	1	0	0
		3	0	-1/2	0
		4	1/2	1/2	0
		5	1/2	1/2	0
		6	0	-1/2	0
	$\psi_{14}$	1	0	1	0
		2	0	1	0
		3	1/2	1/2	0
		4	-1/2	0	0
		5	-1/2	0	0
		6	1/2	1/2	0
	$\psi_{15}$	1	0	0	1
		2	0	0	-1
		3	0	0	-1/2
		4	0	0	-1/2
		5	0	0	1/2
		6	0	0	1/2
$\psi_{16}$	1	0	0	0	
	2	0	0	0	
	3	0	1	0	
	4	1	1	0	
	5	1	1	0	
	6	0	1	0	
$\psi_{17}$	1	0	0	0	
	2	0	0	0	
	3	-1	-1	0	
	4	-1	0	0	
	5	-1	0	0	
	6	-1	-1	0	
$\psi_{18}$	1	0	0	0	
	2	0	0	0	
	3	0	0	1	
	4	0	0	-1	
	5	0	0	1	
	6	0	0	-1	



# Bibliography

- [1] R. Laughlin and D Pines. “The Theory of Everything”. In: *Proceedings of the National Academy of Sciences* **97.1** (2000), pp. 28–31. URL: <https://www.pnas.org/doi/abs/10.1073/pnas.97.1.28>.
- [2] P. W. Anderson. “More Is Different”. In: *Science* **177.4047** (1972), pp. 393–396. URL: <https://www.science.org/doi/abs/10.1126/science.177.4047.393>.
- [3] R Peierls. “Quelques propriétés typiques des corps solides”. In: *Annales de l’institut Henri Poincaré*. Vol. 5. 3. 1935, pp. 177–222.
- [4] N. D. Mermin. “Crystalline Order in Two Dimensions”. In: *Phys. Rev.* **176** (1968), pp. 250–254. URL: <https://link.aps.org/doi/10.1103/PhysRev.176.250>.
- [5] N. D. Mermin and H. Wagner. “Absence of Ferromagnetism or Antiferromagnetism in One- or Two-Dimensional Isotropic Heisenberg Models”. In: *Phys. Rev. Lett.* **17** (1966), pp. 1133–1136. URL: <https://link.aps.org/doi/10.1103/PhysRevLett.17.1133>.
- [6] L. D. Landau and E. Lifshitz. *Statistical Physics, Third Edition, Part 1: Volume 5*. 1980.
- [7] J. Hu et al. “Rippling ultrafast dynamics of suspended 2D monolayers, graphene”. In: *Proceedings of the National Academy of Sciences* **113.43** (2016), E6555–E6561. URL: <https://doi.org/10.1073/pnas.1613818113>.
- [8] P. W. Anderson. “Antiferromagnetism. Theory of Superexchange Interaction”. In: *Phys. Rev.* **79** (1950), pp. 350–356. URL: <https://link.aps.org/doi/10.1103/PhysRev.79.350>.
- [9] N. Motoyama, H. Eisaki, and S. Uchida. “Magnetic Susceptibility of Ideal Spin 1/2 Heisenberg Antiferromagnetic Chain Systems,  $\text{Sr}_2\text{CuO}_3$  and  $\text{SrCuO}_2$ ”. In: *Phys. Rev. Lett.* **76** (1996), pp. 3212–3215. URL: <https://link.aps.org/doi/10.1103/PhysRevLett.76.3212>.
- [10] A. Vasiliev et al. “Milestones of low-D quantum magnetism”. In: *npj Quantum Materials* **3.1** (2018), p. 18. URL: <https://doi.org/10.1038/s41535-018-0090-7>.
- [11] D. Vaknin et al. “Antiferromagnetism in  $\text{La}_2\text{CuO}_{4-y}$ ”. In: *Phys. Rev. Lett.* **58** (1987), pp. 2802–2805. URL: <https://link.aps.org/doi/10.1103/PhysRevLett.58.2802>.
- [12] R. Coldea et al. “Spin Waves and Electronic Interactions in  $\text{La}_2\text{CuO}_4$ ”. In: *Phys. Rev. Lett.* **86** (2001), pp. 5377–5380. URL: <https://link.aps.org/doi/10.1103/PhysRevLett.86.5377>.

- [13] K Matan et al. “Pinwheel valence-bond solid and triplet excitations in the two-dimensional deformed kagome lattice”. In: *Nature Physics* **6.11** (2010), pp. 865–869. URL: <https://doi.org/10.1038/nphys1761>.
- [14] J Villain. “Two-level systems in a spin-glass model. I. General formalism and two-dimensional model”. In: *Journal of Physics C: Solid State Physics* **10.23** (1977), p. 4793. URL: <https://doi.org/10.1088/0022-3719/10/23/013>.
- [15] L. Schiff. *Quantum mechanics*. McGraw Hill, 1955.
- [16] M. Blume, R. E. Watson, and R. E. Peierls. “Theory of spin-orbit coupling in atoms I. Derivation of the spin-orbit coupling constant”. In: *Proceedings of the Royal Society of London. Series A. Mathematical and Physical Sciences* **270.1340** (1962), pp. 127–143. URL: <https://royalsocietypublishing.org/doi/abs/10.1098/rspa.1962.0207>.
- [17] R. Watson and A. Freeman. “Hyperfine Fields, Spin Orbit Coupling, and Nuclear Magnetic Moments of Rare-Earth Ions”. In: *Journal of Applied Physics* **33.3** (1962), pp. 1086–1088. URL: <https://doi.org/10.1063/1.1728611>.
- [18] A. J. Freeman and R. E. Watson. “Theoretical Investigation of Some Magnetic and Spectroscopic Properties of Rare-Earth Ions”. In: *Phys. Rev.* **127** (1962), pp. 2058–2075. URL: <https://link.aps.org/doi/10.1103/PhysRev.127.2058>.
- [19] D. Khomskii. “Multiferroics: Different ways to combine magnetism and ferroelectricity”. In: *Journal of Magnetism and Magnetic Materials* **306.1** (2006), pp. 1–8. ISSN: 0304-8853. URL: <https://www.sciencedirect.com/science/article/pii/S0304885306004239>.
- [20] Y. Tokura, S. Seki, and N. Nagaosa. “Multiferroics of spin origin”. In: *Reports on Progress in Physics* **77.7** (2014), p. 076501. URL: <https://dx.doi.org/10.1088/0034-4885/77/7/076501>.
- [21] N. A. Spaldin and M. Fiebig. “The renaissance of magnetoelectric multiferroics”. In: *Science* **309.5733** (2005), pp. 391–392.
- [22] N. A. Spaldin and R. Ramesh. “Advances in magnetoelectric multiferroics”. In: *Nature materials* **18.3** (2019), pp. 203–212.
- [23] H. Liu and X. Yang. “A brief review on perovskite multiferroics”. In: *Ferroelectrics* **507.1** (2017), pp. 69–85. URL: <https://doi.org/10.1080/00150193.2017.1283171>.
- [24] F. Kagawa et al. “Ferroelectricity in a one-dimensional organic quantum magnet”. In: *Nature Physics* **6.3** (2010), pp. 169–172. URL: <https://doi.org/10.1038/nphys1503>.
- [25] S. Kimura et al. “Ferroelectricity by Bose–Einstein condensation in a quantum magnet”. In: *Nat. Commun.* **7.1** (2016), p. 12822. URL: <https://doi.org/10.1038/ncomms12822>.
- [26] A. Pimenov et al. “Possible evidence for electromagnons in multiferroic manganites”. In: *Nature physics* **2.2** (2006), pp. 97–100. URL: <https://doi.org/10.1038/nphys212>.
- [27] A Pimenov et al. “Electromagnons in multiferroic manganites”. In: *Journal of Physics: Condensed Matter* **20.43** (2008), p. 434209. URL: <https://dx.doi.org/10.1088/0953-8984/20/43/434209>.

- [28] A. Pimenov et al. “Terahertz spectroscopy of electromagnons in  $\text{Eu}_{1-x}\text{Y}_x\text{MnO}_3$ ”. In: *Phys. Rev. B* **77** (2008), p. 014438. URL: <https://link.aps.org/doi/10.1103/PhysRevB.77.014438>.
- [29] A. Sushkov et al. “Electromagnons in multiferroic  $\text{YMn}_2\text{O}_5$  and  $\text{TbMn}_2\text{O}_5$ ”. In: *Physical review letters* **98.2** (2007), p. 027202.
- [30] R. Valdés Aguilar et al. “Origin of Electromagnon Excitations in Multiferroic  $\text{RMnO}_3$ ”. In: *Phys. Rev. Lett.* **102** (2009), p. 047203. URL: <https://link.aps.org/doi/10.1103/PhysRevLett.102.047203>.
- [31] K. Cao, F. Giustino, and P. G. Radaelli. “Theory of Electromagnons in  $\text{CuO}$ ”. In: *Phys. Rev. Lett.* **114** (2015), p. 197201. URL: <https://link.aps.org/doi/10.1103/PhysRevLett.114.197201>.
- [32] S. Furukawa, M. Sato, and S. Onoda. “Chiral Order and Electromagnetic Dynamics in One-Dimensional Multiferroic Cuprates”. In: *Phys. Rev. Lett.* **105** (2010), p. 257205. URL: <https://link.aps.org/doi/10.1103/PhysRevLett.105.257205>.
- [33] H. E. Stanley. *Introduction to Phase Transitions and Critical Phenomena*. Oxford university press, 1987.
- [34] A. Gonis et al. “Use of the Ising model in the study of substitutional alloys”. In: *Phys. Rev. B* **51** (1995), pp. 2122–2131. URL: <https://link.aps.org/doi/10.1103/PhysRevB.51.2122>.
- [35] D. Bitko, T. F. Rosenbaum, and G. Aeppli. “Quantum Critical Behavior for a Model Magnet”. In: *Phys. Rev. Lett.* **77** (1996), pp. 940–943. URL: <https://link.aps.org/doi/10.1103/PhysRevLett.77.940>.
- [36] V. P. LaBella et al. “Microscopic View of a Two-Dimensional Lattice-Gas Ising System within the Grand Canonical Ensemble”. In: *Phys. Rev. Lett.* **84** (2000), pp. 4152–4155. URL: <https://link.aps.org/doi/10.1103/PhysRevLett.84.4152>.
- [37] S. Sachdev. “Quantum criticality: competing ground states in low dimensions”. In: *Science* **288.5465** (2000), pp. 475–480.
- [38] P. Coleman and A. J. Schofield. “Quantum criticality”. In: *Nature* **433.7023** (2005), pp. 226–229. URL: <https://doi.org/10.1038/nature03279>.
- [39] S. Sachdev. “Quantum magnetism and criticality”. In: *Nature Physics* **4.3** (2008), pp. 173–185. URL: <https://doi.org/10.1038/nphys894>.
- [40] I. Frérot and T. Roscilde. “Reconstructing the quantum critical fan of strongly correlated systems using quantum correlations”. In: *Nature communications* **10.1** (2019), p. 577. URL: <https://doi.org/10.1038/s41467-019-08324-9>.
- [41] Bose. “Plancks gesetz und lichtquantenhypothese”. In: *Zeitschrift für Physik* **26.1** (1924), pp. 178–181. URL: <https://doi.org/10.1007/BF01327326>.
- [42] A. Einstein. “Quantentheorie des einatomigen idealen Gases. Zweite Abhandlung”. In: (2005), pp. 245–257. URL: <https://onlinelibrary.wiley.com/doi/abs/10.1002/3527608958.ch28>.
- [43] A. J. Leggett et al. *Quantum liquids: Bose condensation and Cooper pairing in condensed-matter systems*. Oxford university press, 2006.

- [44] L. V. Keldysh and A. N. Kozlov. “Collective properties of excitons in semiconductors”. In: *Sov. Phys. JETP* **27.3** (1968), p. 521. URL: [http://jetp.ac.ru/cgi-bin/dn/e\\_027.03\\_0521.pdf](http://jetp.ac.ru/cgi-bin/dn/e_027.03_0521.pdf).
- [45] J. Kasprzak et al. “Bose–Einstein condensation of exciton polaritons”. In: *Nature (London)* **443**.7110 (2006), p. 409. URL: <https://doi.org/10.1038/nature05131>.
- [46] S. O. Demokritov et al. “Bose–Einstein condensation of quasi-equilibrium magnons at room temperature under pumping”. In: *Nature (London)* **443**.7110 (2006), p. 430. URL: <https://doi.org/10.1038/nature05117>.
- [47] N. P. Proukakis, D. W. Snoke, and P. B. Littlewood, eds. *Universal Themes of Bose-Einstein Condensation*. Cambridge: Cambridge University Press, 2017. ISBN: 9781107085695. URL: <https://doi.org/10.1017/9781316084366>.
- [48] A. C. Anderson et al. “Calorimetric Investigation of the Hyperfine Interactions in Metallic Nd, Sm, and Dy”. In: *Phys. Rev.* **183** (1969), pp. 546–552. URL: <https://link.aps.org/doi/10.1103/PhysRev.183.546>.
- [49] M. Greiner et al. “Quantum phase transition from a superfluid to a Mott insulator in a gas of ultracold atoms”. In: *Nature (London)* **415**.6867 (2002), p. 39. URL: <https://doi.org/10.1038/415039a>.
- [50] M. H. Anderson et al. “Observation of Bose-Einstein Condensation in a Dilute Atomic Vapor”. In: *Science* **269**.5221 (1995), p. 198. URL: <https://doi.org/10.1126/science.269.5221.198>.
- [51] K. B. Davis et al. “Bose-Einstein Condensation in a Gas of Sodium Atoms”. In: *Phys. Rev. Lett.* **75** (1995), p. 3969. URL: <https://link.aps.org/doi/10.1103/PhysRevLett.75.3969>.
- [52] E. G. Batyev and L. S. Braginski. “Antiferromagnet in a strong magnetic field: analogy with Bose gas”. In: *Sov. Phys. JETP* **60** (1984), p. 781. URL: [http://www.jetp.ac.ru/cgi-bin/dn/e\\_060\\_04\\_0781.pdf](http://www.jetp.ac.ru/cgi-bin/dn/e_060_04_0781.pdf).
- [53] T. Giamarchi and A. M. Tsvelik. “Coupled ladders in a magnetic field”. In: *Phys. Rev. B* **59** (1999), p. 11398. URL: <https://link.aps.org/doi/10.1103/PhysRevB.59.11398>.
- [54] T. Nikuni et al. “Bose-Einstein Condensation of Dilute Magnons in  $\text{TlCuCl}_3$ ”. In: *Phys. Rev. Lett.* **84** (2000), p. 5868. URL: <https://link.aps.org/doi/10.1103/PhysRevLett.84.5868>.
- [55] T. Giamarchi, C. Rüegg, and O. Tchernyshyov. “Bose–Einstein condensation in magnetic insulators”. In: *Nat. Phys.* **4.3** (2008), p. 198. URL: <https://doi.org/10.1038/nphys893>.
- [56] V. Zapf, M. Jaime, and C. D. Batista. “Bose-Einstein condensation in quantum magnets”. In: *Rev. Mod. Phys.* **86** (2014), p. 563. URL: <https://link.aps.org/doi/10.1103/RevModPhys.86.563>.
- [57] T. Matsubara and H. Matsuda. “A lattice model of liquid helium, I”. In: *Progress of Theoretical Physics* **16.6** (1956), pp. 569–582. URL: <https://doi.org/10.1143/PTP.16.569>.

- [58] M. A. Continentino. “Interplay of Quantum and Classical Fluctuations Near Quantum Critical Points”. In: *Braz. J. Phys.* **41.2** (2011), p. 201. URL: <https://doi.org/10.1007/s13538-011-0025-2>.
- [59] P. W. Anderson. “Resonating valence bonds: A new kind of insulator?” In: *Mater. Res. Bull.* **8.2** (1973), pp. 153–160. URL: <https://www.sciencedirect.com/science/article/pii/0025540873901670>.
- [60] L. Balents. “Spin liquids in frustrated magnets”. In: *nature* **464.7286** (2010), pp. 199–208. URL: <https://doi.org/10.1038/nature08917>.
- [61] L. Savary and L. Balents. “Quantum spin liquids: a review”. In: *Rep. Prog. Phys.* **80.1** (2016), p. 016502. URL: <https://iopscience.iop.org/article/10.1088/0034-4885/80/1/016502>.
- [62] Y. Zhou, K. Kanoda, and T.-K. Ng. “Quantum spin liquid states”. In: *Rev. Mod. Phys.* **89** (2017), p. 025003. URL: <https://link.aps.org/doi/10.1103/RevModPhys.89.025003>.
- [63] J. Wen et al. “Experimental identification of quantum spin liquids”. In: *npj Quantum Materials* **4.1** (2019), p. 12. URL: <https://doi.org/10.1038/s41535-019-0151-6>.
- [64] J. R. Chamorro, T. M. McQueen, and T. T. Tran. “Chemistry of quantum spin liquids”. In: *Chem. Rev.* **121.5** (2020), pp. 2898–2934. URL: <https://doi.org/10.1021/acs.chemrev.0c00641>.
- [65] H. Bethe. “Zur theorie der metalle: I. Eigenwerte und eigenfunktionen der linearen atomkette”. In: *Zeitschrift für Physik* **71.3** (1931), pp. 205–226. URL: <https://doi.org/10.1007/BF01341708>.
- [66] B. Lake et al. “Quantum criticality and universal scaling of a quantum antiferromagnet”. In: *Nat. Mater.* **4.4** (2005), pp. 329–334. URL: <https://doi.org/10.1038/nmat1327>.
- [67] M. B. Stone et al. “Extended Quantum Critical Phase in a Magnetized Spin- $\frac{1}{2}$  Antiferromagnetic Chain”. In: *Phys. Rev. Lett.* **91** (2003), p. 037205. URL: <https://link.aps.org/doi/10.1103/PhysRevLett.91.037205>.
- [68] C Broholm et al. “Quantum spin liquids”. In: *Science* **367.6475** (2020). URL: <https://www.science.org/doi/10.1126/science.aay0668>.
- [69] H. T. Diep et al. *Frustrated spin systems*. World scientific, 2013.
- [70] M. Hermele et al. “Properties of an algebraic spin liquid on the kagome lattice”. In: *Phys. Rev. B* **77.22** (2008), p. 224413. URL: <https://link.aps.org/doi/10.1103/PhysRevB.77.224413>.
- [71] S. Yan, D. A. Huse, and S. R. White. “Spin-liquid ground state of the  $S = 1/2$  kagome Heisenberg antiferromagnet”. In: *Science* **332.6034** (2011), pp. 1173–1176. URL: <https://www.science.org/doi/10.1126/science.1201080>.
- [72] H. J. Liao et al. “Gapless Spin-Liquid Ground State in the  $S = 1/2$  Kagome Antiferromagnet”. In: *Phys. Rev. Lett.* **118** (2017), p. 137202. URL: <https://link.aps.org/doi/10.1103/PhysRevLett.118.137202>.

- [73] A. Zorko et al. “Coexistence of magnetic order and persistent spin dynamics in a quantum kagome antiferromagnet with no intersite mixing”. In: *Phys. Rev. B* **99** (2019), p. 214441. URL: <https://link.aps.org/doi/10.1103/PhysRevB.99.214441>.
- [74] Y. Ihara et al. “Anisotropic magnetic excitations from single-chirality antiferromagnetic state in Ca-kapellasite”. In: *Phys. Rev. Res.* **2** (2020), p. 023269. URL: <https://link.aps.org/doi/10.1103/PhysRevResearch.2.023269>.
- [75] A. Olariu et al. “ $^{17}\text{O}$  NMR Study of the Intrinsic Magnetic Susceptibility and Spin Dynamics of the Quantum Kagome Antiferromagnet  $\text{ZnCu}_3(\text{OH})_6\text{Cl}_2$ ”. In: *Phys. Rev. Lett.* **100** (2008), p. 087202. URL: <https://link.aps.org/doi/10.1103/PhysRevLett.100.087202>.
- [76] B Fåk et al. “Kapellasite: A kagome quantum spin liquid with competing interactions”. In: *Physical review letters* **109.3** (2012), p. 037208.
- [77] M. Iqbal, D. Poilblanc, and N. Schuch. “Gapped  $\text{Z}_2$  spin liquid in the breathing kagome Heisenberg antiferromagnet”. In: *Phys. Rev. B* **101.15** (2020), p. 155141. URL: <https://link.aps.org/doi/10.1103/PhysRevB.101.155141>.
- [78] M. Fujihala et al. “Gapless spin liquid in a square-kagome lattice antiferromagnet”. In: *Nature communications* **11.1** (2020), p. 3429. URL: <https://doi.org/10.1038/s41467-020-17235-z>.
- [79] V. Zapf, M. Jaime, and C. D. Batista. “Bose-Einstein condensation in quantum magnets”. In: *Rev. Mod. Phys.* **86.2** (2014), p. 563. URL: <https://link.aps.org/doi/10.1103/RevModPhys.86.563>.
- [80] M. Balli et al. “Advanced materials for magnetic cooling: Fundamentals and practical aspects”. In: *Applied Physics Reviews* **4.2** (2017). URL: <https://doi.org/10.1063/1.4983612>.
- [81] N. A. Spaldin. “A beginner’s guide to the modern theory of polarization”. In: *Journal of Solid State Chemistry* **195** (2012). Polar Inorganic Materials: Design Strategies and Functional Properties, pp. 2–10. ISSN: 0022-4596. URL: <https://www.sciencedirect.com/science/article/pii/S0022459612003234>.
- [82] V. F. Sears. “Neutron scattering lengths and cross sections”. In: *Neutron news* **3.3** (1992), pp. 26–37. URL: <https://doi.org/10.1080/10448639208218770>.
- [83] M. Buchner et al. “Tutorial: Basic principles, limits of detection, and pitfalls of highly sensitive SQUID magnetometry for nanomagnetism and spintronics”. In: *Journal of Applied Physics* (2018). URL: <https://api.semanticscholar.org/CorpusID:125658207>.
- [84] D. Blosser, L. Facheris, and A. Zheludev. “Miniature capacitive Faraday force magnetometer for magnetization measurements at low temperatures and high magnetic fields”. In: *Rev. of Sci. Instr.* **91.7** (2020), p. 073905. URL: <https://doi.org/10.1063/5.0005850>.
- [85] Y. Feng, K. Y. Povarov, and A. Zheludev. “Magnetic phase diagram of the strongly frustrated quantum spin chain system  $\text{PbCuSO}_4(\text{OH})_2$  in tilted magnetic fields”. In: *Phys. Rev. B* **98** (2018), p. 054419. URL: <https://link.aps.org/doi/10.1103/PhysRevB.98.054419>.

- [86] A Majchrowski, E Michalski, and A Brenier. "Growth and spectroscopic characterization of Nd<sub>3</sub>BWO<sub>9</sub> single crystal". In: *Journal of Crystal Growth* **247.3** (2003), pp. 467–471. ISSN: 0022-0248. URL: <https://www.sciencedirect.com/science/article/pii/S0022024802020638>.
- [87] Y. Tokura, S. Seki, and N. Nagaosa. "Multiferroics of spin origin". In: *Rep. Prog. Phys.* **77.7** (2014), p. 076501. URL: <https://doi.org/10.1088%2F0034-4885%2F77%2F7%2F076501>.
- [88] J. W. Kim et al. "Manifestation of magnetic quantum fluctuations in the dielectric properties of a multiferroic". In: *Nat. Commun.* **5.1** (2014), p. 4419. URL: <https://doi.org/10.1038/ncomms5419>.
- [89] T.-h. Arima. "Ferroelectricity Induced by Proper-Screw Type Magnetic Order". In: *J. Phys. Soc. Jpn.* **76.7** (2007), p. 073702. URL: <https://doi.org/10.1143/JPSJ.76.073702>.
- [90] C. Jia et al. "Microscopic theory of spin-polarization coupling in multiferroic transition metal oxides". In: *Phys. Rev. B* **76** (2007), p. 144424. URL: <https://link.aps.org/doi/10.1103/PhysRevB.76.144424>.
- [91] S. W. Lovesey. *Theory of Neutron Scattering from Condensed Matter*. Oxford, 1984.
- [92] S. F. Solodovnikov and Z. A. Solodovnikova. "New structure type in the morphotropic series of A<sub>2</sub><sup>+</sup>M<sub>2</sub><sup>2+</sup>(MoO<sub>4</sub>)<sub>3</sub>: crystal structure of Rb<sub>2</sub>Cu<sub>2</sub>(MoO<sub>4</sub>)<sub>3</sub>". In: *J. Struct. Chem.* **38.5** (1997), p. 765. URL: <https://doi.org/10.1007/BF02763890>.
- [93] M. Hase et al. "Magnetic properties of Rb<sub>2</sub>Cu<sub>2</sub>Mo<sub>3</sub>O<sub>12</sub> including a one-dimensional spin-1/2 Heisenberg system with ferromagnetic first-nearest-neighbor and antiferromagnetic second-nearest-neighbor exchange interactions". In: *Phys. Rev. B* **70** (2004), p. 104426. URL: <https://link.aps.org/doi/10.1103/PhysRevB.70.104426>.
- [94] M. Hase et al. "Magnetism of A<sub>2</sub>Cu<sub>2</sub>Mo<sub>3</sub>O<sub>12</sub> (A = Rb or Cs): Model compounds of a one-dimensional spin-1/2 Heisenberg system with ferromagnetic first-nearest-neighbor and antiferromagnetic second-nearest-neighbor interactions". In: *J. Appl. Phys.* **97.10** (2005), 10B303.
- [95] Y. Yasui et al. "Dielectric anomaly in the quasi-one-dimensional frustrated spin- $\frac{1}{2}$  system Rb<sub>2</sub>(Cu<sub>1-x</sub>M<sub>x</sub>)<sub>2</sub>Mo<sub>3</sub>O<sub>12</sub> (M = Ni and Zn)". In: *Phys. Rev. B* **87** (2013), p. 054411. URL: <https://link.aps.org/doi/10.1103/PhysRevB.87.054411>.
- [96] Y. Yasui et al. "Magnetic field induced ferroelectric transition of quasi one-dimensional frustrated quantum spin chain system Rb<sub>2</sub>Cu<sub>2</sub>Mo<sub>3</sub>O<sub>12</sub>". In: *J. Appl. Phys.* **113.17** (2013), p. 17D910. URL: <https://aip.scitation.org/doi/10.1063/1.4795844>.
- [97] Y. Yasui et al. "Low Temperature Magnetic Properties of Frustrated Quantum Spin Chain System Rb<sub>2</sub>Cu<sub>2</sub>Mo<sub>3</sub>O<sub>12</sub>". In: *JPS Conf. Proc.* **3** (2014), p. 014014.
- [98] S. Hayashida et al. "One- and three-dimensional quantum phase transitions and anisotropy in Rb<sub>2</sub>Cu<sub>2</sub>Mo<sub>3</sub>O<sub>12</sub>". In: *Phys. Rev. B* **100** (2019), p. 134427. URL: <https://link.aps.org/doi/10.1103/PhysRevB.100.134427>.

- [99] N. Reynolds et al. “Magnetoelectric coupling without long-range magnetic order in the spin- $\frac{1}{2}$  multiferroic  $\text{Rb}_2\text{Cu}_2\text{Mo}_3\text{O}_{12}$ ”. In: *Phys. Rev. B* **99** (2019), p. 214443. URL: <https://link.aps.org/doi/10.1103/PhysRevB.99.214443>.
- [100] H. Ueda et al. “Emergent spin-1 Haldane gap and ferroelectricity in a frustrated spin- $\frac{1}{2}$  ladder”. In: *Phys. Rev. B* **101** (2020), 140408(R). URL: <https://link.aps.org/doi/10.1103/PhysRevB.101.140408>.
- [101] H. Kuroe et al. “Effects of Hydrostatic Pressure on  $\text{Rb}_2\text{Cu}_2\text{Mo}_3\text{O}_{12}$ : a One-Dimensional System with Competing Ferromagnetic and Antiferromagnetic Interactions”. In: *AIP Conf. Proc.* **850.1** (2006), p. 1049. URL: <https://aip.scitation.org/doi/10.1063/1.2355063>.
- [102] T. Hamasaki et al. “Effects of high pressure on  $\text{A}_2\text{Cu}_2\text{Mo}_3\text{O}_{12}$  ( $\text{A} = \text{Rb}, \text{Cs}$ ): A one-dimensional system with competing ferromagnetic and antiferromagnetic interactions”. In: *J. Magn. Magn. Mater.* **310.2** (2007), e394. URL: <http://www.sciencedirect.com/science/article/pii/S0304885306015782>.
- [103] A. Yagi et al. “NMR study on the competing spin chain  $\text{Rb}_2\text{Cu}_2\text{Mo}_3\text{O}_{12}$ ”. In: *J. Phys.: Conf. Ser.* **828.1** (2017), p. 012016.
- [104] K. Matsui et al. “Rb-NMR study of the quasi-one-dimensional competing spin-chain compound  $\text{Rb}_2\text{Cu}_2\text{Mo}_3\text{O}_{12}$ ”. In: *Phys. Rev. B* **96** (2017), 220402(R). URL: <https://link.aps.org/doi/10.1103/PhysRevB.96.220402>.
- [105] K. Tomiyasu et al. “Conversion method of powder inelastic scattering data for one-dimensional systems”. In: *Appl. Phys. Lett.* **94.9** (2009), p. 092502. URL: <https://aip.scitation.org/doi/10.1063/1.3089566>.
- [106] S. Ohira-Kawamura et al. “Magnetic Properties of One-Dimensional Quantum Spin System  $\text{Rb}_2\text{Cu}_2\text{Mo}_3\text{O}_{12}$  Studied by Muon Spin Relaxation”. In: *JPS Conf. Proc.* **21** (2018), p. 011007. URL: <https://journals.jps.jp/doi/abs/10.7566/JPSCP.21.011007>.
- [107] T. Hikihara et al. “Vector chiral and multipolar orders in the spin- $\frac{1}{2}$  frustrated ferromagnetic chain in magnetic field”. In: *Phys. Rev. B* **78** (2008), p. 144404. URL: <https://link.aps.org/doi/10.1103/PhysRevB.78.144404>.
- [108] J. Sudan, A. Lüscher, and A. M. Läuchli. “Emergent multipolar spin correlations in a fluctuating spiral: The frustrated ferromagnetic spin- $\frac{1}{2}$  Heisenberg chain in a magnetic field”. In: *Phys. Rev. B* **80** (2009), 140402(R). URL: <https://link.aps.org/doi/10.1103/PhysRevB.80.140402>.
- [109] S. Gopalan, T. M. Rice, and M. Sigrist. “Spin ladders with spin gaps: A description of a class of cuprates”. In: *Phys. Rev. B* **49** (1994), pp. 8901–8910. URL: <https://link.aps.org/doi/10.1103/PhysRevB.49.8901>.
- [110] T. Barnes et al. “Excitation spectrum of Heisenberg spin ladders”. In: *Phys. Rev. B* **47** (1993), pp. 3196–3203. URL: <https://link.aps.org/doi/10.1103/PhysRevB.47.3196>.
- [111] K. Kojima et al. “Magnetic Behavior of the 2-Leg and 3-Leg Spin Ladder Cuprates  $\text{Sr}_{n-1}\text{Cu}_{n+1}\text{O}_{2n}$ ”. In: *Phys. Rev. Lett.* **74** (1995), pp. 2812–2815. URL: <https://link.aps.org/doi/10.1103/PhysRevLett.74.2812>.

- [112] M. Bocquet et al. “Finite-temperature dynamical magnetic susceptibility of quasi-one-dimensional frustrated spin- $\frac{1}{2}$  Heisenberg antiferromagnets”. In: *Phys. Rev. B* **64** (2001), p. 094425. URL: <https://link.aps.org/doi/10.1103/PhysRevB.64.094425>.
- [113] D. Blosser et al. “Finite-temperature correlations in a quantum spin chain near saturation”. In: *Phys. Rev. B* **96** (2017), p. 134406. URL: <https://link.aps.org/doi/10.1103/PhysRevB.96.134406>.
- [114] H. Kuroe et al. “Electric Polarization Induced by Néel Order without Magnetic Superlattice: Experimental Study of  $\text{Cu}_3\text{Mo}_2\text{O}_9$  and Numerical Study of a Small Spin Cluster”. In: *J. Phys. Soc. Jpn.* **80.8** (2011), p. 083705. URL: <https://doi.org/10.1143/JPSJ.80.083705>.
- [115] T. Hamasaki et al. “Successive phase transitions to antiferromagnetic and weak-ferromagnetic long-range order in the quasi-one-dimensional antiferromagnet  $\text{Cu}_3\text{Mo}_2\text{O}_9$ ”. In: *Phys. Rev. B* **77** (2008), p. 134419. URL: <https://link.aps.org/doi/10.1103/PhysRevB.77.134419>.
- [116] S. Kimura et al. “Magnetoelectric effect in the quantum spin gap system  $\text{TlCuCl}_3$ ”. In: *Phys. Rev. B* **95** (2017), p. 184420. URL: <https://link.aps.org/doi/10.1103/PhysRevB.95.184420>.
- [117] M. Mostovoy. “Ferroelectricity in Spiral Magnets”. In: *Phys. Rev. Lett.* **96** (2006), p. 067601. URL: <https://link.aps.org/doi/10.1103/PhysRevLett.96.067601>.
- [118] H. Katsura, N. Nagaosa, and A. V. Balatsky. “Spin Current and Magnetoelectric Effect in Noncollinear Magnets”. In: *Phys. Rev. Lett.* **95** (2005), p. 057205. URL: <https://link.aps.org/doi/10.1103/PhysRevLett.95.057205>.
- [119] H. T. Ueda and T. Momoi. “Nematic phase and phase separation near saturation field in frustrated ferromagnets”. In: *Phys. Rev. B* **87** (2013), p. 144417. URL: <https://link.aps.org/doi/10.1103/PhysRevB.87.144417>.
- [120] O. A. Starykh and L. Balents. “Excitations and quasi-one-dimensionality in field-induced nematic and spin density wave states”. In: *Phys. Rev. B* **89** (2014), p. 104407. URL: <https://link.aps.org/doi/10.1103/PhysRevB.89.104407>.
- [121] R. M. Wilcox. “Bounds for the Isothermal, Adiabatic, and Isolated Static Susceptibility Tensors”. In: *Phys. Rev.* **174** (1968), pp. 624–629. URL: <https://link.aps.org/doi/10.1103/PhysRev.174.624>.
- [122] F. Schrettle et al. “Magnetic-field induced multiferroicity in a quantum critical frustrated spin liquid”. In: *Phys. Rev. B* **87** (2013), 121105(R). URL: <https://link.aps.org/doi/10.1103/PhysRevB.87.121105>.
- [123] M. Matsumoto et al. “Magnon Dispersion in the Field-Induced Magnetically Ordered Phase of  $\text{TlCuCl}_3$ ”. In: *Phys. Rev. Lett.* **89** (2002), p. 077203. URL: <https://link.aps.org/doi/10.1103/PhysRevLett.89.077203>.
- [124] A. Narayan et al. “Multiferroic quantum criticality”. In: *Nat. Mater.* **18.3** (2019), p. 223. URL: <https://doi.org/10.1038/s41563-018-0255-6>.
- [125] P. Chandra. “Multifunctionality goes quantum critical”. In: *Nature materials* **18.3** (2019), pp. 197–198. URL: <https://doi.org/10.1038/s41563-019-0302-y>.

- [126] A. Fujimura et al. "Comparison With Ground States of Frustrated Quantum Spin Chain Systems  $A_2Cu_2Mo_3O_{12}$  ( $A = Rb$  and  $Cs$ )". In: *IEEE Trans. Magn* **52.7** (2016), p. 1.
- [127] S. Hayashida et al. "Critical dielectric susceptibility at a magnetic BEC quantum critical point". In: *Phys. Rev. Research* **3** (2021), p. 033053. URL: <https://link.aps.org/doi/10.1103/PhysRevResearch.3.033053>.
- [128] D. Flavián et al. "Magnetic phase diagram of the linear quantum ferro-antiferromagnet  $Cs_2Cu_2Mo_3O_{12}$ ". In: *Phys. Rev. B* **101** (2020), p. 224408. URL: <https://link.aps.org/doi/10.1103/PhysRevB.101.224408>.
- [129] S. Jiang et al. "Where is the Quantum Spin Nematic?" In: *Phys. Rev. Lett.* **130** (2023), p. 116701. URL: <https://link.aps.org/doi/10.1103/PhysRevLett.130.116701>.
- [130] M. Hase et al. "Magnetism of  $A_2Cu_2Mo_3O_{12}$  ( $A = Rb$  or  $Cs$ ): Model compounds of a one-dimensional spin-1/2 Heisenberg system with ferromagnetic first-nearest-neighbor and antiferromagnetic second-nearest-neighbor interactions". In: *Journal of applied physics* **97** (2005), 10B303. URL: <https://doi.org/10.1063/1.1851675>.
- [131] A. Fujimura et al. "Comparison With Ground States of Frustrated Quantum Spin Chain Systems  $A_2Cu_2Mo_3O_{12}$  ( $A = Rb$  and  $Cs$ )". In: *IEEE Transactions on Magnetics* **52** (2016), pp. 1–3. URL: <https://ieeexplore.ieee.org/document/7387772/>.
- [132] T. Hamasaki et al. "Effects of high pressure on  $A_2Cu_2Mo_3O_{12}$  ( $A = Rb, Cs$ ): A one-dimensional system with competing ferromagnetic and antiferromagnetic interactions". In: *Journal of Magnetism and Magnetic Materials* **310** (2007), e394–e396. URL: <https://doi.org/10.1016/j.jmmm.2006.10.370>.
- [133] Y. Hoshino et al. "Ground state of the competing spin chain  $Cs_2Cu_2Mo_3O_{12}$ ". In: *Proceedings of the International Conference on Strongly Correlated Electron Systems (SCES2013)*. 2014, p. 014012. URL: <https://doi.org/10.7566/JPSCP.3.014012>.
- [134] T. Goto et al. "NMR and  $\mu$ -SR study on competing Heisenberg chain  $Cs_2Cu_2Mo_3O_{12}$ ". In: *Journal of Physics: Conference Series*. Vol. 828. IOP Publishing. 2017, p. 012017. URL: <https://iopscience.iop.org/article/10.1088/1742-6596/828/1/012017>.
- [135] A. Yagi et al. " $^{133}Cs$ -NMR study on aligned powder of competing spin chain compound  $Cs_2Cu_2Mo_3O_{12}$ ". In: *Journal of Physics: Conference Series*. Vol. 969. IOP Publishing. 2018, p. 012125. URL: <https://iopscience.iop.org/article/10.1088/1742-6596/969/1/012125>.
- [136] K. Matsui et al. "Ground state of quasi-one dimensional competing spin chain  $Cs_2Cu_2Mo_3O_{12}$  at zero and finite fields". In: *Proceedings of the 14th International Conference on Muon Spin Rotation, Relaxation and Resonance ( $\mu$ SR2017)*. 2018, p. 011008. URL: <https://doi.org/10.7566/JPSCP.21.011008>.
- [137] S. F. Solodovnikov and Z. A. Solodovnikova. "New structure type in the morphotropic series of  $A^{2+}M_2^{2+}(MoO_4)_3$ : Crystal structure of  $Rb_2Cu_2(MoO_4)_3$ ". In: *Journal of structural chemistry* **38** (1997), pp. 765–771. URL: <https://doi.org/10.1007/BF02763890>.

- [138] H. Ueda and S. Onoda. “Roles of easy-plane and easy-axis XXZ anisotropy and bond alternation in a frustrated ferromagnetic spin- $\frac{1}{2}$  chain”. In: *Phys. Rev. B* **101** (2020), p. 224439. URL: <https://link.aps.org/doi/10.1103/PhysRevB.101.224439>.
- [139] N. Reynolds et al. “Magnetoelectric coupling without long-range magnetic order in the spin- $\frac{1}{2}$  multiferroic  $\text{Rb}_2\text{Cu}_2\text{Mo}_3\text{O}_{12}$ ”. In: *Phys. Rev. B* **99** (2019), p. 214443. URL: <https://link.aps.org/doi/10.1103/PhysRevB.99.214443>.
- [140] N. Ng et al. “Electron-beam driven relaxation oscillations in ferroelectric nanodisks”. In: *Applied Physics Letters* **107.15** (2015), p. 152902. URL: <https://doi.org/10.1063/1.4932653>.
- [141] A. K. Jonscher. “Dielectric relaxation in solids”. In: *Journal of Physics D: Applied Physics* **32.14** (1999), R57. URL: <https://dx.doi.org/10.1088/0022-3727/32/14/201>.
- [142] G. G. Raju. *Dielectrics in electric fields: Tables, Atoms, and Molecules*. CRC press, 2017. URL: <https://doi.org/10.1201/9781315373270>.
- [143] P. J. W. Debye. *Polar molecules*. Dover publications, 1929.
- [144] S. H. Glarum. “Dielectric relaxation of polar liquids”. In: *The Journal of Chemical Physics* **33.5** (1960), pp. 1371–1375. URL: <https://doi.org/10.1063/1.1731414>.
- [145] A. North. “Dielectric relaxation in polymer solutions”. In: *Chemical Society Reviews* **1.1** (1972), pp. 49–72. URL: <https://doi.org/10.1039/CS9720100049>.
- [146] B. E. Vugmeister and M. D. Glinchuk. “Dipole glass and ferroelectricity in random-site electric dipole systems”. In: *Rev. Mod. Phys.* **62** (1990), pp. 993–1026. URL: <https://link.aps.org/doi/10.1103/RevModPhys.62.993>.
- [147] F. Kremer and A. Schönhal. *Broadband dielectric spectroscopy*. Springer Science & Business Media, 2002.
- [148] O. Bidault et al. “Space-charge relaxation in perovskites”. In: *Phys. Rev. B* **49** (1994), pp. 7868–7873. URL: <https://link.aps.org/doi/10.1103/PhysRevB.49.7868>.
- [149] R. Viana et al. “Dielectric spectroscopy in  $\text{SrTiO}_3$ ”. In: *Phys. Rev. B* **50** (1994), pp. 601–604. URL: <https://link.aps.org/doi/10.1103/PhysRevB.50.601>.
- [150] C. Ang et al. “Dielectric and ultrasonic anomalies at 16, 37, and 65 K in  $\text{SrTiO}_3$ ”. In: *Phys. Rev. B* **59** (1999), pp. 6661–6664. URL: <https://link.aps.org/doi/10.1103/PhysRevB.59.6661>.
- [151] J. F. Scott. “Comment on the physical mechanisms of the 37 K and 65 K anomalies in strontium titanate”. In: *Journal of Physics: Condensed Matter* **11.41** (1999), p. 8149. URL: <https://dx.doi.org/10.1088/0953-8984/11/41/317>.
- [152] V. N. Krivoruchko. “Electrically active magnetic excitations in antiferromagnets (Review Article)”. In: *Low Temperature Physics* **38.9** (2012), pp. 807–818. URL: <https://doi.org/10.1063/1.4752093>.
- [153] T. N. Stanislavchuk et al. “Magnon and electromagnon excitations in multiferroic  $\text{DyFeO}_3$ ”. In: *Phys. Rev. B* **93** (2016), p. 094403. URL: <https://link.aps.org/doi/10.1103/PhysRevB.93.094403>.

- [154] N. Kida et al. “Electrically driven spin excitation in the ferroelectric magnet  $\text{DyMnO}_3$ ”. In: *Phys. Rev. B* **78** (2008), p. 104414. URL: <https://link.aps.org/doi/10.1103/PhysRevB.78.104414>.
- [155] C. P. Grams et al. “Observation of chiral solitons in  $\text{LiCuVO}_4$ ”. In: *Communications Physics* **5.1** (2022), pp. 1–7. URL: <https://doi.org/10.1038/s42005-022-00811-8>.
- [156] O. Bidault et al. “Polaronic relaxation in perovskites”. In: *Phys. Rev. B* **52** (1995), pp. 4191–4197. URL: <https://link.aps.org/doi/10.1103/PhysRevB.52.4191>.
- [157] D. Emin. “Optical properties of large and small polarons and bipolarons”. In: *Phys. Rev. B* **48** (1993), pp. 13691–13702. URL: <https://link.aps.org/doi/10.1103/PhysRevB.48.13691>.
- [158] L. Zhang and Z.-J. Tang. “Polaron relaxation and variable-range-hopping conductivity in the giant-dielectric-constant material  $\text{CaCu}_3\text{Ti}_4\text{O}_{12}$ ”. In: *Phys. Rev. B* **70** (2004), p. 174306. URL: <https://link.aps.org/doi/10.1103/PhysRevB.70.174306>.
- [159] L. Facheris et al. “Spin Density Wave versus Fractional Magnetization Plateau in a Triangular Antiferromagnet”. In: *Phys. Rev. Lett.* **129** (2022), p. 087201. URL: <https://link.aps.org/doi/10.1103/PhysRevLett.129.087201>.
- [160] A. I. Smirnov et al. “Triangular lattice antiferromagnet  $\text{RbFe}(\text{MoO}_4)_2$  in high magnetic fields”. In: *Phys. Rev. B* **75.13** (2007), p. 134412. URL: <https://journals.aps.org/prb/abstract/10.1103/PhysRevB.75.134412>.
- [161] F. Levy et al. “Field dependence of the quantum ground state in the Shastry-Sutherland system  $\text{SrCu}_2(\text{BO}_3)_2$ ”. In: *EPL (Europhysics Letters)* **81.6** (2008), p. 67004. URL: <https://iopscience.iop.org/article/10.1209/0295-5075/81/67004>.
- [162] N. Wada, K. Ubukoshi, and K. Hirakawa. “Incommensurate magnetic phase transitions in the triangular XY-like antiferromagnet  $\text{RbFeCl}_3$ ”. In: *J. Phys. Soc. Jpn.* **51.9** (1982), pp. 2833–2839. URL: <https://journals.jps.jp/doi/10.1143/JPSJ.51.2833>.
- [163] M. Mourigal et al. “Evidence of a bond-nematic phase in  $\text{LiCuVO}_4$ ”. In: *Phys. Rev. Lett.* **109.2** (2012), p. 027203. URL: <https://link.aps.org/doi/10.1103/PhysRevLett.109.027203>.
- [164] V. K. Bhartiya et al. “Presaturation phase with no dipolar order in a quantum ferro-antiferromagnet”. In: *Phys. Rev. Research* **1.3** (2019), p. 033078. URL: <https://link.aps.org/doi/10.1103/PhysRevResearch.1.033078>.
- [165] E. Kermarrec et al. “Classical Spin Liquid State in the  $S = 5/2$  Heisenberg Kagome Antiferromagnet  $\text{Li}_9\text{Fe}_3(\text{P}_2\text{O}_7)_3(\text{PO}_4)_2$ ”. In: *Phys. Rev. Lett.* **127.15** (2021), p. 157202. URL: <https://link.aps.org/doi/10.1103/PhysRevLett.127.157202>.
- [166] B. Bernu et al. “Exchange energies of kagellite from high-temperature series analysis of the kagome lattice  $J_2$ - $J_2$ - $J_d$ -Heisenberg model”. In: *Phys. Rev. B* **87.15** (2013), p. 155107. URL: <https://link.aps.org/doi/10.1103/PhysRevB.87.155107>.
- [167] H. K. Yoshida. “Frustrated Kagome Antiferromagnets under High Magnetic Fields”. In: *J. Phys. Soc. Jpn.* **91.10** (2022), p. 101003. URL: <https://doi.org/10.7566/JPSJ.91.101003>.

- [168] M. D. LeBlanc et al. “Monte Carlo simulations of the fcc kagome lattice: Competition between triangular frustration and cubic anisotropy”. In: *Phys. Rev. B* **88.9** (2013), p. 094406. URL: <https://link.aps.org/doi/10.1103/PhysRevB.88.094406>.
- [169] H. Yoshida et al. “Unusual Magnetic State with Dual Magnetic Excitations in the Single Crystal of  $S = 1/2$  Kagome Lattice Antiferromagnet  $\text{CaCu}_3(\text{OH})_6\text{Cl}_2 \cdot 0.6\text{H}_2\text{O}$ ”. In: *J. Phys. Soc. Jpn.* **86.3** (2017), p. 033704. URL: <https://doi.org/10.7566/JPSJ.86.033704>.
- [170] R. Okuma et al. “A series of magnon crystals appearing under ultrahigh magnetic fields in a kagomé antiferromagnet”. In: *Nat. Comm.* **10.1** (2019), pp. 1–7. URL: <https://doi.org/10.1038/s41467-019-09063-7>.
- [171] H. O. Jeschke, H. Nakano, and T Sakai. “From kagome strip to kagome lattice: Realizations of frustrated  $S = 1/2$  antiferromagnets in Ti(III) fluorides”. In: *Phys. Rev. B* **99.14** (2019), 140410(R). URL: <https://link.aps.org/doi/10.1103/PhysRevB.99.140410>.
- [172] S. Jahromi et al. “Spin-1/2 kagome Heisenberg antiferromagnet with strong breathing anisotropy”. In: *SciPost Phys.* **9.6** (2020), p. 092. URL: <https://doi.org/10.21468/SciPostPhys.9.6.092>.
- [173] M. Ashtar et al. “A New Family of Disorder-Free Rare-Earth-Based Kagome Lattice Magnets: Structure and Magnetic Characterizations of  $\text{RE}_3\text{BWO}_9$  ( $\text{RE} = \text{Pr}, \text{Nd}, \text{Gd-Ho}$ ) Boratungstates”. In: *Inor. Chem.* **59.8** (2020), pp. 5368–5376. URL: <https://doi.org/10.1021/acs.inorgchem.9b03547>.
- [174] V. Krut’ko, A. Belik, and G. Lysanova. “Structures of nonlinear hexagonal boratungstates  $\text{Ln}_3\text{BWO}_9$  ( $\text{Ln} = \text{La}, \text{Pr}, \text{Nd}, \text{Sm}, \text{Gd}, \text{Tb}, \text{Dy}$ )”. In: *Russian journal of inorganic chemistry* **51** (2006), pp. 884–889. URL: <https://doi.org/10.1134/S0036023606060064>.
- [175] J. B. Goodenough. “Spin-Orbit-Coupling Effects in Transition-Metal Compounds”. In: *Phys. Rev.* **171** (1968), pp. 466–479. URL: <https://link.aps.org/doi/10.1103/PhysRev.171.466>.
- [176] J. Kanamori. “Superexchange interaction and symmetry properties of electron orbitals”. In: *Journal of Physics and Chemistry of Solids* **10.2-3** (1959), pp. 87–98. URL: [https://doi.org/10.1016/0022-3697\(59\)90061-7](https://doi.org/10.1016/0022-3697(59)90061-7).
- [177] K. Stevens. “Matrix elements and operator equivalents connected with the magnetic properties of rare earth ions”. In: *Proceedings of the Physical Society. Section A* **65.3** (1952), p. 209. URL: <https://dx.doi.org/10.1088/0370-1298/65/3/308>.
- [178] M. T. Hutchings. “Point-charge calculations of energy levels of magnetic ions in crystalline electric fields”. In: **16** (1964), pp. 227–273. URL: [https://doi.org/10.1016/S0081-1947\(08\)60517-2](https://doi.org/10.1016/S0081-1947(08)60517-2).
- [179] A. Scheie. “PyCrystalField: software for calculation, analysis and fitting of crystal electric field Hamiltonians”. In: *Journal of Applied Crystallography* **54.1** (2021), pp. 356–362. URL: <https://doi.org/10.1107/S160057672001554X>.

- [180] S Edvardsson and M Klintonberg. "Role of the electrostatic model in calculating rare-earth crystal-field parameters". In: *Journal of Alloys and Compounds* **275-277** (1998), pp. 230–233. URL: <https://www.sciencedirect.com/science/article/pii/S0925838898003090>.
- [181] D. Newman and B. Ng. *Crystal Field Handbook*. Cambridge University Press, 2000.
- [182] S. E. Dutton et al. "Quantum Spin Liquid in Frustrated One-Dimensional LiCuSbO<sub>4</sub>". In: *Phys. Rev. Lett.* **108** (2012), p. 187206. URL: <https://link.aps.org/doi/10.1103/PhysRevLett.108.187206>.
- [183] K. Kimura et al. "Quantum fluctuations in spin-ice-like Pr<sub>2</sub>Zr<sub>2</sub>O<sub>7</sub>". In: *Nat. Comm.* **4.1** (2013), pp. 1–6. URL: <https://doi.org/10.1038/ncomms2914>.
- [184] B Bleaney. "Hyperfine Interactions in Rare-Earth Metals". In: *J. Appl. Phys.* **34.4** (1963), pp. 1024–1031. URL: <https://doi.org/10.1063/1.1729355>.
- [185] B Andracka and Y Takano. "Simultaneous measurements of heat capacity and spin-lattice relaxation time in high magnetic field at low temperature". In: *Review of scientific instruments* **67.12** (1996), pp. 4256–4260. URL: <https://doi.org/10.1063/1.1147523>.
- [186] B Andracka and Y Takano. "Note: Relaxation heat capacity measurements at low temperatures: Dealing with nuclear contribution". In: *Review of Scientific Instruments* **82.1** (2011), p. 016103. URL: <https://doi.org/10.1063/1.3521656>.
- [187] C. Rüegg et al. "Thermodynamics of the Spin Luttinger Liquid in a Model Ladder Material". In: *Phys. Rev. Lett.* **101** (2008), p. 247202. URL: <https://link.aps.org/doi/10.1103/PhysRevLett.101.247202>.
- [188] D. Blosser et al. "z = 2 Quantum Critical Dynamics in a Spin Ladder". In: *Phys. Rev. Lett.* **121** (2018), p. 247201. URL: <https://link.aps.org/doi/10.1103/PhysRevLett.121.247201>.
- [189] V. E. Korepin and N. A. Slavnov. "The time dependent correlation function of an impenetrable Bose gas as a Fredholm minor. I". In: *Commun. Math. Phys.* **129.1** (1990), pp. 103–113. URL: <https://doi.org/10.1007/BF02096781>.
- [190] S. Sachdev, T. Senthil, and R. Shankar. "Finite-temperature properties of quantum antiferromagnets in a uniform magnetic field in one and two dimensions". In: *Phys. Rev. B* **50** (1994), pp. 258–272. URL: <https://link.aps.org/doi/10.1103/PhysRevB.50.258>.
- [191] Y. Kohama et al. "AC measurement of heat capacity and magnetocaloric effect for pulsed magnetic fields". In: *Rev. Sci. Instrum.* **81.10** (2010), p. 104902. URL: <https://doi.org/10.1063/1.3475155>.
- [192] Y. Kohama. "High-Field Calorimetric Studies on Low-Dimensional and Frustrated Quantum Magnets". In: *J. Phys. Soc. Jpn.* **91.10** (2022), p. 101004. URL: <https://doi.org/10.7566/JPSJ.91.101004>.
- [193] M. C. Hatnean et al. "Structural and magnetic investigations of single-crystalline neodymium zirconate pyrochlore Nd<sub>2</sub>Zr<sub>2</sub>O<sub>7</sub>". In: *Phys. Rev. B* **91** (2015), p. 174416. URL: <https://link.aps.org/doi/10.1103/PhysRevB.91.174416>.

- [194] J. Xu et al. “Magnetic structure and crystal-field states of the pyrochlore antiferromagnet  $\text{Nd}_2\text{Zr}_2\text{O}_7$ ”. In: *Phys. Rev. B* **92** (2015), p. 224430. URL: <https://link.aps.org/doi/10.1103/PhysRevB.92.224430>.
- [195] M Ashtar et al. “ $\text{REZnAl}_{11}\text{O}_{19}$  (RE= Pr, Nd, Sm–Tb): a new family of ideal 2D triangular lattice frustrated magnets”. In: *Journal of Materials Chemistry C* **7.32** (2019), pp. 10073–10081. URL: <https://doi.org/10.1039/C9TC02643F>.
- [196] F. A. Cevallos, S. Guo, and R. Cava. “Magnetic properties of lithium-containing rare earth garnets  $\text{Li}_3\text{RE}_3\text{Te}_2\text{O}_{12}$  (RE= Y, Pr, Nd, Sm–Lu)”. In: *Materials Research Express* **5.12** (2018), p. 126106. URL: <https://doi.org/10.1088/2053-1591/aae22c>.
- [197] Y. A. Izyumov, V. E. Naish, and R. P. Ozerov. *Neutron Diffraction of Magnetic Materials*. Springer New York, NY, 2012. URL: <https://doi.org/10.1007/978-1-4615-3658-1>.
- [198] J. Rodríguez-Carvajal. “Recent advances in magnetic structure determination by neutron powder diffraction”. In: *Physica B: Condensed Matter* **192.1** (1993), pp. 55–69. ISSN: 0921-4526. URL: <https://www.sciencedirect.com/science/article/pii/092145269390108I>.
- [199] F. Song et al. “Magnetic field tuned anisotropic quantum phase transition in the distorted kagome antiferromagnet  $\text{Nd}_3\text{BWO}_9$ ”. In: *Phys. Rev. B* **108** (2023), p. 214410. URL: <https://link.aps.org/doi/10.1103/PhysRevB.108.214410>.
- [200] T Sakai and H. Nakano. “Critical magnetization behavior of the triangular- and kagome-lattice quantum antiferromagnets”. In: *Phys. Rev. B* **83.10** (2011), 100405(R). URL: <https://link.aps.org/doi/10.1103/PhysRevB.83.100405>.
- [201] S. Capponi et al. “Numerical study of magnetization plateaus in the spin-1/2 kagome Heisenberg antiferromagnet”. In: *Phys. Rev. B* **88.14** (2013), p. 144416. URL: <https://link.aps.org/doi/10.1103/PhysRevB.88.144416>.
- [202] J.-B. Fouet et al. “Frustrated three-leg spin tubes: From spin 1/2 with chirality to spin 3/2”. In: *Phys. Rev. B* **73** (2006), p. 014409. URL: <https://link.aps.org/doi/10.1103/PhysRevB.73.014409>.
- [203] K. Yonaga and N. Shibata. “Ground state phase diagram of twisted three-leg spin tube in magnetic field”. In: *J. Phys. Soc. Jpn.* **84.9** (2015), p. 094706. URL: <https://doi.org/10.7566/JPSJ.84.094706>.
- [204] T. Sakai et al. “Exotic Quantum Phase Transitions in Spin Nanotubes”. In: *J. Phys.* Vol. 400. IOP Publishing, 2012. URL: <https://iopscience.iop.org/article/10.1088/1742-6596/400/3/032075>.
- [205] O. Tchernyshyov, R Moessner, and S. L. Sondhi. “Order by distortion and string modes in pyrochlore antiferromagnets”. In: *Phys. Rev. Lett.* **88.6** (2002), p. 067203. URL: <https://link.aps.org/doi/10.1103/PhysRevLett.88.067203>.
- [206] T. Senthil et al. “Deconfined quantum critical points”. In: *Science* **303.5663** (2004), pp. 1490–1494. URL: <https://doi.org/10.1126/science.1091806>.
- [207] C. Wang et al. “Deconfined Quantum Critical Points: Symmetries and Dualities”. In: *Phys. Rev. X* **7** (2017), p. 031051. URL: <https://link.aps.org/doi/10.1103/PhysRevX.7.031051>.

- [208] Y. Tokiwa et al. “Characteristic signatures of quantum criticality driven by geometrical frustration”. In: *Science Advances* **1.3** (2015), e1500001. URL: <https://doi.org/10.1126/sciadv.1500001>.
- [209] J Nagl et al. “Excitation Spectrum and Spin Hamiltonian of the Frustrated Quantum Ising Magnet  $\text{Pr}_3\text{BWO}_9$ ”. In: *arXiv preprint arXiv:2402.14107* (2024). URL: <https://doi.org/10.48550/arXiv.2402.14107>.
- [210] K. Y. Zeng et al. “Local evidence for collective spin excitations in the distorted kagome antiferromagnet  $\text{Pr}_3\text{BWO}_9$ ”. In: *Phys. Rev. B* **104.15** (2021), p. 155150. URL: <https://link.aps.org/doi/10.1103/PhysRevB.104.155150>.
- [211] K.-Y. Zeng et al. “Incommensurate Magnetic Order in  $\text{Sm}_3\text{BWO}_9$  with Distorted Kagome Lattice”. In: *Chinese Phys. Lett.* **39.10** (2022), p. 107501. URL: <http://cpl.iphy.ac.cn/Y2022/V39/I10/107501>.
- [212] G. Grüner. “The dynamics of spin-density waves”. In: *Rev. Mod. Phys.* **66** (1994), pp. 1–24. URL: <https://link.aps.org/doi/10.1103/RevModPhys.66.1>.
- [213] O. A. Starykh. “Unusual ordered phases of highly frustrated magnets: a review”. In: *Reports on Progress in Physics* **78.5** (2015), p. 052502. URL: <https://doi.org/10.1088/0034-4885/78/5/052502>.
- [214] S. Kimura et al. “Longitudinal Spin Density Wave Order in a Quasi-1D Ising-like Quantum Antiferromagnet”. In: *Phys. Rev. Lett.* **101** (2008), p. 207201. URL: <https://link.aps.org/doi/10.1103/PhysRevLett.101.207201>.
- [215] E. Canévet et al. “Field-induced magnetic behavior in quasi-one-dimensional Ising-like antiferromagnet  $\text{BaCo}_2\text{V}_2\text{O}_8$ : A single-crystal neutron diffraction study”. In: *Phys. Rev. B* **87** (2013), p. 054408. URL: <https://link.aps.org/doi/10.1103/PhysRevB.87.054408>.
- [216] L Shen et al. “Magnetic phase diagram of the quantum spin chain compound  $\text{SrCo}_2\text{V}_2\text{O}_8$ : a single-crystal neutron diffraction study”. In: *New Journal of Physics* **21.7** (2019), p. 073014. URL: <https://doi.org/10.1088/1367-2630/ab2b7a>.
- [217] L. Wu et al. “Tomonaga–Luttinger liquid behavior and spinon confinement in  $\text{YbAlO}_3$ ”. In: *Nature communications* **10.1** (2019), p. 698. URL: <https://doi.org/10.1038/s41467-019-08485-7>.
- [218] C. E. Agrapidis, J. van den Brink, and S. Nishimoto. “Field-induced incommensurate ordering in Heisenberg chains coupled by Ising interaction: Model for ytterbium aluminum perovskite  $\text{YbAlO}_3$ ”. In: *Phys. Rev. B* **99** (2019), p. 224423. URL: <https://link.aps.org/doi/10.1103/PhysRevB.99.224423>.
- [219] S. E. Nikitin et al. “Multiple fermion scattering in the weakly coupled spin-chain compound  $\text{YbAlO}_3$ ”. In: *Nature communications* **12.1** (2021), p. 3599. URL: <https://doi.org/10.1038/s41467-021-23585-z>.
- [220] L. Facheris et al. “Spin Density Wave versus Fractional Magnetization Plateau in a Triangular Antiferromagnet”. In: *Phys. Rev. Lett.* **129** (2022), p. 087201. URL: <https://link.aps.org/doi/10.1103/PhysRevLett.129.087201>.

- [221] F. D. M. Haldane. “General Relation of Correlation Exponents and Spectral Properties of One-Dimensional Fermi Systems: Application to the Anisotropic  $S = \frac{1}{2}$  Heisenberg Chain”. In: *Phys. Rev. Lett.* **45** (1980), pp. 1358–1362. URL: <https://link.aps.org/doi/10.1103/PhysRevLett.45.1358>.
- [222] N. Bogoliubov, A. Izergin, and V. Korepin. “Critical exponents for integrable models”. In: *Nuclear Physics B* **275.4** (1986), pp. 687–705. URL: [https://doi.org/10.1016/0550-3213\(86\)90579-1](https://doi.org/10.1016/0550-3213(86)90579-1).
- [223] K. Okunishi and T. Suzuki. “Field-induced incommensurate order for the quasi-one-dimensional XXZ model in a magnetic field”. In: *Phys. Rev. B* **76** (2007), p. 224411. URL: <https://link.aps.org/doi/10.1103/PhysRevB.76.224411>.
- [224] S. E. Palmer and J. T. Chalker. “Order induced by dipolar interactions in a geometrically frustrated antiferromagnet”. In: *Phys. Rev. B* **62** (2000), pp. 488–492. URL: <https://link.aps.org/doi/10.1103/PhysRevB.62.488>.
- [225] H. Shiba and N. Suzuki. “Incommensurate Magnetic Structures in Triangular Antiferromagnets Caused by the Dipole-Dipole Interaction: a Realization of Conical-Point Instability”. In: *J. Phys. Soc. Jpn.* **51.11** (1982), pp. 3488–3496. URL: <https://doi.org/10.1143/JPSJ.51.3488>.
- [226] N. Suzuki. “A microscopic theory of the phase transition in RbFeCl<sub>3</sub>-type hexagonal antiferromagnets: effects of the dipole-dipole interaction”. In: *J. Phys. Soc. Jpn.* **52.9** (1983), pp. 3199–3207. URL: <https://doi.org/10.1143/JPSJ.52.3199>.
- [227] R. S. Gekht and V. I. Ponomarev. “Phase transitions in spin systems with frustrations”. In: *Phase Transitions* **20.1-2** (1990), pp. 27–71. URL: <https://doi.org/10.1080/01411599008206867>.
- [228] V. Dyadkin et al. “A new multipurpose diffractometer PILATUS@ SNBL”. In: *Journal of synchrotron radiation* **23.3** (2016), pp. 825–829. URL: <https://doi.org/10.1107/S1600577516002411>.
- [229] H. Nowell et al. “I19, the small-molecule single-crystal diffraction beamline at Diamond Light Source”. In: *Journal of synchrotron radiation* **19.3** (2012), pp. 435–441. URL: <https://doi.org/10.1107/S0909049512008801>.
- [230] G. Winter et al. “DIALS: implementation and evaluation of a new integration package”. In: *Acta Crystallographica Section D: Structural Biology* **74.2** (2018), pp. 85–97. URL: <https://doi.org/10.1107/S2059798317017235>.
- [231] G. Winter. “xia2: an expert system for macromolecular crystallography data reduction”. In: *Journal of applied crystallography* **43.1** (2010), pp. 186–190. URL: <https://doi.org/10.1107/S0021889809045701>.



# Curriculum Vitae

Daniel Flavian Blasco

	<b>Organisation</b>	<b>Duration</b>
PhD / Dr.: PhD in Physics Andrey Zheludev	ETH Zürich - ETHZ, CH Department of Physics	07.2020 - 04.2024 3 years 10 months
Master: M. Sc. in Physics Andrey Zheludev	ETH Zürich - ETHZ, CH Department of Physics	09.2018 - 05.2020 1 year 9 months
Bachelor: B. Sc. in Physics Javier Campo Ruiz	Universidad de Zaragoza, ES Facultad de Ciencias	09.2014 - 07.2018 3 years 11 months



